UNIVERSITY OF CALIFORNIA

Santa Barbara

Understanding Rheology and Microstructure of Thermoresponsive Nanoemulsions as a Model System of Colloidal Suspensions

A dissertation submitted in partial satisfaction of the

requirements for the degree Doctor of Philosophy

in Chemical Engineering

by

Juntae Kim

Committee in charge:

Professor Matthew E. Helgeson, Chair

Professor Jacob Israelachvili

Professor Todd Squires

Professor Philip A. Pincus

December 2016

The dissertation of Juntae Kim is approved.

_____

Jacob Israelachvili

_____

Todd Squires

_____

Philip A. Pincus

_____

Matthew E. Helgeson, Chair

November 2016

Understanding Rheology and Microstructure of Thermoresponsive Nanoemulsions as a Model System of Colloidal Suspensions

by

Juntae Kim

ACKNOWLEDGEMENTS

First of all, I would like to express my sincere gratitude to my thesis advisor Prof. Matthew E. Helgeson, who have encouraged me to pursue my research and guided me to complete my doctoral thesis. His enthusiasm, continuous support and immense knowledge for his research helped me successfully carried out my Ph.D. research. I have been very happy to have him as my academic mentor and very honor to be graduated as his first Ph.D. student.

Besides my advisor, I would like to acknowledge the rest of my thesis committee: Prof. Todd Squires, Prof. Jacob Israelachvili, and Prof. Philip A. Pincus. During my Ph.D. study, they have been steering me in the right direction to complete my thesis. Thanks also to Dr. Yongxiang, Dr. Merger and undergraduates, who have worked with me to complete my research projects. I also would like to acknowledge helpful discussions from our Helgeson group members. I also thank Yun Liu, Katie Weigandt and Paul Butler at NIST, as well as Rachel Behrens in MRL.

I would like to thank my friends, both in Santa Barbara and South Korea, who have been supported me in the last five years. And finally, I must express my sincere thanks to my family, especially my parents and younger brother, for providing me with endless support and encouragement throughout my five years of study. This accomplishment would not have been possible without everyone mentioned above.

VITA OF JUNTAE KIM

November 2016

EDUCATION

Bachelor of Science in Chemical and Biomolecular Engineering, Korea Advanced Institute of Science of Technology, January 2011 (summa cum laude)

Doctor of Philosophy in Chemical Engineering, University of California, Santa Barbara, December 2016 (expected)

PUBLICATIONS

J. Kim, Y. Gao, C. Hebebrand, E. Peirtsegaele, M.E. Helgeson, "Polymer-surfactant complexation as a generic route to responsive viscoelastic nanoemulsions", Soft Matter 9 (29), 6897-6910 (2013).

J. Kim, D. Merger, M. Wilhelm and M.E. Helgeson, “Microstructure and nonlinear signatures of yielding in a heterogeneous colloidal gel under large amplitude oscillatory shear”, Journal of Rheology, 58, 1359 (2014).

Y. Gao, **J. Kim**, and M.E. Helgeson, "Microdynamics and arrest of coarsening during spinodal decomposition in thermoreversible colloidal gels", Soft Matter 11(32): 6360-6370 (2015). Cover Article.

E. Filippidi, D.G. DeMartini, P. Malo de Molina, E.W. Danner, **J. Kim**, M.E. Helgeson, J.H. Waite, M.T. Valentine, “The microscopic Network structure of mussel (Mytilus) adhesive plaques”, Journal of the Royal Society Interface 12.113 (2015): 20150827.

J. Kim and M.E. Helgeson, “Shear-induced clustering of Brownian colloids in associative polymer networks at moderate Peclet number”, Physical Review Fluids, Submitted.

D. Merger, K. Reinheimer, M. Grosso, J.M. Brader, M. Ballauff, **J. Kim**, M.E. Helgeson and M. Wilhelm,“Large Amplitude Oscillatory Shear Applications for the Characterization of Dispersed Systems”, Colloid Process Engineering, 2015, Springer, Switzerland: pp. 113-142.

ABSTRACT

Understanding Rheology and Microstructure of Thermoresponsive Nanoemulsions as a Model System of Colloidal Suspensions

by

Juntae Kim

Nanoemulsions – nanoscale droplet suspensions – in polymeric solution have been widely used in many fields from consumer products to advanced technology. Due to their nanoscopic dimensions, they exhibit unique physical behavior in terms of their rheology and microstructure, both at rest and under flow. However, mechanisms that give rise the interesting phenomena observed in nanodroplet-polymer mixtures are poorly understood. Thus, the goals of this thesis are to develop a model nanoemulsion-polymer system to impart control over polymer-droplet and droplet-droplet interactions, use it to investigate the mechanisms colloidal behavior of nanodroplets in polymeric solutions, and to determine how these behaviors influence suspension microstructure, dynamics and rheology.

For these purposes, we choose to study thermoresponsive oil-in-water nanoemulsions as a model system. The systems include polydimethylsiloxane (PDMS) oil nanodroplets dispersed in aqueous mixtures of functionalized hydrophilic polymer (polyethylene glycol diacrylate, PEGDA) and ionic surfactant (sodium dodecyl sulfate, SDS). Combining calorimetry, rheology and scattering measurements, we show how

molecular self-assembly in the system can be used to control the viscoelasticity of the system, which remarkably follows time-temperature superposition, much like simpler polymer fluids, and suggests that polymer-surfactant complexation forms a transient polymer network between droplets. Systematic changes in the energy scale for complexation allows us to develop a simple model for the modulus and viscoelastic relaxation time. Furthermore, the relaxation time of the network in this model system can be varied by ten orders of magnitudes, providing advantages for fundamental studies.

We exploited the properties of this novel nanoemulsion system to study shear-induced clustering of colloid-polymer mixtures and its impact on fluid rheology. The system allows us to explore several limiting regimes of polymer and suspension dynamics. Combining rheological characterization with three-dimensionally-resolved flow-small angle neutron scattering measurements reveals that an excess of particle fluxes along compressional and vorticity axes of shear are the primary mechanism of clustering, and suggestes that short-range hydrodynamic forces dominate the clustering of Brownian suspensions in viscoelastic fluids.

Lastly, we used the thermoresponsive nanoemulsions to investigate the mechanisms of so-called “two-step” or “delayed” yielding in heterogeneous colloidal gels. At high temperatures, the model system forms colloidal gels with heterogeneous microstructure resembling arrested phase separation at elevated temperature caused by polymer-bridging interactions. Analyzing the sequence of mechanical processes during the intracycle yielding processes elucidates the detailed mechanism of frequency and strain amplitude-dependence of nonlinearlity. The nonlinear analysis also allows for characterization of the strain amplitude and rate-dependent yield stress and strain of the material. Furthermore, combining

large amplitude oscillatory shear measuremetns with simultaneous small and ultra-small angle neutron scattering reveals that, contrary to previous hypotheses, large-scale microstructural processes play an important, if not dominant, role in the yielding of heterogeneous colloidal gels.

The results of this thesis demonstrate that the rheology and the microstructural processes of nanoemulsions can be controlled through thermoresponsive polymer-surfactant-droplet association, which provides for sophisticated tuning of polymer-colloid and colloid-colloid interactions and dynamics, thus providing new routes and design rules for engineering the colloidal behavior of nanoemulsions.

TABLE OF CONTENTS

LIST OF FIGURES

LIST OF TABLES

Chapter 1

Introduction

1.1 Motivation

Emulsions are common in situations ranging from our everyday life to high technological applications such as foods [1], cosmetics [2,3], pharmaceuticals [4] and chemical synthesis [5]. Emulsions are defined as dispersions of droplets of one liquid phase within another, immiscible liquid phase. In order to stabilize the dispersed phase, emulsifiers, i.e. surfactants are typically added to the system. Usually, conventional emulsions are thermodynamically unstable, and diameter of the dispersed phase droplets range of 200 nm to 100 μm. Due to their size, they are typically called emulsions or macroemulsions.

By contrast, nanoemulsions are conventional emulsions in which the droplet size has been driven to the nanoscale. Due to their small droplet size (10~100 nm), nanoemulsions possess more complicated colloidal behavior than larger emulsions [6]. Compared to the macroemulsions, nanoemulsions are kinetically stable, whose physical properties, such as rheology and transparency, remain relatively constant for several months or even years [7]. This is primarily due to two factors. First, the resistance of nanoscale droplets to deformation, as will be described below, significantly reduces the rate of droplet coalescence. Second, the enhanced influence of Brownian motion leads to enhanced colloidal stability against gravitational separation compared to micron-scale emulsions. Nanoemulsions are also typically optically transparent since nanoscale droplets scatter little

lights in the range of visible wavelength [8], while macroscale emulsions appear turbid. Furthermore, nanoemulsions exhibit dramatic changes in rheological behavior compared to larger emulsions [9,10].

The primary reason for these differences lies in the drastic changes in the range of colloidal interactions as the size of the droplets decreases. For instance, in the case of repulsive emulsions, the longer range of soft repulsions (due to electrostatic or steric effects) relative to the droplet size results in a reduction in the volume fraction required for the onset of jamming [9]. By contrast, in the case of attractive emulsions, reduction of droplet size leads to a transition from paste-like to solid-like behaviors, which is derived by the increased relative attraction range [10]. These complicated behaviors make it difficult to formulate and process nanoemulsions for specific applications.

These unique physical properties of nanoemulsions make them ideal candidates for a wide range of applications. As previously mentioned, nanoemulsions have been widely used in foods [1] and consumer products [2-4]. Furthermore, nanoemulsions are appropriate candidates for nanoparticle-based drug delivery and pharmaceutical applications due to their ability to solubilize various biocompatible oil or water-soluble molecules [11-13]. The increased interfacial area due to their nanoscale size also increases transport efficiency of active materials. Finally, compared to microemulsions (which are thermodynamically stable emulsion systems), nanoemulsions are relatively stable to environmental and compositional changes such as temperature and additives in both dispersed and continuous phases. Thus, they are advantageous for use in templating nanoparticles with various morphologies [14].

To facilitate these applications, additives such as surfactants and polymers are added to the continuous phase in order to modify their colloidal behavior and rheology. For

example, polymers have been used as additives to increase the viscosity of nanoemulsions by increasing the viscosity of the continuous phase [15]. However, they can also change interactions between droplets, leading to changes in suspension microstructure. In applications that require precise control of nanoemulsion properties, it is critical to understand the effect of polymers on the colloidal behavior of nanodroplets.

Although polymers in the nanoemulsions influence on the colloidal behaviors, it has been difficult to systematically modified colloidal interactions. For example, in the nanoemulsion systems where the attractions induced by polymer depletion [3], introduction of polymers causes formation of irreversible aggregates [3]. Phillip *et al.* have shown measurements of depletion forces between emulsion droplets in the presence of polyelectrolytes. However, this system also has limitations for direct measurement of colloidal forces in higher polymer concentration regime that induces irreversible aggregation, which leads macroscopic changes in structure and rheological behavior.

The previous work motivates a significant need model nanoemulsion-polymer mixtures, in which polymer-droplet and droplet-droplet interactions can be systematically modified. In this work, we propose that such an ideal system would be nanoemulsions containing stimuli-responsive polymers in which polymer-droplet interactions can be dynamically tuned, allowing for careful study of how these interactions modify colloidal behavior in nanoemulsions. For this purpose, temperature can serve as a convenient stimulus, due to a number of well-established thermoresponsive polymer systems [16-20]. Such thermoresponsive nanoemulsions could also provide benefits in a number of practical engineering applications. For example, thermoresponsive behavior could allow for new and more efficient processing methods for nanoemulsions (e.g. emulsification, mixing, bottling,

etc.) due to better control of their rheological behavior. Therefore, the goal of this thesis is to develop reversible thermoresponsive nanoemulsions, and understand their colloidal behavior so that we can use them as a model system to understand rheology and microstructure of colloid-polymer mixtures, ultimately toward engineering them for new applications.

1.2 Objectives and approach

The ultimate goal of this thesis is to address several important questions regarding the colloidal behavior of nanodroplet-polymer mixtures. What is the molecular origin of polymer-droplet and droplet-droplet interactions? How do these interactions determine suspension microstructure and dynamics in nanoemulsions, and ultimately their rheological properties? To answer these questions, a first objective of the work is to identify and characterize nanoemulsion-polymer mixtures in which known mechanisms of molecular self-assembly can be exploited to produce temperature-responsive colloidal interactions and rheological behavior. Specifically, we choose as a model system involving oil-in-water nanodroplets in the presence of hydrophilic polymers and ionic surfactants. Such polymers and surfactants are known to exhibit molecular complexation [21]. We hypothesize this complexation can give rise to thermoresponsive viscoelasticity, serving as a basis for design of switchable rheological materials. To understand how molecular self-assembly affects the rheology of nanoemulsions, we plan to characterize the thermodynamics of binding between polymer and surfactant, as well as the self-assembled structures they form. From these results, we can quantify interdroplet attractions and relate them to the rheological properties of nanoemulsions. This objective is the focus of Chapter 3.

As a second objective, we use the thermoresponsive nanoemulsions as a model system to investigate two important classes of poorly-understood rheological phenomena in colloid-polymer mixtures. The first is the shear-induced clustering of colloid-polymer mixtures at moderate colloid volume fractions, and its impact on fluid rheology. Employing the thermoresponsive viscoelastic nanoemulsions allows us to explore several limiting regimes of polymer and suspension dynamics in order to test the generality of the clustering phenomenon. Combining rheological characterization with three-dimensionally-resolved flow-SANS measurements allows us to identify the mechanisms of clustering and anisotropic suspension microstructure in these systems. This objective is the focus of Chapter 4.

The second rheological phenomenon will be the broadened, multi-stage yielding process observed previously in the heterogeneous nanoemulsion gels [22], as well as a number of other attractively-driven colloidal gels [23-25]. We will use the thermoresponsive nanoemulsions to study yielding in a colloidal gel that exhibits a heterogeneous structure, consisting of a two-phase bicontinuous network of colloid-rich domains of fractal clusters and colloid-poor domains [10,22]. Combining large amplitude oscillatory shear measurements with simultaneous small and ultra-small angle neutron scattering (rheo-SANS/USANS), we characterize both the nonlinear mechanical processes and strain amplitude-dependent microstructure underlying multi-stage yielding. Specifically, we identify a sequence of mechanical and structural processes that occur during the intracycle yielding process to reveal the mechanisms of delayed yielding in this system. This objective is the focus of Chapter 5.

1.3 Nanoemulsions

As previously mentioned, nanoemulsions are non-equilibrium dispersions of liquid nanodroplets (typically ranging from 10 to 100 nm in size) in another immiscible liquid phase. They are kinetically stable due to their extreme resistance to coalescence and sedimentation [8,15,26]. Because of the (typically) high interfacial energy between the two different liquids, significant amounts of surfactants are required to stabilize the droplet interface. Figure 1.1 shows a cryo-TEM image taken of a concentrated nanoemulsion prepared by high pressure homogenization. Details of cryo-TEM measurement and high pressure homogenization are described in Chapter 2.

To produce nanoemulsions, it is critical to control the size distribution of droplets. Although there are a wide range of emulsification methods, high-energy processes are typically required to form nanoemulsions because nanoscale droplets are driven far from

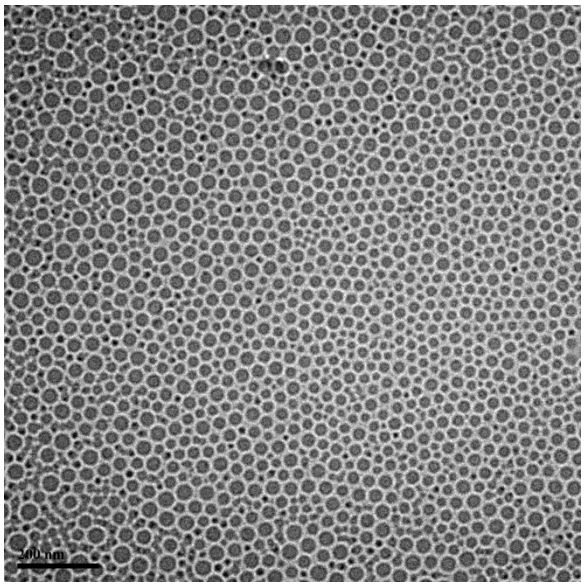

Figure 1.1 Cryo-TEM image of an oil-in-water nanoemulsion.

equilibrium. In such processes, externally-applied viscous stresses break down micron-scale droplets to the nanoscale. The hydrodynamic stresses applied must overcome the Laplace pressure, i.e. the pressure jump across the fluid interface due to surface tension. For a spherical droplet, the Laplace pressure is given by

$$\Delta P = 2\sigma / a \qquad (1.1)$$

where σ is interfacial tension and a is the radius of a droplet [27].

Currently, high pressure homogenization is the most popular method to generate extreme shear for large-scale production of nanodroplets [28]. High-pressure microfluidic valve homogenizers are commonly used in laboratory scale to produce nanoemulsions. In homogenization equipment, the size distribution can be controlled by process parameters such as the flow rate (or pressure drop) and residence time, as well as fluid properties such as the viscosities and compositions of the continuous phase. In general, higher applied energy densities reduce the average size of the droplets [8]. Increased viscosity in the continuous phase reduces size of the droplets when the viscosity of the dispersed phase is fixed [29]. As the size of the droplets decrease, the amount of interfacial area increases. Thus, it is necessary to stabilize the droplets and reduce interfacial tension by maintaining surfactant concentration. In order to achieve low polydispersity of the droplets, emulsions are homogenized multiple times to provide an opportunity for the majority of droplets to experience the highest shear generated in the device for a sufficient residence time [29].

As previously mentioned, it is critical to maintain colloidal stability (i.e. the size distribution and dispersion state) of nanoemulsions over time to facilitate both their characterization and formulation. Ostwald ripening is the primary mechanism of droplet instability in nanoemulsions [30]. During Ostwald ripening, molecules in the dispersed

phase preferentially migrate from smaller droplets into larger droplets through the continuous phase because of the Laplace pressure [31]. Inhibition of Ostwald ripening can be achieved by using a dispersed phase that has low solubility in the continuous phase [32]. The rate of Ostwald ripening is proportional to the solubility of the dispersed phase in the continuous phase, as captured by the Liftshitz-Slezov and Wagner (LSW) theory [33]. Another destabilizing process is coalescence that two droplets fused into a single larger droplet by colliding. This can be inhibited by adding surfactants that provides repulsive interactions between droplets. Another way is to use additives in the continuous phase as a thickener to increase its viscosity, thereby increasing the hydrodynamic resistance to droplet collisions. Compared to macroemulsions, nanoemulsions exhibit significantly reduced rates of coalescence. Since the Laplace pressure scales as $1/a$ that sets the stresses required to deform the droplets, nanodroplets are therefore much less deformable compared to the larger droplets. Delmas *et al*. showed coalescence can be easily prohibited by decreasing the droplet size, leading to long-term kinetic stability [34]. Although significant efforts on the nanoemulsions, it is still not well understood the colloidal behaviors of droplets in nanoemulsions system to provide the applications from consumer products to advanced applications as previously mentioned. Thus, it has driven a need for fundamental studies aimed at understanding and controlling their colloidal behavior.

1.4 Colloidal interactions in nanoemulsions

1.4.1 Electrostatic interactions

The surface of emulsion droplets are often charged due to ionic surfactants at the interface [35]. In such cases, like-charged droplets interact through electrostatic repulsions

[15]. It has been shown that repulsive emulsions/nanoemulsions can exhibit viscoelasticity both below and above the compressive regime, i.e., the concentration above which droplets must deform in order to remain dispersed [36,37]. However, droplet-droplet interactions can change from repulsive-dominated to attractive-dominated by adding salts to the continuous phase, which screen the electrostatic repulsions [38,39]. In such cases, van der Waals attractions dominate, resulting in the formation of droplet aggregates. The electrostatic repulsion between droplets can also be varied by using a mixture of ionic and non-ionic co-surfactants [40]. In these cases, the pair potential between droplets can be successfully described the using Derjaguin-Landau-Verwey-Overbeek (DLVO) theory from the repulsive screened electrostatic forces and attractive van der Waals forces [41]. It is critical to study the electrostatic interactions between droplets in nanoemulsions because electrostatic interactions influence the stability, microstructure and rheological behaviors in nanoemulsions [36,37,40,42,43]. Mason *et al*. represented effective structural factor as a function of volume fractions up to the maximum random jamming limit. However, it is still required the corrections from droplet deformation and the effect of interfacial repulsion due to charged interface [44].

1.4.2 Polymer-induced interactions

Polymers can impact the interactions between dispersed droplets in various ways, determined by whether the polymer is adsorbing or non-adsorbing toward the droplet surface. A recent review described the interactions between two colloidal particles with adsorbed polymer where the molecular weight of the polymer is sufficiently high so that the adsorption is irreversible over the experimental time scale [45]. However, the effect of low

molecular weight adsorbing or non-adsorbing polymer on the interactions with colloidal suspensions is not still well understood. Figure 1.2 (a) represents, in the case of non-adsorbing polymer, polymer-induced depletion, in which the excluded volume of the polymer results in an entropic loss in the continuous phase. This can result in attractive colloidal interactions [46] because of increased osmotic pressure from expelled polymers between droplets [47]. Although the presence of surfactant micelles can also induce depletion forces between droplets [48,49], polymer-induced depletion will be focused on here. The attractive force induced by polymer depletion increases with polymer concentration [50].

Polymer-induced interactions between droplets can also be achieved by associative interactions between the polymer and surfactant at the droplet surface (Figure 1.2 (b)). For example, nonionic hydrophilic polymers, e.g. polyethylene glycol (PEG), are well known to form associative complexes with various ionic surfactants [21,51,52]. Dai *et al.* discovered the PEG-induced micellization of SDS by isothermal titration calorimetry (ITC) [21]. Specifically, at low SDS concentration (but, above the critical aggregation concentration (cac)), PEG forms induced micelle structures with SDS due to hydrophobic interactions between the PEG ethylene groups and alky groups of SDS. At high SDS concentration, ion-dipole association results in formation of PEG and SDS aggregates in which PEG chains are bounding to the SDS head group. In emulsions, these associative interactions provides steric repulsions and, as a result, long-term colloidal stability [53]. This is because adsorbed neutral polymers at the interface of emulsion droplets can be stretched due to their interaction with charged surfactants [53]. In Chapter 3, the effect of polymer-surfactant complexation in nanoemulsions will be described in more detail.

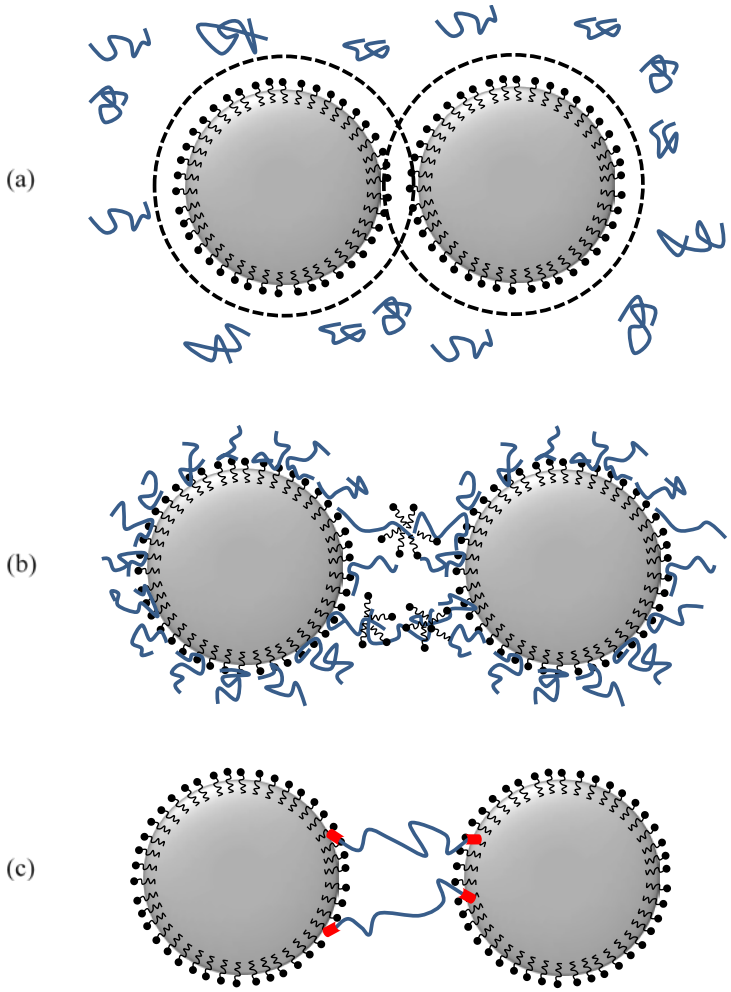

Figure 1.2 Schematic diagram depicting (a) depletion attractions induced by non-adsorbing polymer, (b) steric stabilization induced by polymer-surfactant association, (c) bridging attraction induced by strongly adsorbing polymer.

In the case of adsorbing polymers, bridging of the polymer between droplets can occur, modifying colloidal interactions between droplets. Of particular relevance to this work are end-adsorbing polymers, in which functional end-groups adsorb to the droplet surface. Although mono-functionalized adsorbed polymers give rise to steric repulsions due to a brush-like configuration [54], di-functional or telechelic polymers results in polymer bridging [10,22], which produces entropically-driven attractive interactions [10]. This polymer bridging is depicted in Figure 1.2 (c). Also, weakly absorbing telechelic polymers

can form associative networks between droplets, which are known to produce viscoelasticity in microemulsion systems due to the formation of a physical network of polymer mediated by bridged droplets [55].

1.5 Rheology of colloidal suspensions in polymer solutions

Dispersed nanoparticles are important for improving the mechanical properties of polymeric materials [56]. In many cases, such polymer nanocomposites are processed from solution, and so it is important to understand how particle dispersion impacts polymer rheology, and vice versa. In general, polymer solutions exhibit complicated non-Newtonian viscoelasticity, which is modified by the presence of suspended particles to produce complex rheology. In the case of nanoemulsions, a primary control parameter for the rheology of suspensions in polymer solutions is the droplet volume fraction (ϕ). In the dilute regime, the viscosity increases with increasing ϕ according to the Einstein relationship [57]. In the case of soft repulsion-dominated interactions (e.g. by electrostatics), elasticity arises at moderate ϕ for nanoemulsions because of the contribution of the repulsive potential to the effective volume fraction of the suspension [36]. This repulsion-driven elasticity can be reduced by adding salts that screen the charge interactions [39]. By contrast, in weakly attractive interactions, increasing ϕ produces glassy rheology [58], in which dense attractive interactions resulting in dramatically slowed configurational diffusion that arrests the rearrangement of droplets. At even higher ϕ corresponding to the compressive regime, both repulsion-dominated and attraction-dominated nanoemulsions become glassy due to jamming of deformed droplets [9,59].

Sometimes, suspensions in viscoelastic fluids exhibit other complex rheological features due to the effects of flow on suspension microstructure. For example, in the case of pressure-driven flow in Newtonian fluids, particles are randomly distributed under creeping flow at relatively low volume fractions [60]. By contrast, in viscoelastic fluids the particles are found to migrate and form anisotropic structures [60,61]. Non-Newtonian rheological features of suspensions are also significantly modified in viscoelastic fluids. For example, it has been shown that the addition of suspended particles into polymeric solutions increases the degree of shear thinning of the suspension [62-64].

There has been relatively little theoretical study to understand this coupling between rheological behavior and altered microstructure of non-dilute suspensions in flowing polymer solutions. Analytical solutions were developed to predict the migration of the particles, such as the particle contribution to the first normal stress and the bulk stress of a suspensions in viscoelastic fluids [65]. However, these models were developed in the limit of single particles, and do not account for concentrated effects such as Brownian and hydrodynamic stresses due to deformation of the suspension microstructure under flow. To address these outstanding questions, Chapter 4 is devoted to using thermoresponsive nanoemulsions as a model system to study the rheological behavior of suspensions in viscoelastic fluids, and the microstructural changes it gives rise to.

1.6 Formation and rheology of colloidal gels

In colloidal suspensions including nanoemulsions possessing sufficiently strong attractive interactions, the fluid develops solid-like properties through colloidal gelation. In the gelation process, attractions between suspended particles form aggregates, which at

sufficient size and density participate in the formation of the network that give rise to elastic and solid-like properties, such as a yield stress. In order to design the structure and rheology of colloidal gels for many applications, it is critical to understand the fundamental mechanism(s) of colloidal gelation. Figure 1.3 represents a schematic diagram for colloidal gelation and phase behavior in attractively-driven colloidal systems depending on the attraction strength and volume fraction of colloids.

In systems at moderate volume fraction with relatively weak attractive interactions, the bonds between particles are not permanent, so that attractive clusters break and reform over some finite time scale. As a result, the fluid exhibits a liquid-like state comprised of suspended transient clusters. If the attraction strength between particles is increased, the bond lifetime increases and the average size of clusters grows to form a sample-spanning network, resulting in relatively homogeneous, percolated gels [66,67]. By contrast, further increase in the attraction strength during the kinetic gelation process can lead to colloidal phase instability, in which the fluid tends to separate into two phases by a gas-liquid spinodal boundary, consisting of colloid-poor and colloid-rich domains [68,69]. Both of these processes (percolation and glass formation) can be further complicated by the existence of fluid-fluid phase instability. Once the density of these colloid-rich domains is sufficiently high, the phase separation can become arrested phase due to an attractive glass transition.[70-73] In this arrested phase separation, the system can exhibit significant large-scale heterogeneity in the gel structure [74]. As such, the mechanism of attractive colloidal gelation at relatively moderate volume fraction has not been firmly established, and can vary dramatically depending on the details of the particular material system.

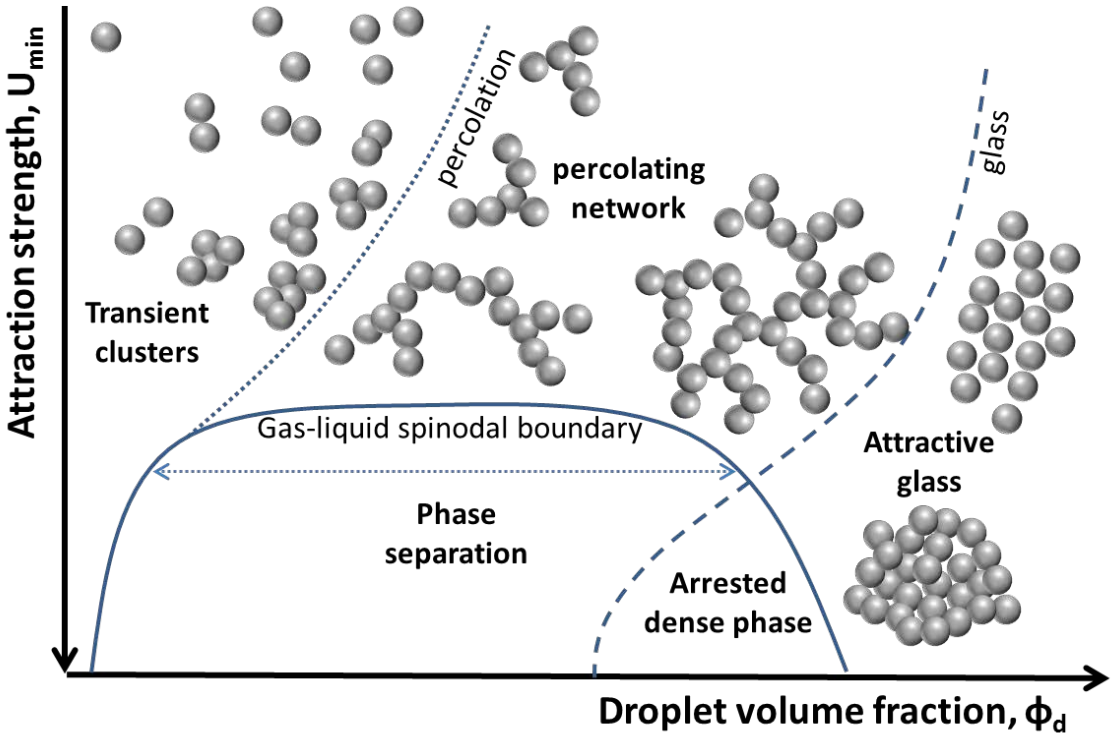

Figure 1.3 Schematic colloidal phase diagram of percolation, phase separation and glass transition in attraction-dominated system.

Helgeson *et al*. recently showed that an attraction-driven thermoresponsive nanoemulsion system exhibits both homogeneous percolation and arrested phase separation depending on the volume fraction of droplets [22]. This was hypothesized to be due to the moderate range and strength of attraction in the system. In further studies, the onset and arrest of spinodal decomposition was found to control the large-scale microdynamics and elasticity of the nanoemulsion colloidal gels [75]. A combination of microscopy and dynamic correlation analysis of the resulting images revealed that the coarsening in this system arises from collective dynamics of dense domains, which undergo slow, intermittent, and ballistic motion [75].

To facilitate their processing, it is also critical to understand the yielding and flow of colloidal gels. In particular, it has been recently found that the microstructural morphology of colloidal gels has a significant influence on their yielding behavior. Specifically, the two different gelation processes identified above (percolation and glass formation) have been reported to result in dramatically different yielding. Percolation gels typically exhibit a single yield point in nonlinear rheological measurements, as reported for both the thermoresponsive nanoemulsions [22] and in hard particle colloidal gels with low volume fraction [76,77]. By contrast, concentrated colloidal gels have been found to exhibit a complicated so called a “two-step” or broadened yielding process in nonlinear rheological measurements [23-25,78]. This broadened yielding process resembles the yielding behaviors in the heterogeneous nanoemulsion colloidal gels [22]. It has been hypothesized that this complicated yielding process can be explained by local-scale rearrangements of the gel network under deformation including bond rupture and cluster rearrangement [23,24]. However, this mechanism of broadened yielding in heterogeneous colloidal gels has never been confirmed by experiment. In Chapter 5, this topic will be thoroughly investigated by detailed analysis of the nonlinear rheology and direct microstructural measurements in concentrated nanoemulsion colloidal gels.

1.7 Thermoresponsive nanoemulsions

Recently, Helgeson *et al.* discovered a new class of oil-in-water nanoemulsions that exhibit an abrupt transition from low viscosity liquids to solid-like colloidal gels with increasing temperature [10]. As a dispersed phase, low viscosity silicone oil (polydimethylsiloxane, PDMS) droplets are emulsified in the aqueous continuous phase. In

the continuous phase, sodium dodecyl sulfate is used as a surfactant to stabilize the oil droplets, and functionalized hydrophilic polymer, polyethylene glycol diacrylate (PEGDA) is used. Small angle neutron scattering (SANS) measurement revealed a microporous microstructure of the nanoemulsion colloidal gel. Remarkably, the gel transition was found to be thermoreversible, making this nanoemulsion system an excellent candidate for carefully studying colloidal behavior in polymer-nanoemulsion mixtures. The mechanism of the thermoresponsive behavior in this system was ultimately hypothesized to involve temperature-responsive adsorption of hydrophobic acrylate end-groups at the interface of the droplets, resulting in polymer bridging at elevated temperature. Specifically, entropically-driven dehydration of hydrophobic end-groups at increased temperature is thought to lead to effective interdroplet attractions, which ultimately give rise to colloidal gelation when the bridging attractions are sufficiently strong. This hypothesis was corroborated by the fact that the gel transition occurs for many other PEGs containing hydrophobic end-group chemistry, and the trend in temperature-dependence of rheological properties was found to scale as expected with the relative hydrophobicitiy of the end-group chemistry for hydrophobically-driven adsorption. In further investigations, the effect of droplet size on thermoreversible gelation was studied, and it was found that the thermoreversible gelation only occurred for nanoemulsions of sufficiently small droplet size.

Later, SANS and cryo-TEM measurements elucidated two different pathways of thermoresponsive colloidal gelation in these systems depending on the volume fraction of the dispersed droplets [22]. Briefly, for volume fraction of droplets (ϕ) lower than 0.2, gels exhibited a homogeneous fractal microstructure, presumably produced by percolation of droplet-droplet clusters during diffusion-limited aggregation. However, for $\phi > 0.2$, gels

exhibit a heterogeneous microstructure with micron-scale correlated features, which were though to result from the formation of dense cluster domains through arrested phase separation. Furthermore, nonlinear rheological measurements revealed two different yielding behaviors depending on the microstructure of nanoemulsion gel. Specifically, gels with homogeneous microstructure exhibit a single, simple yielding transition with increasing strain amplitude, whereas gels with heterogeneous microstructure produced a broadened, multi-stage yielding transition.

These studies provide new routes to control the colloidal structure and rheological behaviors in nanoemulsions by temperature and volume fraction of droplets. First, the reversibility of thermal gelation is different from other irreversible rheological behavior in nanoemulsions [36,79]. Second, the solid-like viscoelasticity found in these nanoemulsion colloidal gels is unique compared to the viscoelasticity found in microemulsion-telechelic polymer mixtures [80,81]. Toward applications, the system provides a pathway to designing and templating materials with hierarchically porous microstructure for many applications [10].

Moreover, these nanoemulsion systems present unique opportunities for studying the process of colloidal gelation and properties of colloidal gels in polymer-colloid mixtures. For example, since the polymer bridging can be controlled by varying the polymer molecular weight and end-group hydrophobicity, the strength, range and temperature-dependence of thermoresponsive attractions can be carefully programmed and tuned. Furthermore, the selection and concentration of surfactant can be used to add and tune electrostatic repulsion, providing a mechanism for studying the effects of combined medium-range attraction and long-range repulsion on aggregation and gelation. We hope

that understanding the mechanism of interdroplet interactions in these systems will ultimately allow for better understanding and design of the resulting microstructure and rheology. This dissertation is therefore intended to make the first steps along this path.

References

[1] D. J. McClements and J. Rao, Critical reviews in food science and nutrition **51**, 285 (2011).

[2] E. Yilmaz and H.-H. Borchert, International journal of pharmaceutics **307**, 232 (2006).

[3] O. Sonneville-Aubrun, J.-T. Simonnet, and F. L'alloret, Advances in Colloid and Interface Science **108**, 145 (2004).

[4] S. Ganta and M. Amiji, Molecular pharmaceutics **6**, 928 (2009).

[5] E. B. Mock, H. De Bruyn, B. S. Hawkett, R. G. Gilbert, and C. F. Zukoski, Langmuir **22**, 4037 (2006).

[6] M. E. Helgeson, Current Opinion in Colloid & Interface Science **25**, 39 (2016).

[7] C. Solans, J. Esquena, A. M. Forgiarini, N. Uson, D. Morales, P. Izquierdo, N. Azemar, and M. J. Garcia-Celma, Surfactant science series, 525 (2003).

[8] T. Mason, S. Graves, J. Wilking, and M. Lin, Condens. Matter Phys **9**, 193 (2006).

[9] T. Mason, M.-D. Lacasse, G. S. Grest, D. Levine, J. Bibette, and D. Weitz, Physical Review E **56**, 3150 (1997).

[10] M. E. Helgeson, S. E. Moran, H. Z. An, and P. S. Doyle, Nature materials **11**, 344 (2012).

[11] M. Kumar, A. Misra, A. Babbar, A. Mishra, P. Mishra, and K. Pathak, International journal of pharmaceutics **358**, 285 (2008).

[12] D. K. Sarker, Current Drug Delivery **2**, 297 (2005).

[13] S. Mura, J. Nicolas, and P. Couvreur, Nature materials **12**, 991 (2013).

[14] P. Malo de Molina, M. Zhang, A. V. Bayles, and M. E. Helgeson, Nano Letters (2016).

[15] T. J. Wooster, M. Golding, and P. Sanguansri, Langmuir **24**, 12758 (2008).

[16] I. Y. Galaev and B. Mattiasson, Trends in biotechnology **17**, 335 (1999).

[17] L. Klouda and A. G. Mikos, European Journal of Pharmaceutics and Biopharmaceutics **68**, 34 (2008).

[18] D. Cohn, A. Sosnik, and A. Levy, Biomaterials **24**, 3707 (2003).

[19] D. Roy, W. L. Brooks, and B. S. Sumerlin, Chemical Society Reviews **42**, 7214 (2013).

[20] E. Kharlampieva, V. Kozlovskaya, J. Tyutina, and S. A. Sukhishvili, Macromolecules **38**, 10523 (2005).

[21] S. Dai and K. Tam, The Journal of Physical Chemistry B **105**, 10759 (2001).

[22] M. E. Helgeson, Y. Gao, S. E. Moran, J. Lee, M. Godfrin, A. Tripathi, A. Bose, and P. S. Doyle, Soft matter **10**, 3122 (2014).

[23] N. Koumakis and G. Petekidis, Soft matter **7**, 2456 (2011).

[24] Z. Shao, A. S. Negi, and C. O. Osuji, Soft matter **9**, 5492 (2013).

[25] H. K. Chan and A. Mohraz, Physical Review E **85**, 041403 (2012).

[26] D. J. McClements, Soft matter **8**, 1719 (2012).

[27] T. Tadros, P. Izquierdo, J. Esquena, and C. Solans, Advances in Colloid and Interface Science **108**, 303 (2004).

[28] H. Schubert and R. Engel, Chemical Engineering Research and Design **82**, 1137 (2004).

[29] K. Meleson, S. Graves, and T. G. Mason, Soft Materials **2**, 109 (2004).

[30] P. Taylor, Advances in Colloid and Interface Science **75**, 107 (1998).

[31] A. Kabal'nov and K. Makarov, Colloid journal of the USSR **52**, 589 (1990).

[32] T. Mason, A. Krall, H. Gang, J. Bibette, and D. A. Weitz, Encyclopedia of emulsion technology **4**, 299 (1996).

[33] B. P. Binks, *Modern aspects of emulsion science* (Royal Society of Chemistry, 1998).

[34] T. Delmas, H. Piraux, A.-C. Couffin, I. Texier, F. Vinet, P. Poulin, M. E. Cates, and J. Bibette, Langmuir **27**, 1683 (2011).

[35] K. Marinova, R. Alargova, N. Denkov, O. Velev, D. Petsev, I. Ivanov, and R. Borwankar, Langmuir **12**, 2045 (1996).

[36] J. N. Wilking and T. G. Mason, Physical Review E **75**, 041407 (2007).

[37] P. Coussot, Soft matter **3**, 528 (2007).

[38] J. Bibette, T. Mason, H. Gang, D. Weitz, and P. Poulin, Langmuir **9**, 3352 (1993).

[39] J. Wilking, S. Graves, C. Chang, K. Meleson, M. Lin, and T. Mason, Physical review letters **96**, 015501 (2006).

[40] L. Wang, R. Tabor, J. Eastoe, X. Li, R. K. Heenan, and J. Dong, Physical Chemistry Chemical Physics **11**, 9772 (2009).

[41] J. Schenkel and J. Kitchener, Transactions of the Faraday Society **56**, 161 (1960).

[42] G. Stalidis, A. Avranas, and D. Jannakoudakis, Journal of Colloid and Interface Science **135**, 313 (1990).

[43] A. Avranas and G. Stalidis, Journal of Colloid and Interface Science **143**, 180 (1991).

[44] T. Mason, S. Graves, J. Wilking, and M. Lin, The Journal of Physical Chemistry B **110**, 22097 (2006).

[45] P. Pincus, Lectures on Thermodynamics and Statistical Mechanics, 74 (1988).

[46] P. J. Lu, E. Zaccarelli, F. Ciulla, A. B. Schofield, F. Sciortino, and D. A. Weitz, Nature **453**, 499 (2008).

[47] S. Asakura and F. Oosawa, The Journal of chemical physics **22**, 1255 (1954).

[48] J. Bibette, D. Roux, and F. Nallet, Physical review letters **65**, 2470 (1990).

[49] O. Mondain-Monval, F. Leal-Calderon, and J. Bibette, Journal de Physique II **6**, 1313 (1996).

[50] X. Ye, T. Narayanan, P. Tong, J. Huang, M. Lin, B. Carvalho, and L. Fetters, Physical Review E **54**, 6500 (1996).

[51] W. Guo, Y. Sun, G. Luo, and Y. Wang, Colloids and surfaces A: physicochemical and engineering aspects **252**, 71 (2005).

[52] E. D. Goddard, Colloids and Surfaces **19**, 255 (1986).

[53] J. Philip, G. G. Prakash, T. Jaykumar, P. Kalyanasundaram, O. Mondain-Monval, and B. Raj, Langmuir **18**, 4625 (2002).

[54] M. Wulff-Pérez, A. Martín-Rodríguez, M. J. Gálvez-Ruiz, and J. de Vicente, Colloid and Polymer Science **291**, 709 (2013).

[55] P. Malo de Molina, C. Herfurth, A. Laschewsky, and M. Gradzielski, Langmuir **28**, 15994 (2012).

[56] R. A. Vaia and E. P. Giannelis, MRS bulletin **26**, 394 (2001).

[57] A. Einstein, Ann. Phys **17**, 549 (1905).

[58] R. G. Larson, *The structure and rheology of complex fluids* (Oxford university press New York, 1999), Vol. 150.

[59] S. Graves, K. Meleson, J. Wilking, M. Lin, and T. Mason, The Journal of chemical physics **122**, 134703 (2005).

[60] M. Jefri and A. Zahed, Journal of Rheology (1978-present) **33**, 691 (1989).

[61] R. Scirocco, J. Vermant, and J. Mewis, Journal of non-newtonian fluid mechanics **117**, 183 (2004).

[62] D. Faulkner and L. Schmidt, Polymer Engineering & Science **17**, 657 (1977).

[63] L. Nicodemo, L. Nicolais, and R. Landel, Chemical Engineering Science **29**, 729 (1974).

[64] T. Kataoka, T. Kitano, M. Sasahara, and K. Nishijima, Rheologica Acta **17**, 149 (1978).

[65] N. A. Patankar and H. H. Hu, Journal of non-newtonian fluid mechanics **96**, 427 (2001).

[66] Y. Chiew and E. Glandt, Journal of Physics A: Mathematical and General **16**, 2599 (1983).

[67] A. P. Eberle, R. n. Castañeda-Priego, J. M. Kim, and N. J. Wagner, Langmuir **28**, 1866 (2012).

[68] E. Zaccarelli, Journal of Physics: Condensed Matter **19**, 323101 (2007).

[69] M. A. Miller and D. Frenkel, The Journal of chemical physics **121**, 535 (2004).

[70] K. Dawson, G. Foffi, M. Fuchs, W. Götze, F. Sciortino, M. Sperl, P. Tartaglia, T. Voigtmann, and E. Zaccarelli, Physical Review E **63**, 011401 (2000).

[71] G. Foffi, G. D. McCullagh, A. Lawlor, E. Zaccarelli, K. A. Dawson, F. Sciortino, P. Tartaglia, D. Pini, and G. Stell, Physical Review E **65**, 031407 (2002).

[72] J. Bergenholtz and M. Fuchs, Journal of Physics: Condensed Matter **11**, 10171 (1999).

[73] F. Sciortino and P. Tartaglia, Advances in Physics **54**, 471 (2005).

[74] M. Laurati, G. Petekidis, N. Koumakis, F. Cardinaux, A. B. Schofield, J. M. Brader, M. Fuchs, and S. U. Egelhaaf, The Journal of chemical physics **130**, 134907 (2009).

[75] Y. Gao, J. Kim, and M. E. Helgeson, Soft matter **11**, 6360 (2015).

[76] T. Gibaud, D. Frelat, and S. Manneville, Soft matter **6**, 3482 (2010).

[77] F. Pignon, A. Magnin, J.-M. Piau, B. Cabane, P. Lindner, and O. Diat, Physical Review E **56**, 3281 (1997).

[78] M. Laurati, S. Egelhaaf, and G. Petekidis, Journal of Rheology (1978-present) **55**, 673 (2011).

[79] B. Cabane and R. Duplessix, Journal de Physique **43**, 1529 (1982).

[80] P. Luisi, R. Scartazzini, G. Haering, and P. Schurtenberger, Colloid and Polymer Science **268**, 356 (1990).

[81] H. Bagger-Jörgensen, L. Coppola, K. Thuresson, U. Olsson, and K. Mortensen, Langmuir **13**, 4204 (1997).

Chapter 2

Materials and methods

2.1 Objective

In this chapter, I describe the materials, preparation and characterization methods for studying our model thermoresponsive nanoemulsion system. Although more specific will be described in each chapter, this chapter describes the general fundamental aspects of the model system, experimental methods and analysis protocols used.

2.2 Materials and preparation

2.2.1 Nanoemulsions

As mentioned previously, our model system is comprised of oil-in-water (O/W) nanoemulsions containing silicone oil droplets dispersed in an aqueous continuous phase. We choose silicone oil because it has been used in wide range of fundamental studies of nanoemulsion behavior [1-3]. Specifically, we chose low-viscosity polydimethylsiloxane (PDMS, Sigma Aldrich, η = 5 cp at 25 °C), since its solubility into an aqueous phase is very small, which retards the rate of Ostwald ripening, and its viscosity is also very small relative to other oils, which facilitates the production of nanodroplets in high-energy emulsification processes. The silicone oil is transparent and has a density of 0.913 g ml^{-1} at 25 °C.

The silicone oil was emulsified into an aqueous continuous phase containing surfactant and polymers. High-pressure homogenization was used to prepare nanoemulsions, which will be described in the next section. In most cases, sodium dodecyl sulfate (SDS,

Sigma Aldrich) was used as a surfactant to stabilize the oil droplets. The polymers solubilized in the continuous phase are composed of a hydrophilic main chain, polyethylene glycol (PEG), and various hydrophobic functionalized end-group chemistries, i.e., acrylate, methyl ether and di-alkyl groups. In most studies, we used PEG with a relatively low molecular weight (600 g mol^{-1}), which is lower than the entanglement molecular weight for entanglement of PEG. Therefore, the polymer in the continuous phase cannot by itself be entangled. For neutron scattering measurements, we used deuterium oxide (D_2O, Cambridge Isotope Laboratories, 99.9%) as the solvent in the continuous phase to enhance the contrast and match the contrast of continuous phase with polymers, which will be discussed in more detail in Section 2.4.2.

In order to determine the stability of the nanoemulsion droplets over the course of experiments, the droplet size was measured before and after performing the rheological measurements by dynamic light scattering. In all cases, including rheological measurements with variation from 5 to 35 °C and high shear rates as high as 2000 s^{-1}, the observed change in average droplet size was never more than 2%, and the change in polydispersity was never more than 10%. Thus, we conclude that the experiments performed in this work have no significant effect on the droplet size distribution. Although the droplet size can increase due to Ostwald ripening, this can be retarded by storing the sample at low temperature (5-10 °C) according to previous study on nanoemulsions stability [4]. As just mentioned, over our experimental time scale, the increase in average droplet size and polydispersity due to the Ostwald ripening is negligible.

2.2.2 Homogenizer

High-pressure homogenization was used for fabricating nanoemulsions. In the process, a macroscale emulsion is forced to pass through a micro-channel in the homogenizing valve, resulting in extreme shear. The generated high shear stress can break down large scale droplets in crude emulsions into nanoscale ones. A crude emulsion was first prepared using dropwise addition and high-speed mixing of silicone oil into the polymer and surfactant solution mixture. Then, this crude emulsion was passed through a pneumatically controlled dynamic valve inside the homogenizer (EmulsiFlex-C5, Avestin) for 10-20 passes and with pressure drops ranging from 5-15 kpsi, depending on the desired ultimate droplet size. The droplet size is determined by the applied shear stress due to the pressure drop. This should exceed the Laplace pressure to deform droplets [5]. Due to the capillary instability, stretched droplets from the applied high stress can break down to form smaller droplets [6].

2.3 Rheological characterization

2.3.1 Viscometry

An Anton Paar rolling ball viscometer (Lovis 2000 M/ME) was used to measure the zero shear rate viscosity of polymer and surfactant solutions. Depending on the viscosity of the sample, different sized capillary was used in order to improve the accuracy of the measurement. After loading the sample, the temperature was equilibrated for at least 5 minutes before the measurement. The rolling time of a stainless steel ball was measured in the capillary, and the sample viscosity is obtained according to the Hoeppler's falling ball principle. Since the density of the sample is measured simultaneously by the device, both

dynamic and kinematic viscosities are determined. The viscosity measurements were performed at various angles for extrapolating the zero shear rate viscosity.

2.3.2 Rotational rheometry

The rheological behavior of the materials was measured using three different rotational rheometers, depending on the desired purpose. An AR-G2 stress controlled rheometer (TA Instruments) was mainly used to measure the rheology of materials, such as viscosity, viscoelastic moduli and steady shear rheology. To do so, we used a 60 mm, 2° upper cone geometry and a Peltier temperature-controlled lower-plate geometry for relatively high viscosity samples. For steady-state shear rheology measurements, the steady shear stress was measured using a Peltier temperature-controlled Couette geometry (inner radius, 14.0 mm; outer radius, 15.2 mm) at equilibrate temperatures ranging between 5 °C and 30 °C. In both cases, a solvent trap was used to prevent evaporation of the sample.

For large amplitude oscillatory shear (LAOS) measurements, an ARES LS strain-controlled rheometer (TA instruments) was used with a 50 mm cone and plate geometries (cone angle α= 0.04 rad). The temperature was controlled by a jacket of circulating water in the lower plate geometry. Also, the solvent trap was used to minimize solvent evaporation. The details of LAOS rheology will be discussed in the next section. Furthermore, ARES rheometer was used for transient rheology of nanoemulsions with Couette geometry (inner radius, 16 mm; outer radius, 17 mm). Temperature was also controlled by a jacket of circulating water in the moving Couette cup geometry.

For combined Rheo-(ultra) small angle neutron scattering (Rheo-USANS/SANS) measurements, Anton Paar MCR 501 rheometer was used with Couette geometry consisting of a cup and a rotating bob. A heated and cooled double air jacket controlled the

temperature. We will discuss the details of Rheo-USANS/SANS measurement in Section 2.4.2.

2.3.3 LAOS rheology

Large amplitude oscillatory shear (LAOS) is a particularly useful flow for probing yielding, as it allows for repetitive, steady state, rate-dependent measurements that span the transition from linear solid-like behavior to fully nonlinear flow. As mentioned previously, LAOS measurements were performed on the strain-controlled ARES LS rheometer (TA Instruments) for studying the rheological signatures of broadened yielding in colloidal gels. In order to prevent wall slip, 600 grit sand paper was attached to the 50mm cone and plate geometries using double sided adhesive tape, following a previous used procedure [7]. Possible errors caused by the sandpaper (e.g., through an error in the gap height or the sandpaper peeling off during the experiment) could be excluded as a strain amplitude sweep (ω=10 rad s^{-1}, $10^{-3}<\gamma_0<10$) with a Newtonian silicone oil (η=8000 Pa·s) gave identical results with and without the sandpaper.

In addition to the data analysis provided by the commercial software of the rheometer, the raw data were sampled with an analog-digital converter (NI-USB-9162, National Instruments) as described by Wilhelm [8] at a sampling rate of 50 kHz. The use of oversampling [9] increased the sensitivity and reduced the sampled time data to a sampling rate of 200 points per oscillation cycle. The raw data were analyzed using a custom-written MATLAB routine in order to convert each wave of a certain frequency and strain amplitude to a complex spectrum.

2.4 Structural characterization

2.4.1 Cryo-transmission electron microscopy

Cryo-transmission electron microscopy (cryo-TEM) is one of the only microscopy techniques using an electron beam that can transmit through a vitrified hydrated sample without significant imaging artifacts [10]. Rapid vitrification is necessary in order to avoid crystallization and variation of colloidal dispersions during transmission electron microscopy measurement [11]. Thus, it is an essential technique for characterization nanoemulsions without affecting structural changes. To vitrify the nanoemulsions, an automated vitrification device (FEI Vitrobot™ Mark IV) was used, which quenches the specimen by plunge-freezing.

All cryo-samples were prepared by following protocol. Before loading the sample, the chamber of the vitrification device was equilibrated at 22°C and 100% relative humidity (RH) to prevent evaporation of the loaded sample. A thin holey carbon film covered TEM grid was cleaned by plasma treatment to optimize the surface charge of the carbon support film. A 2-3 μL drop of aqueous nanoemulsions sample was transferred to the grid. To produce a thin layer of the sample in carbon grid, excess sample was removed by an automated blotting system using filter paper. The sample was blotted twice for 2 seconds each and the blotting force was set to level 3 in the FEI Vitrobot™ Mark IV. Immediately after blotting, the sample grid was rapidly plunged into high purity liquid ethane. The vitrified sample was transferred to a liquid nitrogen dewar, after which it was transferred and placed onto a TEM cryo-holder. The temperature of the specimen was maintained below much lower than the melting point of sample using liquid nitrogen.

Images of nanoemulsion samples were taken using an FEI Tecnai TF20 G2 200kV high resolution TEM, which is equipped with a field emission gun and TIETZ F415MP 4k×4k multiport charge coupled device (CCD) camera. Images were processed using FEI TIA (TEM Imaging and Analysis) software (ES vision).

2.4.2 Small angle neutron scattering

Small angle neutron scattering (SANS) is an essential experimental technique for investigating the microstructure of nanoemulsions [4,12]. This is because the wavelength of neutrons is appropriate for probing the characteristic length scale of droplets or their aggregates in nanoemulsions. Furthermore, contrast variation allows for labeling of a specific part in multicomponent system [13]. In our nanoemulsions system, four components – such as oil, surfactant, polymer and water –compose the structure. By replacing hydrogen with deuterium atoms, we can vary the contrast to reduce the scattering of specific components to investigate the microstructure, as well as reduce multiple scattering and incoherent background scattering. From the scattered intensity, we can obtain the structural information. Assuming the well-established factorization approximation, the scattered intensity is given by

$$I(q) = \phi_p v_p (\Delta\rho)^2 P(q) S(q) + I_b \quad (2.1)$$

where q is the scattering vector, ϕ_p is the volume fraction of oil droplets, v_p is the average volume of the droplets, $\Delta\rho$ is the difference of scattering length density between dispersed and continuous phase and I_b is the incoherent (background) scattering intensity. The form factor, *P(q)*, provides information of the shape and size distribution of discrete scattering objects. The structure factor, *S(q)*, represents the interparticle interactions through the spatial

correlations of scattering objects. By modeling these functions, we can obtain structural information.

Static SANS measurements were performed using NG7 30m SANS instrument at the National Institute of Standards and Technology Center for Neutron Research (Gaithersburg, MD). Samples were loaded in quartz optical cells with a 1 mm path length and placed within the 10CB temperature-controlled sample environment. The temperature of sample cells was left to equilibrate for at least 30 min prior to measurement. Neutrons with a wave length of 6 Å and a full-width at half-maximum (FWHM) of $\Delta\lambda/\lambda$=11% were used with sample-to-detector distances of 1 m (with 25 cm offset), 4 m and 13.5 m. Neutrons with a wavelength of 8.09 Å and a FWHM of $\Delta\lambda/\lambda$=11% with neutron lenses were used for the detector distance of 15.3 m.

Flow-SANS measurements were performed using different types of Couette geometries depending on the required projection of the scattering. There are three different two-dimensional projections of scattering in a Couette geometry, which are (i) the flow-vorticity projection (1-3 plane), (ii) flow-gradient projection (1-2 plane), and (iii) gradient-vorticity projection (2-3 plane). For flow-SANS measurement in the 1-3 and 2-3 planes, an Anton Paar MCR 501 rheometer was used with a Couette geometry consisting of a cup and a rotating bob. Since different sizes of Couette geometry were used for different types of experiment, specification of the geometry will be described in each chapter. The rheometer was placed on the Huber instrument table between the detector and the incident neutron beam. All samples were loaded after initializing the parameters for the rheometer. The cup was aligned and held fixed using a vacuum pump and the temperature was controlled by a heated and cooled double air jacket. Extreme care was taken to minimize the temperature

non-uniformity along the length of the cup in order to ensure a macroscopically homogeneous sample, which was measured by introducing a wire thermocouple probe at various locations along the length of the gap occasionally during measurement. A solvent trap was used to prevent evaporation of nanoemulsion sample during the measurements. The temperature of the sample was left to equilibrate in the relevant sample environments for at least 30 min prior to measurement.

For flow-SANS measurement in the 1-2 plane, a short-gap Couette shear cell developed by Wagner and co-workers was used. This consists of an aluminum inner rotating cylinder and an outer stationary aluminum cup. The inner and outer radii are 25.11 mm and 26.46 mm, respectively. Details of the shear cell and its operation are described elsewhere [14,15]. The 1-2 shear cell was also placed on the same position with the position of the rheometer. In the 1-2 shear cell measurements, the flow-SANS was measured at the center of the gap using a narrow slit aperture (0.38 mm) due to spatial inhomogeneity at different gap positions unless otherwise noted. To find the center of the gap, the total transmitted neutron counts for the empty shear cell were measured by changing the motor position of the Huber instrument table horizontally. The positions of the inner and outer walls can be obtained because of the decrease in transmission of neutron beam through aluminum.

As mentioned previously, rheo-SANS/USANS was performed to investigate the broad yielding behavior in nanoemulsion gel under the LAOS measurement. The 1-3 plane of shear deformation was measured using the BT5 Perfect Crystal Diffractometer (USANS) [16] and NG7 30 m SANS instruments [17] combined with an MCR 501 Anton-Paar rheometer at the National Institute of Standard Technology Center for Neutron Research (Gaithersburg, MD). We note that, due to the tube detection method for BT5 [16], all

USANS data are slit-smeared in the vertical (vorticity) direction. This prevents the characterization of any structural anisotropy, the presence of which could also produce artifacts in the one-dimensional spectra. All the data were reduced and radially averaged (for SANS) using standard Igor SANS and USANS software packages provided by National Institute of Standard and Technology [18], including desmearing of the USANS spectra for direct comparison with the SANS data. Incoherent background intensities were obtained through asymptotic fitting of a Porod plot (Iq^4 vs q^4) at high q-values, the slope of which yields the background intensity, and subtracted from the data to isolate the coherent scattering. The results were reduced and fitted using IGOR software package provided by National Institute of Standard and Technology (NIST) using standard protocols [18].

2.4.3 Light scattering

Dynamic light scattering (DLS) was used to characterize both the sizes of nanoemulsion droplets as well as their dynamics. The scattering intensity shows time-dependent fluctuation due to Brownian motion. We can obtain correlation function that exhibit exponential decay, which is related to the diffusion of the particle. The hydrodynamic radius of particles in a dilute suspension can be calculated using the Stokes-Einstein equation,

$$D = \frac{k_b T}{6\pi\eta R_h} \quad (2.2)$$

where D is translational diffusion of the particle, k_b is the Boltzmann constant, T is measured temperature, η is the viscosity and R_h is the hydrodynamic radius of the particle. Experiments were carried out on a BI-200SM (Brookhaven Instruments) multi-angle detector system with a 637 nm (HeNe continuous wave) laser. The temperature was

controlled using a circulating bath. For size measurements, nanoemulsion samples were diluted to ϕ = 0.01 using the appropriate continuous phase to inhibit multiple scattering. Measurements of the intensity correlation, *g(q,t)*, were made at a temperature of 25 °C (unless otherwise reported) and a scattering angle of 90°. The average hydrodynamic diameter and polydispersity of nanoemulsion droplets were obtained by a cumulant analysis.

DLS was also used to characterize the dynamics of nanoemulsions under concentrated conditions. Samples were filtered before the experiments with 0.45 mm pore size Teflon syringe filters (National Scientific Company). To facilitate comparison of experimental data across different conditions, the intermediate scattering function (ISF), *f(q,s)*, was calculated *via* the Siegert relation,

$$g(q,t)-1=c\left[f(q,t)\right]^2$$

where *c* is the Siegert constant indicating non-idealities in the optical path. This allows us using Siegert constants measured in ergodic states to extract ISF for cases where the observed correlation function does not fully relax within the experimental window. Furthermore, to minimize the error in extrapolating the value of *c*, we select the minimal detector aperture size that still provides sufficient statistical accuracy. To probe the *q*-dependence of dynamics, measurements were made at angles spanning 50–130° (corresponding to scattering vectors, *q*, of 11.5–24.67 μm^{-1}).

2.5 Isothermal titration calorimetry

Calorimetric measurements were carried using a Nano isothermal titration calorimeter (Nano ITC, TA instruments) at a temperature from 15 °C to 35 °C. 7 µL injections of SDS and polymer solution were injected sequentially into a 950 µL sample cell

containing polymer solutions or deionized water at 800 seconds intervals. The reference cell was filled with deionized water. The solution in the sample cell was stirred with a speed of 350 rpm. All samples were degassed before the measurement for at least 10 minutes. The results were analyzed using NanoAnalyze as provided by TA instruments.

References

[1] N. I. Perera, M. P. Maheswaram, D. Mantheni, D. D. Perera, M. E. Matthews, A. Riga, and T. S. Yellowe, American Journal of Analytical Chemistry **2**, 85 (2011).

[2] U. Albrecht, A. Otto, and P. Leiderer, Surface science **283**, 383 (1993).

[3] P. Bahadur, P. S. Yadav, K. Chaurasia, A. Leh, and R. Tadmor, Journal of colloid and interface science **332**, 455 (2009).

[4] M. E. Helgeson, S. E. Moran, H. Z. An, and P. S. Doyle, Nature materials **11**, 344 (2012).

[5] T. Mason, Current Opinion in Colloid & Interface Science **4**, 231 (1999).

[6] S. Chandrasekhar, Journal of Mathematics and Mechanics **10**, 683 (1961).

[7] C. J. Dimitriou, R. H. Ewoldt, and G. H. McKinley, Journal of Rheology (1978-present) **57**, 27 (2013).

[8] M. Wilhelm, Macromolecular materials and engineering **287**, 83 (2002).

[9] D. van Dusschoten and M. Wilhelm, Rheologica acta **40**, 395 (2001).

[10] J. Frank, *Electron tomography* (Springer, 1992).

[11] V. Klang, N. B. Matsko, C. Valenta, and F. Hofer, Micron **43**, 85 (2012).

[12] S. Graves, K. Meleson, J. Wilking, M. Lin, and T. Mason, The Journal of chemical physics **122**, 134703 (2005).

[13] H. Stuhrmann, Journal of Applied Crystallography **7**, 173 (1974).

[14] M. E. Helgeson, P. A. Vasquez, E. W. Kaler, and N. J. Wagner, Journal of Rheology (1978-present) **53**, 727 (2009).

[15] A. K. Gurnon, P. D. Godfrin, N. J. Wagner, A. P. Eberle, P. Butler, and L. Porcar, Journal of visualized experiments: JoVE (2014).

[16] J. Barker, C. Glinka, J. Moyer, M. Kim, A. Drews, and M. Agamalian, Journal of Applied Crystallography **38**, 1004 (2005).

[17] C. Glinka, J. Barker, B. Hammouda, S. Krueger, J. Moyer, and W. Orts, Journal of Applied Crystallography **31**, 430 (1998).

[18] S. R. Kline, Journal of Applied Crystallography **39**, 895 (2006).

Chapter 3

Using polymer-surfactant association to impart thermoresponsive rheology to nanoemulsions[1]

3.1 Introduction

Nanoemulsions are used in many applications from consumer products to advanced materials [1-5]. The rheology of nanoemulsions is critical for their formulation in these applications. Thus, it would be highly advantageous to develop generic schemes for producing nanoemulsions with controlled rheology varying from nearly Newtonian liquids to viscoelastic gels to elastic solids with tunable material parameters, including viscosity, modulus, and yield stress. This has proven difficult, however, due to poor understanding of the rheology of nanoemulsions. Specifically, the nanoscopic nature of the droplets leads to unique behavior as their size is decreased that is not observed for larger emulsions. This includes a transition from a liquid to a repulsive glass with decreasing droplet size in electrostatically-stabilized systems [6], or from a viscoelastic paste to a nearly elastic gel in attractively-driven systems [4]. In both cases, these phenomena are thought to be due to the increase in characteristic length scale of interdroplet interactions relative to the droplet size as the latter is driven to the nanoscale. However, the exact mechanism of these changes is unclear, preventing predictive theories for the rheology of nanoemulsions, or even where these transitions might occur. This calls for a more molecular understanding of colloidal

[1] Portions of This chapter are reproduced with permission of The Royal Society of Chemistry.[70]

interactions and dynamics in nanoemulsions, and how these properties impact their rheology.

Recently, Helgeson *et al.* discovered a class of nanoemulsions with dynamically variable rheology based on thermoresponsive behavior of its molecular constituents [4]. Details of this thermoresponisve gelation are described in Chapter 1 (1.7). The formation of these "organohydrogels" was found to be inextricably linked to interfacial self-assembly of the polymer end groups at the oil-water interface, resulting in colloidal instability due to the formation of interdroplet bridges and, subsequently, the thermoreversible formation of a colloidal gel of droplet clusters. It was identified that both molecular chemistry and nanoscale droplet size were critical to imparting the remarkable rheological properties of the fluid.

The reliance of the rheology of these materials on polymer solution behavior opens up new possibilities for dynamic and thermoresponsive control of nanoemulsion rheology. In this chapter, we propose polymer-surfactant interactions as a novel, more generic mechanism toward this aim. In particular, it is well-known that water-soluble uncharged polymers exhibit complexation or co-aggregation with ionic surfactants in aqueous solution [7-9]. The most well characterized experimental system exhibiting this phenomenon is the aqueous PEG-sodium dodecyl sulfate (SDS) system, with studies dating to the 1950s [10-15]. It has been shown that PEG and SDS interact on a molecular level through a balance of hydrophobic forces and ion-dipole interactions [16], resulting in a number of different possible models for polymer-surfactant complexes [17-19]. Since the former relies primarily on entropic effects whereas the latter is enthalpically-driven, this leads to a complex dependence of the complexation on variables such as temperature [20], polymer molecular

weight [15,21] and concentration [16], and surfactant concentration [13]. Furthermore, the polymer-surfactant interactions can be modulated through the use of chemical additives such as salts [8] and co-surfactants [9]. Despite the complexity of this behavior, it is generally observed in a wide variety of systems, including water soluble homopolymers [13,22], co-polymers [23], hydrophobically-modified polymers [24-26], thermoresponsive polymers [27-29] and naturally-derived polymers [30,31], as well as both cationic and anionic surfactants [32] (although the latter is more common).

More recently, polymer-surfactant complexation at fluid interfaces has received significant interest [7], providing a potential link to its use in modifying the colloidal behavior of emulsions [33,34]. Many studies have focused on the competitive adsorption of various uncharged polymers and SDS at air-water interfaces. In both experiments [35] and molecular simulations [36], SDS is shown to significantly alter the conformation of interfacially adsorbed polymer chains. However, depending on the particular polymer and surfactant, these affects can either lead to a decrease [27] or increase [37] in the surface excess of polymer.

Since many polymer-surfactant mixtures are already in use for preparation and stabilization of nanoemulsions, more judicious selection of their chemistry and composition could allow for complexation as a general method of nanoemulsion rheology control. However, the specific impact of complexation on viscoelasticity of colloidal dispersions, and nanoemulsions in particular, has not been carefully examined. Even in solutions, differential rheological behavior is observed in relevant polymer-surfactant systems. In the case of neutral water-soluble polymers and ionic surfactants, only modest increases in solution viscosity are typically observed [38,39]. Contrastingly, mixtures of polyelectrolytes

or hydrophobically-modified polymers with ionic or non-ionic surfactants can lead to the formation of a cross-linked polymer network with gel-like rheology [30,31,40-42]. It is therefore unknown a priori how polymer-surfactant interactions and complexation will affect the rheology of the nanoemulsions, especially in the presence of an oil-water interface. However, some insight can be gained from thermodynamically stable microemulsion or swollen micellar systems, where temporary networks have been observed in mixtures of telechelic polymers and various microemulsion phases [43-46].

In this chapter, we aim to test whether polymer-surfactant complexation can be used to generally impart control over the viscoelasticity of oil-in-water nanoemulsions. Specifically, we will elucidate how the well-known complexation of PEG and SDS, representative of that found in other systems, can be utilized to create thermoresponsive viscoelastic behavior in nanoemulsions. We will employ a combination of characterization techniques to probe the structure, dynamics, and rheology of these materials over a wide range of length and time scales as well as compositional space. The results will be reconciled with the known behavior of polymer-surfactant complexation both in bulk solution and at fluid interfaces.

3.2 Experimental

Isothermal titration calorimeter (ITC) experiments described in Chapter 2 were performed by injecting 100 mM SDS solution into deionized water at 15, 25 and 35 °C. Also, in order to characterize the binding isotherm of PEGs and SDS, titrations of 100 mM SDS and into polyethylene glycol diacrylate (PEGDA, M_w~700 g/mol) aqueous solutions

were performed. Furthermore, we titrated 100 mM SDS and 1 wt% polymer into 1 wt% polymer to eliminate the contributions due to the dilution enthalpy of the polymer.

Phase studies were used to generate an approximate rheological state diagram for the nanoemulsions as a function of surfactant concentration (C_s) and temperature. Samples were prepared as described above and placed in a peltier-controlled temperature incubation system (Echotherm, Torrey Pines Scientific). Samples were equilibrated at a given temperature for at least 4 hours, and observations of sample behavior were made in 1 °C increments in the range of 10-55 °C. The appearance of the samples at each temperature were assessed by visual inspection as well as tipping of sample vials to observe visible viscosity. Observed phases included transparent low-viscosity, viscous, and gel-like phases, as well as turbid gel-like phases.

Static SANS and dynamic light scattering measurements were performed using the NG7 30m SANS and BI-200SM, respectively. Details of SANS and dynamic light scattering measurement were described in Chapter 2.

Rheological measurements were performed using an AR-G2 stress-controlled rheometer (TA Instruments) with a 60mm, 2° upper-cone geometry and a Peltier temperature-controlled lower-plate geometry. Samples were loaded at 30 °C and cool down to 5 °C before measurement. Thermal rheology was first probed using temperature ramps were performed with a heating rate of 1 °C min^{-1} under small-amplitude oscillatory shear with a strain amplitude of γ_0=1% and an applied frequency of ω=20 rad s^{-1}. Time-temperature superposition measurements of linear viscoelasticity were then performed, in which the dynamic shear moduli were measured using frequency sweeps over a range of 0.02-200 rad s^{-1} at γ_0=1%, at equilibrate temperatures ranging between 5-30 °C. For

representative samples, strain sweeps were carried out to ensure that the strain amplitude of γ_0=1% was well within the linear viscoelastic limit (see Appendix A, Figure A.1).

The polymers used in this experiment were poly(ethylene glycol) diacrylate (PEGDA, M_w~700 g mol^{-1}), dihydroxy-poly(ethylene glycol) (PEG, M_w~600 g mol^{-1}), and polyethylene glycol dimethyl ether (PEGDME, M_w ~ 500 g mol^{-1}). Sodium dodecyl sulfate (SDS) and Tween20 were used as surfactants to reduce the interfacial tension between the oil and water phases. Polydimethylsiloxane (PDMS, viscosity = 5 cp) was used as the dispersed oil phase for the nanoemulsions, and deionized water (18.2 MΩ) was used as the continuous water phase. All chemicals were purchased from the Sigma Aldrich and used without further purification. For neutron scattering measurements, deuterium oxide (D_2O, 99.9%, Cambridge Isotope Laboratories) was used as the water phase to enhance neutron contrast. Distilled water was used for the preparation of all aqueous solutions.

Nanoemulsions were prepared using a high-pressure homogenizer (Avestin Emulsiflex-C5) described in Chapter 2. Briefly, the continuous phase of the nanoemulsion was prepared by mixing of a 10 wt.% surfactant stock solution, pure polymer, and water in appropriate quantities by stirring for 10 min, resulting in a solution containing polymer concentration, P, (v/v) and molar surfactant concentration, C_s. A crude emulsion was then prepared using dropwise addition and high-speed mixing of PDMS. Nanoemulsions were stored at 7 °C in order to avoid significant aging due to Ostwald ripening.

3.3 Thermodynamics of polymer-surfactant complexation

To characterize the thermodynamics of self-assembly of PEGs and SDS, we performed calorimetric measurements using ITC. This technique allows for determining thermodynamic parameters of the binding process. First, we probed micellization of SDS by

itself in deionized water solution. Figure 3.1 shows the resulting differential enthalpy changes associated with demicellization of SDS at different temperatures.

The critical micelle concentration (cmc) of SDS (~8.33 mM) is independent of temperature in the experimental range. It was determined from the first-order differential curve of the ITC result, which agrees with literature values [47]. At SDS concentrations lower than the cmc, the enthalpy changes exhibit a significant temperature dependence. While demicellization at 25 and 35 °C is endothermic, it is exothermic at 15 °C. Therefore, all the measurements of titrating SDS into polymer solution were performed at 15 °C, corresponding to the range of the nanoemulsions that exhibited viscoelasticity. The micellization enthalpy (ΔH_{mic}) was determined from the method illustrated in Figure 3.1.

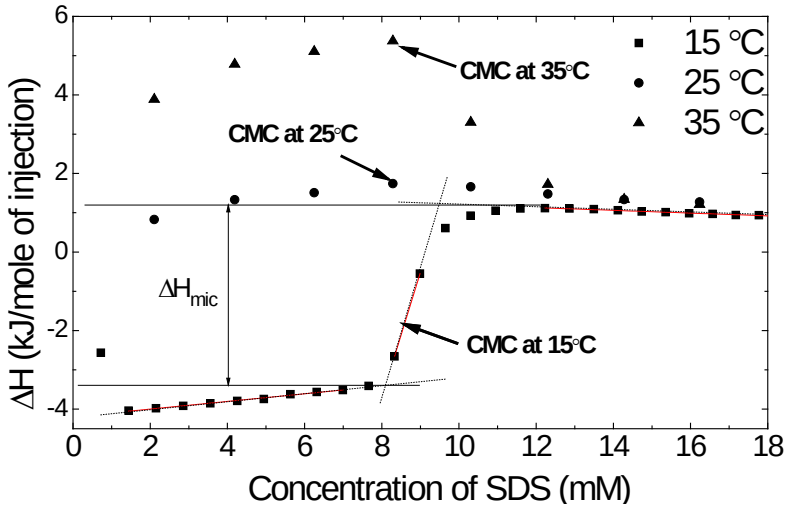

Figure 3.1 The enthalpy changes of titrating SDS into water at 15, 25 and 35°C.

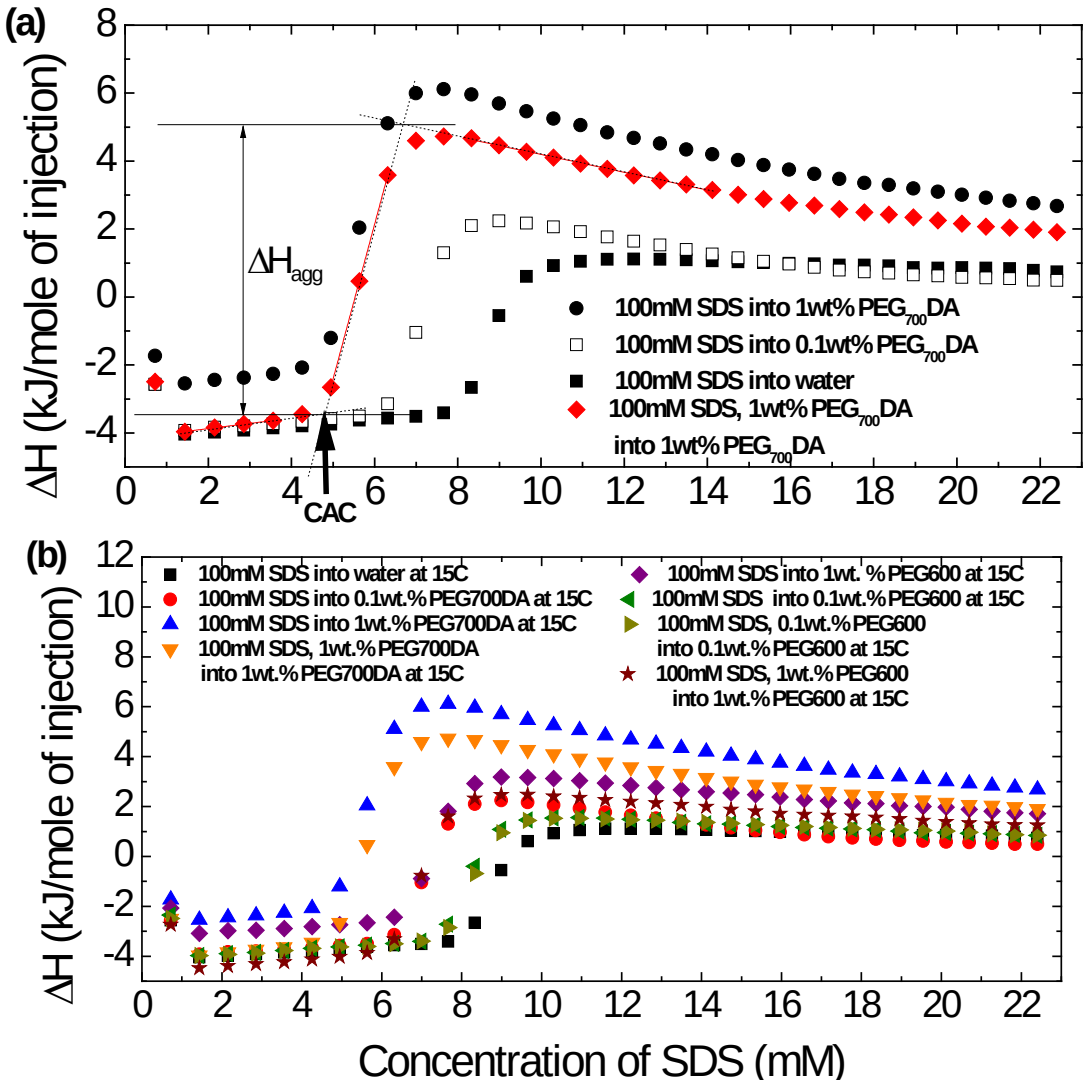

Figure 3.2 Enthalpy changes measured by ITC upon titrating (a) SDS solutions into PEG solutions and (b) SDS and PEG mixtures into SDS and PEG mixtures. Concentrations are described in legend and the measurement temperature is 15 °C.

Due to a large aggregation number of SDS micelles (n > 50) [48], the Gibbs free energy of SDS micellization can be expressed using the pseudo-phase separation approximation,

$$\Delta G_{mic} = RT(2-\alpha)\ln(x_{cmc}) \qquad (3.1)$$

where α is the effective fractional charge dissociation of SDS and x_{cmc} is the mole fraction of SDS at the cmc. For SDS, α was found to be approximately 0.3, in agreement with

previous measurements [49]. The entropy of SDS micellization (ΔS_{mic}) was determined based on the second law of thermodynamics,

$$\Delta S_{mic} = \left(\Delta H_{mic} - \Delta G_{mic}\right)/T \,. \qquad (3.2)$$

ΔG_{mic}, ΔH_{mic} and ΔS_{mic} at 15 °C were found to be 35.84 kJ/mol, 4.52 kJ/mol and 0.14 kJ/mol K, respectively. According to these values, the SDS micellization can be considered to be an entropically-driven process at 15 °C.

Furthermore, binding interactions between SDS and PEGs were characterized using ITC. Figure 3.2 (a) represents the titration of 100 mM of SDS solution into PEGDA solution described in section 3.2. From the data, we observed the critical aggregation concentration (cac), which is the onset of aggregation of SDS in the presence of polymer [50]. The cac of SDS in PEGDA solution is lower than cmc, and it decreases with increasing polymer concentration. In a similar manner illustrated in in Figure 3.2 (a), we can obtain the enthalpy of aggregation (ΔH_{agg}), which decreases with decreasing polymer concentration. Due to a large aggregation number of SDS relative to PEG (n ~ 35 per PEG molecule) [51], the Gibbs free energy of aggregation, ΔG_{agg} can again be approximated by the pseudo-phase separation approximation, while ignoring the polymer contribution,

$$\Delta G_{agg} = RT(2-\alpha)\ln(x_{cac}) \qquad (3.3)$$

where x_{cac} is the mole fraction of SDS at the cac. To investigate the effect of end group chemistry of PEG, titration of SDS into dihydroxy-poly(ethylene glycol) (PEGDOH, M_w ~ 600 g mol^{-1}) solution were performed and are shown in Figure. 3.2 (b). These thermodynamic parameters and the values of the cac are listed in Table 3.1.

Table 3.1Critical aggregation concentration and thermodynamic parameters for SDS in the presence of polymers at 15°C. The dilution effects of 1wt.% polymer are subtracted and that of 0.1wt.% polymer is negligible.

Polymer	CAC (mM)	ΔG_{agg} (kJ/mol)	ΔH_{agg} (kJ/mol)	ΔS_{agg} (kJ/mol K)
$PEG_{700}DA$-0.1wt. %	6.2	-37.06	5.9	0.149
$PEG_{700}DA$-1wt. %	4.8	-38.11	8.3	0.161
$PEG_{600}DOH$-0.1wt. %	7.4	-36.34	5.2	0.144
$PEG_{600}DOH$-1wt. %	6.6	-36.81	6.1	0.149

From the thermodynamic parameters, we again find that aggregation of SDS and PEG is entirely entropically-driven at 15 °C. PEG-SDS aggregation becomes more favorable with increasing polymer concentration and in the presence of polymers containing the hydrophobic acrylic end-groups. The enthalpy of aggregation, ΔH_{agg} becomes more endothermic with increasing polymer concentration, indicating that the enthalpic penalty to aggregation increases. There is a small increase in ΔS_{agg} with increasing polymer concentration. Also, the presence of acrylate end groups on PEG increases ΔS_{agg}, indicating that the aggregation becomes more favorable when PEG contains hydrophobic end-groups. These thermodynamic parameters can explain the mechanism of induced-micelle aggregation when the concentration is lower than cmc, which is thought to be driven by hydrophobic interaction between hydrocarbon chain of PEG and alkyl groups of SDS [51].

From the ITC measurements, we confirmed that the complexation of PEG and SDS depends on the concentration and polymer chemistry. Furthermore, the thermodynamic parameters reveal the complexation is entirely entropically-driven process. Most importantly, the thermodynamics of complexation is significantly temperature-dependent. This suggests that the formation and breakage of the complexation can be controlled by both

temperature and the concentration of polymer and surfactant. Since the polymers also interact with SDS at the interface, it provides the possibility to modify the colloidal behavior of nanoemulsions, resulting changes in rheological behaviors, such as viscoelasticity.

3.4 Temperature-dependent viscoelasticity

In order to test the effects of polymer-surfactant complexation on the rheological properties of nanoemulsions, we first studied O/W nanoemulsions in presence of different polymers and stabilizing surfactants in the continuous phase. The polymers consisted of various PEG chemistries, including PEG and PEGDA. The former was chosen due to its known complexation with a number of surfactants. The latter was chosen because nanoemulsions containing PEGDA are known to from thermoreversible viscoelastic solids at high temperature [4], and to demonstrate compatibility of the results shown here with various strategies for encapsulation of nanoemulsions within PEG hydrogels [4,5]. The surfactants used include SDS (an anionic surfactant known to exhibit complexation with PEG [10-15]) and Tween20 (a nonionic surfactant with no reported complexation with PEG [52]).

We tested the thermal rheology of nanoemulsions containing the different components by measuring the viscoelastic moduli (*G'* and *G"*, respectively) with increasing temperature from 5 to 65 °C at fixed droplet volume fraction (ϕ) of $\phi = 0.33$, and continuous phase concentrations of polymer (P) and surfactant (C_s) of P = 0.33 ($v_{polymer}/v_{continuous\ phase}$) and C_s = 200 mM (in the continuous phase), respectively (Figure 3.3). At high temperatures, the nanoemulsions containing PEGDA and SDS exhibit solid-like behavior. This is consistent with previous reports, which demonstrated that such nanoemulsions exhibit

colloidal gelation at high temperature mediated by telechelic bridging of PEGDA [4]. However, these nanoemulsions also exhibit previously unreported thermoreversible viscoelasticity at low temperature. Specifically, the nanoemulsion exhibits a transition from a low-viscosity liquid (where $G' << G''$) to a viscoelastic phase (with $G' > G''$) with decreasing temperature. This low-temperature rheological transition is significantly broader than the high-temperature gelation.

Nanoemulsions containing PEG exhibit a nearly identical transition at low temperature, occurring over a similar range in temperature and differing only by the ultimate values of the viscoelastic moduli at sufficiently low temperature. However, they exhibit no high-temperature gelation. This suggests that the mechanism of low-temperature viscoelasticity is the same for both polymers, and moreover is relatively insensitive to the

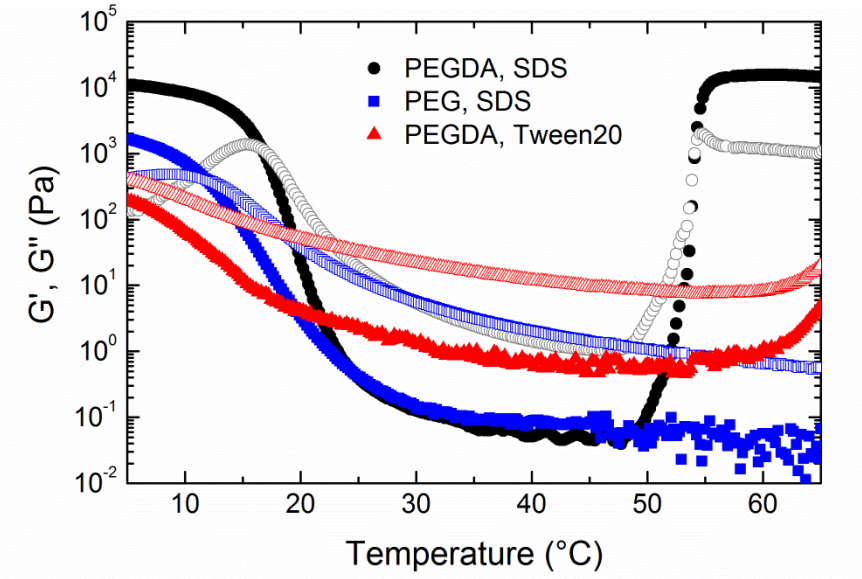

Figure 3.3 Low-temperature thermoreversible gelation in nanoemulsions. Thermal rheology (*G'*, closed symbols; *G"*, open symbols) at 1% strain and 20 rad s^{-1} frequency. Black symbols (circles) represent the sample containing ϕ = 0.33 droplets in water with P=0.33 PEGDA and C_s=200 mM SDS. Blue symbols (squares) represent the sample containing ϕ = 0.33 droplets in water with P=0.33 PEG and C_s=200 mM SDS. Red symbols (triangle) represent the sample containing ϕ = 0.33 PDMS in water with P=0.33 PEGDA and C_s=200 mM Tween 20.

end-group chemistry, unlike the high-temperature gelation [4]. Also, nanoemulsions containing PEGDME exhibit a similar transition at low temperature (Figure 3.4). This implies that the low temperature gelation is not caused directly by acrylate end group of PEG. Importantly, we also note that the continuous phase of the nanoemulsion itself (i.e. aqueous solutions of PEG and SDS) shows no observable viscoelasticity (Figure 3.4). Therefore, we conclude that the low-temperature viscoelasticity is primarily driven by the presence of the nanoemulsion droplets.

In order to test the effect of surfactant chemistry on the observed low-temperature gelation, we examined the thermal rheology of a nanoemulsion containing P = 0.33 PEGDA and C_s = 200 mM Tween20. Interactions between neutral polymers and non-ionic

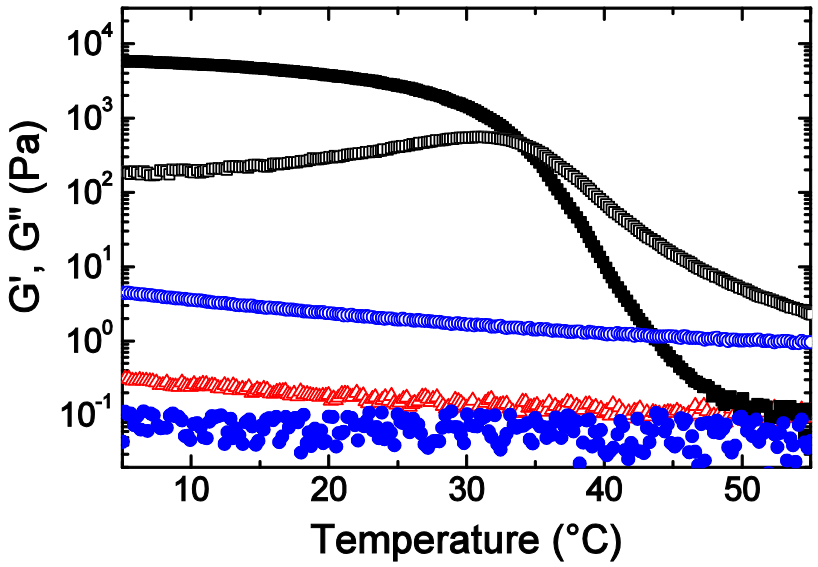

Figure 3.4 Thermal rheology (*G'*, closed symbols; *G"*, open symbols) of nanoemulsions and PEG/SDS mixture from 5 °C to 55 °C at 1% strain and 20 rad s^{-1} frequency. The nanoemulsions (black squares) contain ϕ = 0.33 PDMS droplets in water with P=0.33 PEGDME and C_s=100 mM SDS. The nanoemulsions (blue circles) contain ϕ = 0.33 PDMS droplets in water with P=0.33 PEGDA and C_s=100 mM Tween20. PEG/SDS mixture (red triangles) contains P=0.33 PEGDA and C_s=100 mM SDS in water.

surfactants are typically weak relative to ionic surfactants [52]. Nevertheless, we find that the nanoemulsion containing Tween20 does exhibit viscoelasticity at both low and high temperatures, although to a much lesser degree (Figure 3.3). This implies that even weak polymer-surfactant interactions are sufficient to produce low-temperature gelation. However, we note that lower concentrations of Tween20 (100 mM) show no measurable viscoelasticity at low or high temperatures (Figure 3.4).

To further investigate the observed dependence of low-temperature viscoelasticity on surfactant concentration, we used phase studies to construct a state map for nanoemulsions containing SDS with ϕ = 0.33 PDMS and P = 0.33 PEGDA in a space of C_s and temperature. In general, we observe four regimes of characteristic behavior (Figure 3.5). At high temperatures, the nanoemulsions exhibit gelation concomitant with significant turbidity and an apparent yield stress. This extends previous studies [4] by examining the dependence of the onset of high-temperature gelation on the overall surfactant concentration. We find that the critical temperature for such gelation decreases only modestly with increasing C_s.

As the temperature decreases below the gel temperature, the nanoemulsions transition through a series of transparent phases, including liquid, viscoelastic, and gel-like states. Like the high-temperature gelation, we find that the temperatures at which these approximate transitions occurs decrease with increasing surfactant concentration, although to a larger degree. Critically, we note the optical transparency of the gel-like phase at low-temperature, in contrast with the turbidity observed in the high-temperature gels. This, in combination with the observed thermal rheology in the presence of PEG, suggests that the mechanism of low-temperature viscoelasticity differs significantly from the high-temperature gelation, which was proposed to be due to end-adsorption of hydrophobic

PEGDA end groups leading to interdroplet polymer bridging, which eventually causes colloidal aggregation and gelation.

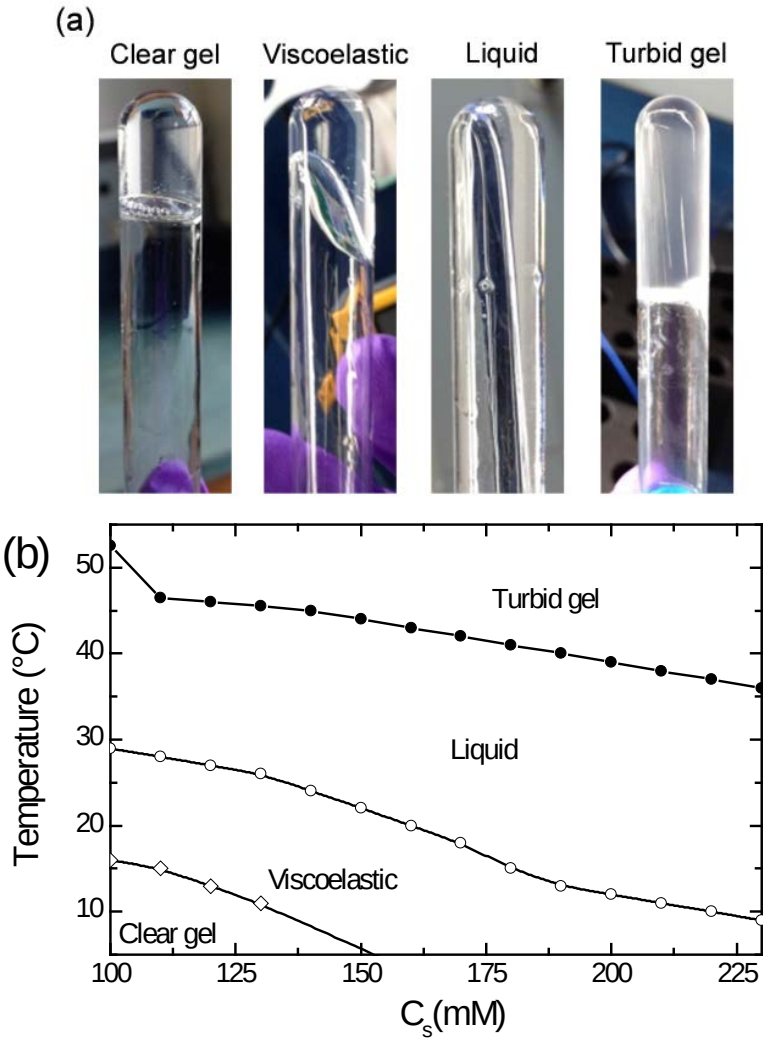

Figure 3.5 Rhelogical phase diagram of nanoemulsions as a function of SDS concentration and temperature. All samples contain ϕ = 0.33 PDMS droplets in water with P=0.33 PEGDA and varying C_s. (a) Photographs of the four regimes. (b) Resulting phase diagram.

3.5 Microstructure and dynamics

To further elucidate the mechanism of the viscoelasticity at low temperature, we performed structural characterization using SANS. Figure 3.6 shows SANS spectra at different temperatures of the sample containing ϕ = 0.33 PDMS droplets with P=0.33 PEG and C_s = 200 mM SDS in D_2O, which exhibits apparent low-temperature gelation (where *G'~G"*) below approximately 20 °C (Figure 3.4). In the high-q regime, the scattering is invariant with decreasing temperature, indicating that the droplet size and polydispersity are unchanged. The scattering intensity in the low-*q* regime is also remarkably insensitive to changes in temperature. This result is consistent with the negligible change of optical properties during this process, and indicates that there is no observable structural change of the nanoemulsions over the entire low-temperature rheological transition.

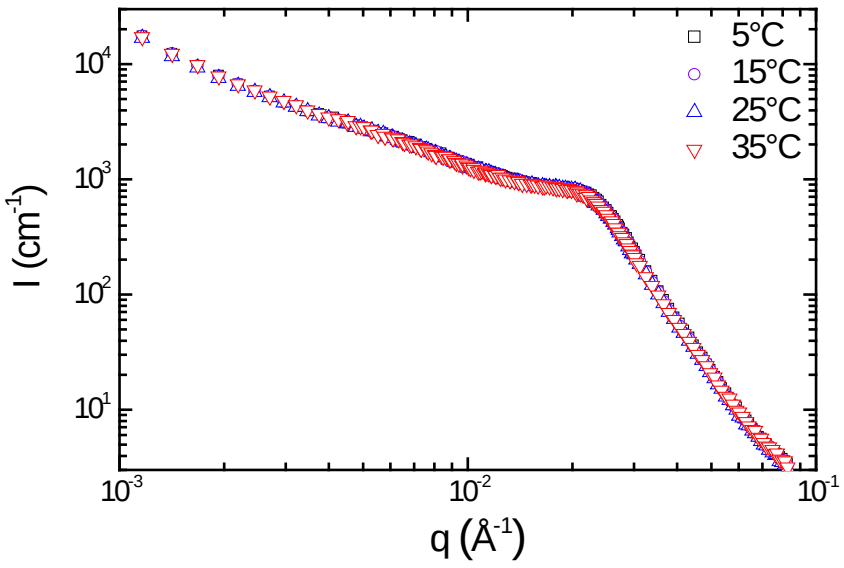

Figure 3.6 Microstructural characterization of nanoemulsions. SANS spectra for a nanoemulsion containing ϕ = 0.33 PDMS droplets with P=0.33 PEG and C_s=200 mM SDS in D_2O at the temperatures indicated.

This temperature-independent microstructure suggests that the low-temperature viscoelasticity is driven entirely by the dynamics of the nanoemulsion. To further probe these dynamics, we performed temperature-dependent DLS measurements on the same sample used in SANS measurements. Figure 3.7 (a) shows the intermediate scattering function (ISF) measured at several different temperatures at a fixed angle θ= 130° (q = 24.67 μm^{-1}). At droplet volume fractions up to ϕ = 0.20, the nanoemulsions exhibit single-mode relaxation of the ISF consistent with diffusive motion of polydisperse droplets, and temperature-dependence of the self-diffusivity that scales as expected for the resulting change in solvent viscosity (see Appendix A, Figure A.2 and A.3).

However, at a volume fraction of ϕ = 0.33, we instead observe two distinct dynamical modes, exemplified as a two-step relaxation of the ISF over the range of temperatures spanning the low-temperature viscoelastic transition. This two-step relaxation is well-captured by a sum of two stretched exponential functionals,

$$f(q,\tau) = A\exp\left[-\left(\frac{\tau}{\tau_1}\right)^{\alpha}\right] + (1-A)\exp\left[-\left(\frac{\tau}{\tau_2}\right)^{\beta}\right] \quad (3.4)$$

as illustrated in Figure 3.7 (a) (See Appendix A, Figure A.4 and A.5 for fit parameter values).

Stretched exponential behavior has been widely observed in chemically crosslinked [53], colloidal [54,55] and physically associating [56] systems, including polymer-surfactant complexes [57], and is typically attributed to a hierarchical distribution of relaxation times for density fluctuations [58]. We observe that stretched exponents (α) of the fast mode are ~0.7 and are essentially independent of temperature within experimental errors. In contrast, the exponents (β) of the slow mode decrease from

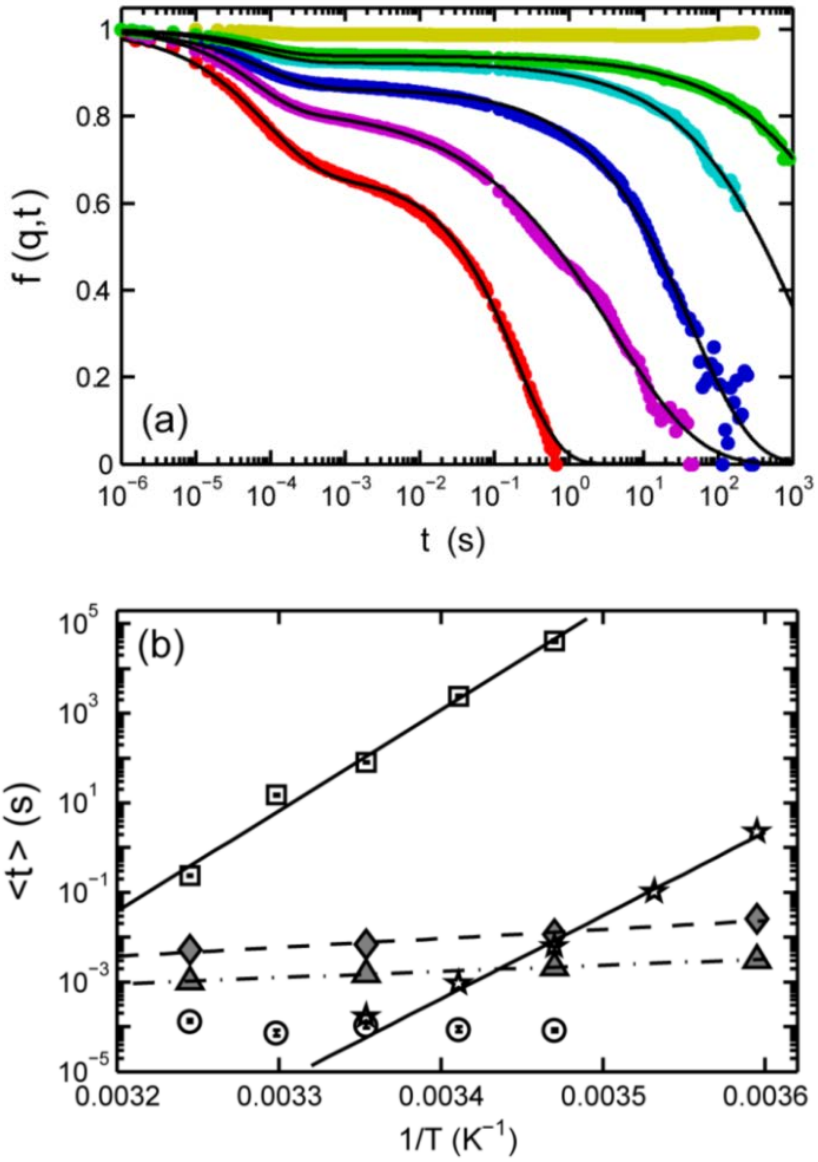

Figure 3.7 Dynamics of nanoemulsions through the low-temperature viscoelastic transition probed by DLS. The diameter of droplets is measured to be 55.4 nm with a polydispersity of 0.21. Nanoemulsions are initially prepared at ϕ=0.33, P=0.33 (PEG) and C_s=200 mM. Nanoemulsions at lower volume fractions are achieved by diluting the concentrated nanoemulsions with a polymer solution of P=0.33 (PEG). (a) Intermediate scattering functions of nanoemuslions measured at T=35 °C, 30 °C, 25 °C, 20 °C, 15 °C, and 5 °C (from bottom to top) for samples prepared at ϕ=0.33. The scattering angle is fixed at θ=130°, corresponding to q=24.67 μm^{-1}. Solid lines are fits to a sum of two stretched exponentials. (b) Arrhenius plot of relaxation times of samples prepared at ϕ=0.01 (filled triangles), 0.20 (filled diamonds) and 0.33 (circles for τ_1 and squares for τ_2). Lines are fits to the Arrhenius equation to extract activation energy E_a, which are 11.4±0.5, 16.5±9.4 and 187±40 k_bT, respectively. For comparison, relaxation times extracted from rheological measurements are also presented for samples of ϕ=0.33, P=0.33 (PEGDA), C_s=100mM (stars).

~0.7 to ~0.5 as temperature decreases from 35 °C to 30 °C or lower. Similar behavior has been observed in both physically associating polymers [59], glassy colloidal suspensions [60], and chemically-crosslinked polymer gels [53], with β ~ 0.5 corresponding to the percolation threshold.

The distribution of relaxation times captured by stretched exponential dynamics can be captured by the average relaxation times,

$$\langle \tau_1 \rangle = \frac{\tau_1}{\alpha}\Gamma\left(\frac{1}{\alpha}\right) \text{ and } \langle \tau_2 \rangle = \frac{\tau_2}{\beta}\Gamma\left(\frac{1}{\beta}\right) \quad (3.5)$$

where Γ(x) is the gamma function, which conveniently capture both the temperature- and q-dependence of the fast and slow modes (Figure 3.7 (b)). We find that the fast mode exhibits an average relaxation time which is nearly independent of temperature, and follows a q^2 dependence (Figure 3.8). Finally, we observe the characteristic time scale for

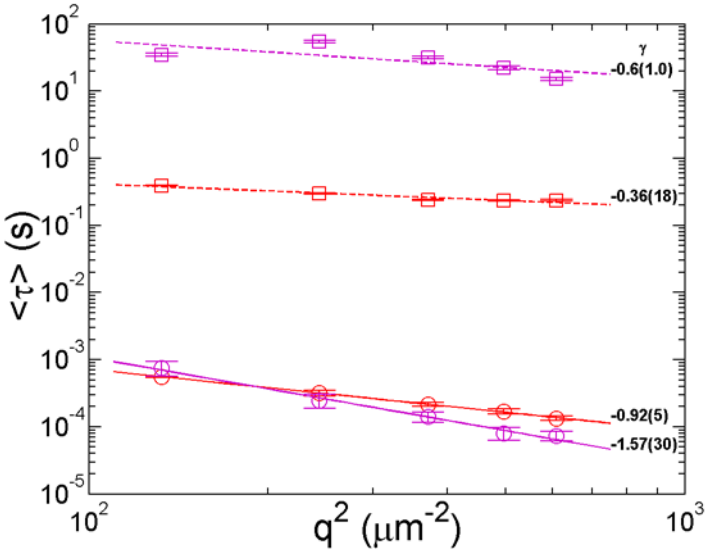

Figure 3.8 q-dependence of average relaxation times (circles for $<\tau_1>$ and squares for $<\tau_2>$) at T=35 °C (red) and 30 °C (purple). Lines are fits to $< \tau_i > \sim (q^2)^{\gamma}$.

relaxation of the fast mode is significantly faster than that of droplets in dilute conditions (Figure 3.7 (b)). Therefore, we attribute the fast mode to diffusive motion of free molecular aggregates in solution, such as micelles or polymer-micelle complexes.

The slow mode has a characteristic time scale which, at low temperatures, is similar to that for self-diffusion of droplets at low volume fraction (See Appendix A, Figure A.6). Therefore, we attribute the slow relaxation to collective hydrodynamic modes of oil droplets. Interestingly, $< \tau_2 >$ exhibits slowing down by 6 orders of magnitude with a moderate change of temperature from 35 °C to 15 °C, which can be captured by an Arrhenius expression, $< \tau_2 > \sim \exp(-E_{a,2}/k_bT)$. A fit to this relation gives $E_{a,2} = 187 \pm 40\ k_bT$, far beyond what is expected for viscous activation of the solvent (See Appendix A, Figure A.7). We also find that $< \tau_2 >$ has a weak dependence on q, implying that the relaxation is largely length scale independent. Similar behavior has been observed in microemulsion systems in the presence of telechelic polymers, and has been attributed to the average relaxation time of polymer network junctions or a breathing mode of the network [46]. In our study, this could arise from the relaxation of the network structure induced by polymer-surfactant complexes as manifest in the collective hydrodynamic modes of droplets.

3.6 Linear viscoelasticity and Time-temperature superposition

To further understand the low-temperature viscoelasticity in nanoemulsions containing PEG and SDS, we measured frequency-dependent linear viscoelastic spectra of the dynamic shear moduli for a range of temperature T=5-30 °C spanning the liquid, viscous, and transparent gel phases (Figure 3.9 (a)). The nanoemulsions exhibit liquid-like behavior at high temperature ($G''>G'$) with the expected frequency-dependence of $G' \sim \omega^2$

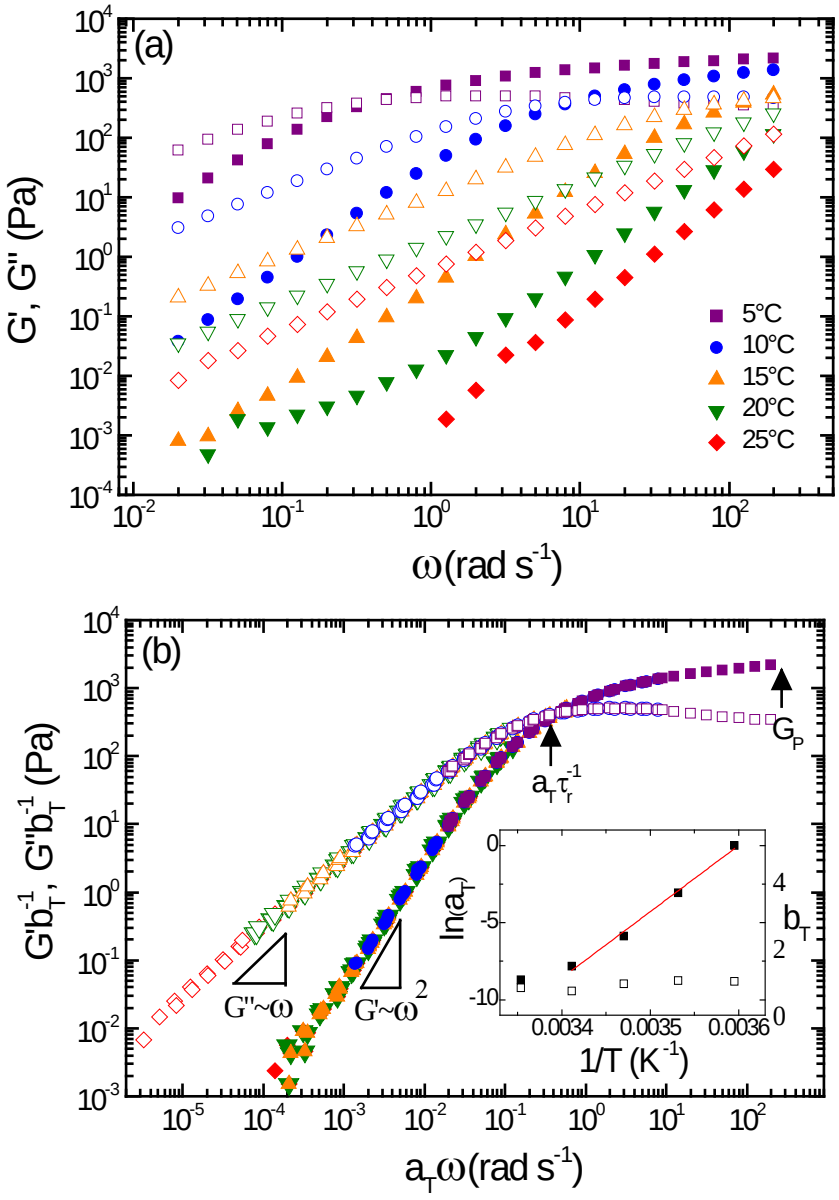

Figure 3.9 Thermal viscoelasticity follows time-temperature superposition. (a) Dynamic shear moduli (*G'*, closed symbols; *G"*, open symbols) as a function of frequency at the temperature indicated. (b) Master curves ($G'b_T^{-1}$, closed symbols; $G"b_T^{-1}$, open symbols) for the sample contains ϕ = 0.33 PDMS droplets in water with P=0.33 PEG and C_s=200mM SDS. Inset: Arrhenius plot of horizontal shifting factors a_T (closed) and vertical shifting factor b_T (open). The reference temperature is T=5°C

and $G''\sim\omega$ (Figure 3.9 (b)). As the temperature decreases, crossover of G' and G'' occurs at moderate frequencies, with a rubbery plateau in G' at high frequencies. At sufficiently low temperature, this plateau persists over the observable frequency range, indicating gel-like behavior.

Given that DLS revealed the dynamics of the nanoemulsions to exhibit marked self-similarity with temperature without significant changes in microstructure, similar behavior might be expected in their rheology. Specifically, we test whether the low-temperature viscoelastic transition obeys time-temperature superposition (TTS). By shifting G' and G'' at different temperatures horizontally (a_T) and vertically (b_T), we find that the data collapse onto a single master curve of the viscoelastic moduli over 9 decades in frequency (Figure 3.9 (b)). TTS is widely observed in viscoelastic polymers, and has been shown previously for polymer-colloid mixtures [61]. However, to our knowledge, this is the first such demonstration of TTS for emulsions, and moreover a system in which the polymer alone exhibits no viscoelasticity.

The linear viscoelastic master curve exhibits remarkable Maxwell-like viscoelasticity. At low relative frequencies, the nanoemulsions exhibit liquid-like behavior, indicated by the scaling of the dynamic moduli where $G'\sim\omega^2$ and $G''\sim\omega$. At moderate frequencies, crossover of G' and G'' indicate a terminal relaxation in the fluid given by its corresponding frequency, $\omega_r(T)=\tau_r^{-1}(T)$, where τ_r is the temperature-dependent characteristic relaxation time. At high frequencies, G' exhibits a plateau of $G_p \sim 2150$ Pa.

The horizontal (a_T) and vertical (b_T) shift factors are plotted as a function of the reciprocal temperature in Figure 3.9 (b, inset). We find that b_T is nearly unity for all

temperatures examined, suggesting that the nanoemulsions obey idealized TTS. Furthermore, a_T exhibits clear Arrhenius behavior over the range of temperatures, with

$$\ln\left(a_T\right) = \frac{E_a}{R}\left(\frac{1}{T} - \frac{1}{T_{ref}}\right) \quad (3.6)$$

Fitting the data to this relationship, we obtain a characteristic activation energy for viscoelasticity of $E_{a,2}$ = 154±9 k_bT. This energy is remarkably similar to the characteristic activation energy $E_{a,2}$ determined for the slow dynamical relaxation mode observed in DLS measurements. This shows that the observed rheology is directly coupled with the relaxation of collective dynamical modes.

From this, we surmise that the viscoelastic network is mediated by effective junctions between nanoemulsion droplets produced by polymer-surfactant complexation. However, we also note that the magnitude of the viscoelastic relaxation time is many orders of magnitude faster than that for the slow mode in DLS. To show this, the magnitude of $< \tau_2(T) >$ fit from DLS measurements and $\tau_r(T)$ estimated from TTS measurements are plotted simultaneously in Figure 3.7 (b). This suggests that although the viscoelastic and dynamical modes are coupled by the same activated process, their relaxation is manifest in a different manner. Specifically, the former will have a time scale set by the dynamic formation and breakage of a number of polymer-surfactant complexes comprising the network structure of a single droplet. By contrast, the latter will have a time scale set by the perturbative effect of many such events on the collective hydrodynamic modes of many droplets.

3.7 Effect of materials composition

To test the generality of the low-temperature viscoelastic transition in our nanoemulsions, we probed the linear viscoelasticity of nanoemulsions containing PEGDA and SDS over a wide range of compositional space, including changes in surfactant and polymer concentration, as well as changes in the average droplet size. In particular, we find that the low-temperature viscoelasticity of the nanoemulsions obeys TTS as described above for all conditions studied. Therefore, the set of TTS parameters G_p, τ_r, and E_a serve as a convenient means by which the dependence of rheological properties on material composition, and thus the specific nature of PEG-SDS interactions, can be assessed.

Table 3.2 TTS viscoelastic parameters of the nanoemulsions containing 33 vol% PDMS droplets.

PEGDA	SDS (mM)	D (nm)	SDS/PEGDA[a]	G_p (Pa) at 5°C	E_a (k_bT_{ref})	τ_r (s)
P=0.33	100	54.4	0.038	4430	206±12	7.82×10^{3}
P=0.33	125	52.2	0.085	3690	170±20	1.52
P=0.33	150	54.5	0.132	2480	138±23	9.86×10^{-2}
P=0.33	175	56.1	0.179	1440	86±28	1.37×10^{-2}
P=0.39	100	57.4	0.032	710	80±12	1.59×10^{-2}
P=0.39	120	50.2	0.064	1940	142±15	0.188
P=0.39	150	46.3	0.113	75	70±2	[b]

[a] Molar ratio of SDS in the bulk continuous phase to PEGDA.
[b] The characteristic relaxation time cannot be obtained in the attainable frequency range.

3.7.1 Effect of surfactant concentration

Figure 3.10 presents TTS master curves of nanoemulsions containing different SDS concentration, C_s, and droplets with average diameter D = 54±2 nm at fixed volume fraction $\phi = 0.33$. All data are shifted to a reference temperature of $T_{ref} = 5$ °C. Two series of samples at different fixed overall polymer concentrations were studied, one with P = 0.33 PEGDA and one with P = 0.39 PEGDA. In these experiments, sample-to-sample deviations of the droplet size are small enough to ignore its influence on the rheological properties. Since samples contain the same volume fraction of oil and similar size of droplets, they require similar amount of the surfactant to stabilize the oil-water interface.

Thus, the increasing overall surfactant concentration represents an increase in free surfactant in the bulk continuous phase at fixed polymer concentration. Note that this also corresponds to a change in the molar ratio of free surfactant and polymer. Table 3.2 shows estimates of this ratio, assuming that 80 mM SDS is the minimum surfactant concentration required to stabilize the PDMS oil droplets with this droplet size. To determine this value, we performed experiments involving homogenization of nanoemulsions under fixed homogenizing conditions, but with different SDS concentration (see Appendix A, Figure A.8). These experiments indicate a significant increase in average droplet size below 80 mM SDS. Therefore, we choose this concentration to be the total concentration of surfactant required to saturate the oil–water interface for droplets with D~54 nm. Table 3.2 shows the corresponding values of G_p and E_a, as well as the relaxation time τ_r for each sample at the reference temperature.

For P = 0.33, the plateau modulus, G_p, and relaxation time, τ_r, both decrease monotonically with increasing surfactant concentration, the latter by several orders of

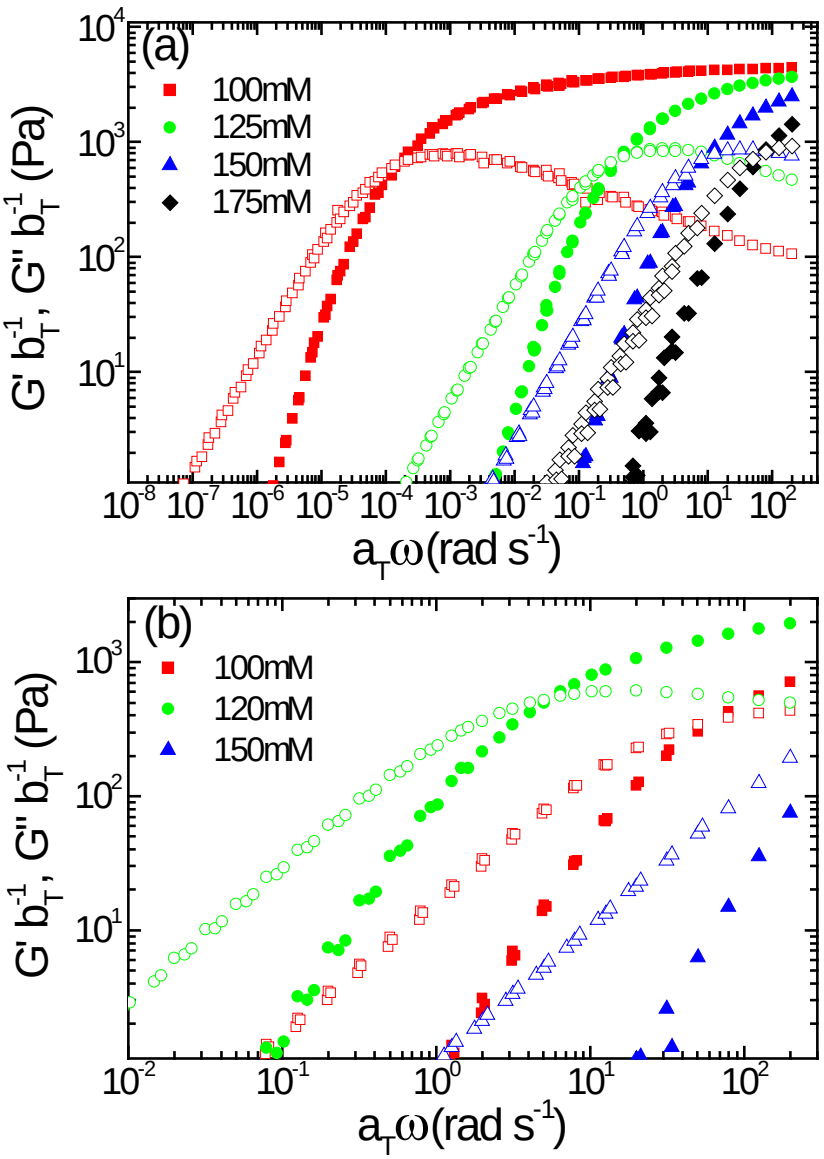

Figure 3.10 Dependence of viscoelasticity ($G'b_T^{-1}$, closed symbols; $G''b_T^{-1}$, open symbols) on SDS concentration. (a) The nanooemulsion samples contain ϕ = 0.33 PDMS droplets with D=54±2nm in water with P=0.33 PEGDA and varying C_s. (b) The nanoemulsion samples contain ϕ = 0.33 PDMS droplets with D=52±5nm in water with P=0.39 PEGDA and varying C_s. The reference temperature is T=5°C

magnitude over the range of C_s studied. This is consistent with the result of phase studies (Figure 3.5 (b)), where higher concentration of surfactant inhibits the transition to low-

temperature viscoelasticity. Also, the characteristic activation energy, E_a decreases monotonically with increasing surfactant concentration.

By contrast, the nanoemulsions containing higher polymer concentration of P=0.39 exhibit non-monotonic changes of both G_p and τ_r with increasing surfactant concentration. Specifically, both quantities exhibit a maximum at an intermediate SDS concentration of C_s = 120mM (SDS:PEG = 0.064) below which the viscoelasticity increases with increasing SDS concentration. E_a also changes non-monotonically with increasing surfactant concentration.

3.7.2 Effect of polymer concentration

The results for the surfactant concentration dependence studies indicate that low-temperature viscoelasticity of nanoemulsions containing PEG and SDS is non-trivially determined by the composition of both polymer and surfactant. To test the specific contribution of the polymer, we characterized nanoemulsions with C_s = 100 mM SDS and varying PEGDA concentration in the range of P=0.27-0.39. Figure 3.11 shows TTS master curves of *G'* and *G"* for the different concentrations of PEGDA, and their respective material parameters are given in Table 3.3. The results show that G_p and τ_r decrease monotonically with increasing polymer concentration, indicating that the added polymer inhibits low-temperature viscoelasticity over this concentration range.

Interestingly, τ_r decreases by four orders of magnitude over this range of polymer concentration. This is markedly different than polymer networks both in the absence [42,62] and presence [63,64] of colloidal species, which typically exhibit increased elastic modulus and relaxation time in the presence of high concentrations of polymer due to an increase in the number of polymer-polymer interactions (either through entanglement or molecular

Table 3.3 Rhelogical parameters of the nanoemulsions containing 33 vol% PDMS droplets and Cs=100mM SDS resulting from the TTS.

PEGDA	D (nm)	SDS/PEGDA[a]	G_p (Pa) at 5 °C	E_a (k_bT_{ref})	τ_r (s)
P=0.27	59.9	0.046	8622	263±13	9.61×10^{6}
P=0.30	54.9	0.042	6475	245±9	6.17×10^{5}
P=0.33	54.4	0.038	4430	206±12	7.82×10^{3}
P=0.36	53.3	0.035	3441	177±13	260

[a] Molar ratio of SDS in the continuous phase to PEGDA single chain.

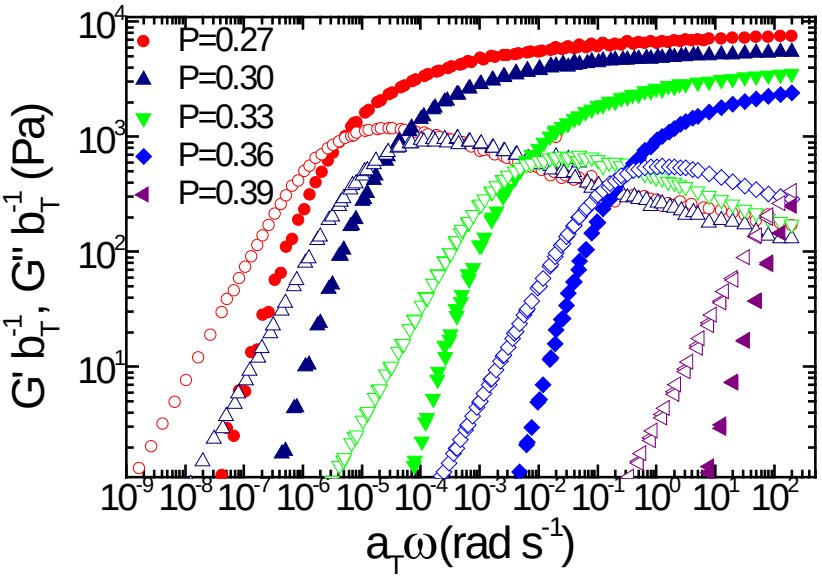

Figure 3.11 Dependence of viscoelasticity ($G'b_T^{-1}$, closed symbols; $G''b_T^{-1}$, open symbols) on polymer concentration. All nanoemulsion samples contain ϕ = 0.33 PDMS droplets with D=56±4nm in water with varying PEGDA and C_s =100mM SDS. The reference temperature is 5 °C.

association). From this, we conclude that the low-temperature viscoelasticity in these nanoemulsions is not a direct result of polymer-polymer interactions alone.

In addition, the characteristic activation energy decreases with the increasing the polymer concentration. We note that these results are analogous with the behavior observed with increasing SDS concentration at relatively low polymer concentration.

3.7.3 Effect of droplet size

The size of nanoemulsion droplets was previously shown to significantly influence the process of colloidal gelation of nanoemulsions at high temperature [4]. Therefore, we performed TTS measurements on nanoemulsions containing different droplet sizes at fixed surfactant and polymer concentrations of C_s = 100 mM and P=0.33 PEGDA and a droplet volume fraction of ϕ = 0.33. The different droplet sizes were obtained by preparing the samples at different homogenization pressures [4,65]. The results of TTS measurements are

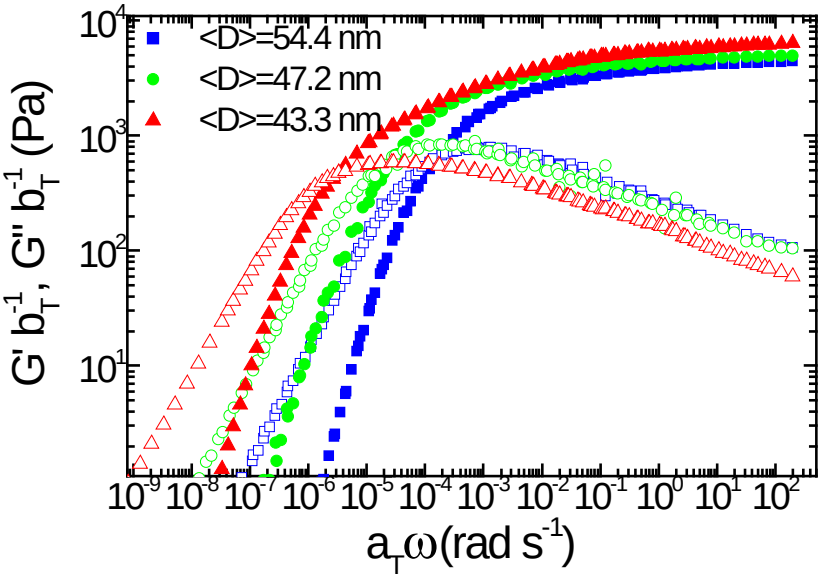

Figure 3.12 Dependence of viscoelasticity (*G'b*$_T^{-1}$, closed symbols; *G"b*$_T^{-1}$, open symbols) on droplet size. All nanoemulsion samples contain ϕ = 0.33 PDMS droplets in water with P = 0.33 PEGDA and C_s = 100mM SDS. The reference temperature is 5 °C.

Table 3.4 Rhelogical parameters of the nanoemulsions containing 33 vol% PDMS droplets and Cs=100mM SDS resulting from the TTS.

PEGDA	D (nm)	G_p (Pa) at 5 °C	E_a (k_bT_{ref})	τ_r (s)
P=0.33	54.4	4430	206±12	7.82×10^3
P=0.33	47.2	4960	232±5	3.22×10^4
P=0.33	43.3	6390	250±13	2.99×10^5

shown in Figure 3.12. We find that, for the same fluid composition, the size of the oil droplets significantly influences the observed rheological parameters. Specifically, G_p increases nearly two-fold and τ_r increases by several orders of magnitude when the droplet size is decreased by as little as 20%. Also, E_a increases with decreasing droplet size.

It is important to note that, although the nanoemulsions were prepared at the same overall surfactant concentration, the change in droplet size requires a significant increase in the amount of surfactant required to stabilize the oil-water interface due to the increase in interfacial area. Therefore, the change in droplet size represents a significant decrease (by as much as 90%) in the amount of free surfactant in the bulk continuous phase. This is consistent with the dependence of low-temperature gel modulus on surfactant concentration at low polymer concentration (Figure 3.9), where a significant increase in G_p with decreasing free surfactant concentration is expected. This also explains why the sample at C_s = 200 mM SDS and P = 0.33 PEGDA shown in Figure 3.3 is significantly more viscoelastic than that at in Figure 10 (a), as the droplet size is significantly smaller in the former case.

We find that the magnitude of the relaxation time, τ_r, decreases much more modestly with droplet size (by several orders of magnitude) than that expected from a decrease in free surfactant concentration alone at fixed droplet size. Therefore, the decreased surfactant

concentration in the continuous phase is insufficient to entirely explain the dependence of low-temperature viscoelasticity on droplet size, and thus the droplet size itself plays a significant role in determining the magnitude of the rheological parameters.

3.8 Discussion

We have demonstrated that polymer-surfactant complexation has a dramatic effect on the rheology of oil-in-water nanoemulsions. Specifically, the nanoemulsions exhibit a previously unobserved thermoreversible transition with decreasing temperature from a low-viscosity liquid to a gel-like state, which we have probed using several different methods. Most significantly, the low-temperature nanoemulsion gels are found to obey time-temperature superposition with Maxwell-like viscoelasticity over a broad range of material parameters, including surfactant and polymer concentration, polymer end group chemistry, and droplet size. Scattering measurements indicate that the origins of this viscoelastic behavior is entirely dynamical, i.e., it occurs in the absence of any observable changes in nanoemulsion microstructure, including suspension instability of the nanoemulsion droplets sometimes observed in polymer bridging systems [4,66]. Thus, the mechanism of low-temperature viscoelasticity (polymer-surfactant complexation) is entirely different from the mechanism of gelation at high temperatures (bridging-induced colloidal aggregation). DLS measurements show the emergence of two dynamical modes – a short-time relaxation due to self-diffusion of structural elements in a viscous solvent, and a long-time relaxation due to cooperative motion of droplets that can be described by a stretched exponential ISF (i.e. a hierarchical distribution of relaxation times). The average relaxation time of the cooperative mode follows Arrhenius behavior with an anomalously large activation energy. Remarkably,

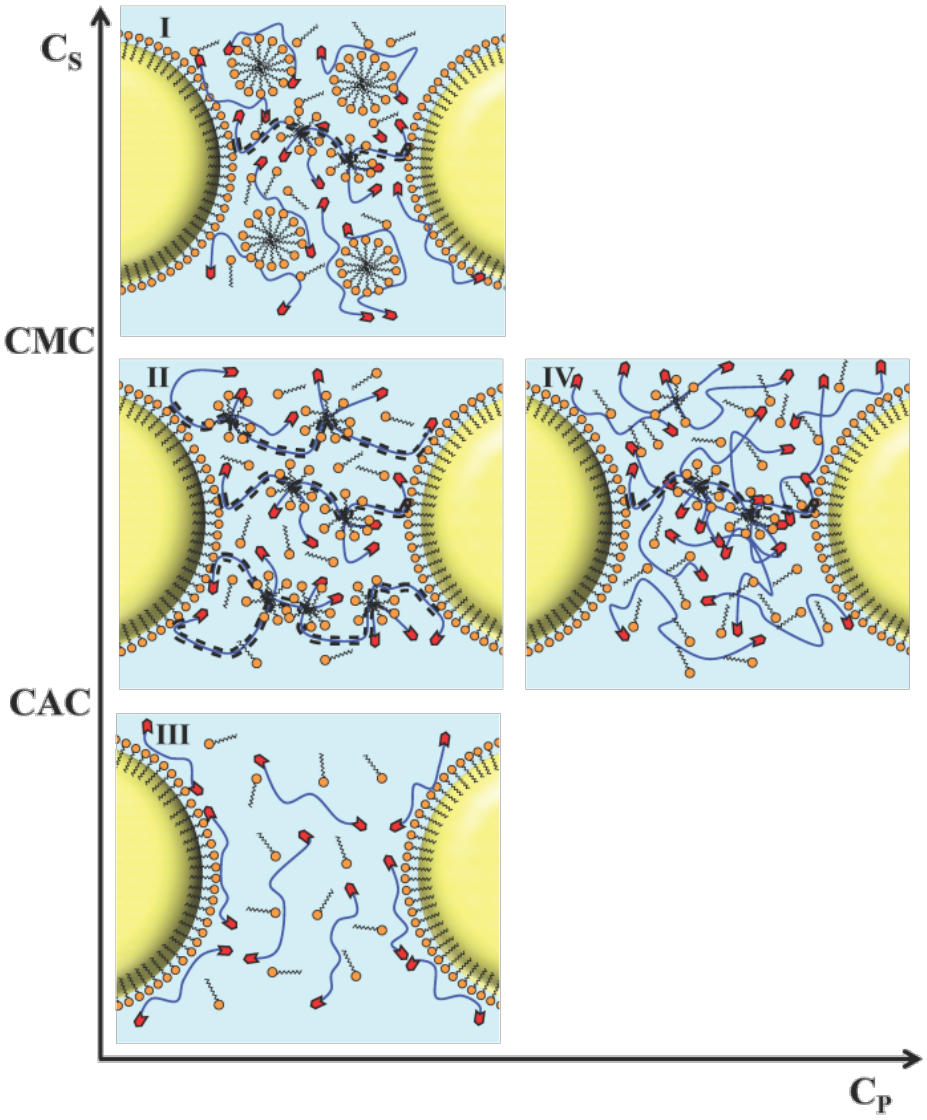

Figure 3.13 Schematic diagram of low temperature gelation mechanism as a function of SDS and PEGDA concentration. (Panel I) At Cs below cac, the conformation of PEG with SDS at the oil-water interface due to the ion-dipole interactions. (Panel II) At Cs above cac, the formation of polymer-induced SDS micelles create a transient force chains between droplets. (Panel III) At Cs above cmc, the number of free micelles increases with increasing SDS concentration, resulting in association between free SDS micelles and PEG both in free solution and absorbed at the oil-water interface. This gives rise to decreases the number of transient force chain between droplets. (Panel IV) As the polymer concentration increases at fixed surfactant concentration, the number of polymer-induced SDS micelles per chain decreases, resulting in the decrease of the number of transient force chain between droplets.

this activation energy is in quantitative agreement with that obtained from TTS measurements, demonstrating that the slow mode is responsible for viscoelasticity in the nanoemulsions.

From this, we hypothesize that the low-temperature viscoelasticity results from the formation of a transient gel mediated by the equilibrium formation of a network of interdroplet junctions connected by transient polymer-surfactant complexes (Figure 3.13). As discussed previously, such complexes have been widely observed in a number of polymer-surfactant systems, both in bulk solution and at fluid interfaces, and can exhibit strongly concentration-dependent behavior. As such, the ability of this mechanism to explain the observed dependence of rheological parameters on material composition requires careful explanation.

We first note that low-temperature gelation is observed for combinations of polymer and surfactant which are known to undergo complexation in bulk solution. Specifically, complexation between PEG and SDS has been well-characterized in dilute and semi-dilute solutions for the relevant range of PEG molecular weight studied here [16]. It is also possible that PEG-SDS complexes adsorb at the oil-water interface. The molecular mechanisms of this complexation include both ion-induced dipole interactions between the surfactant headgroup and ether moieties of the polymer, as well as hydrophobic interactions between polymer and surfactant tail [16]. It appears that both types of interactions are necessary for complexation. By contrast, non-ionic ethoxylated surfactants, such as Tween20, show much weaker interactions with PEG [52], and as a result, much lower viscoelasticity (Figure 3.3). These results suggest that the surfactants most likely to induce

low-temperature gelation due to polymer-surfactant interactions are ionic surfactants which can interact strongly with PEG through dipolar interactions.

Furthermore, we importantly observe that low-temperature viscoelasticity cannot be obtained in the absence of oil droplets for the same compositions in the continuous phase of the nanoemulsions. This is in contrast to some other polymer-surfactant systems such as purely ionic coacervates [67] or hydrophobically-associating [42] systems where significant viscoelasticity and gel-like behavior are observed without the colloid. There are several reasons for this. First, PEG-surfactant complexation is very weak compared to these interactions. Thus, the lifetime of PEG-SDS associations in free solution is insufficient to produce a viscoelastic network that relaxes on observable time scales. Second, the former systems generally involve higher molecular weight polymers, which can entangle even in the absence of surfactant, whereas the PEG molecular weights we choose to study are well below the entanglement molecular weight.

It is important to discuss the potential role of interdroplet attractions in these materials due to the depletion of PEG or PEG-SDS complexes near the droplet surface. If such depletion attractions exist, our results clearly show that they are not important to any of the low-temperature behavior we describe. Firstly, one would expect depletion attractions to alter the suspension microstructure or colloidal stability of nanoemulsion droplets, which is not the case in our materials. Secondly, since the strength of depletion interactions increases monotonically with the concentration of excluded material, one would expect a monotonic increase in depletion-driven viscoelasticity with PEG or SDS concentration, which we clearly do not observe here. Therefore, we can rule out depletion as a possible mechanism to explain the low-temperature gelation.

3.8.1 Concentration dependence of viscoelasticy

We turn our attention to the dependence of the rheological properties on surfactant concentration. In general, two different mechanisms of PEG-SDS complexation have been observed under two different SDS concentration regimes. At relatively low surfactant concentration, polymer-surfactant interactions are sufficient to induce surfactant micellization via co-aggregates with the polymer [11,17]. This occurs above the critical aggregation concentration (cac), defined by the onset of complexation between PEG and SDS, which typically occurs below the critical micelle concentration (cmc) of the pure surfactant in aqueous solution. This co-aggregation is thought to be driven by hydrophobic interaction between hydrocarbon chains of PEG and alkyl groups of SDS [17]. At surfactant concentrations above the cmc, ion-dipole interactions between sulfonate headgroups and ether oxygen moieties are thought to result in wrapping of the polymer chain around the surface of SDS micelles in a “necklace of beads” configuration [13].

Figure 3.13 illustrates a hypothesized mechanism of transient network formation based on this behavior, which can be used to rationalize the effects of surfactant concentration on the material parameters G_p, τ_r, and E_a. In the limit of nearly zero free surfactant in the continuous phase (i.e. when the surfactant concentration is marginally sufficient to stabilize the oil-water interfacial area), PEG chains interact with the surface of oil droplets as though they are effectively micelles, resulting in equilibrium association with the interface due to ion-dipole interactions, resulting in a flat adsorbed polymer conformation (Figure 3.13, Panel I). Such association was revealed by molecular dynamics simulation of mixed PEG and SDS at air/water interfaces [36], whereby a small surface excess of SDS is sufficient to recruit a large fraction of PEG chains to the interface. Since

such structures do not persist into the continuous phase, this prohibits viscoelasticity at sufficiently low surfactant concentrations. Since the free surfactant concentrations associated with this regime will be extremely low, we believe that such conditions are not observed in our measurements.

As the SDS concentration increases (but remains below the cac), free surfactant monomers in the continuous phase can associate with the loops and tails of PEG chains adsorbed at the oil-water interface, resulting in stretching of the polymer conformation into the continuous phase at low ionic strength [35]. It is possible that such structures can bridge between droplet surfaces, producing a temporary network. However, the diameter of gyration (~2 nm) [4] of the low-molecular weight PEGDA, which sets the length scale for bridging [66], is significantly smaller than the mean interdroplet separation at the volume fractions studied here (8-10 nm). Thus, on average, such bridging will be entropically unfavored, and its contributions to the viscoelasticity will be small below the cac.

On the other hand, as the concentration rises above the cac, SDS will prefer to form polymer-induced SDS micelles with both adsorbed and free PEG chains, whereby the PEG chain is solubilized in the hydrophobic core of SDS micelles [16]. Thus, if one polymer-induced micelle can solubilize multiple chains, polymer-surfactant complexes can persist sufficiently into the continuous phase to bridge between droplet surfaces, thereby creating transient force chains between droplets (Figure 3.13, Panel II). The lifetime of these force chains will be relatively short. However, considering the large surface area available on the droplets for bridging, a large number of force chains will exist per droplet in dynamic equilibrium, thereby creating a transient network with the droplets serving as high-

functionality crosslinks. Therefore, the lifetime of a crosslink will involve many realizations of the lifetime of an individual force chain.

This could explain several important observations in our measurements. Firstly, it would explain why PEG-SDS complexation results in significant observable viscoelasticity in the nanoemulsions, whereas for the bulk solution it does not. Furthermore, it could explain the two-mode relaxation observed in DLS measurements, in that the short-time mode could be attributed to the characteristic diffusion time of polymer-induced micelles, whereas the long-time mode represents a distribution of collective hydrodynamic modes of droplets due to the perturbative effect of bridging structures. Finally, it could also explain the abnormally large magnitude of the dynamic and viscoelastic activation energy, as the dynamic relaxation will be governed by the breakage of a number of crosslinks for each junction (i.e. droplet), producing a multiplicative effect on the energy of formation or breakage energy of a single junction.

This mechanism can explain the observed increase in plateau modulus and relaxation time of the nanoemulsions with increasing C_s at low surfactant concentration and P = 0.39 (Figure 3.10 (b)). However, it does not explain the decrease in G_p and τ_r at higher surfactant concentrations or lower polymer concentration. To explain this latter observation, we recognize that as the free surfactant concentration continues to increase above the cmc, the surfactant will preferentially form free micelles. These free micelles will recruit polymer both in free solution and adsorbed at the oil-water interface in a similar manner to the oil-water interface at nearly zero free surfactant concentration [35], with ion-dipole interactions as the driving force [13]. This happens at the expense of polymer-surfactant complexes which can bridge between droplets (Figure 3.13, Panel III), and summarily results in a net

decrease in the connectivity of the network (reflected in G_p), the lifetime of network junctions (reflected in τ_r), and the number of force chains per junction (reflected in E_a). This effect could explain both the monotonic decreases in these quantities with increasing C_s at low polymer concentration, as well as their non-monotonic dependence with C_s at higher polymer concentration.

Another consideration is the relative free amounts of SDS and PEG in the continuous phase, as estimated in Table 3.2 and 3.3. In general, we observe that G_p and τ_r increase with increasing ratio of SDS to PEG, as evident in the trends in viscoelasticity with increasing SDS concentration at fixed polymer concentration, and vice versa. This trend can be interpreted in the following manner. If the polymer concentration is increased at fixed surfactant concentration (as in Figure 3.11), the number of polymer-induced micelles per chain will necessarily decrease, thereby removing critical polymer-surfactant complexes for the formation of transient bridges between droplets and decreasing the overall viscoelasticity (Figure 3.13, Panel IV).

In other words, the minimal amount of free surfactant needed to form interdroplet junctions increases as the concentration of PEG increases. This is one possible explanation for the anomalous result in Figure 3.11, in which G_p, τ_r, and E_a all decrease with increasing PEGDA concentration at fixed SDS concentration. However, additional SDS will compensate for this only insomuch as the free SDS concentration remains below the cmc, as explained above. Thus, we emphasize the ratio of SDS to PEG as a critical parameter to the formation of a low-temperature nanoemulsion gel. This result is consistent with the observed increase of G_p with decreasing concentration of PEG at C_s=100mM SDS, whereas a maximum in G_p was obtained with increasing C_s for P = 0.39 PEGDA nanoemulsion

samples. Contrary to the previous results, we have seen that the G_p, τ_r and E_a change non-monotonically with increasing the concentration of SDS at higher concentration of PEGDA (P=0.39) in Figure 3.9. As shown the Table 3.2 and 3.3, this non-monotonic change is related to the SDS/PEGDA ratio in the continuous phase.

We note that this complex behavior is distinct from other mechanisms of transient gel formation between associative polymers and their mixtures with colloids, which all typically exhibit a monotonic dependence of the rheological properties with increasing polymer concentration. This includes telechelic associative polymer solutions, where G_p and τ_r increase with increasing the concentration of the polymers having hydrophobic chain ends [44], as well as microemulsions containing hydrophobically-modified multiarm star polymers, which exhibit increased G_p and τ_r with increasing the concentration of stars [46]. Thus, we would not expect our low-temperature nanoemulsion gels driven by polymer-surfactant complexation to follow simple models for the scaling of transient networks of associative polymers and colloids with concentration [68].

Finally, we explain the observed dependence of low-temperature nanoemulsion viscoelasticity with decreasing droplet size. Specifically, the observed increase in G_p and τ_r and relaxation time with decreasing droplet size (Figure 3.12) can be interpreted in several ways. Smaller droplets increase both the available surface area as well as the number of oil droplets. The latter trivially leads to a more highly crosslinked network, and therefore an increase in G_p. The former leads to a decrease in the amount of free surfactant, which we have shown to increase viscoelasticity if the free surfactant concentration is above the cmc. It also leads to a larger number of effective force chains per droplet, which requires a longer characteristic time for their dynamic breakage, as captured by an increase in τ_r [69]. As

shown in Figure 3.12, this effect is sufficient to significantly counteract the effect of free surfactant on τ_r in the regime of C_s > cmc.

3.8.2 Energetic scaling of viscoelasticity

The Arrhenius dependence of both the dynamics and viscoelasticity of low-temperature nanoemulsion gels suggests the appearance of an activation energy, E_a/k_bT_{ref} for the formation of a network of polymer-surfactant complexes physically crosslinked by droplets. Although the compositional dependence of the activation energy in our materials is complex, one might still anticipate that the rheology of the gels formed to scale with this important quantity.

Therefore, using the classical temporary network theory of Tanaka and Edwards as a guide [68], we test this concept by plotting G_p and τ_r from the data in Tables 3.2-3.4 against the corresponding values of E_a/k_bT_{ref} obtained from TTS measurements (Figure 3.14). We find that all of the data collapse onto master curves of the modulus and relaxation time. This is remarkable, considering that this data represents not only a wide cross-section of material composition (polymer concentration, surfactant concentration, and droplet size), but also that E_a exhibits highly complex and non-monotonic behavior over the range of conditions studied.

We observe relatively simple scaling of the viscoelastic parameters with the activation energy. Specifically, we find that G_p increases linearly as E_a increases, i.e. that the strength of the nanoemulsion gel is proportional to the characteristic energy for formation and breakage of droplet crosslinks. We rationalize this linear dependence using recent modeling work by Uneyama et al. [44], who considered sparse networks of associative polymers and found the following scaling of the modulus,

$$\frac{G_p}{k_b T} = \left(\overline{n}_{eff}\,\rho_0\right)\frac{W}{k_b T} \quad (3.7)$$

where $\left(\overline{n}_{eff}\,\rho_0\right)$ is equal to the effective density of "superbridges" (corresponding to force chains of structural elements between crosslinking centers). The quantity W is the average work required to dissociate a force chain from the crosslinking center, and

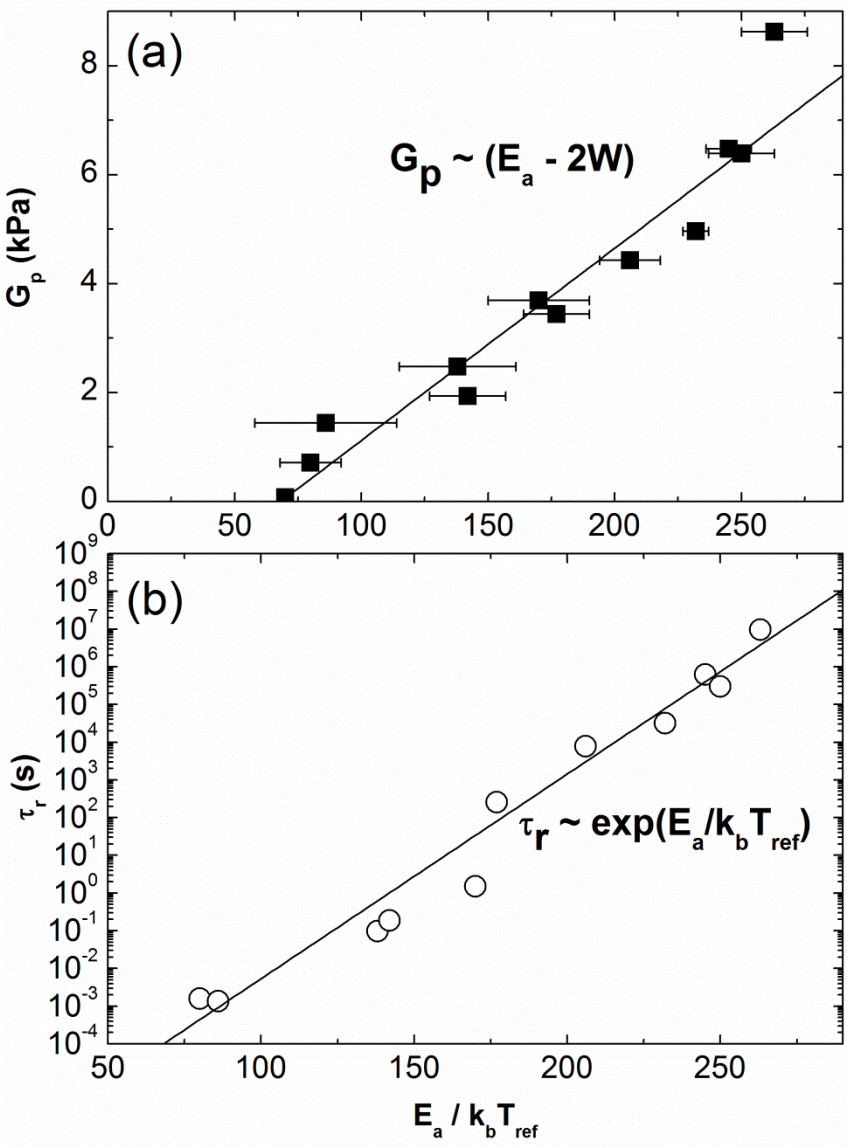

Figure 3.14 Scaling of the viscoelastic parameters (a) G_p and (b) τ_r with the characteristic energy scale for network formation, E_a/k_bT_{ref}. Points represent data in Tables 3.2-3.4. Lines are fits to the relationships shown.

involves a convolution integral over all possible configurations. Thus, the model anticipates the linear scaling of the modulus we observe, assuming that W is proportional to E_a, the viscoelastic activation energy. As discussed above, we hypothesize that the force chains comprise polymer-surfactant co-aggregates, and the crosslinking centers comprise a number of such structures associated with droplets. Therefore, the viscoelastic activation energy corresponds to the dissociation of $\left(\overline{f}-2\right)=\left(\overline{n}_{eff}\rho_c\right)/\rho_d$ superbridges, where $\overline{f}$ is the average number of force chains per droplet, and ρ_d is the number density of droplets. Thus, $W \approx E_a/\overline{f}$, and substitution in eq. (3.7) yields

$$\frac{G_p}{k_bT}=\rho_d\frac{W\left(\overline{f}-2\right)}{k_bT} \quad (3.8)$$

A linear fit of the collapsed data in Figure 3.14 yields W = 34±3 k_bT_{ref}, which is reasonable for bridges formed by molecular aggregates [69]. Furthermore, the fit yields ρ_d ~ 8300±1500 μm^{-3}, which is in quantitative agreement with the magnitude to the droplet density for the volume fraction ϕ = 0.33 contained in all samples (ρ_d ~ 7000-9000 μm^{-3} for the droplet sizes studied here). With this, the fit of eq. (3.8) to the data yields an average number of force chains per droplet of $\overline{f}$ ~ 3-8 over the range of materials studied. This number of effective crosslinks per droplet is reasonable, considering the relative size of polymers and micelles compared to the average droplet size. We note that eq. (3.8) also suggests that, for a fixed number and dissociation energy of force chains and volume of droplets, the modulus should scale as $G_p \sim D^{-3}$. This could partially explain the observed dependence of G_p with droplet size that we observe. However, more careful studies

involving variation in droplet size at fixed free surfactant concentration (nottotal concentration as done here) are required to rigorously test this result.

Furthermore, we find that the relaxation time exhibits an exponential dependence with activation energy, $\tau_r \sim E_a/k_bT_{ref}$, over 9 orders of magnitude in the relaxation time. Such exponential dependence is expected for physically associating networks, and arises due to the kinetics of the formation and breakage of bridging structures [69]. Nevertheless, it is striking that such simple scaling of the viscoelastic parameters can arise from such a complex mechanism of network formation.

3.9 Conclusion

In this chapter, we have shown that polymer-surfactant complexation can be used as a highly controllable method for imparting thermoreversible viscoelasticity to nanoemulsions. This has been demonstrated for oil-in-water nanoemulsions in the presence of low-molecular weight PEGs of different end group chemistry and an ionic surfactant, SDS. The interactions between droplets and polymer-surfactant complexes lead to the formation of a viscoelastic network at low temperature. Remarkably, the nanoemulsions exhibit viscoelasticity that follows time-temperature superposition over a wide range of temperature and composition, demonstrating the generality of this phenomenon.

Scattering measurements show that whereas the colloidal microstructure is insensitive to temperature through the low temperature viscoelastic transition, collective hydrodynamic modes exhibit a self-similar slowing down with temperature, with a characteristic energy scale far above what is expected for viscous activation and identical to that observed in rheological measurements. This energy scale represents the formation of

force chains that bridge nanoemulsion droplets while maintaining their colloidal stability. The activation energy is thus a critical parameter setting the magnitude of both the modulus and relaxation time of the material.

Counterintuitively, the activation energy decreases with increasing surfactant and polymer concentration in nanoemulsions with intermediate droplet and polymer concentrations, and even exhibits non-monotonic behavior under some conditions, which distinguishes these materials from temporary networks of associative polymers and their mixtures with colloids.

To explain this, we invoke the previously observed concentration dependence of PEG-SDS complexation both in bulk solution and at fluid interfaces. From these comparisons, we hypothesize that the observed temporary polymer network is mediated by polymer-induced micellar complexes, which act as effective crosslinks between droplets. At intermediate concentrations of polymer and oil, this leads to a complex dependence of the viscoelasticity on fluid composition, and identifies concentration regimes with differential dependence of the viscoelastic material functions on surfactant and polymer concentration, with the cac, cmc, and surfactant-polymer molar ratio as critical parameters delineating the various regimes. Nevertheless, we find that the viscoelastic material parameters show universal correlation with the network activation energy identified from TTS measurements, as expected for physically associating networks.

These results suggest polymer-surfactant complexation is a broadly applicable mechanism for controlling the rheology of nanoemulsions. However, our studies indicate significant differences between the networks formed and those observed in networks mediated by associative polymers alone. This calls for further studies into this new class of

viscoelastic nanoemulsions. For example, studies of polymer-surfactant interactions at oil-water interfaces should be extended to more concentrated conditions, such that the effects of bulk self-assembly in different concentration regimes can be probed. Such studies could also inform the refinement of temporary network models to account for the complicated concentration-dependence of the viscoelastic parameters we observe in our experiments. Ultimately, these advances will provide a means by which to tailor nanoemulsions as novel responsive “smart” fluids with dynamically switchable rheology.

References

[1] E. Yilmaz and H.-H. Borchert, International journal of pharmaceutics **307**, 232 (2006).

[2] G. Guglielmini, Clinics in dermatology **26**, 341 (2008).

[3] N. Anton, J.-P. Benoit, and P. Saulnier, Journal of Controlled Release **128**, 185 (2008).

[4] M. E. Helgeson, S. E. Moran, H. Z. An, and P. S. Doyle, Nature materials **11**, 344 (2012).

[5] H. Z. An, M. E. Helgeson, and P. S. Doyle, Advanced Materials **24**, 3838 (2012).

[6] J. N. Wilking and T. G. Mason, Physical Review E **75**, 041407 (2007).

[7] E. D. Goddard, Colloids and Surfaces **19**, 255 (1986).

[8] C. A. Herb and R. K. Prud'homme, *Structure and flow in surfactant solutions* (American Chemical Society, 1994).

[9] K. C. Tam and E. Wyn-Jones, Chemical Society Reviews **35**, 693 (2006).

[10] S. Saito, Kolloid-Zeitschrift und Zeitschrift für Polymere **215**, 16 (1967).

[11] M. N. Jones, Journal of colloid and interface science **23**, 36 (1967).

[12] M. Schwuger, Journal of colloid and interface science **43**, 491 (1973).

[13] B. Cabane and R. Duplessix, Colloids and Surfaces **13**, 19 (1985).

[14] J. Xia, P. L. Dubin, and Y. Kim, The Journal of Physical Chemistry **96**, 6805 (1992).

[15] L. Bernazzani, S. Borsacchi, D. Catalano, P. Gianni, V. Mollica, M. Vitelli, F. Asaro, and L. Feruglio, The Journal of Physical Chemistry B **108**, 8960 (2004).

[16] S. Dai and K. Tam, The Journal of Physical Chemistry B **105**, 10759 (2001).

[17] E. Ruckenstein, G. Huber, and H. Hoffmann, Langmuir **3**, 382 (1987).

[18] Y. Nikas and D. Blankschtein, Langmuir **10**, 3512 (1994).

[19] R. D. Groot, Langmuir **16**, 7493 (2000).

[20] K. Y. Mya, A. M. Jamieson, and A. Sirivat, Langmuir **16**, 6131 (2000).

[21] R. Mészáros, I. Varga, and T. Gilányi, The Journal of Physical Chemistry B **109**, 13538 (2005).

[22] P. Bahadur, P. Dubin, and Y. K. Rao, Langmuir **11**, 1951 (1995).

[23] M. Almgren, J. Van Stam, C. Lindblad, P. Li, P. Stilbs, and P. Bahadur, The Journal of Physical Chemistry **95**, 5677 (1991).

[24] K. Lindell and B. Cabane, Langmuir **14**, 6361 (1998).

[25] C. Rufier, A. Collet, M. Viguier, J. Oberdisse, and S. Mora, Macromolecules **44**, 7451 (2011).

[26] S. Biggs, J. Selb, and F. Candau, Langmuir **8**, 838 (1992).

[27] B. Jean, L.-T. Lee, and B. Cabane, Langmuir **15**, 7585 (1999).

[28] B. Jean, L.-T. Lee, and B. Cabane, Colloid and Polymer Science **278**, 764 (2000).

[29] L.-T. Lee and B. Cabane, Macromolecules **30**, 6559 (1997).

[30] J. Yang, S. Chen, and Y. Fang, Carbohydrate Polymers **75**, 333 (2009).

[31] H. Bu, A.-L. Kjøniksen, A. Elgsaeter, and B. Nyström, Colloids and Surfaces A: Physicochemical and Engineering Aspects **278**, 166 (2006).

[32] Y. Moroi, H. Akisada, M. Saito, and R. Matuura, Journal of colloid and interface science **61**, 233 (1977).

[33] J. Philip, G. G. Prakash, T. Jaykumar, P. Kalyanasundaram, O. Mondain-Monval, and B. Raj, Langmuir **18**, 4625 (2002).

[34] J. Philip, G. Gnanaprakash, T. Jayakumar, P. Kalyanasundaram, and B. Raj, Macromolecules **36**, 9230 (2003).

[35] N. Péron, R. Mészáros, I. Varga, and T. Gilányi, Journal of colloid and interface science **313**, 389 (2007).

[36] M. Darvas, T. Gilányi, and P. Jedlovszky, The Journal of Physical Chemistry B **115**, 933 (2011).

[37] I. M. Tucker, J. T. Petkov, C. Jones, J. Penfold, R. K. Thomas, S. E. Rogers, A. E. Terry, R. K. Heenan, and I. Grillo, Langmuir **28**, 14974 (2012).

[38] W. Brown, J. Fundin, and M. d. G. Miguel, Macromolecules **25**, 7192 (1992).

[39] K. Chari, B. Antalek, M. Lin, and S. Sinha, The Journal of chemical physics **100**, 5294 (1994).

[40] K. Loyen, I. Iliopoulos, R. Audebert, and U. Olsson, Langmuir **11**, 1053 (1995).

[41] O. Rosén, J. Sjöström, and L. Piculell, Langmuir **14**, 5795 (1998).

[42] A. Tripathi, K. C. Tam, and G. H. McKinley, Macromolecules **39**, 1981 (2006).

[43] E. Michel, M. Filali, R. Aznar, G. Porte, and J. Appell, Langmuir **16**, 8702 (2000).

[44] T. Uneyama, S. Suzuki, and H. Watanabe, Physical Review E **86**, 031802 (2012).

[45] L. Ramos and C. Ligoure, Macromolecules **40**, 1248 (2007).

[46] P. Malo de Molina, C. Herfurth, A. Laschewsky, and M. Gradzielski, Langmuir **28**, 15994 (2012).

[47] M. J. Rosen and J. T. Kunjappu, *Surfactants and interfacial phenomena* (John Wiley & Sons, 2012).

[48] N. J. Turro and A. Yekta, Journal of the American Chemical Society **100**, 5951 (1978).

[49] Y. Wang, B. Han, H. Yan, and J. C. Kwak, Langmuir **13**, 3119 (1997).

[50] S. Dai and K. Tam, Langmuir **20**, 2177 (2004).

[51] E. Lissi and E. Abuin, Journal of colloid and interface science **105**, 1 (1985).

[52] O. Anthony and R. Zana, Langmuir **10**, 4048 (1994).

[53] M. Shibayama, Y. Fujikawa, and S. Nomura, Macromolecules **29**, 6535 (1996).

[54] A. Krall and D. Weitz, Physical Review Letters **80**, 778 (1998).

[55] M. J. Solomon and P. Varadan, Physical Review E **63**, 051402 (2001).

[56] B. Nystroem, K. Thuresson, and B. Lindman, Langmuir **11**, 1994 (1995).

[57] B. Nystroem and B. Lindman, Macromolecules **28**, 967 (1995).

[58] J. E. Martin, J. Wilcoxon, and J. Odinek, Physical Review A **43**, 858 (1991).

[59] M. Tsujimoto and M. Shibayama, Macromolecules **35**, 1342 (2002).

[60] D. El Masri, G. Brambilla, M. Pierno, G. Petekidis, and A. Scho, J. Stat. Mech.: Theory Exp, P07015 (2009).

[61] V. K. Daga and N. J. Wagner, Rheologica acta **45**, 813 (2006).

[62] L. Bromberg, Macromolecules **31**, 6148 (1998).

[63] S. K. Agrawal, N. Sanabria-DeLong, G. N. Tew, and S. R. Bhatia, Langmuir **24**, 13148 (2008).

[64] M. Surve, V. Pryamitsyn, and V. Ganesan, The Journal of chemical physics **125**, 064903 (2006).

[65] T. Mason, S. Graves, J. Wilking, and M. Lin, Condens. Matter Phys **9**, 193 (2006).

[66] M. E. Helgeson and N. J. Wagner, The Journal of chemical physics **135**, 084901 (2011).

[67] Y. Lapitsky and E. W. Kaler, Colloids and Surfaces A: Physicochemical and Engineering Aspects **282**, 118 (2006).

[68] F. Tanaka and S. Edwards, Macromolecules **25**, 1516 (1992).

[69] M. E. Helgeson, T. K. Hodgdon, E. W. Kaler, N. J. Wagner, M. Vethamuthu, and K. Ananthapadmanabhan, Langmuir **26**, 8049 (2010).

[70] J. Kim, Y. Gao, C. Hebebrand, E. Peirtsegaele, and M. E. Helgeson, Soft Matter **9**, 6897 (2013).

Chapter 4

Rheology and structure of shear-induced clustering in polymer-colloids mixtures[2]

4.1 Introduction

The previous chapter demonstrated how polymer-surfactant complexes can be used to impart thermoresponsive control over the viscoelasticity of polymer-nanoemulsion mixtures. In this chapter, we exploit this behavior in order to systematically probe the flow-induced microstructure of associative polymer-colloid mixtures and resulting rheology.

Polymer nanocomposites have been widely used to enhance the mechanical properties of polymeric materials [1]. Their properties and performance depend critically on the structure of the dispersed particle phase [2]. Thus, optimizing the final properties of nanocomposites requires careful control of particle dispersion and, therefore, rheology during processing. Since many nanocomposites are processed from solution [3], it is thus critically important to understand the influence of flow on polymer-particle interactions and suspension microstructure of colloidal suspensions in polymer liquids.

There have been many studies demonstrating shear-induced clustering of both Brownian and non-Brownian particles in polymer fluids. Although early studies of this phenomenon involved *ex situ* observations of solid composite structures, later work involved the direct observation of anisotropic clustering under flow. Interestingly, two significantly different anisotropic orientations of shear-induced clusters have been observed. In one case, Michele *et al.* [4] and Lyon *et al.* [5] observed string-like particle clusters oriented along the

[2] This chapter was reproduced by permission of Americal Physical Soceity [50].

flow direction in highly viscoelastic solutions under shear. However, vorticity-aligned clusters of particles have also been observed in attractive polymer-colloid mixtures [6,7]. More recently, Pasquino *et al*. observed a transition to vorticity-aligned clustering with decreasing the particle size, suggesting that colloidal interactions and Brownian motion may be important in determining the mechanism and orientation of shear-induced particle clusters [8]. Recently, Haddadi and Morris have shown using lattice-Boltmann simulations that pair-sphere trajectories in finite inertia shear flow prefer vorticity alignment [9]. Note that similar clustering has also been observed in systems whose suspension microstructure is aggregated at rest [3], although it is not clear whether the same physics of clustering apply in these systems, or whether the behavior is rather dominated by interparticle attractions. The mechanism of clustering in polymer-colloid mixtures also appears to be different from that observed in highly confined suspensions in Newtonian liquids, which is dominated by hydrodynamic effects of the confining walls [10,11].

From these studies, several hypotheses have been proposed for the mechanism of shear-induced clustering. Some groups have proposed that clustering is driven by the growth of polymer normal stresses at sufficiently high shear rates [12,13]. Others have argued that the formation of string-like clusters is also influenced by the shear thinning viscosity of polymeric fluids [14,15]. More recent studies have cast some doubt on the role of elasticity in shear-induced clustering. Specifically, shear-induced particle clustering was not observed in a highly elastic Boger fluid for Weissenberg numbers (Wi) exceeding 260, while in highly shear thinning polymeric fluids, the flow-induced clusters form only at low shear rates in which the observed rheology is uncorrelated with polymer elasticity [14]. Furthermore, in a

recent study of non-Brownian particles in viscoelastic fluids by Snijkers *et al*., the formation of particle pairs was shown in very weakly shear thinning Boger fluids [15].

In principle, the microstructure of suspensions in viscoelastic polymer solutions under shear flow is highly complex, due to the many coupled contributions to the total fluid stress. These include: (i) viscoelastic stresses due to the effect of shear flow on the polymer network (typically shear thinning viscosity and positive first normal stress difference), (ii) hydrodynamic interactions arising from the coupling of flow disturbances due to the presence of particles and the suspending viscoelastic polymer flow, and (iii) Brownian stresses induced by deformation of the suspension microstructure away from its equilibrium configuration. Models for the former two contributions, and their effects on particle motion, have been extensively studied for the case of dilute, non-Brownian suspensions in polymer solutions, primarily in the context of the second order fluid (SOF) model. Early work found that isolated spheres in various shear flows of a SOF produce a secondary flow around the particle [16,17]. It was later found that such secondary flows result in significant normal stress disturbances in the vicinity of the particle, and cause pairs of particles to rotate and align with the flow direction [18,19], and by extension cause chaining in dilute suspensions. Similar analysis has been used to predict the rheology of non-Brownian suspensions in a SOF [20,21]. It is notable that all of these theories predict shear-induced particle clusters aligned along the flow direction, and not along the vorticity direction as observed in some experiments. As such, the propensity to form vorticity-aligned clusters is presumably due to either non-dilute suspension effects, or due to the effects of Brownian motion on the suspension and hydrodynamic stresses.

By comparison, the theory for non-dilute, Brownian suspensions in polymer solutions, including hydrodynamic interactions, is underdeveloped. Here, it is important to distinguish between suspensions of Brownian and non-Brownian particles. In the former case, Brownian motion competes with hydrodynamic interactions to restore the suspension microstructure to its equilibrium state. These competing processes introduce competing time scales for the influence of polymer-particle and particle-particle interactions on the fluid microstructure and rheology. One of these is the viscoelastic relaxation time for the polymer network, τ_r , which defines a characteristic dimensionless shear rate, the Weissenberg number $Wi = \tau_r \dot{\gamma}$, where $\dot{\gamma}$ is the applied shear rate. The other is the characteristic time scale for Brownian relaxation of the suspension microstructure, τ_{Br} , which defines another characteristic dimensionless shear rate, the Peclet number $Pe = \tau_{Br} \dot{\gamma}$.

One can therefore anticipate a range of shear-induced microstructures depending on the relative magnitude of these two time scales. Unfortunately, systematic theoretical studies of flowing suspensions in viscoelastic solutions under various limits of *Wi* and *Pe* have yet to be made. However, there has been significant modeling of suspension microstructure in Newtonian fluids, to which some analogies might be made. For example, clustering due to an excess of particle pairs along the compressional axis has been demonstrated in shear flow by both experiment [22] and simulation [23]. Brady and Morris analyzed the influence of hydrodynamic interactions and Brownian diffusion on such structural anisotropy at large *Pe* using Stokesian dynamic simulations [24]. However, it is currently unclear whether similar effects are dominant in viscoelastic suspending media, and over what range of *Wi* they would apply.

Similarly, previous experimental studies of shear-induced clustering have yet to systematically explore the effects of competing viscoelastic and Brownian time scales. Recently, we developed a model system of non-aggregating, viscoelastic Brownian suspensions in polymer solutions in which such studies can be made (Chapter 3). The colloidal fluid is comprised of oil-in-water nanoemulsions in the presence of polyethylene glycol (PEG) and sodium dodecyl sulfate (SDS). These fluids form non-aggregating viscoelastic networks that can be considered to be rheologically similar to the materials previously studied by Belzung and co-workers in which vorticity-aligned clustering was observed in scattering measurements [25]. However, the present material system is advantageous in that it provides an unprecedented ability to fine-tune the characteristic time scales of viscoelasticity and shear-induced structuring. Specifically, in the previous chapter, these nanoemulsions were shown to exhibit strongly thermosensitive viscoelasticity at low temperatures, which was hypothesized to result from the formation of transient polymer-surfactant complexes that are physically crosslinked by the suspended colloids. Detailed hypothesized mechanisms are described in Chapter 3. In this system, the viscoelastic relaxation time (τ_r) varies by several orders of magnitude with modest changes in temperature, even though the viscosity of the underlying suspension medium remains nearly constant. This provides a route by which *Wi* and *Pe* can be easily tuned relative to one another with temperature.

In this chapter, this model system will be used to perform rheological and three-dimensionally resolved rheo-small angle neutron scattering (rheo-SANS) measurements to explore shear-induced clustering in several limits of the relative magnitudes of the viscoelastic relaxation time and the Brownian relaxation time, i.e., *Wi* >> *Pe*, *Wi* ~ *Pe*, and

Wi < *Pe*. As will be shown later, an advantage of our thermoresponsive nanoemulsions is that all of these limits can be accessed within relatively narrow ranges of composition and temperature. These studies overcome several drawbacks of previous microstructural measurements involving direct visualization [6,26,27] and scattering [25,28-30]. First, the small size of the nanodroplets (< 50 nm in radius) avoids the use of highly confined systems, as confinement alone is known to force structure formation in the vorticity direction [6,10,11]. Second, whereas most previous scattering studies have been by light scattering, SANS enables particle-scale examination of the structuring process. Finally, rheo-SANS measurements in multiple orthogonal projections allow for a fully three-dimensional understanding of shear-induced clustering and its relation to macroscopic rheology and flow [31]. Similar combined studies involving light and x-ray measurements have elucidated the mechanisms of shear-induced structuring in aggregated colloidal suspensions [27,30]. However, it is not clear whether the phenomena examined in those studies can explain the clustering observed in a number of polymer-colloid systems that are non-aggregating at rest [25,32].

4.2 Experimental

4.2.1 Sample preparation

The oil-in-water nanoemulsions used this chapter were prepared as described in Chapters 2 and 3. They contain a volume fraction ϕ_o = 0.33 of polydimethylsiloxane (PDMS) oil nanodroplets in an aqueous continuous phase containing 120 mM SDS and various volume fractions of PEG (ϕ_p = 0.33, 0.36, and 0.40). This surfactant concentration was chosen in order to produce viscoelasticity in the nanoemulsions at low temperature as in

Table 4.1 Viscosity of continuous phase at different temperatures

Suspending medium Fluid	Suspending medium viscosity, η_m (mPa s)					
	5 °C	10 °C	15 °C	20 °C	25 °C	30 °C
33 vol% PEG with 48mM SDS	12.48	10.03	8.19	6.79	5.69	4.84
36 vol.% PEG with 41mM SDS	15.26	12.17	9.85	8.09	6.76	5.70
40 vol.% PEG with 50mM SDS	21.82	17.09	13.66	11.09	9.15	7.64

Chapter 3. For rheo-SANS measurements, the nanoemulsion was prepared in 82/18 (v/v) H2O/D2O in order to match the scattering length density of the solvent to that of the polymer and reduce multiple scattering from the droplets [33]. The average radius of droplets measured by DLS depends on the sample to sample difference ($<a>$ = 34.6 nm for ϕ_p = 0.33, $<a>$ = 31.7 nm for ϕ_p = 0.36, and $<a>$ = 35.4 nm for ϕ_p = 0.40). Given the overall surfactant concentration and the size of the nanodroplets, we estimate that the nanoemulsions contain approximately 40-50 mM “free” SDS in the continuous phase, with the remainder at the oil-water interface of the nanodroplets. The viscosity of the continuous phase at this SDS concentration was measured using a falling ball capillary viscometer (Anton Paar Lovis) at temperatures ranging from 5 to 30 °C. The resulting measured viscosities are listed in Table 4.1. Also, the shear rate dependent viscosity of the continuous phases are plotted in Appendix B, Figure B.1. We find that the suspending media are essentially Newtonian over the entire range of shear rates studied.

4.2.2 Rheological characterization

Rheological measurements were performed using a stress-controlled rheometer (TA Instruments AR-G2). For time-temperature superposition measurements of linear viscoelasticity, the dynamic shear moduli were measured using a 60 mm, 2° upper cone

geometry and a Peltier temperature-controlled lower-plate geometry. Samples were pre-sheared at 10 rad s^{-1} for 60 seconds. Frequency sweeps were performed over a range of 0.02-200 rad s^{-1} at 1% strain amplitude and equilibrated temperatures ranging between 5 and 30 °C. Above this temperature range, the linear viscoelasticity becomes immeasurable (see Appendix B, Figure B.2). For steady state shear rheology measurements, the steady shear stress was measured using a Peltier temperature-controlled Couette geometry (inner radius, 14.0 mm, outer radius, 15.2 mm) at equilibrate temperatures ranging between 5 and 30 °C. The shear rate sweeps were performed over a range of 0.01-2000 s^{-1} with steady state sensing for 30 seconds at 5% tolerance. We found that there is no history dependence of the steady shear rheology using forward-backward shear rate sweep measurements to test for hysteresis (see Appendix B, Figure B.3). Furthermore, since the particle-scale Reynolds number, $Re = \rho_m \dot{\gamma} a^2 / \eta_m$, where ρ_m is the density of the suspending medium, is less than $O(10^{-7})$ for all shear rates and temperatures, particle inertia effects can be safely neglected for all experiments.

4.2.3 Rheo-SANS measurement

Small angle neutron scattering (SANS) measurements were performed using the NG7 30m and NGB 10m SANS instruments at NCNR (Gaithersburg, MD). A schematic depiction of the rheo-SANS measurements is shown in Figure 4.1. For measurements in the flow-vorticity projection (1-3 plane), samples were loaded in a 50 mm optical quartz outer cylinder with a 48 mm titanium inner cylinder, and measured at a sample to detector distance of 13 m and 4.6 m. For measurements in the flow-gradient projection (1-2 plane), a short-gap Couette shear cell with inner and outer radii of 25.1 mm and 26.5 mm, respectively, was used. Samples were measured at a sample to detector distance of 15.3 m.

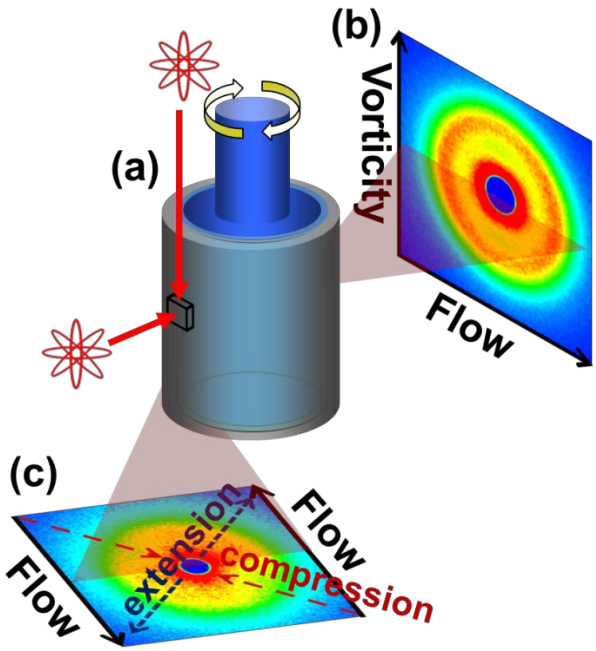

Figure 4.1 (a) Schematic diagram of the Couette shear cell for the 2D flow-SANS scattering. 2D scattering projections for the (b) flow-vorticity (1-3) and (c) flow-gradient (1-2) plane.

Details of the shear cell and its operation are described elsewhere [34,35]. The temperature of the sample was left to equilibrate in the relevant sample environments for at least 30 minutes prior to measurement. Steady shear flow-SANS measurements were performed at several shear rates ranging from 0 to 2000 s^{-1}. For each measurement, at least 3 minutes are waited to reach steady state. In the 1-2 shear cell measurements, the flow-SANS was measured at center of the gap due to spatial inhomogeneity at different gap positions (see Appendix B, Figure B.4). Also, we measured flow-SANS under both forward and backward shear directions to check for reversibility. The resulting data were reduced using IGOR software package provided by NIST using standard protocols [36]. For time-resolved flow-SANS measurement in 1-3 plane, the NGB30 SANS instruments at NCNR was used. Cyclic step shear rate measurements were performed, with alternating periods of step shear and

flow cessation, with 8 s for each cycle (4 s for step shear and 4 s for cessation). For each shear rate, at least 4000 step shear rate measurements were repeated. Instead of the standard binning procedure using software provided by the NCNR, the sliding binning procedure proposed by Calabrese *et al*. was used to improve the time resolution [37].

4.3 Characteristic time scales

The nanoemulsions exhibit viscoelasticity at low temperature and obey time-temperature superposition (TTS), in agreement with the previous chapter. To demonstrate this, we measured the frequency-dependent linear viscoelastic spectra for the nanoemulsions at temperatures ranging from 5 to 30 °C. Figure 4.2 (a,c and e) shows the linear viscoelastic master curves obtained by shifting *G'* and *G"* to the reference temperature, T = 15 °C, for each of the samples studied. From this, we obtain the temperature-dependent viscoelastic relaxation time, $\tau_r(T)$, which corresponds to the time scale for dynamic formation and breakage of a network structure comprised of polymer-nanodroplet junctions hypothesized in Chapter 3. Specifically, the TTS master curve is first used to determine $\tau_r(T_{ref})$ for a particular sample at the reference temperature, which is equal to the inverse of the frequency at crossover between *G'* and *G"*. The remaining values of at all other temperatures for that sample are then computed from the horizontal shift factors ($a_T(T)$) by

$$\tau_r(T) = \tau_r(T_{ref}) / a_T(T) \quad (4.1)$$

τ_r decreases with increasing temperature by as much as two orders of magnitude over the range of temperature studied. In what follows, we will use τ_r to scale the shear rate to construct the Weissenberg number *Wi*. We also computed the Brownian relaxation time for the suspension microstructure. In principle, τ_{Br} is most closely related to the time scale

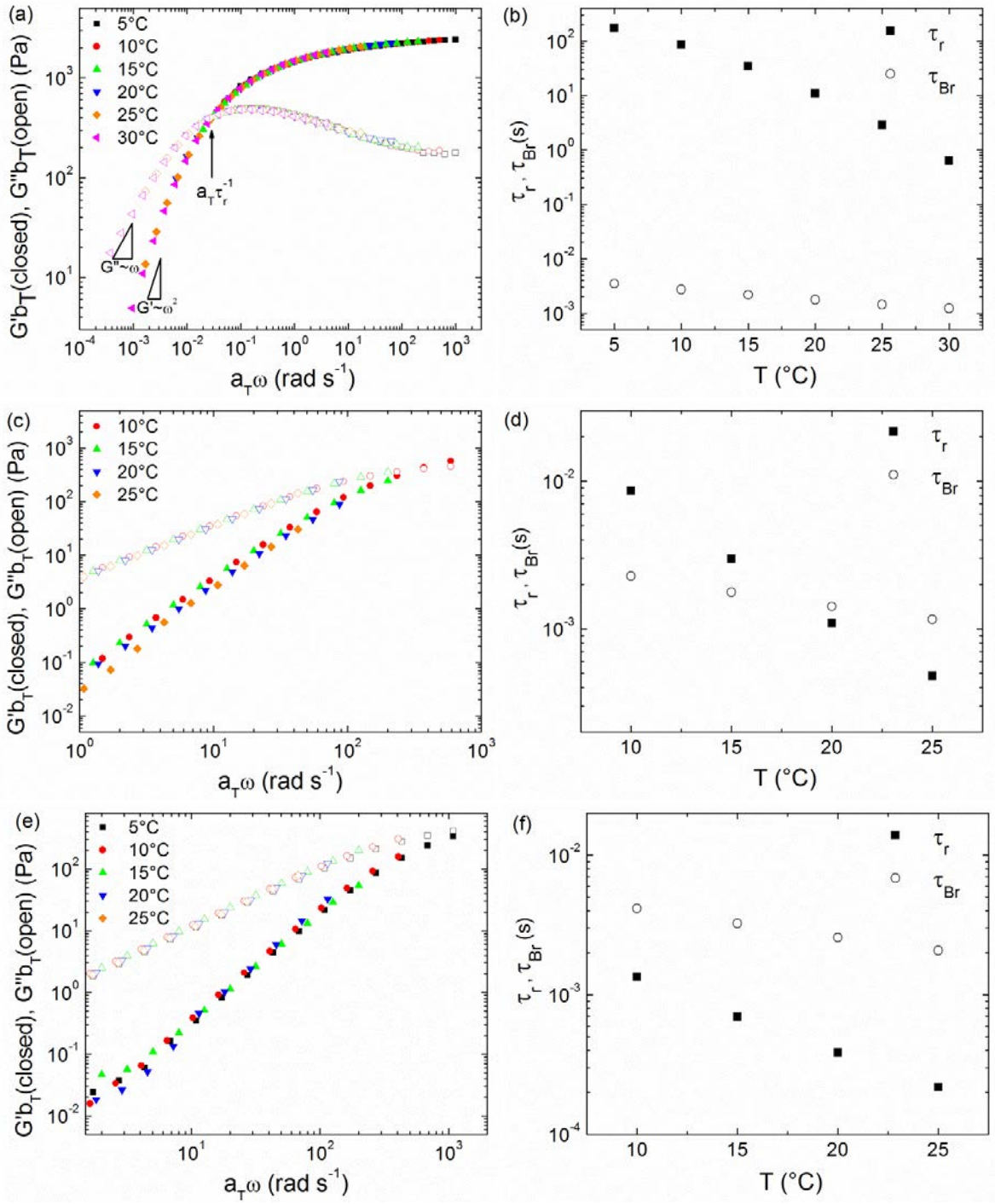

Figure 4.2 TTS master curves and characteristic time scales. Nanoemulsions contain ϕ_o = 0.33 PDMS droplets with PEG and C_s = 120mM SDS, with (a, b) $\langle a \rangle$ = 34.6nm and ϕ_p = 0.33, (c, d) $\langle a \rangle$ = 31.7 nm and ϕ_p = 0.36, (e, f) $\langle a \rangle$ = 35.4 nm and ϕ_p = 0.40. The reference temperature is 15 °C. (see Appendix B, Figure B.4 for the horizontal and vertical shifting factors.)

associated with the long-time diffusivity of the suspension (which depends on the volume fraction) by $\tau_{Br} = a^2 / D_\infty(\phi_o)$. However, in the present system, the long-time dynamics exhibit sub-diffusive behavior due to the collective dynamics of the polymer-droplet network as shown in Chapter 3, preventing quantification of $D_\infty(\phi_o)$. Therefore, we resort to replacing the long-time diffusivity of the suspension with the self-diffusivity of an isolated sphere, such that

$$\tau_{Br} = 6\pi a^3 \eta_m / k_B T \quad (4.2)$$

where a is the average droplet radius, η_m is the suspending medium viscosity, k_B is the Boltzmann constant and T is the temperature. A more realistic treatment for τ_{Br} would include hindered diffusion due to interactions between droplets at the relatively large concentrations studied here. Thus, this choice of τ_{Br} serves as a lower bound, such that the actual value of *Pe* for a fixed shear rate will be larger than we report.

Figure 4.2 (b, d, and f) shows the temperature-dependence of the relative magnitudes of τ_r and τ_{Br} for the three samples studied. We found that each sample lies in a different limit of these time scales. For the sample depicted in Figure 4.2 (b), we found that $\tau_r >> \tau_{Br}$ over the entire temperature range, i.e., the suspension microstructure relaxes significantly faster than the viscoelastic polymer network. Thus, for this sample, *Wi* >> *Pe*. For the sample in Figure 4.2 (d), τ_r and τ_{Br} are of similar magnitude, and in fact the two time scales crossover in the measured temperature range, so that *Wi* ~ *Pe*. Finally, for the sample depicted in Figure 4.2 (f), $\tau_r << \tau_{Br}$ over the measured temperature range, such that *Wi* <<

Pe. Thus, these three samples are convenient for examining how the relative magnitude and *Wi* and *Pe* influence the process of shear-induced clustering, and as we will show later helps to identify its dominant mechanism. One might expect to be able to probe these different regimes in the same sample by performing measurements at elevated temperatures. However, for all samples studied, the viscoelasticity becomes immeasurable for temperatures larger than 35 °C, preventing a clear quantification of τ_r (see Appendix B, Figure B.2).

4.4 Steady shear rheology

To investigate the nonlinear shear rheology, we performed steady shear measurements at temperatures spanning the same range as that for linear viscoelastic measurements. Figure 4.3 (a) shows the steady shear stress and viscosity of the three samples whose linear viscoelasticity is shown in Figure 4.2. In Chapter 3, the polymer concentration and droplet size were shown to significantly affect the linear viscoelastic rheology; specifically, the viscoelasticity decreases with increasing droplet size, and exhibits a complex, non-monotonic dependence on polymer concentration due to the thermodynamics of polymer-surfactant complexation. In all cases, the material exhibits significant shear thinning over a range of shear rates. At sufficiently low temperatures (e.g. in Figure 4.2 (a)), this shear thinning resembles a near plateau in the shear stress with increasing shear rate. In some systems, such a plateau is interpreted as reflecting a yield stress in the material. However, given the remarkable collapse of the linear viscoelastic data by time-temperature superposition, we interpret this feature not as a yield stress, but simply

as a failure to achieve low enough shear rates to probe the low shear rate, pseudo-Newtonian regime of the fluid.

In all cases, the material exhibits two distinct regimes of shear thinning. This could be because, in these systems, there are two dominant contributions to the dynamics of the

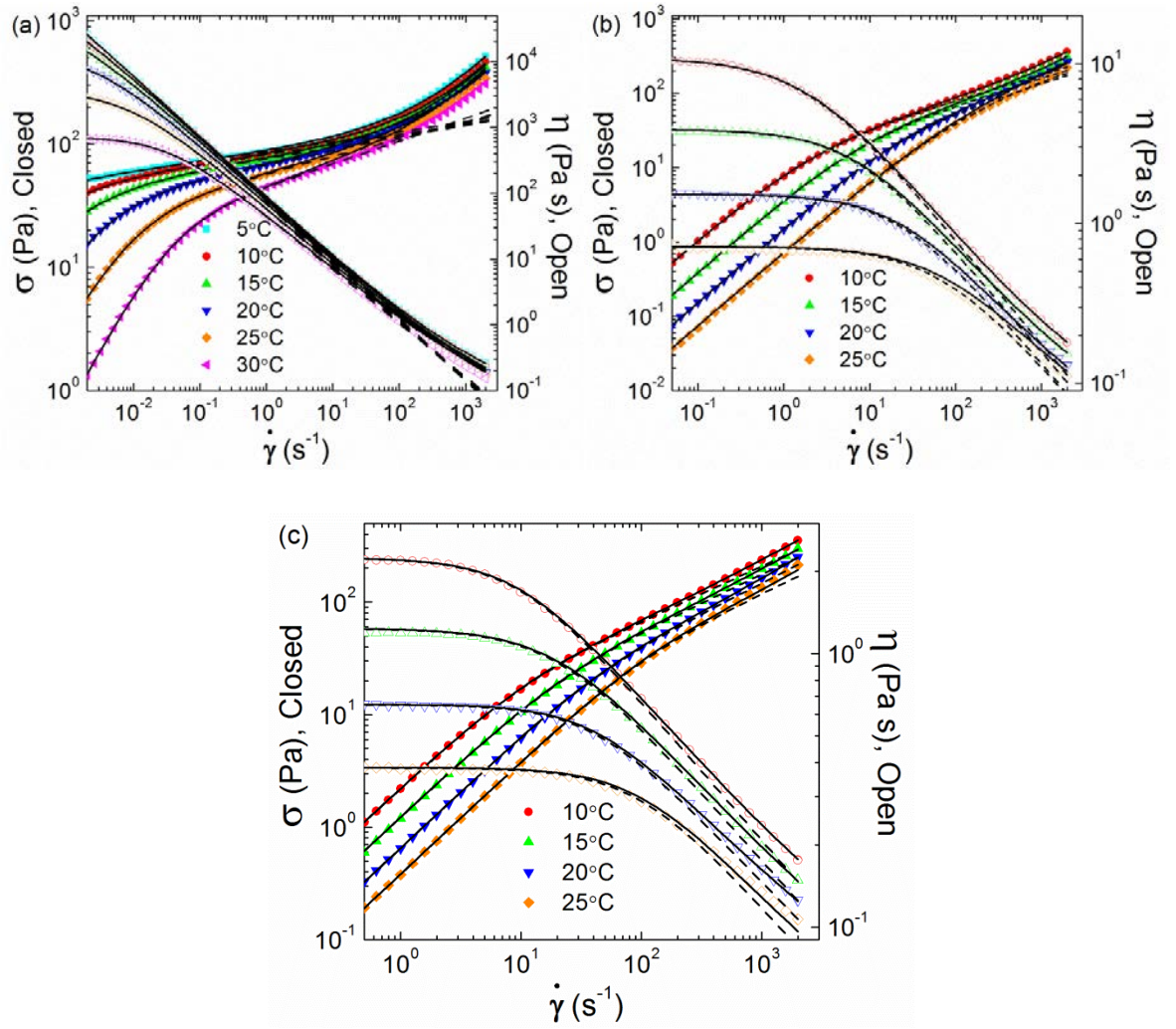

Figure 4.3 Steady shear rheology for several nanoemulsions at the indicated temperatures. Nanoemulsions contain ϕ_0 = 0.33 PDMS droplets with PEG and Cs = 120mM SDS, with (a) <*a*> = 34.6nm and ϕ_p = 0.33, (b) <*a*> = 31.7 nm and ϕ_p = 0.36, and (c) <*a*> = 35.4 nm and ϕ_p = 0.40. Dashed lines represent the Carreau-Yasuda model fitting at low shear rates, and solid lines represent the fitting result by proposed the perturbation model (Eq. 4.6).

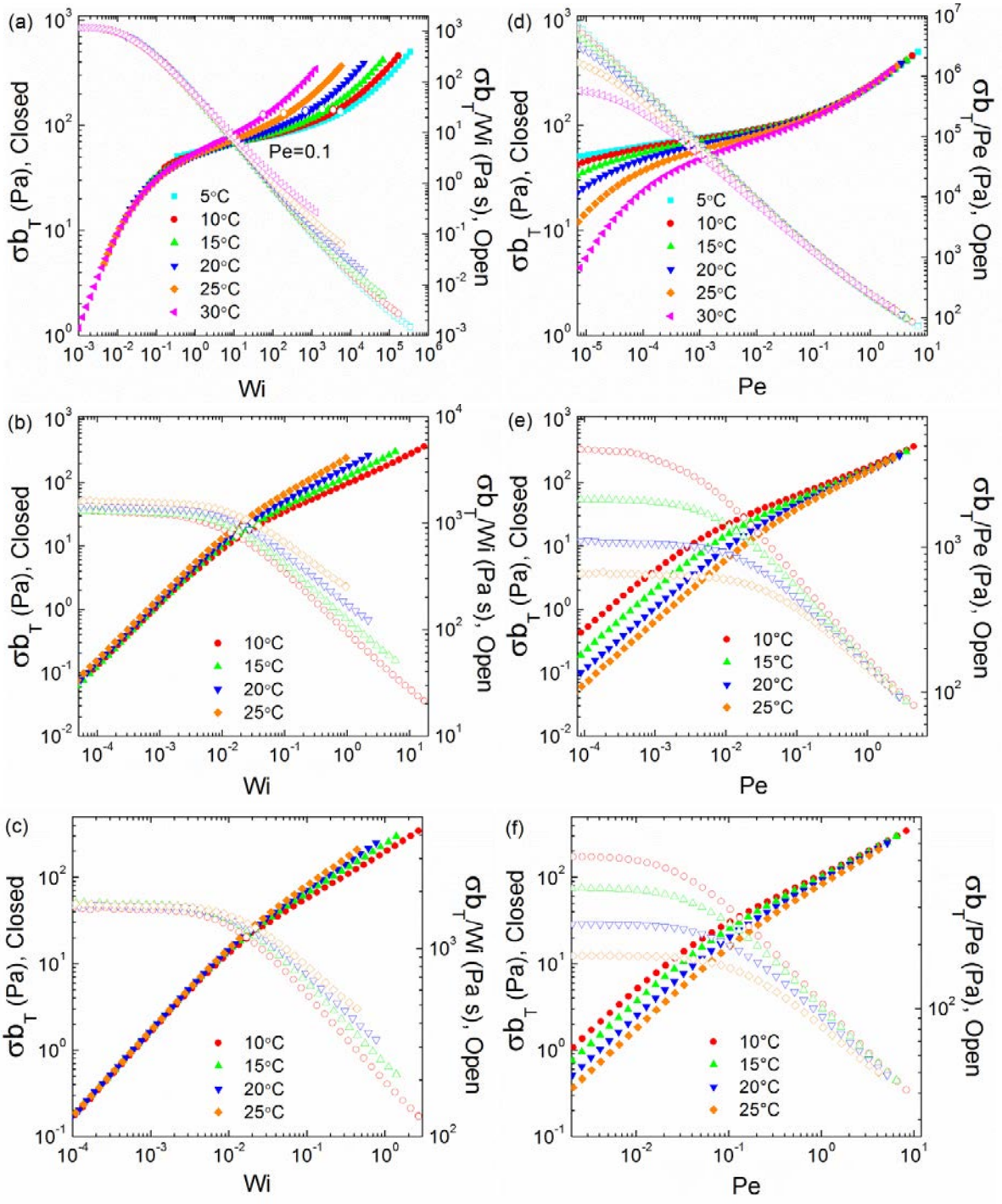

Figure 4.4 Scaled steady shear rheology. (a-c) Weissenberg number scaling. (d-f) Peclet number scaling. Nanoemulsions contain ϕ_o = 0.33 PDMS droplets with PEG and C_s = 120mM SDS. (a, d) <*a*> = 34.6 nm and ϕ_p = 0.33. (b, e) <*a*> = 31.7 nm and ϕ_p = 0.36. (c, f) <*a*> = 35.4 nm and ϕ_p = 0.40.

fluid as mentioned earlier. I.e., there will be one time scale for breakage and reformation of the viscoelastic network, and another related to the relaxation of the suspension microstructure through Brownian motion. In order to test this hypothesis, we computed the Weissenberg number $Wi = \tau_r \dot{\gamma}$ and the Peclet number $Pe = 6\pi a^3 \eta_m \dot{\gamma} / k_B T$. The steady shear rheology data were then scaled by these dimensionless groups to test their ability to describe the observed regimes of shear thinning. Figure 4.4 shows the data rescaled by *Wi* (Figure 4.4 a-c) and *Pe* (Figure 4.4 d-e). To account for a small temperature-dependence of the linear elastic modulus, the stress is scaled by the vertical shifting factor b_T from the time-temperature superposition measurements. Furthermore, the steady shear viscosity is scaled by the dimensionless shear rate (for dimensional consistency) and b_T (for the same reason just described).

For all sample compositions and temperatures, the rheology data for each composition collapse by scaling with *Wi* for low shear rates corresponding to the first shear thinning regime. This suggests that the initial shear thinning is dominated by the viscoelastic relaxation of the transient network, and the nonlinear disruption thereof. However, the data at individual temperatures deviate from this collapse at significantly high shear rates, the onset of which depends on the composition and temperature of the material. In this range of shear rates, the high-shear rheology collapses by scaling with *Pe*, suggesting that the second shear thinning is dominated by disruption of the equilibrium suspension microstructure due to the hydrodynamic interactions between droplets (this will be tested using the SANS measurements to follow). Furthermore, the onset of this collapse of the second shear thinning regime, which occurs at $Pe \sim 0.1$, coincides precisely with the shear rates at which

the steady shear rheology begins to deviate from the *Wi* scaling of the low shear rate rheology (Figure 4.4 (a)).

It is surprising to find that the collapse of these two shear thinning regimes, one at low shear rates with *Wi* and one at high shear rates with *Pe*, occurs regardless of whether *Wi* >> *Pe*, *Wi* ~ *Pe*, or *Wi* < *Pe*. Note, however, that for samples corresponding to the latter two cases (i.e. Figure 4.4 (c) and (f)) that the *Pe* scaling of the steady shear rheology begins to become inadequate to collapse the data at high shear rates. We anticipate that this is due to the emergence of a new limiting behavior when *Wi* < *Pe*. This hypothesis will be further tested using the perturbative rheological model to follow.

4.5 Shear-induced microstructure

To further understand how these phenomena relate to the shear-induced structuring of the polymer-colloid mixture, we performed flow-SANS measurements in a Taylor-Couette geometry both in the 1-3 (flow-vorticity) and 1-2 (flow-gradient) projections. The measurements are performed under contrast-matched conditions for the polymer, such that only the suspension microstructure is observed. Figure 4.5 (a) shows reduced 2D-flow SANS patterns with heat plots of the absolute intensity for both shear planes at various values of *Pe* for the sample with *Wi* >> *Pe*. In order to emphasize the effect of shear on the suspension microstructure, we also show a representation of the scattering in which the absolute scattering intensity at zero shear rate is subtracted from the data (Figure 4.5(b)).

At vanishingly small Peclet number ($Pe = 6.88\times10^{-5}$), the 2D SANS patterns exhibit isotropic scattering, with a correlation peak at $q = 0.015$ Å^{-1} due to droplet-droplet correlations in the suspension microstructure. We note that this correlation peak is

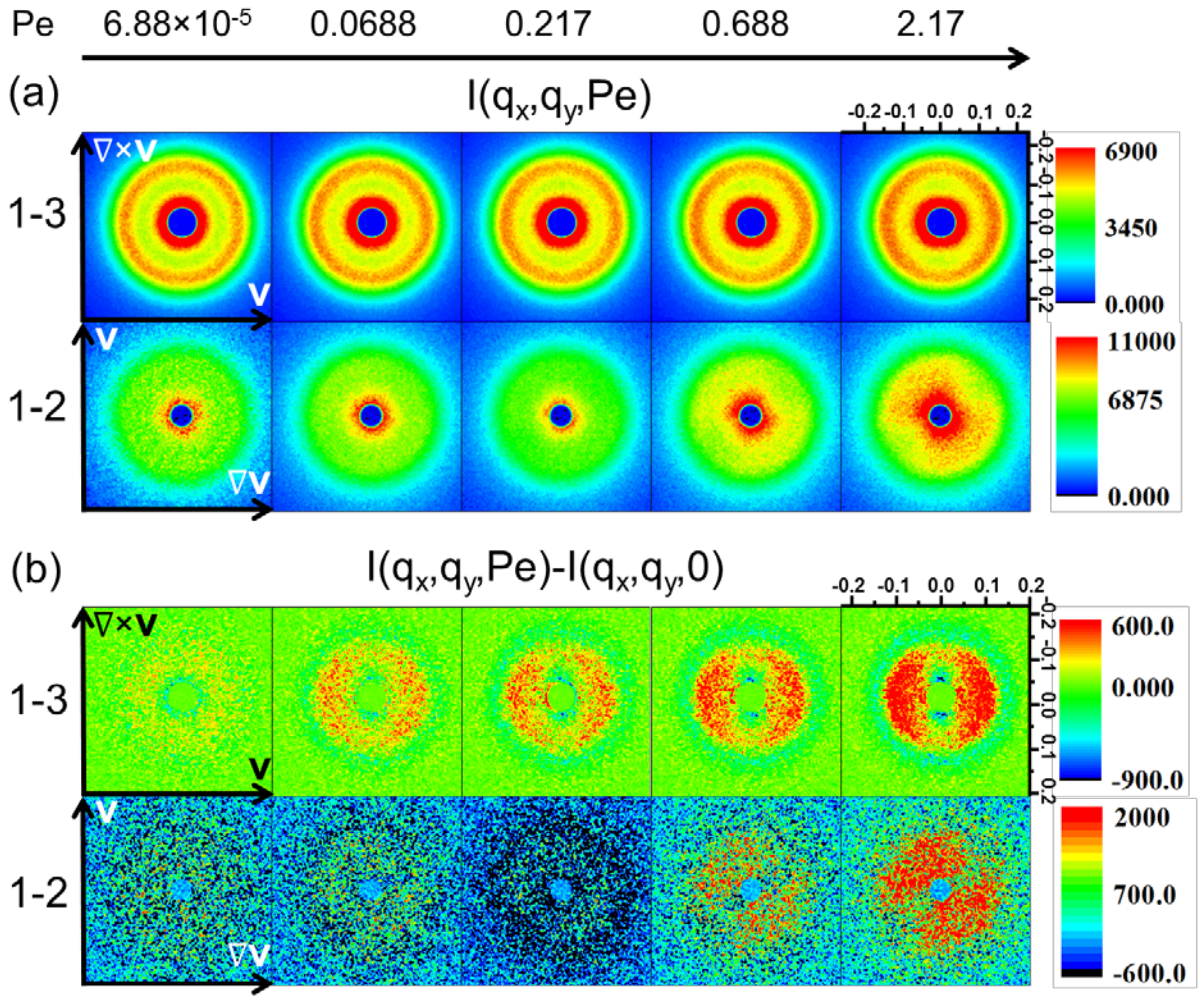

Figure 4.5 2D flow-SANS scattering patterns showing heat plots of absolute intensity (a) before and (b) after subtracting the intensity at zero shear rate in both 1-3 (flow-vorticity) and 1-2 (flow-gradient) planes at the Peclet numbers indicated. Data is for the nanoemulsion containing ϕ_0 = 0.33 PDMS droplets (<a>=34.6nm) with ϕ_p = 0.33 PEG and C_s = 120 mM SDS. Scale tick labels represent values of q_x and q_y in nm^{-1}, and the color intensity scales represent the absolute scattering intensity in cm^{-1}.

diminished in the 1-2 plane measurements, possibly due to the corrupting effects of multiple scattering, which are enhanced by the longer sample path length. Nevertheless, the scattering at vanishingly small shear rates is consistent with a concentrated dispersion of non-aggregated droplets interacting primarily through repulsive (excluded volume and electrostatic) interactions, in agreement with Chapter 3.

At $Pe \sim 1$, the fluid develops a so-called "butterfly" scattering pattern, i.e., an anisotropic scattering pattern with lobes of excess scattering oriented along a preferred direction. The degree of anisotropy appears to increase with increasing *Pe*. The *q*-values associated with the observed anisotropy in the scattering patterns encompasses a range of $0.15 < qa/2\pi < 0.65$, such that we can associate it with pairs or small groups of suspended particles. This is different from previous scattering studies that were performed at much smaller *q*-values [3,25], and will be important in the interpretation of the data to follow.

In the 1-3 (flow-vorticity) plane, the excess scattering is oriented along the flow direction, suggesting that there is an excess of particle pairs along the vorticity direction. In the 1-2 (flow-gradient) plane, we also find butterfly scattering; however, with lobes of excess scattering oriented along the extensional axis of shear (i.e. at 45° with respect to the flow direction). This suggests that there is also an excess of particle pairs oriented along the compressional axis of deformation. As a further proof of this anisotropy in the 1-2 plane, we confirmed that the flow-induced anisotropy is reversible with respect to the direction of the shear (see Appendix B, Figure B.4). As previously mentioned, the droplets are essentially undeformable under the measurement conditions due to the small dimension of the droplets, i.e., the estimated maximum capillary number at the highest shear rates probed is less than 10^{-4} [38]. Thus, it is highly unlikely that the observed scattering anisotropy is caused by the deformability of individual droplets.

The observed anisotropy indicates shear-induced clustering in the fluid, consistent with previous observations of Brownian suspensions in viscoelastic liquids [7,8]. However, our measurements include measurements in all of the orthogonal directions (flow, gradient and vorticity), suggest a clustered microstructure that is qualitatively different than what was

inferred from previous studies of scattering in the 1-3 (flow-vorticity) plane alone at smaller q-values [3,25]. Specifically, those studies hypothesized the formation of chains of particles whose long dimension is oriented along the vorticity axis. However, our measurements show that this clearly cannot be the case for the present materials, since the scattering indicates preferred orientation of particle pairs along both the vorticity (in the 1-3 projection) and compressional (in the 1-2 projection) axes of flow. Our studies therefore highlight the need for structural measurements in multiple shear projections, and suggest that the mechanism for shear-induced clustering (at least in the present fluids) is different than what was hypothesized based on measurements in the 1-3 plane alone.

4.6 Analysis of SANS anisotropy

To further understand the anisotropic structure under shear, we compute the anisotropy factor [39], given by

$$A_f(q) = -\frac{\int_0^{2\pi} I(q,\phi)\cos(2(\phi-\phi_0))d\phi}{\int_0^{2\pi} I(q,\phi)d\phi} \quad (4.3)$$

To perform this calculation, an annular average of the 2D scattering intensity $I(q,\phi)$ with an average q-value of 0.007 Å^{-1} and Δq of 0.004 Å^{-1} was computed for both scattering projections. This particular q-range corresponds to the location of the maximum intensity in the butterfly pattern. In Eq. (4.3), the weighting term $\cos\left(2(\phi-\phi_o)\right)$ assumes two-fold symmetry of the scattering pattern, and accounts for the possibility of average orientation away from the flow direction along an angle ϕ_0 , which may be different in the different flow projections. In order to account for any non-uniformities in the neutron detector, the

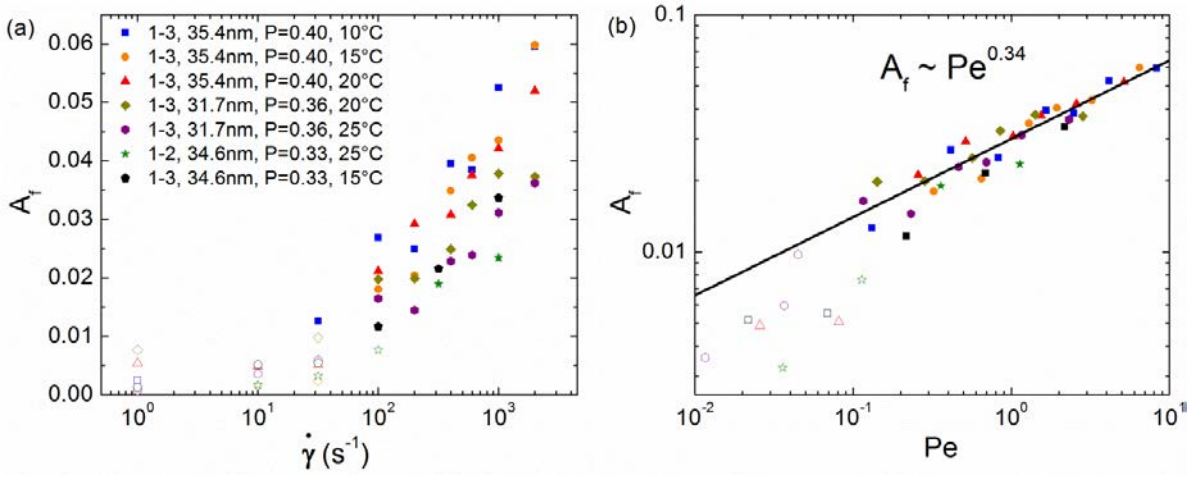

Figure 4.6 Anisotropy factors as a function of (a) shear rate and (b) *Pe* with power law scaling. The power law exponent is 0.34±0.026. Legend represents scattering plane, average radius of droplets, concentration of polymer and temperatures. Open symbols represent values that represent unresolvable anisotropy.

value of A_f measured at rest was subtracted from each data set, so that $A_f = 0$ corresponds to isotropic structures, and A_f increases with increasing degree of anisotropy.

Figure 4.6 (a) shows values for A_f across all samples and shear rates measured, including both the projections in the 1-2 and 1-3 planes of shear. The anisotropy factor increases systematically with increasing shear rate, but to a different extent depending upon the sample. However, due to the differences in composition, temperature and particle size, the samples also have widely varying values of the characteristic time scales τ_r and τ_{Br}. Therefore, to test whether these data collapse considering the characteristic time scales of the fluid, we rescaled the data by *Pe*. We found that all of the data nearly collapse onto a single master curve over two decades in the Peclet number (Figure 4.6 (b)), whereas scaling of the shear rate by *Wi* does not collapse the data. We note that this plot includes data from both projections of the structure, and values of the viscoelastic relaxation time τ_r spanning four orders of magnitude. In all cases, the anisotropy factor is immeasurably small until *Pe* ~

0.1, and increases with increasing *Pe* thereafter. Interestingly, this threshold value of *Pe* ~ 0.1 for the onset of anisotropy is quantitatively similar to that for the onset of the second shear thinning regime in steady shear rheology.

These results suggest that hydrodynamic interactions between suspended particles, and not viscoelasticity of the polymer network, dominate the formation of anisotropic cluster structure. Interestingly, we furthermore find that the anisotropy factor follows a power-law at high *Pe*, with $A_f \sim Pe^{0.34\pm0.026}$. This suggests that, at length scales corresponding to individual particles, the average degree of anisotropy of particle pairs increases according to the strength of interparticle hydrodynamic interactions.

4.7 Clustering during flow startup and cessation

To further understand the dynamics of formation and relaxation of shear-induced particle clusters at high Pe, we performed time-resolved flow-SANS measurements both under startup and after cessation of shear for *Pe* > 0.1. The measurements are performed for the sample containing ϕ_o = 0.33 PDMS droplets (<a>=34.6nm) with ϕ_p = 0.33 PEG and C_s = 120 mM SDS at 25 °C. Figure 4.7 shows the transient shear stress (one cycle) of the nanoemulsions using cyclic step rate measurements at three different *Pe* values (*Pe*~1, 0.32, and 0.2). In all cases, shear stresses increase drastically (t > 0s) and achieve the steady state values within 0.2 seconds. An exponential growth model

$$\sigma(t) = \sigma_{steady}\left(1-\exp\left(-t/\tau_f\right)\right) \quad (4.5)$$

provides a reasonable fit to the transient startup rheology, which provides the characteristic time scale of stress buildup (Table 4.2).

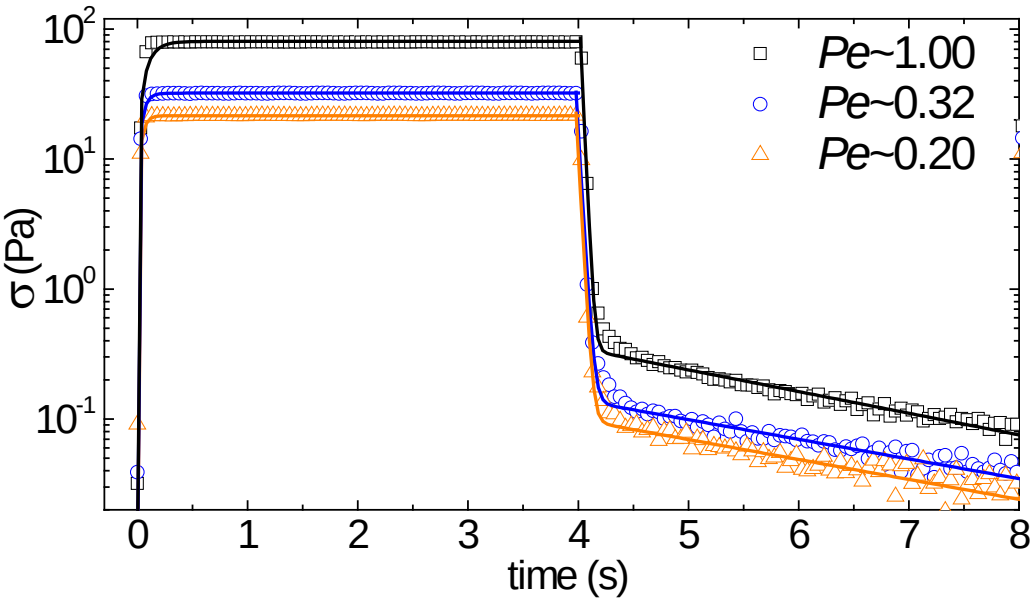

Figure 4.7 The transient shear stress of the nanoemulsions containing ϕ_o = 0.33 PDMS droplets (<a>=34.6nm) with ϕ_p = 0.33 PEG and C_s = 120 mM SDS at 25 °C. Lines represent the exponential decay fitting results generalized by Maxwell model.

After cessation of shear (t > 4 s), the shear stress decreases rapidly in similar time scale (~0.1 s) to an intermediate value, and then slowly relax to zero. This suggests that the stress relaxation in the system is correlated with two different time scales. In order to estimate the two characteristic stress relaxation time scales, the transient shear stress was fit to a two-mode Maxwell model,

$$\sigma(t) = k_{r,1}\exp\left(-(t-4)/\tau_{r,1}\right) + k_{r,2}\exp\left(-(t-4)/\tau_{r,2}\right) \quad (4.4)$$

where $\tau_{r,1}$ and $\tau_{r,2}$ are characteristic time scales for stress relaxation, and $k_{r,1}$ and $k_{r,2}$ are adjustable constants that reflect the proportion of the stress relaxation due to the first and second relaxation process, respectively. The fitting results are tabulated in Table 4.1. Rapid and slow stress relaxations are captured by the values of $k_{r,1}$ and $\tau_{r,1}$, and the values of $k_{r,2}$ and $\tau_{r,2}$, respectively. In all cases, the time scales for the first rapid stress relaxation ($\tau_{r,1}$)

Table 4.2 Fitting parameters for the stress relaxation at 25 °C

	Pe	σ_{steady} or $A_{f,\,steady}$	τ_f	$k_{r,1}$	$\tau_{r,1}$	$k_{r,2}$	$\tau_{r,2}$
Transient stress measurement	1.00	80.47	0.090	49.83	0.0333	0.3445	2.645
	0.32	32.18	0.046	16.96	0.0306	0.1401	2.867
	0.20	21.59	0.039	11.10	0.0284	0.0990	2.827
Transient anisotropic factor	1.00	0.027	0.152	0.023	0.0900	0.0077	1.280
	0.32	0.019	0.145	0.016	0.2009	0.0051	0.695
	0.20	0.017	0.112	0.017	0.0798	0.0034	10.500

are similar and significantly less than the viscoelastic relaxation time (τ_r ~2.86 s at 25 °C, Figure 4.2 (b)) by two orders of magnitude. However, the second slow stress relaxation time ($\tau_{r,2}$) exhibit similar values with the viscoelastic relaxation time of the material. This suggests that the viscoelastic relaxation is responsible for the slow stress relaxation in the transient measurements, but that a distinct process is responsible for the initial stress relaxation, and that this process acts over a similar time scale during shear startup and cessation.

Simultaneously, we also obtained the time-resolved 2D SANS pattern in the flow-vorticity (1-3) plane. In Figure 4.8, reduced time-binned 2D SANS patterns show both the formation and relaxation of anisotropic structuring in the cyclic step shear rate measurement at Pe ~ 1. The transient development of anisotropy is emphasized in the representation of the scattering in which the absolute scattering intensity at zero shear rate is subtracted from the data (lower panels). Note that both the formation and relaxation of the anisotropic scattering patterns occur over a time scale of O(0.1 s), similar to the time scale for stress buildup and initial relaxation.

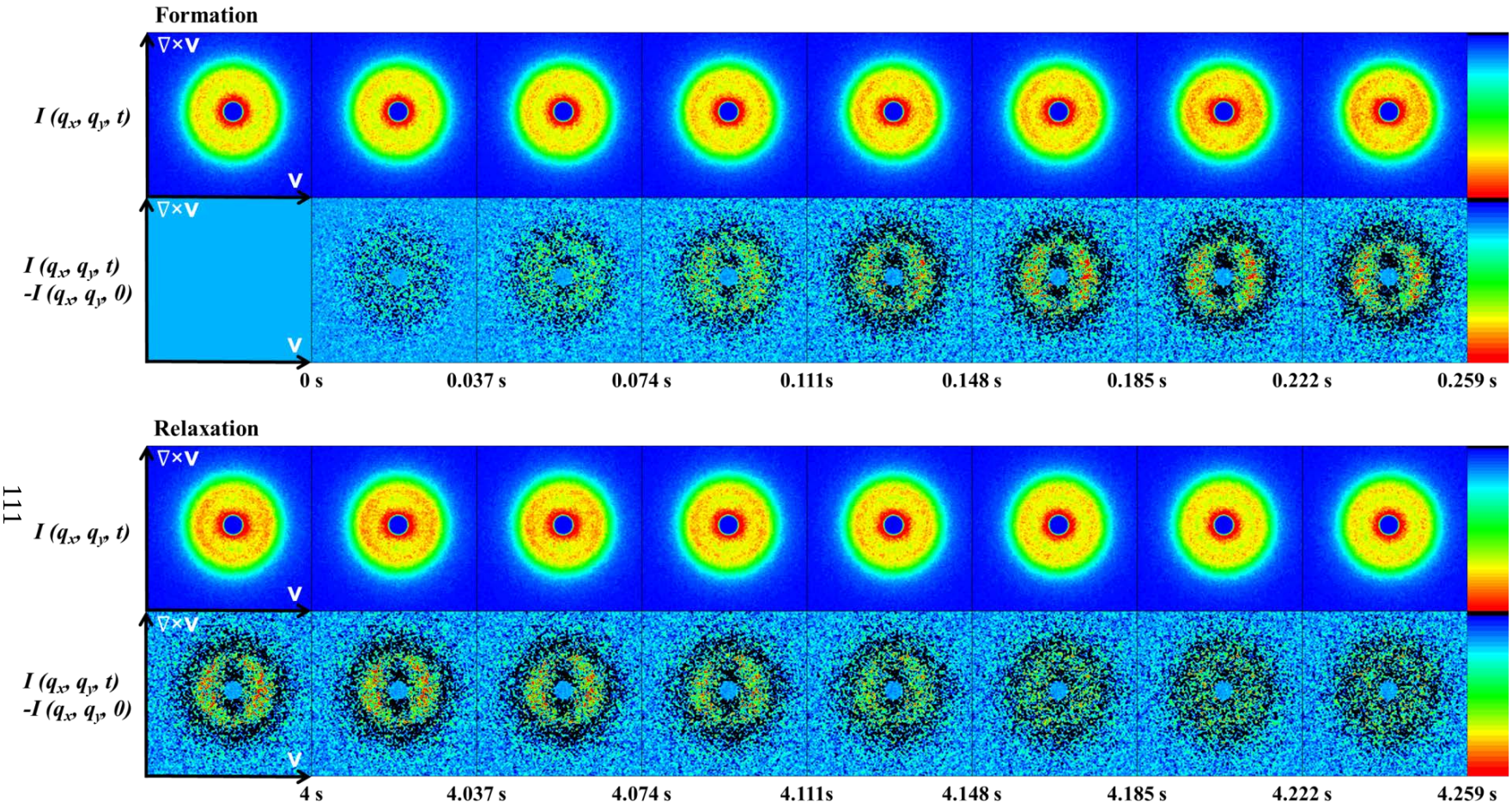

Figure 4.8 The evolution of 2D flow-SANS scattering patterns of absolute intensity before and after subtracting the intensity at zero shear rate in 1-3 plane at Pe~1.

To further understand the transient structuring, we also compute the anisotropy factors from the annular average of the 2D scattering intensity as before, i.e. in the q-range corresponding to the location of the maximum intensity of the butterfly scattering. Figure 4.9 shows the calculated time-resolved anisotropy factors in the cyclic measurement at various values of *Pe*. As we expect from the 2D SANS patterns, the degree of anisotropy increases drastically (t > 0 s) at relatively short times and saturates at steady state values, although the anisotropy factor fluctuating around steady state at all achieved shear rates (*Pe*~1, 0.32 and 0.2). These fluctuations may simply be due to experimental resolution, or they may represent steady state fluctuations in the pair anisotropy. After cessation of shear (*t* > 4 s), the degree of anisotropy decreases drastically, resulting in immeasurably small values after a time scale of *O*(1 s).

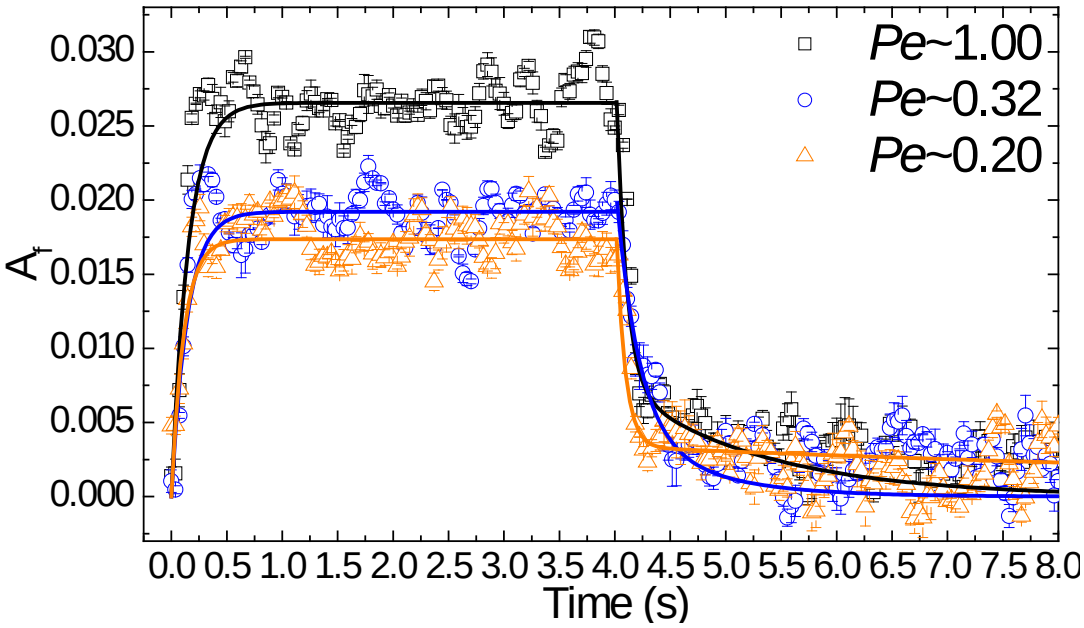

Figure 4.9 Anisotropic factors in the cyclic step shear rate measurement at the *Pe* numbers indicated. Lines represent the exponential decay fitting results generalized by Maxwell model.

To obtain the characteristic time scale for the formation and relaxation of the shear-induced clustering, we also fit the anisotropic factor data by the model used for transient stress rheology. Interestingly, the characteristic time scales of the growth of anisotropic factor (τ_f) are same order of magnitude as the time scale for the stress buildup. After cessation of shear, the first rapid relaxation time of anisotropic factor are also same order of magnitude as the rapid stress relaxation, except the data at *Pe*~0.2. Although second relaxation process in shear induced clustering formation are not convincing due to the poorly resolved data, the characteristic time scale for this process are also similar magnitude of viscoelastic relaxation time from the TTS measurement (τ_r ~2.86s at 25 °C, Figure 4.2 (b)). These results suggest that the time scales for the structuring and breakage of the anisotropic clustering are closely related with the characteristic time scale of the transient stress changes.

4.8 Discussion

We have presented rheology and flow-SANS measurements to understand the mechanism of shear-induced clustering of nanoparticles in viscoelastic polymer-colloid mixtures, and its dependence on the characteristic time scales of viscoelasticity and Brownian motion. This shear-induced clustering is significantly different than what was hypothesized in previous studies on similar systems, where complete vorticity-alignment was inferred from measurements in the 1-3 plane [7,8]. Interestingly, Eberle *et al*. showed similar anisotropic scattering in colloidal gels in Newtonian fluids that are aggregated at rest, where the shear stress was found to scale with the degree of anisotropy of particle clusters [40]. However, since our fluids are not significantly aggregated, and do not possess a yield stress, it is impossible to directly compare the results. Nevertheless, it is remarkable

that we find that both the rheology and shear-induced anisotropy exhibit the same scaling, regardless of the relative magnitudes of *Wi* and *Pe*. Combined with the fact that the anisotropy is dominated by scaling with *Pe*, this strongly suggests that hydrodynamic interactions, which act to deform the suspension microstructure from its equilibrium state, are primarily responsible for shear-induced clustering in the system.

We rationalize these results by analogy to the shear-induced structure and rheology of Brownian suspensions in Newtonian fluids. Specifically, Wagner and Ackerson showed that the Brownian and hydrodynamic contributions to the stress for creeping flows are proportional to the degree of anisotropy of particle pairs through a spherical harmonic expansion of the non-equilibrium suspension microstructure [35]. For suspensions in Newtonian fluids, it follows that the shear stress scales as a power law with respect to *Pe*. More recently, this analysis was found to explain how the emergence of hydrodynamically-induced clusters at high *Pe* served as the basis for shear thickening of model near hard-sphere suspensions [41]. Therefore, by analogy one might expect the effect of anisotropic suspension microstructure and clustering on the total stress in a non-Newtonian suspending fluid should arise from a contribution through the Brownian and hydrodynamic suspension stress, proportional to the degree of anisotropy, which in this case also follows a power-law behavior with respect to *Pe*. What is not known, however, is the degree to which the non-Newtonian behavior of the suspending fluid affects this contribution.

As previously mentioned, there are three contributions to the total stress affected by the non-Newtonian behavior of the suspending fluid: (i) the viscoelastic shear thinning of the polymer network stress due to the combined shearing flow and disturbance flow around the equilibrium suspension microstructure, (ii) the effect of non-Newtonian viscosity on

particle-particle hydrodynamic interactions (which drive the deformation of the suspension microstructure), and (iii) the effect of deformation of the suspension microstructure on the shear thinning of the fluid. Since our experiments are performed mostly in a regime where $Wi >> 1$, the shear thinning will contribute negligibly to the background viscosity of the suspending medium in this limit. Therefore, we anticipate that (iii) will be vanishingly small, and so the primary effect of suspension anisotropy on the total stress will be due to interparticle hydrodynamic forces (ii). Furthermore, for $Pe \sim O(1)$, we expect that (ii) will be non-negligible, but still small relative to (i).

4.8.1 Modification of the viscoelastic polymer stress

Given the above discussion, we hypothesize that the total stress in the limit of $Pe \sim O(1)$ can be captured by a modification of the viscoelastic polymer stress that includes a small correction term due to the suspension anisotropy and its associated dependence on Pe:

$$\sigma_{total}(\dot{\gamma}) = \sigma_{viscoelastic}(\dot{\gamma})\left(1 + cPe^{x}\right) \quad (4.6)$$

where $\sigma_{viscoelastic}(\dot{\gamma})$ corresponds to (i), the viscoelastic polymer network contribution to the total stress (which includes both linear and nonlinear features). Eq. (4.6) is expected to be approximately valid only in the case where the characteristic relaxation time scales for the viscoelastic and suspension hydrodynamic contributions to the total fluid stress are well-separated, and that the perturbative stress due to the suspension anisotropy is small compared to the background viscoelastic stress. The coefficient c is such that $c > 0$ corresponds to a shear-thickening contribution of (ii), and $c < 0$ corresponds to a shear thinning contribution of (ii). We already see that, because the shear thinning exponent for Pe

> 1 is larger than that for *Pe* < 1 (Figure 4.4), the coefficient *c* is positive, and therefore the suspension anisotropy exerts a shear-thickening response on the fluid. We recall that Brownian particles in a Newtonian suspending medium also exhibit a shear-thickening contribution to the stress [24]. It is interesting to note that, in the case of a Newtonian suspending medium, the critical shear rates for the onset of shear thickening in the hydrodynamic stress are typically when *Pe* ~ 1 [42], which is similar to where we find the onset of anisotropic clustering. This suggests that the contribution of suspension hydrodynamics to structuring and bulk rheology for suspensions in viscoelastic fluids at high *Wi* may be similar to that for suspensions in Newtonian fluids.

We test the applicability of Eq. (4.6) by applying it to the steady shear rheology of the system (Figure 4.3). We note that the intent here is not to devise a wholly accurate model for the rheology of the system, but rather to test whether the rheological behavior of the system at moderate *Pe* can be explained by a consistent underlying behavior, and that the

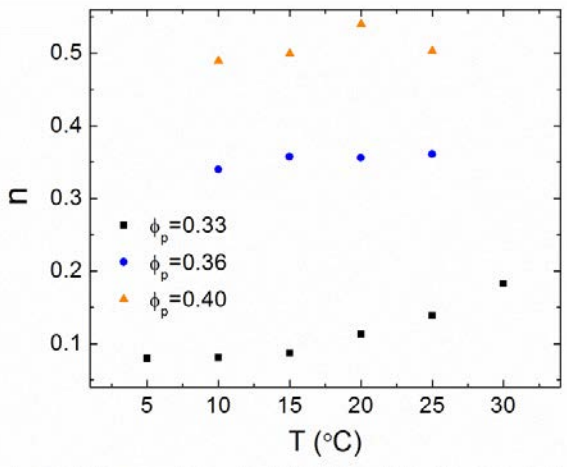

Figure 4.10 Temperature dependence of the Carreau-Yasuda power-law slope for the samples indicated, obtained by fits to shear rates in the low *Wi* regime.

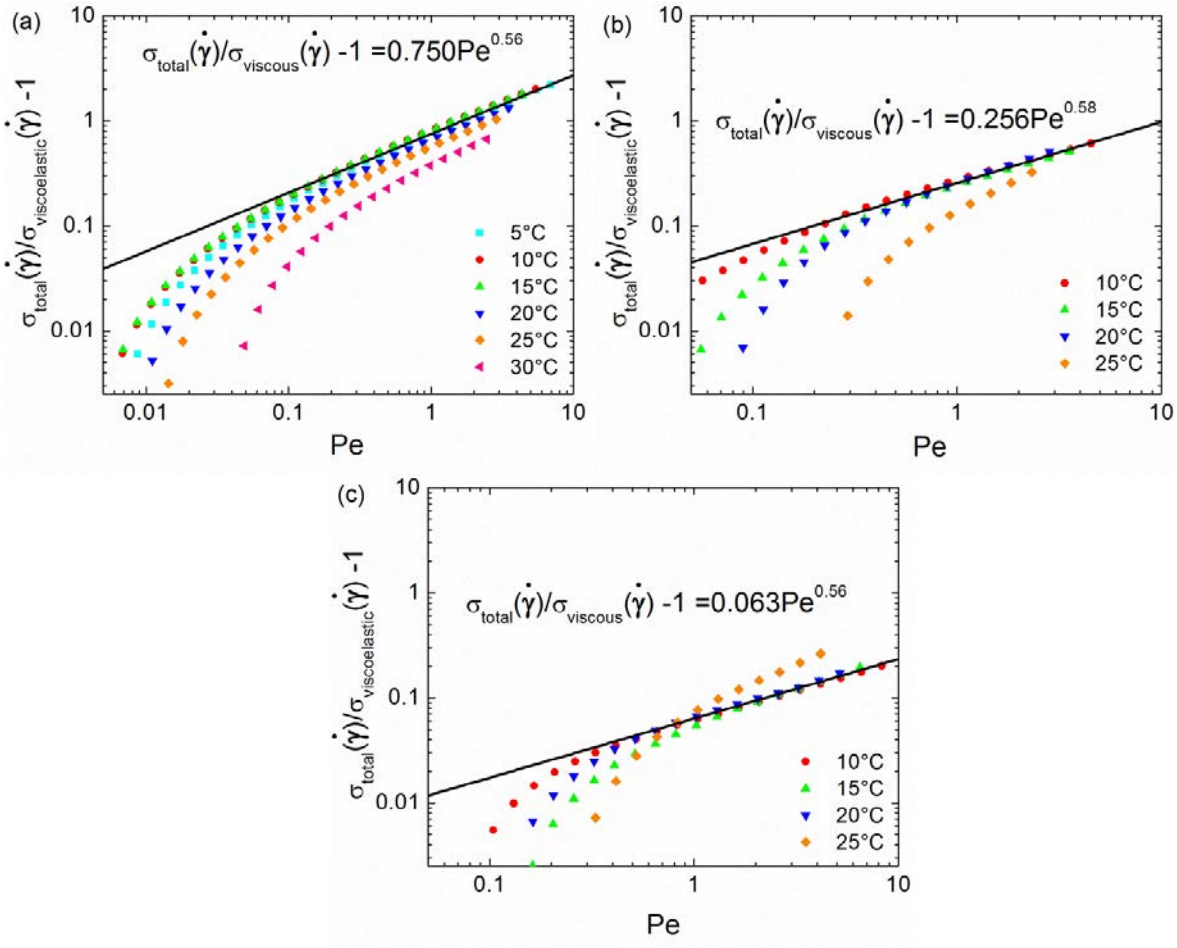

Figure 4.11 $\sigma_{total}(\dot{\gamma})/\sigma_{viscoelastic}(\dot{\gamma})-1$ **as a function of *Pe* for the nanoemulsions containing (a)** ϕ_p**= 0.33, (b)** ϕ_p**= 0.36 and (c)** ϕ_p**= 0.40.**

mechanism for the behavior is consistent with the observed anisotropic clustering of the suspension. As such, since we do not currently have a detailed constitutive model for $\sigma_{viscoelastic}(\dot{\gamma})$ for the system under study, we empirically capture the viscoelastic shear thinning (i.e. the shear thinning regime at low shear rates) of the polymer network by fitting the rheological data at *Pe* << 1 to the Carreau-Yasuda model,

$$\sigma_{viscoelastic}(\dot{\gamma}) = \left[\eta_\infty + \frac{\eta_0 - \eta_\infty}{\left\{1+\left(\lambda\dot{\gamma}\right)^b\right\}^{1-n/b}}\right]\dot{\gamma} \quad (4.7)$$

The zero shear rate viscosity, η_0 , is treated as an adjustable parameter, and we further assume that the high-shear viscosity, η_∞ , at infinite shear rate is the viscosity of water due to the limited range of shear rates in this initial shear thinning regime. $1/\lambda$ is the critical shear rate at which the viscosity begins to shear thin, and n is the asymptotic power law slope for shear thinning at large shear rates (but still small *Pe*). The parameter b sets the width of the transition region between and the power-law regime.

To fit this initial shear thinning, we only use the shear rates corresponding to $Pe < 0.01$, where presumably the hydrodynamic interactions between droplets are insufficient to produce a non-equilibrium suspension stress. The corresponding fits to the Carreau-Yasuda model are presented in Figure 4.2 as the dashed lines. From this fitting, we found that the power-law slope n increases monotonically with increasing temperature (Figure 4.10), and this dependence becomes more significant at relatively small polymer concentrations and large temperatures. In Chapter 3, we showed that the time scale for the transient network decreases with increasing polymer concentration and temperature at fixed surfactant concentration.

As expected, we find that the Carreau-Yasuda model cannot describe the second regime of shear thinning that occurs in the limit of $Wi >> Pe$ and $Pe \sim O(1)$ (Figure 4.3, dotted lines). Instead, we fit the empirical asymptotic relationship given by Eq. (4.6). To do so, we first attempt to extract the perturbative stress contribution arising from hydrodynamic interactions between droplets, i.e., $\sigma_{total}(\dot{\gamma})/\sigma_{viscoelastic}(\dot{\gamma}) - 1 = cPe^x$. The results are shown in Figure 4.11. As hypothesized, the proposed Eq. (4.6) collapses nearly all of the experimental data at sufficiently high *Pe*, suggesting that the second regime of shear thinning can indeed be captured by an extra contribution involving *Pe* alone. A notable exception is the data at

relatively high temperatures. However, as discussed previously, these temperatures correspond to relatively short values of τ_r, such that the asymptotic approximation *Wi* > *Pe* will be invalid for these conditions.

In the region of data collapse in Figure 4.11, all of the data, regardless of polymer concentration, exhibit power-law behavior as anticipated by Eq. (4.6). We further assume that the scaling exponent *x* is independent of the details of the material, and that *c* depends only on the composition (and not the temperature). A global fit of the power-law exponent *x* to all of the data results in an exponent $x = 0.57 \pm 0.011$ at high shear rate (*Pe* > 1). The values of the coefficient *c* are fit to each distinct sample composition, from which we find values of *c* ranging from 0.06-0.75. Since *c* is always positive, we observed that the hydrodynamic interactions produce a shear thickening contribution to the overall shear thinning of the fluid.

From these results, we expect that the rheology of Brownian suspensions in viscoelastic fluids in the limit of *Wi* > *Pe* and *Pe* ~ *O*(1) can be adequately described by Eq. (4.6). To test this, we combine fits of the first shear thinning regime using the Carreau-Yasuda model (Eq. (4.7)) with the additional power-law correction due to hydrodynamic interactions at moderate *Pe*,

$$\sigma_{total}(\dot{\gamma}) = \sigma_{viscoelastic}(\dot{\gamma})\left(1 + cPe^{x}\right) = \left[\eta_{\infty} + \frac{\eta_0 - \eta_{\infty}}{\left\{1 + \left(\lambda\dot{\gamma}\right)^{b}\right\}^{1-n/b}}\right]\dot{\gamma}\left(1 + cPe^{x}\right), \quad (4.8)$$

where all of the model parameters are now fixed as described above. The resulting comparisons to the steady state shear stress and viscosity data (with no adjustable parameters) are represented by the solid lines in Figure 4.3 (see Appendix B, Table B.1 for fitting parameters). We found that excellent quantitative agreement between the model and

experimental data, except for at relatively high temperatures (and correspondingly short τ_r) when *Wi* < *Pe*, where modest deviations are observed at sufficiently high shear rates. Presumably, this is due to the failure of the limit *Wi* > *Pe* assumed in the model. We thus conclude that the proposed empirical correction term is successful at capturing the additional contribution of hydrodynamic interactions on the total fluid stress when *Wi* is sufficiently large compared to *Pe*.

4.8.2 Microscopic mechanism of shear-induced clustering

We have established the effect of shear-induced clustering on the macroscopic rheology of the fluid. Now, we turn our attention to the microscopic mechanism of clustering in the limit where *Wi* >> *Pe*. Again, due to the negligible influence of the shear thinning on interparticle hydrodynamic forces in this limit, we draw analogy to the shear-induced microstructure of Brownian suspensions in Newtonian fluids. We find that our SANS results are qualitatively similar to Stokesian Dynamics simulations of the pair-probability distribution in flow-gradient and flow-vorticity plane for suspensions in Newtonian fluids [43,44]. Specifically, at sufficiently high *Pe*, deformation of the suspension microstructure away from equilibrium results in anisotropic hydrodynamic forces. Initially, this results in a shear-thinning contribution to the shear stress, which saturates at moderate *Pe*. In the present experiments, we hypothesize that this shear thinning of the suspension stress is very small compared to the polymeric stress at the corresponding shear rates, and so it will have a minor contribution to the viscoelastic shear stress fit by Eq. (4.7). At higher *Pe*, however, the contribution of short-range hydrodynamic forces on the microstructure becomes dominant due to the very thin boundary layer of the nearest-neighbor particles [44]. This results in excess and depleted particle fluxes along the

compressional and extensional axes, respectively, as the Brownian forces attempt to restore particles to their equilibrium configuration. As such, one would expect to observe anisotropic scattering in the 1-2 plane indicating the shear-induced clustering oriented along the compressional axes, which is precisely what we find in the present system involving Brownian suspensions in viscoelastic liquids. Note that this discussion ignores frictional forces between particles in contact as well as elastohydrodynamic deformation of particles, which are known to play a significant role in shear thickening at sufficiently high shear rates [45,46]. However, we believe such effects to be negligibly small in the present system, since in the former case the oil-water interface is molecularly smooth and contact would cause coalescence of nanodroplets, and in the latter case the capillary number, which sets the relative deformation of droplets [47], is less than 10^{-4} for all conditions studied.

From this discussion, we hypothesize that the excess of particle fluxes along the compressional and vorticity axes due to short-range hydrodynamic forces gives rise to the shear-induced clustering in our Brownian suspensions in viscoelastic fluids when $Wi > Pe$. This is corroborated by the collapse of the scattering anisotropy in both shear projections as well as the high-shear rate rheology by scaling with Pe. It is also corroborated by the fact that clustering in the present system produces a shear-thickening contribution to the total shear stress, similar to the formation of so-called “hydroclusters” observed at large Pe for suspensions in Newtonian fluids [48,49]. However, it is interesting to find that, in these viscoelastic fluids, a shear-thickening contribution to the stress is found even when $Pe \sim O(0.1)$, which is significantly smaller than that typically predicted and observed for the continuous shear thickening of Brownian suspensions in Newtonian fluids [41,44]. One

possible explanation is the choice of the single particle self-diffusivity as a choice for τ_{Br}, which underestimates the Peclet number.

Lastly, we have investigated the transient process of shear induced clustering in nanoemulsions using time-resolved flow-SANS measurements. Although the detailed kinetic processes of the clustering have yet to be identified, we found that the time scales for the cluster formation and breakup correspond to the time scales for the stress buildup and initial relaxation. Compared to the Brownian relaxation time (τ_{Br} ~0.0014 s at 25 °C, Figure 4.2(b)), the time scales from the rapid process of formation and breakup are at least an order of magnitude larger than τ_{Br} . The results indicate that the buildup of the Brownian contribution to the stress dominates the clustering process, and sets the time scale for cluster formation and relaxation. Furthermore, the clusters relax relatively quickly compared to the viscoelastic relaxation time (τ_r ~2.86s at 25 °C, Figure 4.2 (b)). This further suggests that the dynamics of clustering are only weakly coupled with the viscoelasticity. This is consistent with the assumption made in the semi-empirical modeling of the stress, which is that clustering produces a relatively small extra contribution to the total stress. In terms of the second slow relaxation processes of clustering, the time scale of them is similar magnitude of both the viscoelastic relaxation time and the fluid slow stress relaxation time. This suggests that the second relaxation of the shear stress, which coincides with the period of nearly zero anisotropy, may be governed by the viscoelastic relaxation process of the network system. However, to confirm this result will require time-resolved flow-SANS data with finer resolution of the anisotropy over a wider range of *Pe*.

4.9 Conclusions

We identified the relationship between rheology and microstructure for non-aggregating, viscoelastic and Brownian suspensions in associative polymer solutions. The steady shear behavior is governed by two competing time scales: the relaxation time of the transient network (and associated shear rate scale *Wi*) and the time scale for the Brownian motion (and associated shear rate scale *Pe*). The present work covers several limits including $Wi >> Pe$, $Wi \sim Pe$, and $Wi < Pe$. Remarkably, the same qualitative behavior is observed in all of these limits. At low *Pe*, where interparticle hydrodynamic interactions are negligible, the shear thinning of the fluid is dominated by polymer viscoelasticity, which is collapsed by *Wi*. At $Pe > 0.1$, however, the steady shear rheology is collapsed by *Pe* due to suspension hydrodynamic contributions to the stress.

In this regime, rheo-SANS measurements reveal that anisotropic scattering patterns develop and become enhanced with increasing *Pe* in both the flow-vorticity (1-3) and flow-gradient (1-2) planes. The orientation of the anisotropic scattering indicates concentration fluctuations oriented along both the vorticity and compressional axes of shear. The degree of anisotropy over a wide range of material parameters and shear rates collapse onto a master curve, which follows a scaling of $A_f \sim Pe^{1/3}$. To our knowledge, this is the first to report of such a power-law scaling of pair correlation anisotropy with Peclet number in polymer-colloid mixtures. From this, we proposed and validated a simple empirical model to capture the steady shear rheology of the fluid, in which the clustering of particles imparts a perturbative contribution to the shear stress that modifies the underlying viscoelastic shear stress. We find that this clustering contribution to the shear stress is shear thickening, which

is reminiscent of the “hydrocluster”-driven shear thickening of suspensions in Newtonian fluids, but occurs at significantly smaller *Pe*.

Our results provide clear evidence for the role of interparticle hydrodynamic interactions in the formation of anisotropic particle clusters in viscoelastic fluids, and that this clustering is responsible for modified shear thinning at high *Pe*. The influence of hydrodynamic interactions also suggests the possibility that the clusters may in fact be dynamic structures, rather than the persistent chains inferred from previous measurements. However, we caution that it is unknown whether the structures and interactions identified here also dominate in viscoelastic fluids other than associative polymer-colloid networks (such as entangled solutions with negligible polymer-colloid interactions). Nevertheless, our results highlight the importance of using simultaneous structural and rheological measurements, and fully-3D resolved structural measurements in particular, to elucidate the mechanisms of shear-induced clustering of suspensions in non-Newtonian fluids. We note that the rheological description of the system in terms of viscoelastic and hydrodynamic stresses proposed here is merely a first attempt to capture the dominant physics of clustering, and hope that our work will motivate further theoretical modeling of non-dilute suspension microstructure in viscoelastic liquids where polymeric, Brownian and hydrodynamic contributions all contribute to the behavior of the fluid. Ultimately, such studies should provide a more rational basis to control the rheology and microstructure of polymer-colloid mixtures.

References

[1] R. A. Vaia and E. P. Giannelis, MRS bulletin **26**, 394 (2001).

[2] D. N. Bikiaris, A. Vassiliou, E. Pavlidou, and G. P. Karayannidis, European Polymer Journal **41**, 1965 (2005).

[3] J. V. DeGroot, C. W. Macosko, T. Kume, and T. Hashimoto, Journal of colloid and interface science **166**, 404 (1994).

[4] J. Michele, R. Pätzold, and R. Donis, Rheologica Acta **16**, 317 (1977).

[5] M. Lyon, D. Mead, R. Elliott, and L. Leal, Journal of Rheology (1978-present) **45**, 881 (2001).

[6] A. Montesi, A. A. Peña, and M. Pasquali, Physical review letters **92**, 058303 (2004).

[7] L. Silbert, J. Melrose, and R. Ball, Journal of Rheology (1978-present) **43**, 673 (1999).

[8] R. Pasquino, F. Snijkers, N. Grizzuti, and J. Vermant, Rheologica Acta **49**, 993 (2010).

[9] H. Haddadi and J. F. Morris, Physics of Fluids (1994-present) **27**, 043302 (2015).

[10] X. Cheng, X. Xu, S. A. Rice, A. R. Dinner, and I. Cohen, Proceedings of the National Academy of Sciences **109**, 63 (2012).

[11] C. O. Osuji and D. A. Weitz, Soft Matter **4**, 1388 (2008).

[12] D. Highgate and R. Whorlow, Rheologica Acta **8**, 142 (1969).

[13] D. Highgate and R. W. Whorlow, Rheologica Acta **9**, 569 (1970).

[14] R. Scirocco, J. Vermant, and J. Mewis, Journal of Non-Newtonian Fluid Mechanics **117**, 183 (2004).

[15] F. Snijkers, R. Pasquino, and J. Vermant, Langmuir **29**, 5701 (2013).

[16] P. Brunn, Rheologica Acta **15**, 589 (1976).

[17] H. Giesekus, Some secondary flow phenomena in general viscoelastic fluids, 1965.

[18] R. J. Phillips and L. Talini, Journal of Non-Newtonian Fluid Mechanics **147**, 175 (2007).

[19] D. Joseph and J. Feng, Journal of Non-Newtonian Fluid Mechanics **64**, 299 (1996).

[20] P. Kaloni and V. Stastna, Polymer Engineering & Science **23**, 465 (1983).

[21] F. Greco, G. D'Avino, and P. Maffettone, Journal of Non-Newtonian Fluid Mechanics **147**, 1 (2007).

[22] F. Parsi and F. Gadala-Maria, Journal of Rheology (1978-present) **31**, 725 (1987).

[23] T. N. Phung, J. F. Brady, and G. Bossis, Journal of Fluid Mechanics **313**, 181 (1996).

[24] J. F. Brady and J. F. Morris, Journal of Fluid Mechanics **348**, 103 (1997).

[25] B. Belzung, F. Lequeux, J. Vermant, and J. Mewis, Journal of colloid and interface science **224**, 179 (2000).

[26] S. Lin-Gibson, J. Pathak, E. Grulke, H. Wang, and E. Hobbie, Physical review letters **92**, 048302 (2004).

[27] H. Hoekstra, J. Vermant, J. Mewis, and G. Fuller, Langmuir **19**, 9134 (2003).

[28] A. Woutersen, R. May, and C. De Kruif, Journal of Rheology (1978-present) **37**, 71 (1993).

[29] F. Pignon, A. Magnin, and J.-M. Piau, Physical review letters **79**, 4689 (1997).

[30] H. Hoekstra, J. Mewis, T. Narayanan, and J. Vermant, Langmuir **21**, 11017 (2005).

[31] J. Vermant and M. Solomon, Journal of Physics: Condensed Matter **17**, R187 (2005).

[32] J. R. de Bruyn, F. Pignon, E. Tsabet, and A. Magnin, Rheologica Acta **47**, 63 (2008).

[33] M. E. Helgeson, S. E. Moran, H. Z. An, and P. S. Doyle, Nature materials **11**, 344 (2012).

[34] M. E. Helgeson, P. A. Vasquez, E. W. Kaler, and N. J. Wagner, Journal of Rheology (1978-present) **53**, 727 (2009).

[35] A. K. Gurnon, P. D. Godfrin, N. J. Wagner, A. P. Eberle, P. Butler, and L. Porcar, JoVE (Journal of Visualized Experiments), e51068 (2014).

[36] S. R. Kline, Journal of applied crystallography **39**, 895 (2006).

[37] M. A. Calabrese, N. J. Wagner, and S. A. Rogers, Soft matter **12**, 2301 (2016).

[38] A. Kanellopoulos and M. Owen, Transactions of the Faraday Society **67**, 3127 (1971).

[39] L. M. Walker and N. J. Wagner, Macromolecules **29**, 2298 (1996).

[40] A. P. Eberle, N. Martys, L. Porcar, S. R. Kline, W. L. George, J. M. Kim, P. D. Butler, and N. J. Wagner, Physical Review E **89**, 050302 (2014).

[41] A. K. Gurnon and N. J. Wagner, Journal of Fluid Mechanics **769**, 242 (2015).

[42] J. Bergenholtz, J. Brady, and M. Vicic, Journal of Fluid Mechanics **456**, 239 (2002).

[43] G. Bossis and J. F. Brady, The Journal of chemical physics **91**, 1866 (1989).

[44] D. R. Foss and J. F. Brady, Journal of Fluid Mechanics **407**, 167 (2000).

[45] E. Brown, N. A. Forman, C. S. Orellana, H. Zhang, B. W. Maynor, D. E. Betts, J. M. DeSimone, and H. M. Jaeger, Nature materials **9**, 220 (2010).

[46] A. S. Lim, S. L. Lopatnikov, N. J. Wagner, and J. W. Gillespie, Journal of Non-Newtonian Fluid Mechanics **165**, 1342 (2010).

[47] P. Maffettone and M. Minale, Journal of Non-Newtonian Fluid Mechanics **78**, 227 (1998).

[48] N. J. Wagner and J. F. Brady, Physics Today **62**, 27 (2009).

[49] Y. S. Lee and N. J. Wagner, Rheologica Acta **42**, 199 (2003).

[50] J. Kim and M. E. Helgeson, Physical Review Fluids **1**, 043302 (2016).

Chapter 5

Microstructure and nonlinear signatures of yielding in a heterogeneous colloidal gel[3]

5.1 Introduction

In Chapter 3, we demonstrated the formation of thermoresponsive viscoelastic nanoemulsions through polymer-surfactant complexation. At low temperatures, we found the development of self-similar viscoelasticity of the fluid. In this Chapter, we shift our attention to on the behavior of the thermoresponsive nanoemulsions at high temperature in the presence of the telechelic bridging polymer (e.g. PEGDA) that gives rise to thermoreversible gelation mediated by [1]. In this chapter, we will use the system to investigate the mechanisms for broadened yielding in heterogeneous colloidal gels.

Colloidal gels are non-equilibrium structures comprised of attractively driven, sample-spanning particle networks whose arrested dynamics give rise to solid-like rheology under small-amplitude deformation. Their rheology has long been of significant technological interest in foods [2,3], paints[4] and consumer products, and more recently for guiding the synthesis of highly structured materials [1,5,6]. As such, significant study has been devoted to the relationships between the rheology and microstructure of colloidal gels. To date, there has been significant progress in understanding how the linear viscoelasticity of colloidal gels is related to their quiescent microstructure [7-10], and furthermore how this microstructure relates to the interactions and conditions under which the gel is formed [11-18].

[3] This chapter was reproduced by permission of AIP Publishing LLC [79].

It is common for colloidal gels at moderate volume fraction to exhibit heterogeneous microstructure [19-22]. In many systems, this heterogeneity is reminiscent of (or perhaps caused by) arrested phase separation, typically occurring as a bicontinuous structure of colloid-rich and colloid-poor domains [5,15,20,23-25]. Recent experiments have shown that the linear rheological properties of such heterogeneous gels manifest over a range of length scales much larger than the primary particle size [1,26].

However, the influence that such microstructural heterogeneity has on nonlinear rheological processes in colloidal gels is an outstanding fundamental question. Yielding (i.e., the transition from elastic behavior to flow) is perhaps the most important of such nonlinear processes, as it is germane to a number of flows including mixing [27], jetting [28], coating[29], and pipe flows [30]. Yielding in dynamically arrested fluids, such as colloidal gels, is also of significant fundamental interest. The simplest description of yielding involves a characteristic yield stress or strain, below which solid-like behavior dominates and above which viscous behavior dominates [31]. In reality, however, yielding is a time-dependent phenomenon that depends significantly on the dynamics of the fluid and the flow it is subjected to [32,33]. As such, the apparent signatures of yielding qualitatively depend on the type and time-dependence of the applied deformation.

Large amplitude oscillatory shear (LAOS) is a particularly useful flow for probing yielding, as it allows for repetitive, steady state, rate-dependent measurements that span the transition from linear solid-like behavior to fully nonlinear flow. Recently, LAOS has been used to make detailed measurements of yielding in attractive suspensions at moderate volume fraction. In many cases, a broadened or so-called “two-step” yielding process is observed, in which the transition from a nonlinear material response to flow occurs over an

order of magnitude or more in strain amplitude, γ_0 [7,34-36]. This is in contrast to more dilute gels, which typically exhibit a distinct, unique yield point defined by a simultaneous maximum in the linear viscous modulus, *G"*, and crossover of *G"* and the linear elastic modulus, *G'* [37,38]. The two-step process is signified by two local maxima in either the viscous modulus, $G"(\gamma_0)$, or average elastic stress, $\sigma' = \gamma_0 G'(\gamma_0)$, with increasing strain amplitude. Detailed measurements have shown that the locations of the local maxima are relatively insensitive to the applied frequency of oscillation, although the corresponding values of the stress and moduli can be either frequency-dependent or -independent depending on the details of the material system [35,36]. In some cases, two separate maxima are not distinctly evident, although a broadened yielding transition is still observed [39,40]. It was also shown that a transition between one-step and two-step yielding could be induced by screening interparticle repulsions in a jammed suspension [36].

We note that these previous studies focused on measurement and analysis of the linearized moduli, *G'* and *G"*, despite the fact that yielding is an intrinsically nonlinear phenomenon. Therefore, much more information can potentially be obtained by examining the details of the nonlinear mechanical response during yielding of colloidal gels using previously established methods for analyzing LAOS data, including various representations of the nonlinear stress waveform in strain-controlled measurements [41]. In particular, Rogers recently developed a method for parameterizing strain controlled waveform data in an instantaneous, time-dependent fashion [42], providing a quantitative framework for examining the nonlinear response as a sequence of physical processes (SPP) [42,43]. Such nonlinear analyses, including the SPP approach, have already provided significant insight

into the yielding process in repulsive colloidal glasses [43-47]. However, such analysis has not been applied to the nonlinear response of colloidal gels during yielding.

The previous studies show that yielding is dominated by microstructural processes and have been used to develop a phenomenological picture of yielding in moderately concentrated colloidal gels that involve the convolution of two strain-dependent microscopic processes [35,36,40]. The first is "bond rupture," which is proposed to coincide with the first local maximum, where individual interactions between neighbors are thought to be mobilized after a critical strain required to excite a particle out of its local potential well. Between maxima, particle bonds then rearrange within a local cage-like cluster of neighboring particles. This provides a mechanism by which stress can be dissipated while retaining network structure and is hypothesized to result in the observed broadened yielding. The second and final process is then "cage breakage," where the cluster of nearest neighbors is broken and particles can be advected in the flow. We note that similar phenomenology has been used to explain the yielding behavior of repulsive glassy suspensions of soft particles, where a broad yielding transition was hypothesized to occur due to a similar convolution of particle-scale and larger-scale processes [47,48].

Unfortunately, the hypothesized bond rupture and cage breakage mechanisms have never been tested by direct microstructural observation. Furthermore, since this phenomenology presumes that yielding is inherently a particle-scale process, it ignores any effects of large-scale structural heterogeneity, despite the prevalence of heterogeneity in many systems. However, Helgeson et al. recently showed that heterogeneity can lead to qualitative differences in the yielding observed under LAOS deformation [26]. Specifically, gels with homogeneous mass fractal structure at relatively low volume fraction displayed

simple, one-step yielding, whereas heterogeneous gels arising from arrested phase separation exhibited broadened yielding of the type found in more concentrated systems.

These results call for more direct microstructural studies of yielding processes in colloidal gels, and in particular those aimed at identifying the influence of large-scale structural heterogeneity. Some progress has already been made toward these aims. Specifically, direct observation of suspension microstructure under shear by confocal microscopy has been used to probe yielding processes in colloidal gels induced by depletion attractions under both step strain [39] and startup of steady shear [40]. Rajaram and Mohraz showed that the structure of depletion-induced colloidal gels at relatively large strains follows from a series of local rupturing events of particle-particle contacts to produce a flowing suspension of disconnected clusters. Hsiao et al. found that the strain-dependent value of *G'* at large strains correlated well with the concentration of "rigid" clusters (i.e., dense clusters with large contact number). However, both of these studies were performed at strains corresponding to multiple orders of magnitude above the apparent yield strain, which was required in order to resolve changes in microstructure at the particle scale. Moreover, these studies focus on microstructural correlations at length scales corresponding to 1–10 particle volumes, despite clear larger-scale heterogeneity in the quiescent state.

Although the phenomenology of bond rupture and cage breakage for broadened yielding has never been directly tested through microstructural measurements under LAOS deformation, methods to do so currently exist. In particular, small angle neutron scattering with simultaneous rheological measurement (rheo-SANS) has allowed for detailed in situ interrogation of the microstructural processes leading to a number of nonlinear rheological phenomena, including strain-dependent measurements of self-assembled surfactant systems,

such as shear banding in wormlike micelles [42,49] and yielding of ordered crystalline phases [50].

Given the previous work, the goals of this chapter are two-fold. The first is to present the first detailed analysis of the nonlinear mechanical response of concentrated colloidal gels under LAOS, in order to better characterize the rheological signatures of broadened yielding. The second is to extend rheo-SANS to larger length scales using time-averaged ultra-SANS (USANS), which has proven critical in elucidating the mechanisms of gelation in our previous work [26]. Rheo-USANS thus allows direct measurement of the strain amplitude-dependent microstructural changes that accompany yielding at length scales ranging from one to thousands of primary particles. Specifically, we hope to test whether heterogeneity itself is the fundamental cause for broadened yielding, as suggested by our previous experiments [26].

As a model colloidal gel, we employ a well-characterized material system comprised oil-in-water (O/W) nanoemulsions with low polydispersity [1,26]. Because of the small size of the nanoemulsion droplets (<50 nm), and the resulting large Laplace pressure associated with deformation of the droplet surface, the nanoemulsions can be regarded as nearly hard spheres below volume fractions corresponding to the compressive regime [51]. A temperature-responsive bridging polymer in the continuous phase allows for careful control over interparticle attractions, including the process of gelation, such that we are able to prepare gels with reproducible microstructure [1] without the need for shear rejuvenation that is required in many systems. As such, we are able to make careful measurements of the rheological properties (including yielding) of pristine gels, as opposed to rejuvenated gels whose microstructure can be significantly altered by flow history [52]. We believe such

measurements are critical to establishing the influence of large-scale microstructure on the nonlinear yielding process. We first present detailed LAOS measurements of yielding in such gels, including nonlinear waveform analysis of both strain amplitude- and frequency-dependent measurements. We then turn our attention to time-averaged rheo-SANS/USANS studies of in situ fluid microstructure throughout the yielding transition.

5.2 Experimental

5.2.1 Sample preparation

Nanoemulsions were prepared using a high-pressure homogenization method described in Chapter 2. Briefly, polydimethylsiloxane (PDMS, η=5 mPa·s at 25 °C) was used as the dispersed phase for the O/W nanoemulsion sample. The aqueous continuous phase consisted of poly(ethylene glycol) diacrylate (PEGDA, M_n = 700 g mol^{-1}) and sodium dodecyl sulfate (SDS) dissolved in deionized water (18.2 MΩ). All chemicals were purchased from Sigma Aldrich. For USANS/SANS measurements, deuterium oxide (D_2O, 99.9%, Cambridge Isotope Laboratories) was used in the aqueous phase to enhance neutron contrast. The size was measured by DLS as described in Chapter 2.

The sample used in this work is a nanoemulsion containing 33 vol.% PDMS, the continuous phase containing 230 mM SDS and 33 vol.% PEGDA. The nanoemulsion was prepared in a solvent of 50/50 (v/v) H_2O/D_2O in order to both enhance contrast and avoid multiple scattering from the droplets. The average droplet radius measured by DLS was r = 21 nm with a polydispersity of 0.238. These conditions were chosen in order to produce heterogeneous gels with structure resembling arrested phase separation [26]. The large pressure jump across the oil-water interface due to surface tension renders the droplets

essentially undeformable under the conditions measured in this work (for the most extreme conditions studied here, we estimate a capillary number, $Ca < 10^{-4}$). We note that, in addition to the attractive interdroplet interactions produced by the thermosensitive PEGDA polymer, the droplets are stabilized by an anionic surfactant SDS which provides additional electrostatic repulsion. Based on our estimations, the screening length of electrostatics is approximately 0.8 nm for this sample, which is significantly less than the size of the polymer [1], and so the effect of electrostatics on the overall interparticle potential will be a quantitative (but not qualitative) change in the attractive minimum.

Figure 5.1 shows the hypothetical phase diagram for the nanoemulsion system [53]. It was previously measured the temperature dependence of the dilute pair potential using small angle neutron scattering [1]. A square well potential can quantitatively describe the

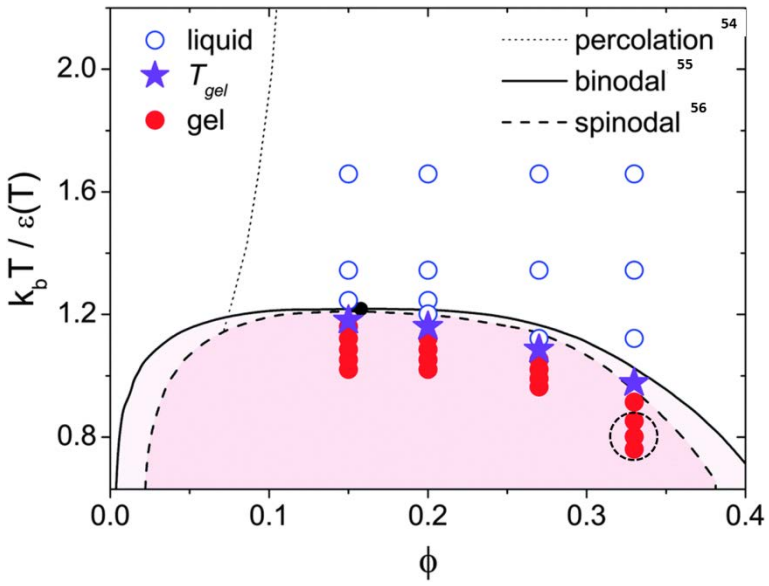

Figure 5.1 Hypothetical phase diagram for the nanoemulsion system. Lines indicate theoretical predictions [54-56] for the square well fluid with well depth ε and width λ = 0.5σ.

dilute structural factor in the nanoemulsions exhibiting colloidal gelation at elevated temperature. The nanoemulsions used in this study exhibit gelation due to arrested phase separation, resulting the bicontinuous network of a dense fractal-like phase and an unstructured dilute phase [26]. The sample used in this study is placed in the dotted circle in the phase diagram.

5.2.2 Thermoreheological characterization

Small amplitude oscillatory shear measurements were performed using an AR-G2 stress-controlled rheometer (TA Instrument) with a 60 mm, 2° upper-cone geometry and a Peltier temperature controlled lower-plate geometry. The sample was loaded at 25 °C and thermal rheology was performed by heating the sample from 25 °C to 55 °C at a rate of 1 °C min^{-1} with a strain amplitude of $\gamma_0 = 0.005$ and an applied frequency of $\omega = 20$ rad s^{-1}. Recently, we found that the long-time linear viscoelasticity of our nanoemulsion gels does not significantly depend on the heating rate applied for temperatures relatively close to the gel temperature [26], and so we believe our experiments probe thermal equilibrium of the sample. Frequency sweep measurements were performed over a range of 0.2–200 rad s^{-1} at a strain amplitude of $\gamma_0 = 0.005$ at 48 °C. A solvent trap with deionized water was used to prevent evaporation of the sample. The applied strain amplitude of $\gamma_0 = 0.005$ for the measurement was within the linear viscoelastic limit.

5.2.3 Large amplitude oscillatory shear (LAOS) measurements

All LAOS measurements were taken by Dimitri Merger and the method is described in Chapter 2. The sample was loaded at 25 °C in the liquid state and was gelled in the geometry by raising the temperature to 50 °C, which is well above the gel transition

temperature for this sample. Subsequently, a LAOS test was performed at a fixed frequency covering three decades in strain amplitude from the linear region until well after the yielding of the material ($10^{-3} < \gamma_0 < 1$). At least 9 oscillation cycles per amplitude were recorded. All LAOS experiments at different frequencies were always performed on a freshly loaded, gelled sample, and the linear viscoelastic moduli at a given frequency were reproducible between different loadings. This was done to ensure measurements on pristine gels.

The raw data were analyzed using a custom-written MATLAB routine in order to convert each wave of a certain frequency and strain amplitude to a complex spectrum. Since even harmonics were insignificantly small ($I_{2/1}<3\times10^{-3}$) in all measurements, only odd harmonics up to the 21st harmonic were used to reconstruct the waveforms [57] and further calculate the nonlinear measures to follow.

5.2.4 Rheo-USANS/SANS

Rheo-USANS/SANS measurements were performed to investigate yielding behavior in this system. General methods for rheo-USANS/SANS are described in Chapter 2. Samples were loaded in a geometry consisting of a 50mm inner diameter quartz cup and a 49mm diameter quartz rotating bob. A solvent trap wetted with 50/50 (v/v) H_2O/D_2O was used to inhibit evaporation of nanoemulsion samples. The quartz Couette cell was placed vertically with the incident beam in the radial direction, such that the collected SANS and USANS spectra were of projected structures in the flow-vorticity (1–3) plane.

For both SANS and USANS, transmission and scattering were measured for both the sample at various strain amplitudes as well as for the empty Couette cell, in accordance with standard methods for obtaining absolute scattering intensities [58]. Note that none of the measured SANS spectra showed any observable anisotropy, nor did supplementary rheo-

small angle light scattering (rheo-SALS) measurements under identical conditions (see Appendix C, figure C.1 and C.2).

Thermal rheology of the sample was measured using temperature ramp with a heating rate of 1 °C min^{-1} under small amplitude oscillatory shear with a strain amplitude of γ_0 = 0.001 and an angular frequency of ω = 10 rad s^{-1}. In order to ensure the yielding behavior of rheo-USANS/SANS sample is similar with that of LAOS sample, LAOS measurement was performed using an amplitude sweep from γ_0 = 0.002 to 0.5 at 48 °C and ω = 10 rad s^{-1}. Rheo-USANS/SANS measurements were performed using time sweeps at desired strain amplitudes from γ_0 = 0.003 to 50 at a frequency and temperature coinciding with LAOS measurements. It is important to note that this procedure produces time-averaged USANS/SANS data, resulting in strain-amplitude dependent scattering that is averaged over an entire LAOS cycle. In this case, time-resolved measurements of intracycle structure are unattainable due to the significant measurement times (typically several hours) currently required to obtain a single USANS spectrum. Therefore, the spectra at a given strain amplitude will be dominated by the particular intracycle microstructural processes which occupy a majority of a cycle.

5.3 Linear viscoelasticity

To investigate the yielding behavior of the nanoemulsion gel, we first measured the thermal rheology and frequency-dependent linear viscoelasticity of the sample. The nanoemulsions containing similar chemical composition exhibited an abrupt transition from a viscous liquid to a solid-like gel with increasing temperature [1]. To determine the gel transition temperature (T_{gel}), we measured the viscoelastic moduli (*G'*: storage modulus and

G": loss modulus) with increasing temperature from 25 °C to 55 °C at fixed strain amplitude of γ_0 = 0.005 and applied frequency of ω = 20 rad s^{-1} in Figure 5.2. We found that the gel transition temperature, T_{gel}, for this sample (approximately where $G' \sim G''$) is at 45 °C. In previous work, we showed that T_{gel} so defined is consistent with other measures of the gel point, including the criterion of Winter and Chambon ($G' \sim G'' \sim \omega^{1/2}$) [59] as well as the point at which the structure becomes percolated [1,26]. Above T_{gel}, the sample exhibits solid-like viscoelasticity with a plateau modulus G_p~20 kPa. For the frequency-dependent linear viscoelasticity above T_{gel}, we performed a frequency sweep at fixed temperature of T = 48 °C and strain amplitude of γ_0 = 0.005 (Figure 5.2(b)). The dynamic shear moduli depend only mildly on the frequency, in agreement with previous measurements [1].

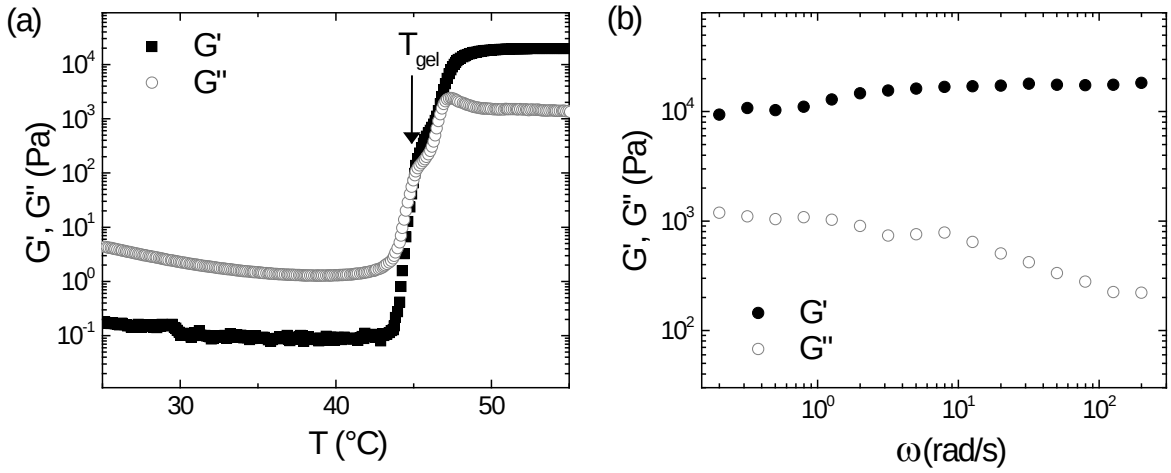

Figure 5.2 (a) Thermal rheology of the sample from 25°C to 55°C at γ_0 = 0.005 and ω = 20 rad/s. (b) Frequency sweep of the sample from 0.2 to 200 rad s^{-1} at 48°C at γ_0 = 0.005.

5.4 Yielding behavior during LAOS

We investigated the yielding behavior of the nanoemulsion gel using LAOS experiments at various strain amplitudes and angular frequencies. We begin by analyzing the linear Fourier coefficients, *G'* and *G"*, which are displayed in Figure 5.3 (a). The storage and loss moduli are well known to the general reader, and in older publications are often used to describe the material's behavior even beyond the linear regime [41]. For strain amplitudes $\gamma_0 > 0.01$, *G'* monotonically decreases from its linear plateau value and shows no frequency dependence within experimental variability. In contrast, *G"* displays a distinct peak at $\gamma_0 \sim 0.03$. Therefore, according to Hyun *et al*. [41], it can be classified as a "Type III" material, which displays a weak strain overshoot. Specifically, the fact that *G"* shows a maximum is known as the "Payne Effect" in the rheology of filled elastomers, where the

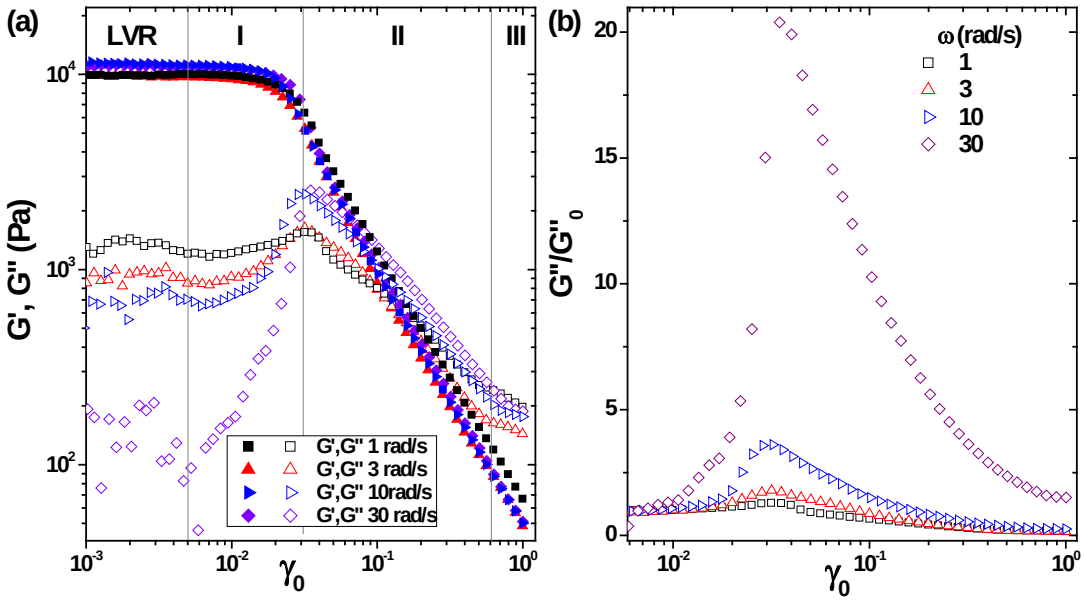

Figure 5.3 (a) Storage and loss moduli versus strain amplitude at various angular frequencies of deformation. Lines indicate the linear viscoelastic regime (LVR) and different regions of the yielding stages that will be discussed in a subsequent section. (b) Increasing peak height in the *G"* curve with increasing angular frequency as shown by the loss modulus normalized to the plateau value of the linear regime $G"_0$.

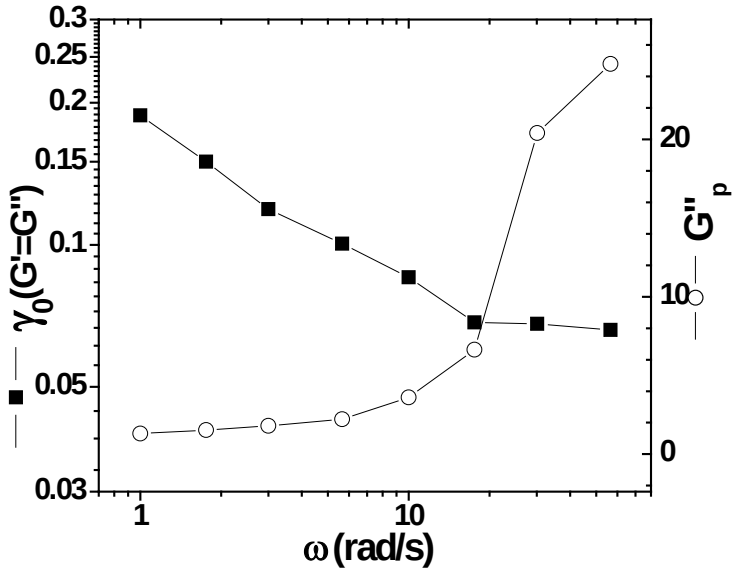

Figure 5.4 Frequency dependence of the strain amplitude at which storage and loss modulus cross (left axis), and the relative peak height of the loss modulus $G''_p = \max(G''/G''_0)$ (right axis).

maximum is associated with bond breaking between load-bearing elements [60]. The peak position does not change significantly when the angular frequency is increased, whereas the peak height increases dramatically, as shown more clearly by normalizing *G"* to its linear value G_0'' in Figure 5.3 (b) (intermediate frequencies have also been measured but are not displayed for clarity). The increasing peak height in *G"* causes the crossover of *G'* and *G"*, which is often regarded as the onset of yielding, to occur at smaller strain amplitudes for increasing ω. The peak heights and the crossover strains amplitudes are summarized in Figure 5.4. We note that the observed trend in peak height is opposite to that observed in glassy microgel suspensions with effective interparticle attractions [36], suggesting a qualitatively different yielding behavior.

We have defined three different regimes of yielding based on analysis of the nonlinear response (to be discussed subsequently) to aid in the presentation and analysis of

the data to follow, and find that this partition coincides with characteristic features of *G'* and *G"*. In Region I, *G'* exhibits a modest decrease from its value in the linear viscoelastic regime (LVR), whereas *G"* increases significantly toward its peak value. Region II begins at the maximum in *G"*, and continues through the crossover strain amplitude, ultimately asymptoting to power law behavior of *G'* and *G"* with increasing strain amplitude. In Region III, the power law slope of *G"* exhibits an observable decrease.

5.5 Nonlinear waveform analysis

5.5.1 Waveform reconstruction

The linear viscoelastic moduli *G'* and *G"* do not sufficiently describe the material's response beyond the linear regime due to the fact that the stress wave is no longer sinusoidal. Therefore we now examine the time-resolved stress signals and analyze the waveform using the Lissajous-Bowditch representation, where the stress is plotted versus the instantaneous strain or strain rate for the elastic or the viscous projection, respectively. Figure 5.5 shows a typical waveform response of the sample recorded at ω = 10 rad s^{-1} and γ_0 = 0.046 (corresponding to Region II). In all measurements the raw stress signal started to show a transient decay in amplitude as soon as the linear viscoelastic regime was exceeded ($\gamma_0 > 0.01$). This decay corresponds to slow intercycle thixotropic behavior or aging, and prevents the Lissajous-Bowditch curves from forming closed loops. Thixotropy is a common rheological feature of gel-like systems [61] and is therefore also present in LAOS experiments, in contrast to colloidal glasses, where a quasi-stationary state under LAOS can be reached almost immediately [46]. Since our measurements did not reach a quasi-

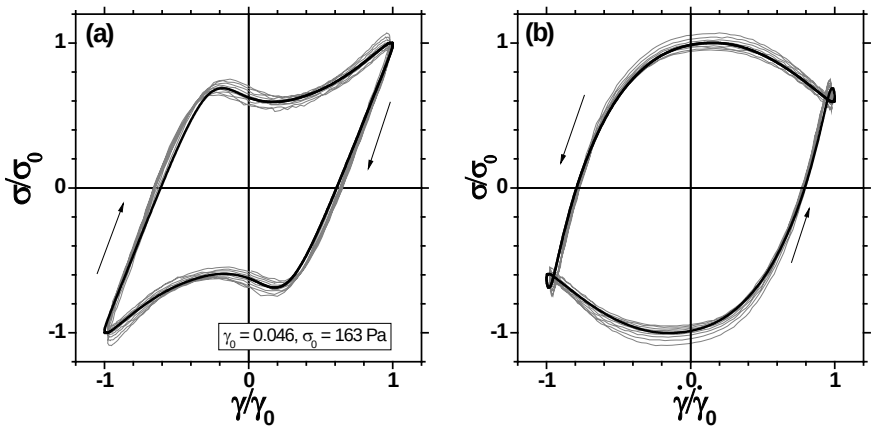

Figure 5.5 Normalized plots of stress versus (a) strain – elastic projection, and (b) shear rate – viscous projection recorded at ω = 10 rad s^{-1} and γ_0 = 0.046. The gray line represents the raw signal, whereas the black line shows the reconstructed signal averaged over eight cycles.

stationary state even after over 100 oscillation cycles for a specific set of ω and γ_0, data from only the first 8 cycles for each amplitude were used for analysis. The 8 cycles per amplitude have been decomposed to Fourier coefficients according to

$$\sigma(t) = \gamma_0 \sum_{n=1} [G_n^{'} \sin(n\omega t) + G_n^{''} \cos(n\omega t)] \quad (5.1)$$

Each representative cycle was thus reconstructed in the time domain using odd harmonics up to n = 21. Since all odd harmonics with n > 21 displayed relative intensities smaller than 0.1 %, we consider that all significant contributions to the stress have been taken into account. Even harmonics were negligible as $I_{2/1}$, which is the most prominent of them, was always below 0.3 % of the total signal and showed no time dependence. The reconstruction procedure is essentially a comb filter and all following waveform data represents an average over the intracycle transient behavior during a strain amplitude sweep. We caution that this procedure renders the later extracted nonlinear parameters to be time-dependent to some extent. However, the alternative of waiting for the sample to reach a

stationary oscillatory state is unfeasible due to the long measuring times, especially at low frequencies.

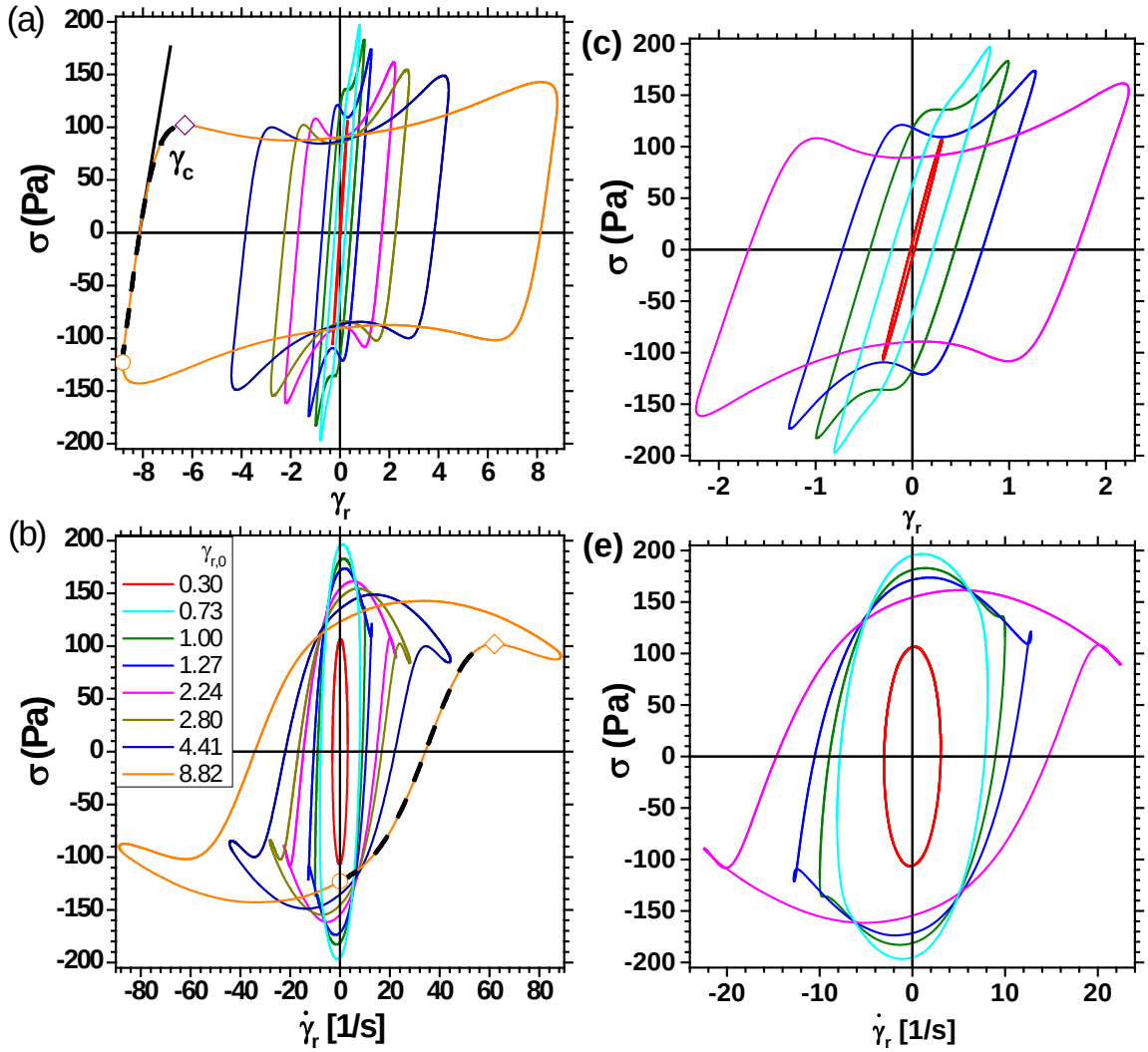

Figure 5.6 (a) and (b) show the elastic and viscous Lissajous-Bowditch plots of reconstructed time data from selected amplitudes at ω = 10 rad s^{-1}; odd harmonics up to n = 21 were used for the reconstruction. The strain and strain rate axes have been normalized by the strain amplitude of 0.0322 where *G"* is at its maximum ($\gamma_r = \gamma/0.0322$) in order to be able to compare them to the data of the SANS sample. The circle and diamond symbols show the points at flow reversal ($\gamma = -\gamma_0$ and $\dot{\gamma} = 0$) and the following local stress maximum, respectively. The broken black line illustrates the accumulated strain γ_c that is necessary to yield the material. The black tangent represents the residual modulus after yielding G_R (equals $d\sigma/d\gamma$ at $\sigma = 0$). (c) and (d) are magnifications of (a) and (b) and show the waveforms at low amplitudes ($0.3 < \gamma_{r,0} < 2.24$) in more detail.

In Figure 5.6 (a) and (c), we show the elastic and viscous Lissajous-Bowditch curves for strain amplitudes spanning Region I and Region II. Note that from now on, all strain axes have been normalized by the value of the strain amplitude where *G"* is at its maximum (in this case, $\gamma_r = \gamma/0.0322$), in order to be able to compare this data to the data of the SANS sample in a subsequent section. In Region I ($0.16 < \gamma_{r,0} < 1$, or $0.005 < \gamma_0 < 0.03$) a transition was observed, where the waveform transformed from a simple ellipse representing the linear response to a complex nonlinear shape. This transition is shown in detail in Figure 5.6 (c), (d) and is also reflected in the viscoelastic moduli in Figure 5.3 (a) by the strong increase of *G"*. Starting in Region II ($\gamma_{r,0} = 1$, or $\gamma_0 = 0.0322$), distinct features appear in the Lissajous-Bowditch curves, which persist qualitatively throughout the course of the ongoing strain amplitude sweep. These include an approximately linear region after the reversal of shear direction and a local maximum in the instantaneous stress in the upper left quadrant of the elastic representation. The quantitative changes in the waveform will be analyzed in the following section.

5.5.2 Nonlinear measures

5.5.2.1 Sequence of physical processes

Rogers et al. [43] recently suggested a framework for the analysis of LAOS data which tracks the intracycle features of the stress-strain-rate curve and associates them with a sequence of physical processes (SPP). We use this approach to rationalize the distinct waveform in our experiments by the following progression of events during one half cycle of the oscillation. Starting at the point where the flow direction is reversed ($\gamma/\gamma_0 = \pm 1$, circle symbol in Figure 5.6 (a)) the gel network of agglomerated droplets is strained, and the material initially behaves elastically and therefore the stress increases linearly with the

accumulated strain. This part of the cycle can be characterized by the instantaneous derivative of the stress with respect to the strain at the point of zero stress,

$$G_R = \left.\frac{d\sigma}{d\gamma}\right|_{\sigma=0} \quad (5.2)$$

which has been introduced by Rogers et al. [43] as the "cage modulus" for glassy colloidal systems. Since our material is a colloidal gel with a volume fraction where particle cages are not the significant structural unit, we will instead refer to this derivative as the residual modulus, G_R. Note that in the linear regime, G_R is identical to G'.

After the initial linear region, the stress continues to increase until a strain equal to γ_c has been accumulated (broken gray line), where it shows a local maximum γ_c (diamond symbol in Figure 5.6 (a)). We hypothesize that this overshoot in the stress curve is due to yielding of the gel network, and afterwards the sample begins to flow (this will be confirmed later). The stress subsequently decreases with further increasing shear rate until a minimum is reached. With further increasing strain, the stress begins to increase again, suggesting thixotropic behavior where the structure is gradually rebuilt as the shear rate is decreasing. This continues until the end of the half-cycle ($\gamma_r = +\gamma_{r,0}$, $\dot{\gamma} = 0$), and subsequently the sequence is repeated in the opposite direction.

5.5.2.2 Time dependent moduli

Based on the work of Rogers et. al. [42] , we further elucidate the intracycle yielding by calculating the instantaneous moduli $R'(t)$ and $R''(t)$. R'(t) and R''(t) are projections of the binormal vector in a 3D Lissajous-Bowditch plot (stress vs. strain vs. strain rate) onto the strain-stress and shear rate-stress plane. Details can be found in the work by Rogers *et. al.*

[42]. These measures can be interpreted as time-dependent analogues of *G'* and *G"* and are defined for every point of the response orbit. *R'* and *R"* for the strain amplitude sweep at ω = 10 rad/s are displayed as surfaces in Figure 5.7. If viewed in the *R'*, *R"* versus strain amplitude projection, Figure 5.7 is reminiscent of the standard representation of a dynamic strain amplitude sweep as in Figure 5.3 (a). In the LVR, *R'* and *R"* are constant in time and

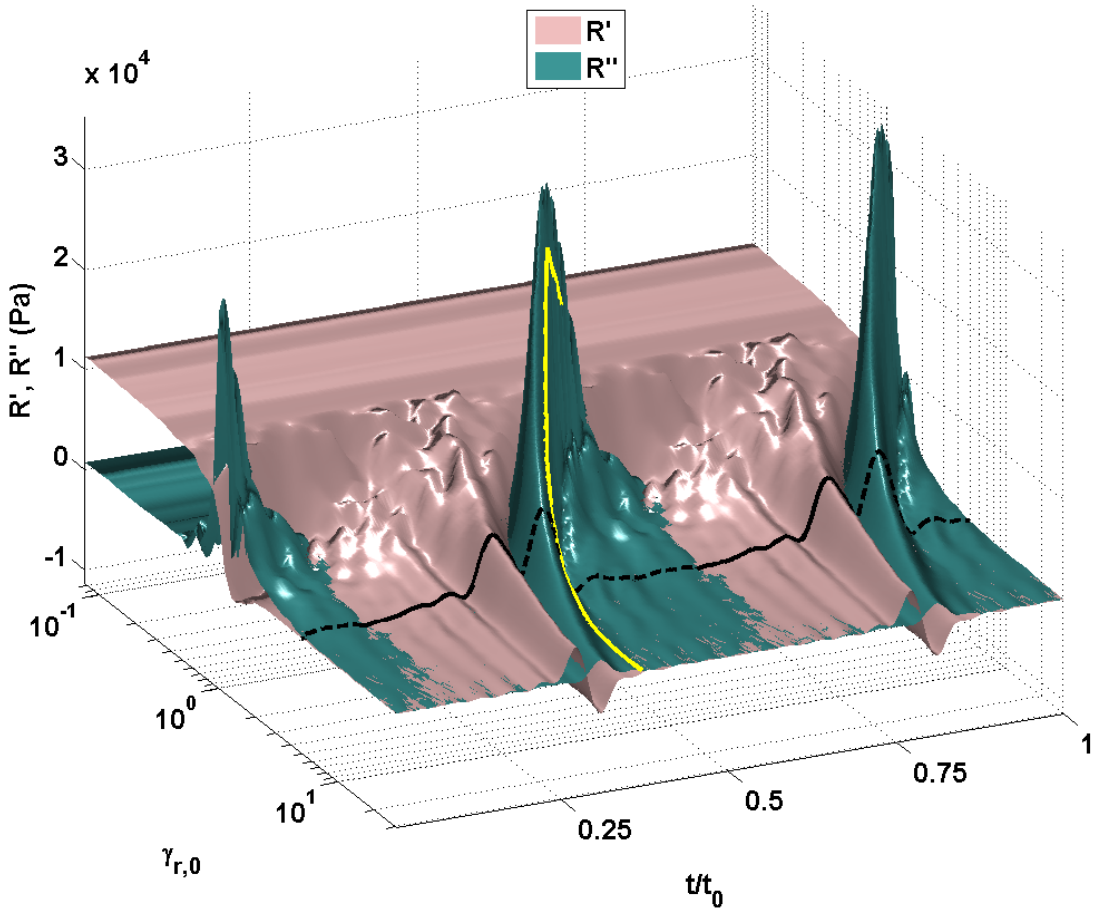

Figure 5.7 Surface plot of the instantaneous moduli R'(t) and R"(t) as a function of reduced strain amplitude $\gamma_{r,0}$ and normalized time throughout the oscillation cycle for a fixed frequency of 10 rad/s. A single LAOS cycle corresponds to a portion of the surface at fixed reduced strain amplitude, $\gamma_{r,0}$ and increasing time, t/t_0, where t_0 is the time of one cycle. This is indicated by the black line for $\gamma_{r,0}$ = 5 (solid for *R'* > *R"* and broken for *R'* < *R"*). The yellow line shows the yield point as determined from the local maximum in the Lissajous-Bowditch curve.

equal *G'* and *G"*, respectively. As the strain amplitude increases (moving from the back to the front in Figure 5.7), the response becomes nonlinear and distinct features develop in the time dependence of both surfaces. Looking at the time dependence at fixed strain amplitude, the sequence of physical processes that was described previously is evident. However, this analysis reveals additional details about the intracycle yielding that were not evident from the waveform analysis, where yielding was assumed to occur at a single point where the stress shows an overshoot.

The fully nonlinear material behavior can be observed by tracing the intracycle response at a fixed strain amplitude of $\gamma_{r,0} \sim 0.1$. The starting point of the sequence of processes (i.e. at the point of flow reversal), corresponds in this representation to $t/t_0 = 0.25$ or 0.75. Starting from this point in time, elastic straining is first observed, where *R'>R"* and both moduli are roughly constant in time. As the cycle proceeds, this gives way to a small region in which *R'* increases (i.e., strain stiffening occurs). We find that the maximum value of *R'* for each strain amplitude is higher by about 30% than G_R but has the same strain amplitude dependence (only G_R will be used subsequently). Shortly after this, *R'* abruptly decreases (i.e., strain softening occurs) and *R"* abruptly increases, until eventually *R"* exceeds *R'*. Since this portion of the cycle still corresponds to strains in the region of the waveform where the stress is increasing nearly linearly with strain, we attribute this behavior to elastoplastic behavior, in which the deformation is first dominated by softening (*R' > R"*), followed by viscoplastic behavior (*R" > R'*). After this, a pronounced maximum in *R"* is observed, which corresponds closely (though not exactly) with the stress maximum in the Lissajous-Bowditch curve used previously to define the yield stress and strain (yellow line in Figure 5.7). At this point, the material has yielded and begins to flow. Subsequently,

both *R'* and *R"* decrease dramatically, indicating shear thinning, after which rejuvenation of the structure can be observed as a second crossover in *R'* and *R"* that occurs at $t/t_0 < 0.75$, before the end of the half-cycle.

Using the prominent features of the *R'* and *R"* landscapes in Figure 5.7 and the position of the yield point from Figure 5.6, we produce a "phase plot" for the yielding process in Figure 5.8 in a space of the normalized instantaneous strain (a) or strain rate (b), which represent the time within a cycle, and strain amplitude. Lines have been drawn that represent the various features of *R'* and *R"*, including the initial maximum in *R'*, followed by the crossover where *R' = R"*, and finally the maximum in *R"*. Also shown is the yield point defined by the stress maximum extracted from the Lissajous-Bowditch curves. The regions in between these curves thus show the boundaries in a nonlinear deformation space between elastic straining (A), elastoplastic softening (B), viscoplastic behavior (C), yielding (D) and flow (E). Note that after yielding only flow und restructuring are present as the shear rate decreases back to zero, and therefore the aforementioned transitions do not occur in the reverse direction. Accordingly, Figure 5.8 is not a true phase plot as all borders indicate "one-way" transitions. The filled symbols represent borders for the path from $\gamma/\gamma_0 = -1$ to $\gamma/\gamma_0 = 0$, whereas open symbols show borders for the path from $\gamma/\gamma_0 = 1$ to $\gamma/\gamma_0 = 0$.

Both the surface plots in Figure 5.7 and the borders in Figure 5.8 show that with increasing strain amplitude, the portion of the cycle where the material is yielded (both in time and in shear rate dimension) increases. This supports the idea that information averaged over the entire oscillation cycle with increasing strain amplitude, such as the time-averaged neutron scattering data to follow, increasingly reflects the yielded state. This is shown in Figure 5.8 by overlaying the boundaries of Regions I, II and III obtained from intercycle

analysis of the waveforms (vertical lines) with the phase plot obtained from intracycle analysis. In doing so, we find that Region I is dominated entirely by elastoplastic softening of the gel network, i.e. the entire cycle is spent in phases A and B. In Region II, the behavior transitions from becoming elastically-dominated to viscous-dominated with increasing strain amplitude, i.e., the fraction of the cycle spent in the flowing state increases with increasing strain amplitude. Finally, in Region III, the fraction of each cycle spent in flow becomes insensitive to the applied strain amplitude.

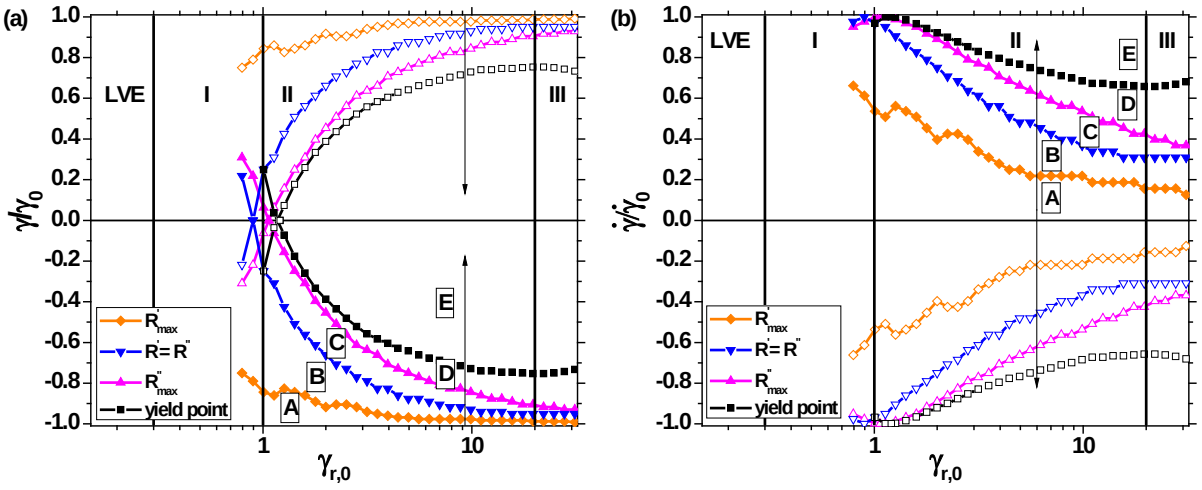

Figure 5.8 Phase plot constructed using the various nonlinear parameters from the waveform analysis in the (a) elastic and (b) viscous representations, respectively. Starting from γ/γ_0 = 1 or -1 ($\dot{\gamma}/\dot{\gamma}_0$= 0) the material's response changes following the arrow through a series of elastic (A), elastoplastic softening (B), viscoplastic responses (C), yielding (D), and finally flow (E). Note that after yielding only flow und restructuring is present, therefore these transitions do not occur in the reverse direction as the shear rate is reduced to zero. Filled symbols represent borders for the path from γ/γ_0 = - 1 to γ/γ_0 = 0, and open symbols show borders for the path γ/γ_0 = 1 to γ/γ_0 = 0.

5.5.2.3 Time dependent moduli

Based on the work of Rogers et. al. [42] , we further elucidate the intracycle yielding by calculating the instantaneous moduli *R'*(*t*) and *R"*(*t*). *R'*(t) and *R"*(t) are projections of the binormal vector in a 3D Lissajous-Bowditch plot (stress vs. strain vs. strain rate) onto the strain-stress and shear rate-stress plane. Details can be found in the work by Rogers *et. al.* [42]. These measures can be interpreted as time-dependent analogues of *G'* and *G"* and are defined for every point of the response orbit. *R'* and *R"* for the strain amplitude sweep at ω = 10 rad/s are displayed as surfaces in Figure 5.7. If viewed in the *R'*, *R"* versus strain amplitude projection, Figure 5.7 is reminiscent of the standard representation of a dynamic strain amplitude sweep as in Figure 5.3 (a). In the LVR, *R'* and *R"* are constant in time and equal *G'* and *G"*, respectively. As the strain amplitude increases (moving from the back to the front in Figure 5.7), the response becomes nonlinear and distinct features develop in the time dependence of both surfaces. Looking at the time dependence at fixed strain amplitude, the sequence of physical processes that was described previously is evident. However, this analysis reveals additional details about the intracycle yielding that were not evident from the waveform analysis, where yielding was assumed to occur at a single point where the stress shows an overshoot.

The fully nonlinear material behavior can be observed by tracing the intracycle response at a fixed strain amplitude of $\gamma_{r,0} \sim 0.1$. The starting point of the sequence of processes (i.e. at the point of flow reversal), corresponds in this representation to $t/t_0 = 0.25$ or 0.75. Starting from this point in time, elastic straining is first observed, where *R'*>*R"* and both moduli are roughly constant in time. As the cycle proceeds, this gives way to a small region in which *R'* increases (i.e., strain stiffening occurs). We find that the maximum value

of *R'* for each strain amplitude is higher by about 30% than G_R but has the same strain amplitude dependence (only G_R will be used subsequently). Shortly after this, *R'* abruptly decreases (i.e., strain softening occurs) and *R"* abruptly increases, until eventually *R"* exceeds *R'*. Since this portion of the cycle still corresponds to strains in the region of the waveform where the stress is increasing nearly linearly with strain, we attribute this behavior to elastoplastic behavior, in which the deformation is first dominated by softening (*R' > R"*), followed by viscoplastic behavior (*R" > R'*). After this, a pronounced maximum in *R"* is observed, which corresponds closely (though not exactly) with the stress maximum in the Lissajous-Bowditch curve used previously to define the yield stress and strain (yellow line in Figure 5.7). At this point, the material has yielded and begins to flow. Subsequently, both *R'* and *R"* decrease dramatically, indicating shear thinning, after which rejuvenation of the structure can be observed as a second crossover in *R'* and *R"* that occurs at $t/t_0 < 0.75$, before the end of the half-cycle.

Using the prominent features of the *R'* and *R"* landscapes in Figure 5.7 and the position of the yield point from Figure 5.6, we produce a "phase plot" for the yielding process in Figure 5.8 in a space of the normalized instantaneous strain (a) or strain rate (b), which represent the time within a cycle, and strain amplitude. Lines have been drawn that represent the various features of *R'* and *R"*, including the initial maximum in *R'*, followed by the crossover where *R' = R"*, and finally the maximum in *R"*. Also shown is the yield point defined by the stress maximum extracted from the Lissajous-Bowditch curves. The regions in between these curves thus show the boundaries in a nonlinear deformation space between elastic straining (A), elastoplastic softening (B), viscoplastic behavior (C), yielding (D) and flow (E). Note that after yielding only flow und restructuring are present as the

shear rate decreases back to zero, and therefore the aforementioned transitions do not occur in the reverse direction. Accordingly, Figure 5.8 is not a true phase plot as all borders indicate “one-way” transitions. The filled symbols represent borders for the path from $\gamma/\gamma_0 = -1$ to $\gamma/\gamma_0 = 0$, whereas open symbols show borders for the path from $\gamma/\gamma_0 = 1$ to $\gamma/\gamma_0 = 0$.

Both the surface plots in Figure 5.7 and the borders in Figure 5.8 show that with increasing strain amplitude, the portion of the cycle where the material is yielded (both in time and in shear rate dimension) increases. This supports the idea that information averaged over the entire oscillation cycle with increasing strain amplitude, such as the time-averaged neutron scattering data to follow, increasingly reflects the yielded state. This is shown in Figure 5.8 by overlaying the boundaries of Regions I, II and III obtained from intercycle analysis of the waveforms (vertical lines) with the phase plot obtained from intracycle analysis. In doing so, we find that Region I is dominated entirely by elastoplastic softening of the gel network, i.e. the entire cycle is spent in phases A and B. In Region II, the behavior transitions from becoming elastically-dominated to viscous-dominated with increasing strain amplitude, i.e., the fraction of the cycle spent in the flowing state increases with increasing strain amplitude. Finally, in Region III, the fraction of each cycle spent in flow becomes insensitive to the applied strain amplitude.

5.5.2.4 Strain amplitude-dependence of nonlinearity

In order to compare our results with previous work on yielding colloidal systems [44,46,62-64], we will rely on the definitions for the yield strain, the yield stress and the residual modulus established by Rogers *et al*. [43] to quantify the changes in the waveform with increasing amplitude (Figure 5.6). Additionally, we show the intensity of the third harmonic normalized to the fundamental, $I_{3/1}$, as it has been used frequently in other studies

of colloidal systems to describe the deviation from the linear regime [44,45,65,66]. In order to follow the changes in the flowing part of the oscillation cycle throughout the strain amplitude sweep, we furthermore monitor the instantaneous viscosity $\eta_L = \sigma_L/\dot{\gamma}_L$ at the point of maximum shear rate.

In the linear regime ($\gamma_{r,0} < 0.16$), G_R coincides with *G'*, as expected for a linear material that shows predominantly elastic behavior and the nonlinear parameters γ_c and σ_c are not defined as the Lissajous curves are elliptical. In the weakly nonlinear Region I ($0.16 < \gamma_{r,0} < 1$), the waveform's distortion from an ellipse becomes visible which is accompanied by an increasing intensity of the normalized third harmonic $I_{3/1,}$ but the overall distortion is still small ($I_{3/1} \leq 0.1$) and the stress does not yet show the local maximum (in a mathematical sense) that is associated with intracycle yielding here. Therefore, γ_c and σ_c are still not defined and G_R remains almost constant but is not equal to *G'* anymore due to mild nonlinear softening.

Upon entering Region II ($\gamma_{r,0} > 1$) the waveforms begin to exhibit the characteristic yield point, where γ_c and σ_c can now be observed as a function of strain amplitude. The yield strain γ_c, indicated by the broken line in Figure 5.8 (b), is approximately constant for a small range of strain amplitudes. Therefore, the strain required to yield the material makes up only a small portion of the total strain that can be acquired by an elastic material within one half-cycle ($2\gamma_{r,0}$). Afterwards, γ_c increases sublinearly throughout Region II, approaching a linear increase in strain amplitude ($\gamma_c \approx 0.25\ \gamma_{r,0}$) entering Region III. This behavior is quite different from what Rogers *et al.* [43] and van der Vaart *et al.* [47] observed with colloidal glasses; both found a power law behavior of $\gamma_c \propto \gamma_0^{0.2}$ for glassy suspensions. Van der Vaart *et al.* [47] also presented a more complex dependence of γ_c on γ_0 for a glassy suspension of

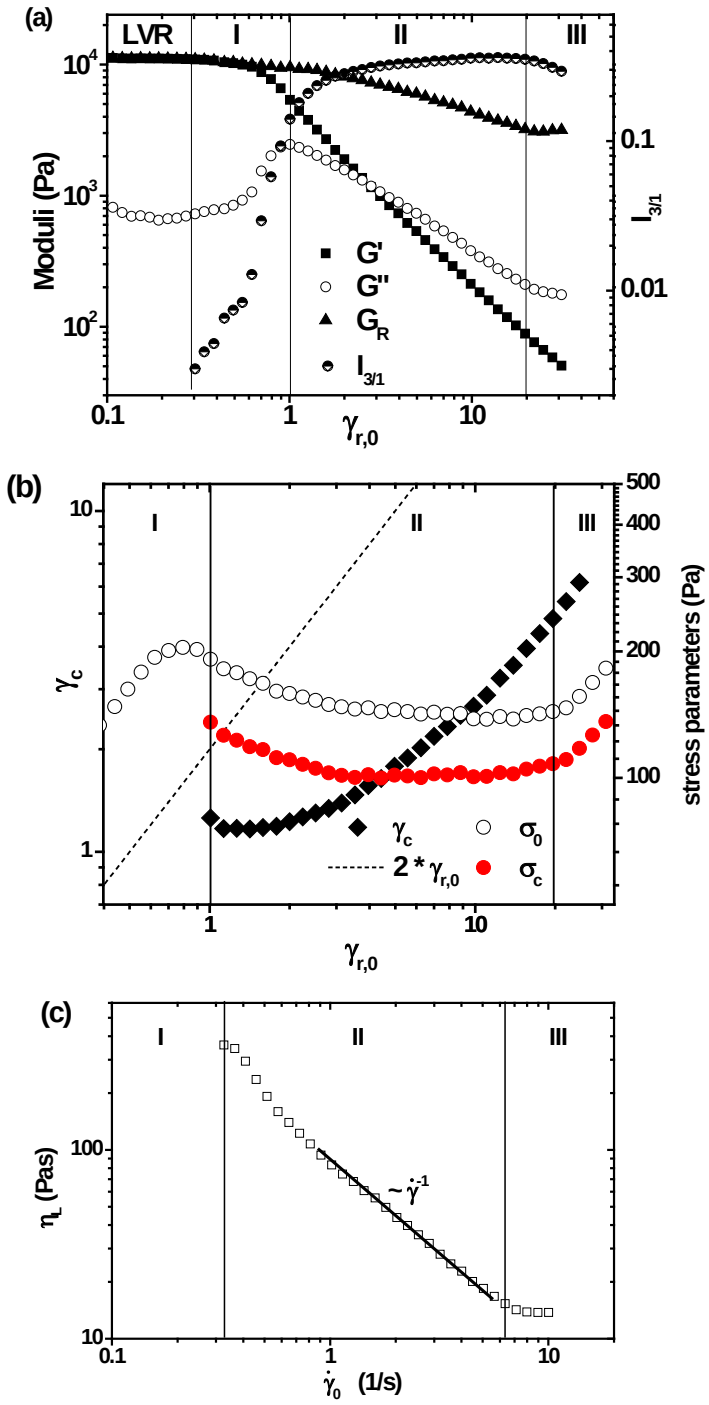

Figure 5.9 (a) Residual modulus G_R (equals dσ/dγ at σ = 0) together with the storage and loss modulus at ω = 10 rad/s and the relative intensity of the 3rd harmonic $I_{3/1}$. (b) Normalized nonlinear yielding parameters extracted from the waveform data of the LAOS measurements: γ_c represents the strain that has been accumulated between the point of flow reversal (circle symbol) and the local stress maximum (diamond) in Figure 5.6 (a) and the corresponding stress value σ_c with the stress amplitude σ_0 as reported by the rheometer software. (c) Instantaneous viscosity at the point of zero strain and maximum shear rate as a function of increasing shear rate amplitude.

soft spheres, which was more similar to our findings. This deviation from the power law might therefore be an indication of the soft character of the subunits in both systems, which would be cages of soft particles in their case and compressible droplet clusters in our case. Nevertheless, the increase of the yield strain itself is a clear deviation from the constant yield strain of a Bingham material and remains unexplained so far.

The yield stress σ_c in Region II is found to decrease initially and shows roughly the same trend as the overall stress amplitude σ_0, their ratio being $\sigma_c/\sigma_0 \approx 0.75$. Furthermore, G_R continuously decreases to roughly a third of its initial value. η_L exhibits shear thinning, i.e. a decrease with increasing shear rate. The shear thinning of η_L (Figure 5.9 (c)) follows a power law with an exponent of -1 over the largest portion of this region, which corresponds to the extreme shear thinning common in yield stress fluids, with a stress that is independent of the shear rate [67].

In Region III (for $\gamma_{r,0} > 20$), both the yield strain and stress increase linearly with strain amplitude ($\gamma_c \approx 0.25\ \gamma_{r,0}$) and the other nonlinear parameters reach their high strain amplitude limiting behaviors with $G_R/G_0 \approx 0.15$, $\sigma_c/\sigma_0 \approx 0.75$ and $\eta_L = 14$ Pa·s.

5.5.3 Frequency dependent nonlinearity

To examine the frequency dependence of the yielding processes in the sample, we measured the waveforms at a fixed value of $\gamma_{r,0}$ at various frequencies in the range from 0.1 to 56.55 rad/s. The waveform at a specific amplitude is distinctively frequency dependent, as can be seen in Figure 5.10, where waveforms for $\gamma_{r,0} = 1$, 2.8 and 20 are shown (corresponding to the beginning, middle and end of Region II). With increasing frequency, the Lissajous-Bowditch curves become more box-shaped and the local stress minimum in

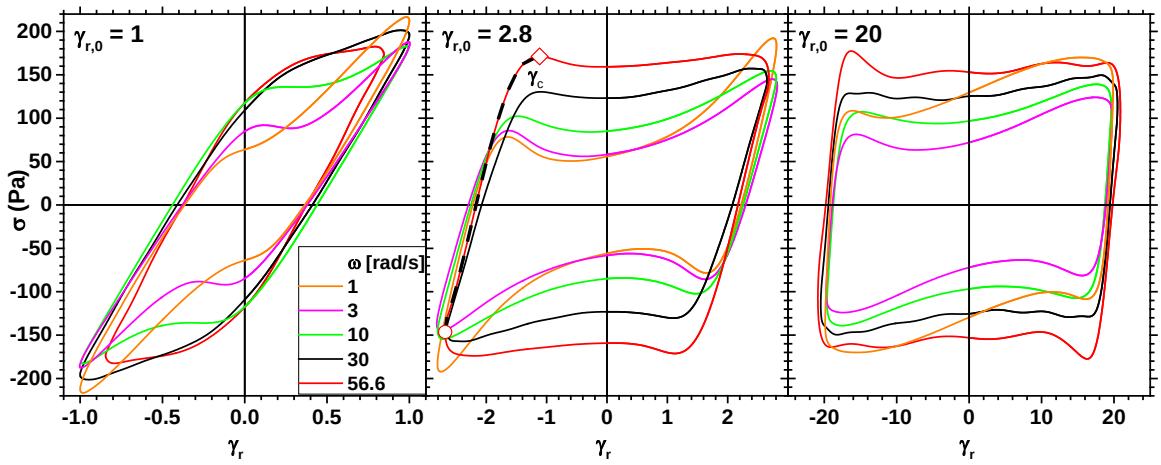

Figure 5.10 Elastic Lissajous-Bowditch plot of reconstructed waveforms measured at different angular frequencies at γ_r values of 1, 2.8 and 20. The circle and diamond symbols shown for $\gamma_{r,0}$ = 2.8 denote the points at flow reversal (γ = - γ_0 and $\dot{\gamma}$ = 0), the local stress maximum.

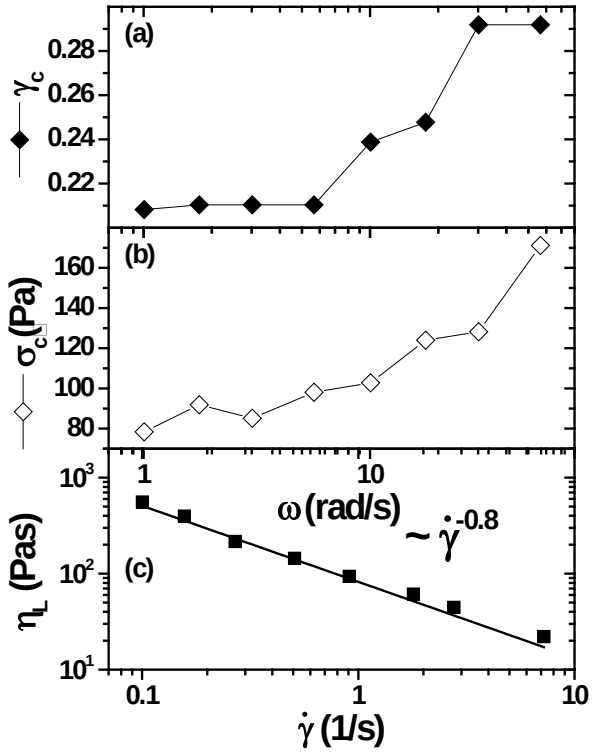

Figure 5.11 Nonlinear yielding parameters as a function of angular frequency at $\gamma_{r,0}$ = 2.8 (center panel in Figure 5.9): (a) γ_c is the strain that has been accumulated from flow reversal to the local stress maximum, (b) local stress maximum σ_c, (c) instantaneous viscosity at the point of zero strain and maximum shear rate as a function of the instantaneous shear rate at that point, which is increasing with increasing angular frequency.

the vicinity of the shear rate maximum (γ_r = 0) becomes less prominent. At the highest amplitudes and frequencies (right panel) a second local minimum in the stress appears which follows the first one. This feature is not an artifact of the data processing as it is present also in the raw data and was furthermore observed by other researchers [45,66].

The waveform parameters for γ_r = 2.8 are displayed in Figure 5.11 and show the trends of the waveform evolution more clearly. With increasing ω the normalized local yield stress, σ_c / σ_0 increases. The accumulated strain at which yielding occurs, γ_c, first shows a plateau for ω < 6 rad/s and then increases afterwards. Figure 5.11 (c) shows the dependence of the instantaneous viscosity η_L as a function of shear rate. As previously shown in the strain amplitude dependent waveform analysis, increasing the shear rate leads to shear thinning in the flowing portion of the oscillation cycle ($\eta_L \sim \dot{\gamma}^{-0.8}$). In this case we keep the strain amplitude constant and the increasing angular frequency causes higher shear rates (see Appendix C, Figure C.3 for a Pipkin diagram). The fact that the shear thinning exponent varies depending on whether the strain amplitude or frequency is varied violates the so-called “Delaware Rutgers rule” [68], further suggesting thixotropic behavior in the sample.

5.6 Rheo-USANS/SANS

5.6.1 Comparison rheology between different geometry

In order to understand the origins of the broad yielding behavior and rationalize the observed nonlinear mechanical response, we performed combined rheo-SANS/USANS measurements under LAOS deformation at a number of applied strain amplitudes spanning Regions I, II, and III. We note that the sample used for these measurements constituted a separate batch of the fluid. Although the two batches have the same composition, we found

differences in the linear moduli between the two batches (~ 50%), as well as in the strain amplitude where the maximum in *G"* occurs (~ 60%). In these nanoemulsions, such batch-to-batch variations are common due to the sensitivity of the viscoelasticity of the gels to unavoidable small differences in size distribution [1].

To compare the rheology between the two samples in the quartz Couette geometry used during the scattering experiments and the sandpaper cone-plate geometry from the LAOS experiments, we thus normalize the moduli by the linear value of *G'* in Figure 5.12. On these normalized scales, we find no significant differences between the two samples at both low and high strain amplitudes, including Regions II and III. Furthermore, the normalized values of *G"* are nearly identical over the entire range of measurement,

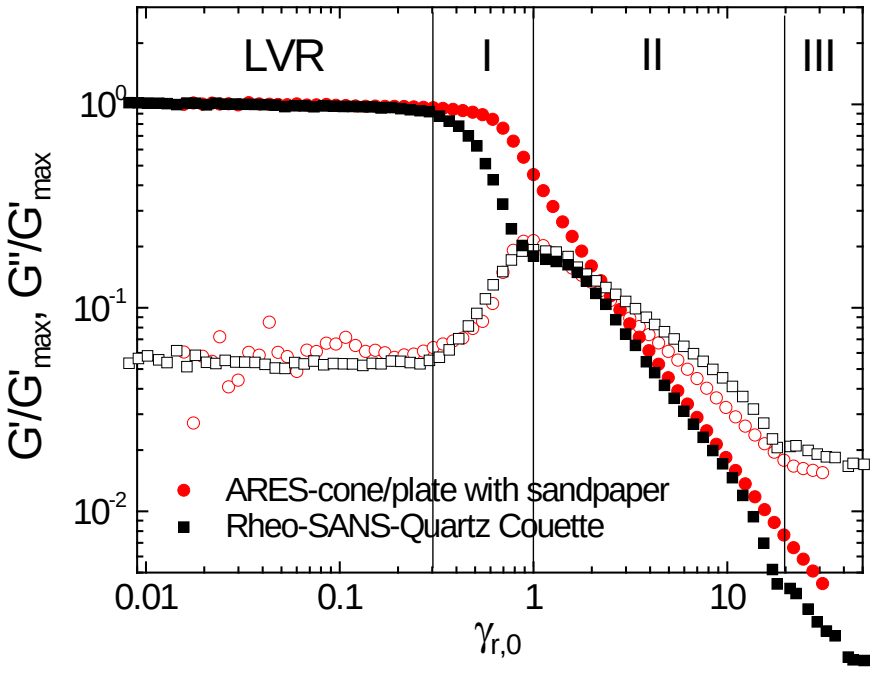

Figure 5.12 Large amplitude oscillatory shear (LAOS) rheology of two different samples containing ϕ = 0.33 PDMS droplets with an aqueous continuous phase of 33 vol.% PEGDA and C_s = 230 mM SDS at 48°C used in LAOS measurement (red) and rheo-USANS/SANS measurement (black). G'/G'_{max} (closed symbols) and G''/G'_{max} (open symbol) at ω = 10 rad/s versus $\gamma_{r,0}$ through the yielding transition.

suggesting that the modest batch-to-batch differences in linear viscoelasticity do not significantly alter the nonlinear viscoelasticity of the material aside from a systematic shift in moduli. However, we do find a discrepancy in the values of *G'* in Region I, with *G'* exhibiting a significant decrease in the non-linear regime. We believe that this is an artifact due to wall slip in the quartz Couette geometry, since the observed behavior is qualitatively similar to that measured in the cone-plate geometry without sandpaper (see Appendix C, Figure C.4). Thus, we conclude that the observed yielding behavior is identical in Regions II and III, but not in Region I. Therefore, rheo-SANS/USANS measurements in Region I were kept to a minimum, and only used to compare with the quiescent microstructure.

5.6.2 Rheo-USANS/SANS spectra

Figure 5.13 shows the combined rheo-USANS and SANS spectra at various normalized strain amplitudes. The scattering vector is presented here as qr, where r is the droplet radius, in order to emphasize the length scales involved in units of the number of particles. In previous work, we performed detailed studies of the quiescent microstructure of this sample composition through the gel transition [26]. In brief, the high-q data ($qr > 1.47$) are well-described by polydisperse (~20%) spherical droplets with long-range attractive interactions due to the presence of the polymer in the continuous phase [26]. The low-q data ($qr < 1.47$) are well described by a combination of two structural features. The first, appearing at moderate length scales (1-20r), is a fractal microstructure consisting of droplet clusters, and is signified by a power-law decay of the coherent scattering intensity, ($I(q) - I_b$), over a significant q-range, where $I(q)$ and I_b are the measured total and incoherent background intensities, respectively. The second, appearing at larger length scales (~100r), is a spatially correlated bicontinuous structure of droplet-lean (containing primarily solvent)

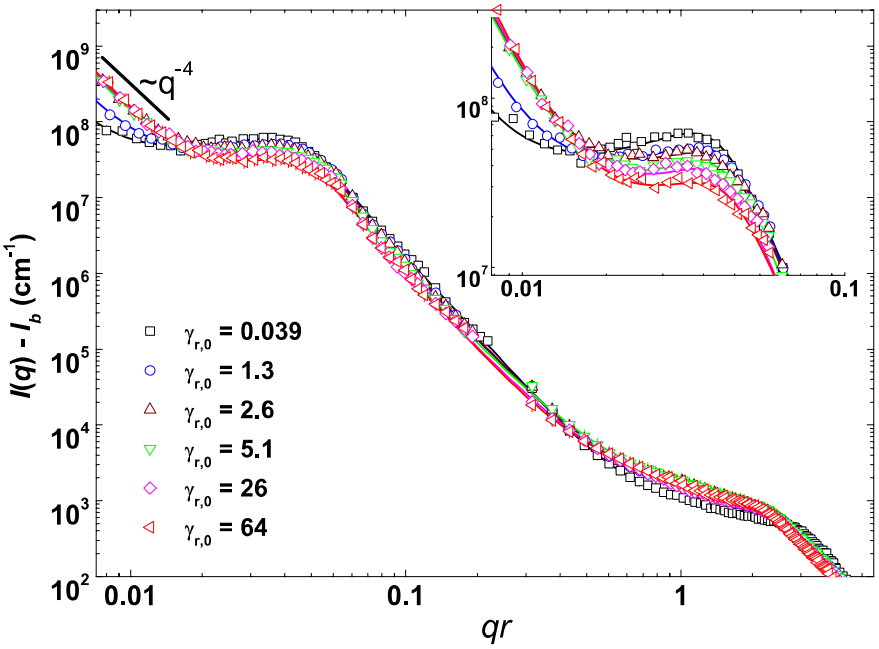

Figure 5.13 Combined rheo-USANS and SANS spectra of nanoemulsion sample containing ϕ = 0.33 PDMS droplets with 33 vol. % PEGDA and C_s = 230 mM SDS in 50/50 (v/v) H_2O/D_2O at the normalized strain amplitudes indicated. Lines are fits to equation (5.3). Inset: Magnification of low-q portion of USANS data with model fitting.

and droplet-rich domains (containing the fractal cluster microstructure) reminiscent of arrested spinodal decomposition. The significant feature of the bicontinuous structure is a local maximum in intensity at $q = \beta_{max}$, such that β_{max}^{-1} represents the characteristic distance between domains in the bicontinuous structure. This structure is consistent with the observed scattering for the present sample in the quiescent state.

Upon increasing the strain amplitude into the nonlinear regime, the scattering spectra exhibit several important differences from the quiescent microstructure. First, in the very low-q regime (qr < 0.011), a significant upturn in low-q scattering is observed, which increases with increasing strain amplitude and follows power-law behavior according to $(I(q) - I_b) \sim q^{-4}$. Such scaling is consistent with Porod scattering from porous media due to

the surface of large length-scale inhomogeneities (henceforth referred to as “voids”). Second, the low-q peak ($qr \sim 0.03$) decreases in intensity with increasing strain amplitude, suggesting that the corresponding spacing between dense domains decreases. It is important to note that the high-q scattering corresponding to individual droplets does not exhibit significant changes with increasing strain amplitude, suggesting that for this range of amplitudes the local droplet microstructure is relatively insensitive to the incipient yielding process. However, there is a modest shift in the high-q shoulder originally occurring at $qr \sim 2.73$, corresponding to the diameter of the droplets. Further analysis shows that this shift is due to slow coarsening of the droplets due to Ostwald ripening, which is unavoidable at the elevated temperatures of these measurements, and continues even after cessation of shear (see Appendix C, Figure C.5). Specifically, the entire shift in the high-q shoulder would correspond to a 15% increase in droplet size if it were entirely due to coarsening, which is quantitatively consistent with previously measured rates of Ostwald ripening in this system [1].

5.6.3 Insights into the microstructural process by model fitting

To further understand the strain amplitude dependence of these new features in the low-q scattering, we fit the data to a model combining three primary contributions to the structure: (i) a low-q contribution to capture the Porod scattering, (ii) a model for off-critical phase separation at moderate q-values to capture the local maximum due to bicontinuous structure, and (iii) a high-q contribution due to the fractal cluster microstructure (note that we have chosen not to include the higher-q scattering due to individual droplets):

$$I(q)-I_b=\frac{K_1\xi_{c1}^3}{\left(1+(q\xi_{c1})^2\right)^2}+\frac{K_2\left[\dfrac{\xi_{c2}}{1+\left(q-\beta_{\max}\right)^2\xi_{c2}^2}-\dfrac{\xi_{c2}}{1+\left(q+\beta_{\max}\right)^2\xi_{c2}^2}\right]}{\left(\beta_{\max}q\right)}$$
$$+\frac{K_3\sin\left[\left(d_m-d_s+2\right)\operatorname{atan}\left(\xi_s q\right)\right]}{\left(\xi_s q\right)\left[1+\left(\xi_s q\right)^2\right]^{\frac{d_m-d_s+2}{2}}}+\frac{K_4\sin\left[\left(d_m-1\right)\operatorname{atan}\left(\xi_m q\right)\right]}{\left(d_m-1\right)\left(\xi_m q\right)\left[1+\left(\xi_m q\right)^2\right]^{\frac{d_m-1}{2}}} \quad (5.3)$$

where K_1, K_2, K_3 and K_4 signify the relative contribution of each term to the total scattering. The first term is a two-phase Debye-Bueche model [69] to describe the large-scale voids, where ξ_{c1} is their correlation length. The second term is a summation of two Lorentzian terms corresponding to correlated density inhomogeneities consistent with phase separation under the Cahn-Hilliard model for spinodal decomposition [70], which captures both the peak and its sharpness. The wavelength $\beta_{\max}^{-1}$ is associated with the position of the peak, and the correlation length ξ_{c2} is associated with a presumed exponentially decaying length scale for density fluctuations. From this, the sharpness of the peak can be quantified by the product of $\xi_{c2}\beta_{\max}$, which signifies the breadth of the size distribution of domains about $\beta_{\max}^{-1}$. The third and fourth term correspond to a model for combined surface and mass fractal scattering, respectively [71]. The mass fractal, which dominates at high q-values, has associated dimension d_m and cutoff size ξ_m. Likewise, the surface fractal, which dominates at relatively low q-values, has dimension d_s and cutoff size ξ_s. The scattering spectra obtained for all normalized strain amplitudes are well-fit by the combined model (Figure 5.13, solid lines), and the best fit values of all model parameters are shown in Table 5.1.

Table 5.1 Best fit model parameters of rheo-USANS/SANS data to equation (5.3)

$\gamma_{r,0}$	K_1 (cm^{-1})	ξ_{c1} (μm)	K_2 (cm^{-4})	ξ_{c2} (μm)	β_{max} (μm^{-1})	K_3 (cm^{-1})	d_s	ξ_s (μm)	K_4 (cm^{-1})	d_m	ξ_m (nm)
0.039	8.88×10^{-4}	947	1.49×10^{21}	1.25	1.80	3.81×10^{6}	1.81	0.354	1.37×10^{3}	1.83	15.2
1.286	1.74×10^{-3}	707	1.41×10^{21}	1.20	1.88	5.28×10^{6}	1.89	0.531	1.77×10^{3}	1.69	15.3
2.569	3.35×10^{-3}	554	1.35×10^{21}	1.17	1.89	4.14×10^{6}	1.96	0.532	1.78×10^{3}	1.70	14.6
5.139	3.24×10^{-3}	545	1.17×10^{21}	1.21	1.91	4.51×10^{6}	2.10	0.628	1.58×10^{3}	1.68	12.5
25.694	3.49×10^{-3}	539	9.30×10^{20}	1.29	1.89	6.91×10^{6}	1.90	0.577	2.24×10^{3}	1.69	22.5
64.234	3.22×10^{-3}	456	8.67×10^{20}	1.18	1.92	4.10×10^{6}	1.97	0.460	3.58×10^{3}	1.88	26.6

Unfortunately, we find that fit values of the void correlation length ξ_{c1} are unphysically large due to the absence of any shoulder or plateau in the extremely low-q scattering (i.e. the *q*-dependent term in the denominator is much greater than unity, and so ξ_{c1} only contributes to the relative intensity of the Porod scattering, and can be absorbed into K_1). Instead, we resort to asymptotic analysis of the voids by calculating the specific surface area in the Porod regime. Assuming that the droplet-rich domains contain a homogeneous density of droplets at length scales corresponding to the Porod scattering, model-independent asymptotic analysis in the Porod limit yields [72]

$$\Sigma = \frac{\lim_{q\to o}\left(I(q)q^4\right)}{2\pi(\Delta\rho)^2} \quad (5.4)$$

where Σ is the specific surface area of the voids, and $\Delta\rho$ is the difference in scattering density between the void phase (assumed to contain no droplets) and the droplet-rich region. We assume that the droplet-rich domains contain a volume fraction of droplets, ϕ, consistent with the observed value of d_m, i.e., $\phi \sim 0.5$ for 33 vol.% oil. We note that the proportional trend of Σ is independent of the precise value of the droplet concentration. The calculated

strain amplitude-dependent values of Σ are plotted Figure 5.14 (a). Except for the lowest strain amplitude, other measurements are in the Porod limit at very low-q and fitted well. In Region I ($\gamma_{r,0} < 1$), Σ increases mildly with increasing strain amplitude. In Region II, Σ exhibits a significantly more pronounced increase, until strain amplitudes close to the onset of Region III, at which point it saturates. We note that the reduced strain amplitude at which Σ saturates ($\gamma_{r,0} \sim 4$) is similar to the point at which a number of the nonlinear yielding measures ($I_{3/1}$, γ_c and σ_c) also saturate.

In this context, the Porod scattering represents a two-phase system, where one "phase" consists of voids and the other consists of the bicontinuous gel structure. If we assume the interfacial profile between the void phase and the gel phase is strain amplitude-independent, Σ can thus be thought of as representing the overall density of voids in the system, which grows continually through Regions I-III. Since presumably the droplets remain at fixed overall number density, this necessitates that the volume of the network phase must decrease as Σ increases, i.e., the network phase must be compressed.

This compression can only occur in the bicontinuous structure if the correlation length between domains, β_{max}^{-1}, decreases continually in the same fashion. Looking at the strain amplitude dependence of β_{max}^{-1} (Figure 5.14 (b)), we find that this is indeed the case, with the domain size decreasing significantly over the same range in which Σ increases significantly. At the same time, the quantity $\xi_{c2}\beta_{max}$, corresponding to the sharpness of the distribution of domain sizes in the bicontinuous phase, increases significantly in Region II before exhibiting a clear maximum precisely at the onset of Region III. This suggests that, in

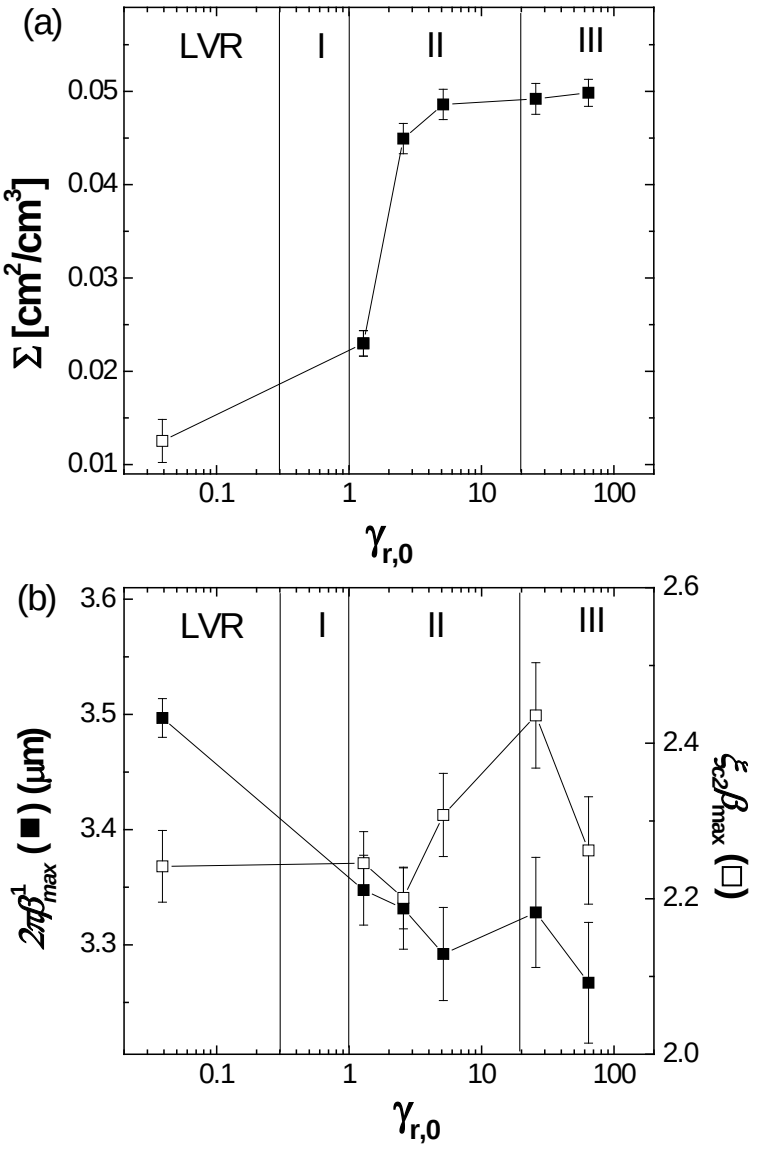

Figure 5.14 (a) Specific surface area from the Porod-regime at very low-*q*. (b) Characteristic length scale of the microphase separation (closed squares) and the peak sharpness (open squares) from the model (ω = 10 rad s^{-1}).

Region II, domains of fractal clusters become homogenized until the end of the yielding process, at which point they become more polydisperse.

We can gain further insight into the interplay of the void structures and the bicontinuous network phase by examining the correlated scaling of Σ and β_{max}^{-1}. Consider a case in which the bicontinuous phase is compressed isotropically, i.e., both the droplet-rich and droplet-poor regions compress equally and thus $\beta_{max}^{-1} \sim \gamma_{r,0}^{-1}$, in order for the voids to expand. Note that such a case is unlikely, since the fractal clusters are compressible, whereas the suspending medium to a first approximation is not. Nevertheless, from conservation considerations, we thus find that for the case of isotropic compression of the gel phase, $\beta_{max}^{-1} \sim \Sigma^{-3/2}$, i.e. a plot of β_{max}^{-1} versus Σ will yield a power law exponent of -3/2. If we further assume that the density of the droplet-poor regions in the gel phase is the same as the density of the voids, then deviations of the power law exponent from -3/2 mean that the different domains comprising the gel phase are compressed differentially, with a negative deviation (exponent < -3/2) signifying a greater degree of compression of the droplet-rich domains and a positive deviation (exponent > -3/2) signifying a greater degree of compression of the droplet-poor domains.

Figure 5.15 shows a plot of the decrease in the correlation length for the gel phase with increasing specific surface area of the voids. This empirical correlation is fit to a power law relationship, $2\pi\beta_{max}^{-1} = A + B\Sigma^{c}$, where the constant A is necessary to capture the observed behavior in Figure 5.14, where both Σ and β_{max}^{-1} saturate at sufficiently large strain amplitude. The resulting best-fit exponent of c = -2.2 ± 0.6 is significantly smaller than -3/2, suggesting that the growth of the voids corresponds to a greater degree of compression within the droplet-rich regions, which is expected due to the compressibility of the fractal microstructure of the droplet clusters.

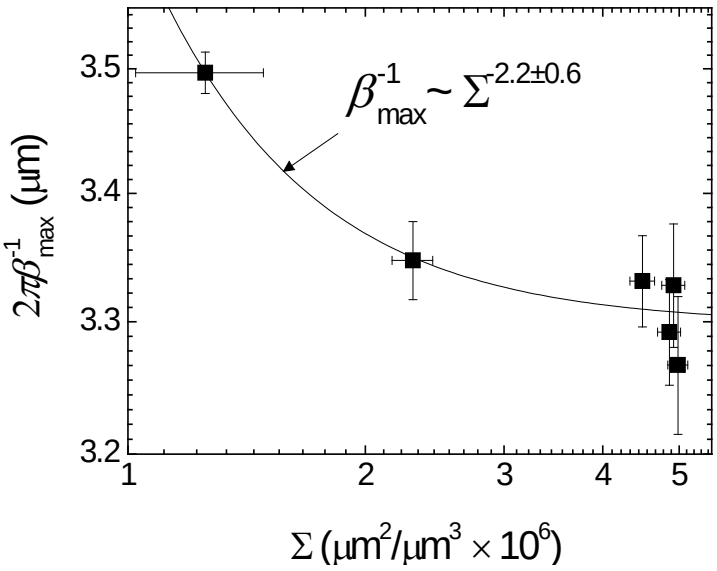

Figure 5.15 Scaling of domain size with specific surface area. Line gives the best fit to a power law relationship.

5.7 Discussion

5.7.1 Compariosn with previous studies of yielding

In previous sections provide a detailed explanation of the broadened, "two-step" yielding of heterogeneous colloidal gels under LAOS deformation. Specifically, the intracycle oscillatory response in the nonlinear regime can be rationalized as a sequence of elastic straining, elastoplastic thinning, and flow that occurs over each half cycle, with the proportional contributions of each process to the total cycle evolving during the yielding transition (Figure 5.3). The intracycle yielding process is marked by overshoots in both *R"* and the instantaneous stress, and is reminiscent of the peaks observed in the average elastic stress with increasing strain amplitude [35,36]. Interestingly, a recent study on colloidal gels of microgel beads above the repulsive glass transition gelled by electrostatic screening found a qualitatively different nonlinear response [36], although the waveforms were not quantitatively analyzed. Specifically, in their case, no intracycle stress overshoot was

observed, and the waveform resembled a distorted ellipse throughout the full strain amplitude sweep and therefore waveform analysis was not considered further. We note that this distorted ellipse is similar to that observed in waveforms during yielding of concentrated colloidal glasses, and so one might expect that yielding of a gel formed from an initially repulsive glass.

As so far no further waveform data on yielding gels is available, we compare our results to studies of other solid-like colloidal systems, mostly repulsive glasses. It appears that many glassy suspensions display a rather boxlike waveform at high deformations in the elastic Lissajous-Bowditch representation that is absent of or displays only a very weak stress overshoot [44,46,47,62-64] furthermore confirmed this using micromechanical simulations. The processes responsible for this behavior are similar to our case: elastic straining, yielding and flow. However, a qualitative difference lies in the structural units comprising the elastic network of the material; in the case of glasses, elasticity arises from entropic caging of individual particles, whereas in the case of gels it arises from a percolated network of adhesive structures. We hypothesize this explains the contrasting waveform behavior between gels and glasses, i.e., the plastic flow region after yielding of most glasses exhibits a stress that is almost independent of the strain, whereas our gels exhibit a stress overshoot with a subsequent local minimum after which the stress increases again. However, qualitatively similar waveforms to ours were observed by van der Vaart *et al.* [47] investigating a glass of soft particles, although in contrast to our study no stress minimum followed the yield point.

With regards to the microstructural processes leading to yielding, we note that most studies to date argue for a scenario in which yielding is dominated by processes occurring at

the particle scale, such as the bond rupture and cage breakage hypothesis [35,36,40]. Indeed, previous experimental and theoretical studies of yielding in attractive systems have focused almost exclusively on particle-scale structural metrics, such as the average contact number of particle clusters [39,40,73] or the thermal rupture forces of pairs or small chains of particles [8]. We note that such metrics appear to only provide an adequate description of microstructural changes significantly after yielding, e.g. at strains corresponding to hundreds or thousands of times the yield strain [39,40]. By contrast, we observe significant microstructural processes at strains near or slightly above the yield strain that manifest at length scales corresponding to thousands or even millions of particles, with surprisingly little change in the particle-scale microstructure. As such, we hypothesize a mechanism for broadened yielding that differs significantly from those put forth in studies where only the mechanical response of the gel was measured under LAOS deformation.

5.7.2 Hypothesized microstructural processes during yielding

The results of rheo-SANS/USANS measurements suggest that, as the intracycle mechanical response becomes progressively more dominated by the yielded and flowing states, the microstructure of the gel evolves at progressively smaller length scales (Figure 5.13). We note that, due to the time-averaged nature of the SANS/USANS measurements, the changes in microstructure observed with increasing strain amplitude represent a moving average over the various dynamic stages of nonlinear behavior indicated by Figure 5.3. As such, the amount of time per cycle spent in the yielded state will increase with increasing strain amplitude, and thus the measured time-average microstructure will evolve toward the fully flowing state. Therefore, in what follows, we will assume that the contribution of each of the instantaneous microstructural processes to the overall, time-averaged scattering is

proportional to the time per cycle spent in a particular stage of nonlinear behavior. Time-dependent intracycle rheo-USANS measurements, which are currently infeasible due to unrealistically long measurement times, would be required to test this assumption. However, since intracycle structural rearrangements have already been observed for other soft matter systems [50,74] by neutron or x-ray scattering experiments with sufficiently high temporal resolution, our assumption is a fairly safe one.

The proposed time-averaged, strain-amplitude dependent structure is depicted in Figure 5.16. In the linear regime, the microstructure is comprised of a bicontinuous network of droplet-lean "pores" and droplet-rich network strands (middle panel), the latter of which

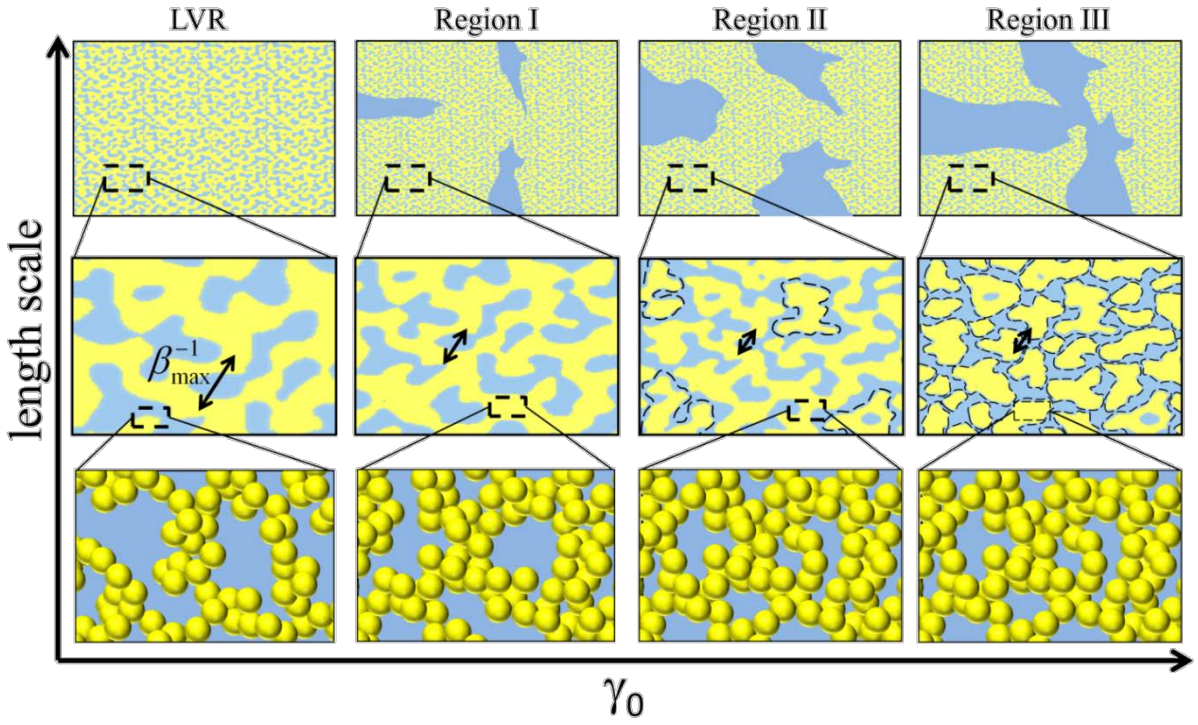

Figure 5.16 Schematic of time-averaged gel microstructure through the various regimes of yielding: (bottom) Fractal clusters of droplets (yellow) with diameter *D*. (middle) Bicontinuous network structure consisting of droplet-lean (blue) and droplet-rich (yellow) domains on the length scale of 10-100 *D*. (top) Macroscopic structure at a length scale of 100-1000 *D*.

are comprised of fractal clusters of droplets (bottom panel). The bicontinuous structure exhibits a domain size proportional to $\beta_{\max}^{-1}$. Upon increasing the strain amplitude into the nonlinear regime, nonlinear deformation causes compression of the network due to compressibility of the droplet-rich domains. This results in the formation of voids at length scales significantly larger than the domain size (top panel), as evident by the significant Porod scattering that develops in Region I, which then saturates in Region II. Such voids are reminiscent of those observed in other gelling systems after yielding under startup of steady shear [40], and could be a pre-cursor for the shear-induced macroscopic heterogeneities that subsequently develop at large strains. In order to conserve the overall density of droplets, these voids must form at the expense of the bicontinuous structure, resulting in compression of the network and a decrease in $\beta_{\max}^{-1}$ (middle panel). As previously discussed, this requires significant compression of the fractal droplet-rich domains relative to the droplet-lean domains (Figure 5.13), which in turn requires yielding of the dense phase. As the strain amplitude is increased further, the compression of the dense network becomes increasingly difficult, resulting in eventual saturation of both the voids and the domain size in Region II.

Once the void structures saturate, additional strain input becomes sufficient to rupture the effective "bonds" between network strands, producing discrete agglomerates of fractal clusters (middle panel, dotted lines). The primary signature of this process is the observed increase in the sharpness of the distribution of domain sizes, given by the product $\xi_{c2}\beta_{\max}$. This occurs because the most likely size of an agglomerate formed by rupturing of the bicontinuous network will have a characteristic size given by the characteristic domain size. As such, any irregular network strands will be annealed into smaller, disconnected domains with an average size given by $\beta_{\max}^{-1}$. This concept could be viewed as similar to that

put forth by Hsiao et al. [39], who proposed that the yielding of shear-rejuvenated colloidal gels under step strain was dominated by the rupture of weak network contacts with a small average contact number. However, it should be noted that in our material it is rupture of contacts between network strands, rather than individual particles, that is responsible for yielding.

Eventually, at a critically high strain amplitude, enough bonds between domains will be ruptured in order to compromise the integrity of the network, resulting in (on average) a suspension of disconnected domains with a relatively narrow size distribution around β_{max}^{-1}, similar to what has been observed on colloidal gels at much larger strains after yielding is complete [40]. It is notable that the peak sharpness $\xi_{c2}\beta_{\max}$ exhibits a maximum precisely at the onset of Region III, suggesting that the distribution of domain sizes is most homogeneous at the final transition to flow. Previously, we observed a similar maximum during the incipient gelation of bicontinuous nanoemulsion gels that corresponded precisely with the critical gel point measured by rheology [26]. We hypothesized that such a maximum in homogeneity is a distinct signature of percolation of heterogeneous gels, and similar observations have been made in other gelling colloidal systems exhibiting phase separated microstructure [7]. It is thus tempting to consider that the final stage of yielding in the present study arises from "de-percolation" of the bicontinous gel network into a suspension of disconnected clusters. However, we do not discount the possibility that this common signature, i.e., a maximum in homogeneity of the network at both the critical gel point and the point at which *G'* and *G"* obtain their terminal scaling, is merely a coincidence.

We stress that the preceding is a time-averaged description of the gel microstructure, which is averaged over the sequence of processes (elastoplastic straining, yielding and flow) comprising one LAOS half-cycle. In reality, it is reasonable to expect that the intracycle structure will exhibit a continuous transition between the various average microstructures depicted in Regions I-III. Indeed, we will implicitly consider this to be true in order to rationalize the observed time-dependent nonlinear mechanical response with the observed time-averaged microstructure in what follows.

5.7.3 Relation between microstructure and nonlinear mechanical response

5.7.3.1 Regimes of yielding

Our LAOS measurements have identified three distinct regimes of yielding in heterogeneous colloidal gels, where three qualitatively different intracycle responses are observed. We now present a comprehensive scenario by which the time-averaged microstructures observed for each of these regions can be reconciled with the nonlinear mechanical signatures observed during LAOS. We stress again that this scenario implicitly assumes that the time-averaged microstructure can be seen as a convolution of the instantaneous microstructures during the various intracycle processes (the elastic strain softening, viscoplastic behavior, yielding and flow indicated by Figure 5.8). As such, in Region I the observed microstructure is dominated by that during the elastic response, in Region II it evolves from primarily structures dominated by elastoplastic behavior to structures dominated by flow, and finally in Region III it is dominated by flow.

5.7.3.1.1 Linear viscoelastic region ($\gamma_{r,0} < 0.3$)

At sufficiently small strain amplitudes the network structure of the material is only slightly perturbed by the shear forces, such that the gel network remains intact and the

imposed strain produces a linear, predominantly elastic stress response, as can be seen by the storage modulus being over an order of magnitude higher than the loss modulus.

5.7.3.1.2 Region I: Onset of nonlinearity and pre-yielding ($0.3 < \gamma_{r,0} < 1$)

In this regime, we hypothesize that internal rupture and reconfiguration of bonds between clusters within the dense domains (ultimately resulting in compression of the gel network) weakens the elastic network due to nonlinear plastic deformation, resulting in intracycle strain softening. This is evidenced by a moderate decrease in G_R from its plateau value, as well as a decrease in *R'* from its linear value in this region. Furthermore, $I_{3/1}$ begins to increase with increasing strain amplitude in this regime, signaling the onset of nonlinear behavior, as visible distortions of the waveform from its elliptical shape appear and *R'* and *R"* begin to show significant intracycle variations. Moreover, the compression of the dense domains requires the expulsion and drainage of interstitial fluid within the fractal microstructure in order to create additional large voids. This fluid motion causes a strong increase in the dissipated energy, which is evident in both the significant increase in *G"* as well as the development of significant viscous behavior in the nonlinear waveform (corresponding to an increase in *R"* in the middle of the half-cycle). The structural changes which are responsible for the nonlinear mechanical behavior of the gel mark this part of the strain sweep as a transition region to the highly nonlinear region II.

5.7.3.1.3 Region II: broad yielding transition ($1 < \gamma_{r,0} < 20$)

In this region, the most important yielding process occurs: the large-scale, dense domains of fractal agglomerates are compressed even stronger than in Region I (Figure 5.14(a)). As the network structure is gradually disintegrated by the breakup of large dense

domains during flow, the number of elastic junctions in the percolated structure that can be reformed at the end of a half-cycle is decreasing, as evident in the significant softening in G_R (Figure 5.9 (a)). This has severe consequences for the rheological properties. Due to the decreasing number of elastic junctions, the amount of elastic strain that the material can accumulate within the oscillation cycle is increasing slower than the applied strain amplitude. This is reflected in the intracycle response by the emergence of a catastrophic decrease of *R*' and subsequent increases and maxima in *R"* that appear at sufficient strain, signifying the onset of yielding. It is also reflected in the specific nonlinear measures of the yield point, including a sublinear increase of the yield strain with increasing strain amplitude and marked decrease in G_R (Figure 5.9 (a)), proving a drastic weakening of the reversible network. In the flowing portion of the cycle, we observe a shear rate amplitude thinning behavior that is caused by the breakage of larger dense domains into smaller ones, resulting in the thixotropic behavior observed during the flowing portion of the intracycle response as a non-monotonicity in the waveform (Figure 5.6 (c)). This process homogenizes the domain size distribution and leads to an increase in the peak sharpness, $\xi_{c2}\beta_{\max}$. It is important to note that the flowing portion of the response occurs well before the crossover in *G'* and *G"*, even though this is often used to define the yield point of the gel. This highlights the need for intracycle interpretations of LAOS in order to better characterize the yielding process.

5.7.3.1.4 Region III: post-yielding flow ($\gamma_{r,0} > 20$)

For even higher strain amplitudes, the process of domain rearrangement and breakdown that is predominant in Region II is completed. From this point on, all of the intracycle measures we consider, including the transitions between various intracycle processes as well as the residual modulus G_R, become independent of strain-amplitude, and

the intracycle yield strain and stress show a linear increase with strain amplitude. Thus, in every half-cycle only a small fraction of the applied strain is recovered by the elasticity of the network, and the mechanical response in this region is dominated by the yielded structure. The remaining strain is acquired through flowing of the now-suspended agglomerated domains. With the number of recoverable bonds between the dense domains minimized, the increasing strain amplitude results in further breaking of cluster-cluster bonds, but now within the suspended domains, and therefore some of the domains decrease in size even further. Thus the domain size distribution is broadened it this region, which is evident from a decrease of $\xi_{c2}\beta_{\max}$.

5.7.3.2 Frequency Dependence

The frequency-dependent mechanical measurements clearly indicate that the yielding process is not only strain amplitude-dependent but strain rate amplitude-dependent, as the yield strain and yield stress at a fixed strain amplitude increase with increasing frequency. We thus attribute the frequency dependence of the nonlinear waveform measures to the dominant structural processes, i.e., the internal rupture and compression of dense fractal domains and the corresponding formation of large fluid voids. As discussed above, these processes require the expulsion of a significant amount of fluid from the interstices of the fractal droplet aggregates. Therefore, it is reasonable to expect poroelastic effects to play a significant role. Since current models for poroelastic flow [75,76] do not take viscoplastic deformation of the solid network into account, we cannot make direct theoretical comparisons to our data. However, the trends we observe in our LAOS measurements, including the increase in the maximum of *R"* and the increase in normalized yield stress with increasing frequency are consistent with an increase in the viscous stress due to a

resistance to drainage of fluid from the porous gel phase into the void phase under compression [77].

To demonstrate this, we estimate the time scale for drainage of the voids based on Darcy's law for the flow of fluid in a porous material, which gives as the characteristic drainage time

$$t_{drain} \sim \frac{\mu L_c^2}{k_{abs}\sigma} \quad (5.5)$$

where μ is the fluid's viscosity (in this case of the continuous phase, ~ 6 mPa·s), k_{abs} is the hydraulic permeability, σ is the hydraulic stress (on the order of the yield stress, ~ 100 Pa), and L_c is the characteristic length scale for drainage, which we assume to be on the order of the size of the bicontinuous domains (~1-10 μm). We estimate the permeability from a model for flow through a fractal porous medium [78],

$$k_{abs} \sim \frac{d^2}{72}\frac{\phi^3}{(1-\phi)^2 \tau^2} \quad (5.6)$$

where $d \sim 2\pi\beta_{max}^{-1}$ is the average pore size, ϕ is the volume fraction of pores, and τ is the tortuosity of the fractal pores. Assuming that the dense phase of the bicontinuous network comprises an attractive glass (~60% by volume droplets), then we estimate $\phi \sim 0.45$ and $\tau \sim 1.5$.

Using these characteristic values, we obtain a drainage time of t_{drain} ~ 0.01-0.1 s. Thus, at low frequencies, including that probed by rheo-SANS/USANS, the characteristic time for formation and relaxation of voids is much smaller than the cycle time, and so the hydrodynamics arising from drainage of fluid required to form the voids will not contribute

significantly to the intracycle response. However, above a critical frequency where $t_{drain}\omega/2\pi \sim O(1)$, the suspending medium will begin to contribute a significant viscous contribution to the stress due to hydrodynamic resistance to drainage during yielding. This is entirely consistent with the observed increase in the yield stress with increasing frequencies above ~20 rad/s, and in fact this frequency is consistent with the preceding argument ($t_{drain}\omega/2\pi \sim 0.3$).

At high frequencies, these trends ultimately manifest in qualitative changes in the waveform, as the initially pronounced stress overshoot is gradually smoothed out and the waveform becomes box-shaped, similar to the results obtained from experiments on colloidal glasses. We attributed this behavior to the time-averaged structure in Region III, i.e. homogenized, suspended domains at relatively high effective volume fraction dominated by the flowing portion of the cycle. It is thus reasonable to expect that the waveform at high frequencies becomes reminiscent of the cage structure in colloidal glasses, since the suspended clusters can experience caging in the same manner as a repulsive glass, though at a much larger length scale due to the resistance to drainage of fluid between cluster domains.

5.8 Conclusion

This chapter has elucidated the detailed nonlinear mechanical response and microstructural processes underlying LAOS yielding of a concentrated colloidal gel with heterogeneous microstructure. We find that broad or so-called “two step” yielding in concentrated gels can be linked to two dominant microstructural process, where the initial

yield strain amplitude (at which intracycle flow is initially observed) coincides with internal rupture and compression of dense fractal domains, and the strain amplitude signifying the completion of yielding (where the intracycle yielding and flow processes saturate) results from breakage and suspension of dense clusters. At moderate frequencies, this results in three regions of yielding with increasing strain amplitude. In Region I, the bicontinuous gel structure is only weakly perturbed, and the nonlinear waveform can be described by an elastoplastic intracycle strain softening of the residual gel network. In Region II, the dense phase undergoes significant compression-mediated viscoplastic rupture of fractal domains, resulting eventually in a sequence of intracycle yielding and flow. In this region, significant frequency dependence is also observed, which we hypothesize is due to poroelastic flow of fluid from the dense domains into newly formed fluid voids at large length scales. Ultimately, the rupture of fractal domains at sufficiently high strain amplitudes results in degradation of the network, eventually causing suspension of fractal clusters in Region III. This results in a relatively "simple" intracycle yielding response in the flowing state, where the residual nonlinear elastic modulus, yield stress, and recoverable strain all become independent of the applied strain amplitude.

From our analysis, it is clear that traditional interpretations of the linearized moduli G' and G" are insufficient to describe yielding. As such, we have identified a number of nonlinear rheological measures relevant to the yielding of colloidal gels, including a "phase map" for intracycle yielding determined by the instantaneous moduli R' and R". This allows for more specific parameterization of the yielding material, including a residual modulus characterizing the remaining elasticity of the network, a yield stress and strain characterizing the yield point, and a local viscosity during the flowing portion of the strain cycle

reminiscent of that observed in steady shear measurements. Such measures could easily be applied to the analysis of LAOS measurements on other colloidal gels, including those with both homogeneous and heterogeneous microstructure. Comparing these measures across different compositions and material systems could provide more complete exploration of the differences between various types of gels (dilute versus concentrated, homogeneous versus heterogeneous, etc.). In the case of the dense, heterogeneous gels formed in the present system, the yielding process is clearly both strain amplitude and rate-dependent.

Perhaps most importantly, we have identified large-scale microstructure, on the order of hundreds or even thousands of particles, to be critical in determining the important processes governing yielding in heterogeneous colloidal gels. Our results call for expanded studies that examine the effects on fluid microstructure of a number of variables not explored here (most pressing of which being the rate dependence of the applied deformation), as well as new experiments and models that can access these length scales in a time-dependent, intracycle fashion in order to more directly connect microstructure with various nonlinear mechanical signatures of yielding.

References

[1] M. E. Helgeson, S. E. Moran, H. Z. An, and P. S. Doyle, Nature materials **11**, 344 (2012).

[2] C. Gallegos and J. Franco, Current opinion in colloid & interface science **4**, 288 (1999).

[3] R. Mezzenga and P. Fischer, Reports on Progress in Physics **76**, 046601 (2013).

[4] N. Doshi, G. Cinacchi, J. Van Duijneveldt, T. Cosgrove, S. Prescott, I. Grillo, J. Phipps, and D. Gittins, Journal of Physics: Condensed Matter **23**, 194109 (2011).

[5] J. C. Conrad, S. R. Ferreira, J. Yoshikawa, R. F. Shepherd, B. Y. Ahn, and J. A. Lewis, Current opinion in colloid & interface science **16**, 71 (2011).

[6] M. N. Lee and A. Mohraz, Journal of the American Chemical Society **133**, 6945 (2011).

[7] M. Laurati, S. Egelhaaf, and G. Petekidis, Journal of Rheology (1978-present) **55**, 673 (2011).

[8] J. P. Pantina and E. M. Furst, Physical review letters **94**, 138301 (2005).

[9] C. Rueb and C. Zukoski, Journal of Rheology (1978-present) **41**, 197 (1997).

[10] J. A. Yanez, E. Laarz, and L. Bergström, Journal of colloid and interface science **209**, 162 (1999).

[11] A. P. Eberle, R. n. Castañeda-Priego, J. M. Kim, and N. J. Wagner, Langmuir **28**, 1866 (2012).

[12] A. P. Eberle, N. J. Wagner, and R. Castañeda-Priego, Physical review letters **106**, 105704 (2011).

[13] G. Foffi, K. A. Dawson, S. V. Buldyrev, F. Sciortino, E. Zaccarelli, and P. Tartaglia, Physical Review E **65**, 050802 (2002).

[14] H. Guo, S. Ramakrishnan, J. L. Harden, and R. L. Leheny, The Journal of chemical physics **135**, 154903 (2011).

[15] M. A. Miller and D. Frenkel, Physical review letters **90**, 135702 (2003).

[16] M. A. Miller and D. Frenkel, The Journal of chemical physics **121**, 535 (2004).

[17] E. Zaccarelli, Journal of Physics: Condensed Matter **19**, 323101 (2007).

[18] E. Zaccarelli and W. C. Poon, Proceedings of the National Academy of Sciences **106**, 15203 (2009).

[19] A. Duri and L. Cipelletti, EPL (Europhysics Letters) **76**, 972 (2006).

[20] M. Laurati, G. Petekidis, N. Koumakis, F. Cardinaux, A. B. Schofield, J. M. Brader, M. Fuchs, and S. U. Egelhaaf, The Journal of chemical physics **130**, 134907 (2009).

[21] E. Nazockdast and J. F. Morris, Journal of Fluid Mechanics **713**, 420 (2012).

[22] P. Varadan and M. J. Solomon, Langmuir **19**, 509 (2003).

[23] F. Cardinaux, T. Gibaud, A. Stradner, and P. Schurtenberger, Physical review letters **99**, 118301 (2007).

[24] P. J. Lu, E. Zaccarelli, F. Ciulla, A. B. Schofield, F. Sciortino, and D. A. Weitz, Nature **453**, 499 (2008).

[25] S. Manley, H. Wyss, K. Miyazaki, J. Conrad, V. Trappe, L. Kaufman, D. Reichman, and D. Weitz, Physical review letters **95**, 238302 (2005).

[26] M. E. Helgeson, Y. Gao, S. E. Moran, J. Lee, M. Godfrin, A. Tripathi, A. Bose, and P. S. Doyle, Soft matter **10**, 3122 (2014).

[27] D. M. Wendell, F. Pigeonneau, E. Gouillart, and P. Jop, Physical Review E **88**, 023024 (2013).

[28] J. R. Evans, M. J. Edirisinghe, and J. H. Song, Journal of the American Ceramic Society **85**, 2113 (2002).

[29] P. J. Burnett and D. Rickerby, Thin Solid Films **148**, 41 (1987).

[30] S. Livescu, Journal of Petroleum Science and Engineering **98**, 174 (2012).

[31] H. A. Barnes, Journal of Non-Newtonian Fluid Mechanics **81**, 133 (1999).

[32] D. C. Cheng, Rheologica Acta **25**, 542 (1986).

[33] J. R. Stokes and W. J. Frith, Soft matter **4**, 1133 (2008).

[34] H. K. Chan and A. Mohraz, Physical Review E **85**, 041403 (2012).

[35] N. Koumakis and G. Petekidis, Soft matter **7**, 2456 (2011).

[36] Z. Shao, A. S. Negi, and C. O. Osuji, Soft matter **9**, 5492 (2013).

[37] T. Gibaud, D. Frelat, and S. Manneville, Soft matter **6**, 3482 (2010).

[38] F. Pignon, A. Magnin, J.-M. Piau, B. Cabane, P. Lindner, and O. Diat, Physical Review E **56**, 3281 (1997).

[39] L. C. Hsiao, R. S. Newman, S. C. Glotzer, and M. J. Solomon, Proceedings of the National Academy of Sciences **109**, 16029 (2012).

[40] B. Rajaram and A. Mohraz, Physical Review E **84**, 011405 (2011).

[41] K. Hyun, S. H. Kim, K. H. Ahn, and S. J. Lee, Journal of Non-Newtonian Fluid Mechanics **107**, 51 (2002).

[42] S. A. Rogers, Journal of Rheology (1978-present) **56**, 1129 (2012).

[43] S. A. Rogers, B. M. Erwin, D. Vlassopoulos, and M. Cloitre, Journal of Rheology (1978-present) **55**, 435 (2011).

[44] A. Le Grand and G. Petekidis, Rheologica Acta **47**, 579 (2008).

[45] F. Renou, J. Stellbrink, and G. Petekidis, Journal of Rheology (1978-present) **54**, 1219 (2010).

[46] S. A. Rogers, B. M. Erwin, D. Vlassopoulos, and M. Cloitre, Journal of Rheology (1978-present) **55**, 733 (2011).

[47] K. van der Vaart, Y. Rahmani, R. Zargar, Z. Hu, D. Bonn, and P. Schall, Journal of Rheology (1978-present) **57**, 1195 (2013).

[48] M. E. Helgeson, N. J. Wagner, and D. Vlassopoulos, Journal of Rheology (1978-present) **51**, 297 (2007).

[49] M. E. Helgeson, P. A. Vasquez, E. W. Kaler, and N. J. Wagner, Journal of Rheology (1978-present) **53**, 727 (2009).

[50] C. R. López-Barrón, L. Porcar, A. P. Eberle, and N. J. Wagner, Physical review letters **108**, 258301 (2012).

[51] T. Mason, S. Graves, J. Wilking, and M. Lin, Condens. Matter Phys **9**, 193 (2006).

[52] B. Chung, S. Ramakrishnan, R. Bandyopadhyay, D. Liang, C. Zukoski, J. Harden, and R. Leheny, Physical review letters **96**, 228301 (2006).

[53] Y. Gao, J. Kim, and M. E. Helgeson, Soft matter **11**, 6360 (2015).

[54] S. Netemeyer and E. D. Glandt, The Journal of chemical physics **85**, 6054 (1986).

[55] F. Del Rio, E. Avalos, R. Espindola, L. F. Rull, G. Jackson, and S. Lago, Molecular Physics **100**, 2531 (2002).

[56] E. El Mendoub, J.-F. Wax, I. Charpentier, and N. Jakse, Molecular Physics **106**, 2667 (2008).

[57] R. H. Ewoldt, A. Hosoi, and G. H. McKinley, Journal of Rheology (1978-present) **52**, 1427 (2008).

[58] C. Glinka, J. Barker, B. Hammouda, S. Krueger, J. Moyer, and W. Orts, Journal of Applied Crystallography **31**, 430 (1998).

[59] H. H. Winter and F. Chambon, Journal of Rheology (1978-present) **30**, 367 (1986).

[60] G. Allegra, G. Raos, and M. Vacatello, Progress in Polymer Science **33**, 683 (2008).

[61] J. Mewis and N. J. Wagner, Advances in Colloid and Interface Science **147-148**, 214 (2009).

[62] J. M. Brader, M. Siebenbürger, M. Ballauff, K. Reinheimer, M. Wilhelm, S. J. Frey, F. Weysser, and M. Fuchs, Physical Review E **82**, 061401 (2010).

[63] N. Koumakis, J. Brady, and G. Petekidis, Physical review letters **110**, 178301 (2013).

[64] L. Mohan, C. Pellet, M. Cloitre, and R. Bonnecaze, Journal of Rheology (1978-present) **57**, 1023 (2013).

[65] S. Kallus, N. Willenbacher, S. Kirsch, D. Distler, T. Neidhöfer, M. Wilhelm, and H. W. Spiess, Rheologica Acta **40**, 552 (2001).

[66] A. S. Poulos, J. Stellbrink, and G. Petekidis, Rheologica Acta **52**, 785 (2013).

[67] H. A. Barnes, Journal of Non-Newtonian Fluid Mechanics **70**, 1 (1997).

[68] D. Doraiswamy, A. Mujumdar, I. Tsao, A. Beris, S. Danforth, and A. Metzner, Journal of Rheology (1978-present) **35**, 647 (1991).

[69] P. Debye and A. M. Bueche, Journal of Applied Physics **20**, 518 (1949).

[70] J. C. Li and D. K. Ross, J. Phys.-Condes. Matter **6**, 351 (1994).

[71] P. Z. Wong and Q. Z. Cao, Physical Review B **45**, 7627 (1992).

[72] O. Spalla, S. Lyonnard, and F. Testard, Journal of Applied Crystallography **36**, 338 (2003).

[73] R. Seto, R. Botet, M. Meireles, G. K. Auernhammer, and B. Cabane, Journal of Rheology (1978-present) **57**, 1347 (2013).

[74] M. Lettinga, P. Holmqvist, P. Ballesta, S. Rogers, D. Kleshchanok, and B. Struth, Physical review letters **109**, 246001 (2012).

[75] R. Showalter and B. Momken, Mathematical methods in the applied sciences **25**, 115 (2002).

[76] C. Song and L.-H. Huang, Journal of engineering mechanics **126**, 358 (2000).

[77] J. H. Hong, M. S. Mun, and T.-H. Lim, KSME international journal **15**, 1032 (2001).

[78] G. Mavko and A. Nur, Geophysics **62**, 1480 (1997).

[79] J. Kim, D. Merger, M. Wilhelm, and M. E. Helgeson, Journal of Rheology (1978-present) **58**, 1359 (2014).

Chapter 6

Conclusion and Future work

6.1 Introduction

The goal of this thesis was to develop nanoemulsions that can be used as a model system to study the colloidal behavior of polymer-colloid mixtures, and characterize their interactions and microstructure to understand the detailed mechanisms of their colloidal behavior and rheology, ultimately to support the design of nanoemulsions for a wide range of applications. In this chapter, I will summarize the primary findings and impact of the work, and suggest future directions that would further develop this model system for various applications.

6.2 Thermoresponsive viscoelastic nanoemulisons by polymer-surfactant complexation

In Chapter 3, we presented a new scheme for imparting thermoreversible viscoelasticity to O/W nanoemulsions through polymer-surfactant self-assembly, both in the suspending medium and at the droplet interface. Well-known associative polymer-surfactant interactions [1,2] were demonstrated to exert control over the viscoelasticity of the nanoemulsion fluid. Specifically, weak thermoresponsive bridging of polymer-surfactant complexes in the suspending medium gives rise to a transient polymer network with droplets acting as physical crosslinkers without compromising their colloidal stability.

We characterized the structure, dynamics, and rheological properties of this system over a broad range of material chemistries and compositions. Remarkably, the linear

viscoelasticity of this system follows time-temperature superposition over a wide range of temperature and composition. DLS and SANS measurements showed that this viscoelasticity is driven entirely by the dynamics of the transient polymer network, without noticeable structure changes. This allowed for quantification of the activation energy for network formation, which is correlated with the viscoelastic properties across a number of parameters, including polymer and surfactant concentration as well as droplet size. Since our system exhibits a complex dependence of activation energy on fluid composition (i.e. non-monotonic and counterintuitive behaviors under some conditions), it distinguishes these novel viscoelastic nanoemulsions from other types of transient gels. These results provide a new route to control the mechanism of viscoelastic properties in nanoemulsions.

6.3 Shear-induced clustering in polymer-colloid mixtures

Shear-induced clustering of particles is an important phenomenon in polymer-colloid mixtures that affects both the rheology and morphology materials processed from them. In Chapter 4, we sought to better understand this phenomenon by using the thermoresponsvie viscoelastic nanoemulsions as a model system. Specifically, the relative magnitudes of the characteristic time scales for relaxation of polymer viscoelasticity and suspension microstructure can be widely and controllably varied with temperature. In doing so, we explored the several limits of relative magnitude of the relevant dimensionless shear rates, the Weissenberg number (*Wi*) and the Peclet number (*Pe*). In all of these limits, we found that the nanoemulsions represent two distinct regimes of shear thinning at relatively low and high shear rates. At low (but still nonlinear) shear rates, the shear thinning rheology

collapses by scaling with *Wi*. By contrast, the shear thinning rheology at relatively high shear rates collapses by scaling with *Pe*.

Three-dimensional flow-SANS was used to investigate microstructural changes in the moderate *Pe* regime. In contrast to previous two-dimensional scattering measurements, we observed anisotropy of particle pairs with projected orientation along the vorticity direction (in the flow-vorticity plane) and along the extensional axis of shear (in the flow-gradient plane). This anisotropy initiates above $Pe \sim 0.1$ over a wide range of fluid conditions. Furthermore, the degree of anisotropy in both shear planes collapses by scaling with $Pe^{1/3}$ over a wide range of compositions. From these results, we formulated a semi-empirical model for the shear stress and viscosity was formulated, in which the viscoelastic network stress augmented by an asymptotic shear thickening contribution due to hydrodynamic clustering. The model exhibits quantitative agreement with a wide range of rheological data, suggesting that hydrodynamic clustering is the dominant driving force for clustering in the range of material behavior we study.

6.4 Microstructural processes of yielding in heterogeneous colloidal gels

Many types of dense colloidal gels exhibit so-called “two-step” or “delayed” yielding, the mechanism(s) for which have yet to be elucidated. Therefore, in Chapter 5, we used the thermoreversible nanoemulsions as a model system to study the microstructural and nonlinear mechanical origins of yielding in a heterogeneous colloidal gel. In this system, the nanoemulsion gels exhibit heterogeneous microstructure that is consist with arrested phase separation, i.e. a bicontinuous structure of coexisting colloid-rich domains of fractal clusters and colloid-poor domains [3,4]. By employing large amplitude oscillatory shear (LAOS)

measurements, we analyzed the intracycle response during yielding as a sequence of physical processes. This analysis provides a novel route for quantification of instantaneous, rate-dependent non-linear parameters associated with yielding (e.g. yield stress, yield strain, etc.). We find that such heterogenenous gels exhibit broad yielding, with a slow transition from elastic straining to elastoplastic thinning and eventually yielding and flow with increasing strain amplitude. We find that the nonlinear yield strain and stress exhibit significant strain rate toughening above a characteristic frequency that is dominated by the viscous response of the fluid, which we argue is governed by poroelastic effects associated with fluid drainage from the phase separated structure.

We employed the first ever rheo-USANS/SANS measurements under LAOS to correlate the rheological information with the microstructural process occurring during yielding. The experiments revealed that the material passes through a cascade of structural breakdown from large to progressively smaller length scales. In the region where the non-linearity and pre-yielding initiated, compression of the dense fractal domains leads to the formation of large voids. During the broad yielding transition and post-yielding flow regions, cluster-cluster correlations become increasingly homogeneous, suggesting breakage and eventually depercolation of intercluster bonds at the yield point. Overall, all significant structural changes occur on the micron-scale, suggesting that large-scale rearrangements of hundreds or thousands of particles, rather than the homogeneous rearrangements of particle-particle bonds, dominate the initial yielding of heterogeneous colloidal gels. This is in contrast to previous hypotheses formulated from macroscopic rheological measurements, and establishes large-scale structure as an important design criterion for the mechanics of colloidal gels.

6.5 Future work

Although this work has uncovered a number of mechanisms for rheological behavior in nanoemulsions, more through studies are still needed to understand how these mechanisms can be used to formulate and engineer nanoemulsions for a wider range of applications. As previously shown, the nanoemulsions exhibit complex thermoresponsive rheological behaviors by two separate mechanisms at relatively high and low temperatures. At high temperatures, it has been hypothesized that functionalized hydrophobic end-groups of PEG adsorb to the droplet surface, inducing interdroplet attractions that mediate the formation of colloidal gels with remarkably solid-like properties [3]. Previously, this was indirectly confirmed by tracking changes in the gel transition and mechanical properties with increasing hydrophobicity of the PEG end-group chemistry. However, in order to better understand the physics that controls the final structure and the rheology of the fluid, the system should be thoroughly investigated for how the temperature-dependent attractions between droplets depend on the characteristics of the bridging polymer. For this purpose, it is suggested that polymers having systematically changes in their hydrophobicity of end-group and molecular weights (i.e. dialkyl PEG) be synthesized, and their behavior in nanoemulsions systematically studied. By introducing these polymers to our nanoemulsion system, the temperature-dependent interaction potential between dispersed droplets can be measured using static SANS and light scattering measurements. Ultimately, this would provide rational criteria for designing the strength, range and temperature-dependence of polymer bridging interactions in nanoemulsions.

A potentially significant complication in the analysis of these SANS measurements could be the effect of polydispersity, which can be as high as 20-30% in this system. In this

limit, the so-called average structure factor approximation may fail, and we will need to resort to multi-component structure factor models to adequately fit the data, particularly for large volume fractions of droplets. To facilitate these models, the Helgeson group has established a collaboration with Yun Liu at NCNR who has developed numerical codes for performing the necessary calculations. With this, reliable interaction potentials across a range of volume fractions can be obtained, even in the case where polydispersity effects are significant. Alternatively, one could explore advanced nanoemulsification or separation methods in order to decrease the polydispersity of the nanoemulsions.

Another key compositional variable to control thermoreversible gelation at elevated temperature in nanoemulsions is the "free" surfactant in the continuous phase (i.e. the portion that is not adsorbed at the oil-water interface). However, it is still unclear how the presence of surfactant in the bulk solution influences the bridging interactions at elevated temperature. Excess amount of surfactant in the continuous phase may alter the electrostatic interaction between droplets, resulting in changes to the effective potentials between droplets. Alternatively, free micelles in solution might impart depletion attractions between the droplets that modify the underlying bridging attractions. Thus, it is also needed to probe the effect of the "free" surfactant concentration on the temperature-dependent interactions using scattering measurements.

Also, at relatively low temperatures, the nanoemulsions exhibit transient gelation, which is observed at low surfactant concentration and is relatively insensitive to the end-group chemistry. Due to the well-studied interactions between PEG and surfactants in solution, along with the scaling of the rheological properties with concentration of surfactant and polymer, it is hypothesized that low-temperature gelation arises from the formation of

polymer-surfactant complexes that form dynamic force chains between droplets (in Chapter 3). In both types of thermoreversible gelation at high and low temperatures, it is clear that the mechanisms depend critically on the self-assembly of polymer and surfactant at the droplet surface. This calls for a more thorough investigation of structure and interactions of PEG and surfactants at the oil and water interface. This could involve neutron reflectivity (NR) measurements to study the structure of polymer and surfactant at the interface. In these measurements, contrast variation could be used to isolate the density profiles of the individual components. These measurements could be augmented with surface force apparatus (SFA) measurements to directly measure the attractive interactions imparted between PDMS surfaces in the presence of PEG and SDS. In particular, at high temperatures, it can be tested whether temperature-induced desolvation of hydrophobic end-groups results in interfacial adsorption of polymer at the oil and water interface. By contrast, at low temperatures, it can be investigated whether the conformation of PEGs, and their complexes with SDS, near the oil and water interfaces are significantly altered by both temperature and surfactant concentration.

In Chapter 4, the microstructure of sheared colloidal suspensions in polymer solutions was investigated using the nanoemulsions as a model system. Many groups have reported shear-induced clustering of suspensions in non-Newtonian fluids, sometimes with conflicting behavior. For example, Michele *et al.* [5] and Lyon *et al.* [6] observed string-like particle clusters oriented along the flow direction under shear in highly viscoelastic solutions. However, vorticity-aligned clustering has also been reported in attractive polymer-colloid mixtures [7,8]. These anisotropic microstructures are believed to be related to the development of polymer normal stress. However, in Chapter 4, flow-SANS

measurements have shown that, in the limit where the viscoelastic polymer relaxation time is much longer than the Brownian diffusion time of the suspended colloids, vorticity-aligned clustering under shear is primarily driven by the influence of hydrodynamic interactions between colloids.

Clearly, much remains to be understood about what factors determine (i) the orientation of shear-induced clusters, and (ii) how they emerge and evolve under shear. A critical question is whether the clusters persist at steady state once formed (both in size and orientation). For example, if we find that the orientation angle evolves along with the degree of anisotropy, it will suggest a structure which forms, persist and then rotates in the flow plane. By contrast, if the orientation angle remains fixed (with projections along the compressional and vorticity axes) during the entire transient processes, it will suggest the formation of transient clusters with particle fluxes preferred along these orientational axes. Moreover, the time scale at which theses transitions occur during the transient flow relative to the viscoelastic and Brownian time scales will help to identify the specific forces acting on the colloids to induce clustering. From further studies to answer these questions, I believe we could understand the nature and mechanistic origin of shear-induced clusters. Ultimately, this would lead to rational guidelines for either enhancing or suppressing shear-induced clustering in polymer-colloid mixtures, which may find significant application in polymer nanocomposite processing.

Finally, our thermoresponsive nanoemulsions open up the possibility that, with minor modification of the polymer chemistry, they could beused as a suitable colloidal platform for switchable materials, since mild changes of interactions between droplets were shown to give rise to drastic changes of its rheology and morphology. Materials that respond

to a variety of external stimuli, such as temperature [3], pH [9], electric or magnetic fields [10,11], ultrasound [12], and light[13-15], have been developed for control of flow properties. Switchable smart materials are particularly useful in micro- or nano-scale devices, such as microfluidics and lab-on-chip devices [16]. Also, dynamically controlled electro/magneto-rheological fluids or suspensions can be used for shock absorbers and vibration reducers [17,18]. Another important application of stimuli-responsive material is in biology. By mimicking the dynamic properties of biological systems in smart materials, researchers can modulate biomolecule activity and develop artificial tissues or scaffolds [19,20]. For example, using a reversible sol-gel transition, injectable hydrogel scaffolds have been developed [21,22].

Of these different external stimuli, perhaps the most widely studied is light. Typical photo-responsive compounds, such as spiropyrans, spirooxazines, azobenzene and quinones, can be used for molecular self-assembly combining with surfactants or polymers [13-15,23-25]. Specifically, their photo-induced conformational changes can change the self-assembled structure, thus leading to the reversible changes in rheology. Another common external stimulus is pH, which can control the interactions between weak acid or alkaline groups by accepting or releasing protons [26]. The addition of minor acid or base can modify the viscosity through the control of surfactant self-assembly aggregates [27-29], which is rapid, cost-effective and reversible process. Also, electric field can be used for controlling the viscoelasticity of the fluid using electro-responsive compounds [30], which method can be applied to the controlled release of substance, such as inkjet printers. As is clear from this review, previous studies have focused on using switchable chemistries to induce changes in molecular self-assembly to achieve switchable rheology. Using our nanoemulsions, one

could propose a new approach, in which switchable behavior induces changes in colloidal assembly for “smart” material design. Furthermore, since the dispersed nanoemulsions are comprised of a liquid phase, the droplets can be easily loaded with active cargoes [31], showing great promise for applications in cosmetics, drug delivery, and biotechnologies.

References

[1] S. Dai and K. Tam, The Journal of Physical Chemistry B **105**, 10759 (2001).

[2] E. D. Goddard, Colloids and Surfaces **19**, 255 (1986).

[3] M. E. Helgeson, S. E. Moran, H. Z. An, and P. S. Doyle, Nature materials **11**, 344 (2012).

[4] M. E. Helgeson, Y. Gao, S. E. Moran, J. Lee, M. Godfrin, A. Tripathi, A. Bose, and P. S. Doyle, Soft matter **10**, 3122 (2014).

[5] J. Michele, R. Pätzold, and R. Donis, Rheologica Acta **16**, 317 (1977).

[6] M. Lyon, D. Mead, R. Elliott, and L. Leal, Journal of Rheology (1978-present) **45**, 881 (2001).

[7] A. Montesi, A. A. Peña, and M. Pasquali, Physical Review Letters **92**, 058303 (2004).

[8] L. Silbert, J. Melrose, and R. Ball, Journal of Rheology (1978-present) **43**, 673 (1999).

[9] Z. Chu and Y. Feng, Chemical Communications **46**, 9028 (2010).

[10] W. J. Wen, X. X. Huang, S. H. Yang, K. Q. Lu, and P. Sheng, Nature Materials **2**, 727 (2003).

[11] S. Odenbach, Int. J. Mod. Phys. B **14**, 1615 (2000).

[12] J. M. J. Paulusse and R. P. Sijbesma, Angew. Chem.-Int. Edit. **45**, 2334 (2006).

[13] H. Oh, A. M. Ketner, R. Heymann, E. Kesselman, D. Danino, D. E. Falvey, and S. R. Raghavan, Soft Matter (2013).

[14] J. Hu, H. Yu, L. H. Gan, and X. Hu, Soft Matter **7**, 11345 (2011).

[15] B. Song, Y. Hu, and J. Zhao, Journal of Colloid and Interface Science **333**, 820 (2009).

[16] S. R. Sershen, G. A. Mensing, M. Ng, N. J. Halas, D. J. Beebe, and J. L. West, Advanced Materials **17**, 1366 (2005).

[17] A. Milecki and M. Hauke, Mechanical Systems and Signal Processing **28**, 528 (2012).

[18] J. E. Lindler and N. M. Wereley, Journal of Intelligent Material Systems and Structures **10**, 652 (1999).

[19] M. N. Yousaf, B. T. Houseman, and M. Mrksich, Angewandte Chemie International Edition **40**, 1093 (2001).

[20] M. P. Lutolf and J. A. Hubbell, Nat. Biotechnol. **23**, 47 (2005).

[21] A. Gutowska, B. Jeong, and M. Jasionowski, The Anatomical Record **263**, 342 (2001).

[22] Y. Lee, H. J. Chung, S. Yeo, C.-H. Ahn, H. Lee, P. B. Messersmith, and T. G. Park, Soft Matter **6**, 977 (2010).

[23] H. Sakai, Y. Orihara, H. Kodashima, A. Matsumura, T. Ohkubo, K. Tsuchiya, and M. Abe, J. Am. Chem. Soc. **127**, 13454 (2005).

[24] J. Eastoe and A. Vesperinas, Soft Matter **1**, 338 (2005).

[25] N. Fomina, J. Sankaranarayanan, and A. Almutairi, Advanced Drug Delivery Reviews **64**, 1005 (2012).

[26] K.-S. Chen, Y.-A. Ku, C.-H. Lee, H.-R. Lin, F.-H. Lin, and T.-M. Chen, Materials Science and Engineering: C **25**, 472 (2005).

[27] Z. L. Chu and Y. J. Feng, Chemical Communications **46**, 9028 (2010).

[28] M. Bergsma, M. L. Fielden, and J. Engberts, Journal of Colloid and Interface Science **243**, 491 (2001).

[29] W. J. Chen, G. Z. Li, G. W. Zhou, L. M. Zhai, and Z. M. Li, Chemical Physics Letters **374**, 482 (2003).

[30] K. Tsuchiya, Y. Orihara, Y. Kondo, N. Yoshino, T. Ohkubo, H. Sakai, and M. Abe, Journal of the American Chemical Society **126**, 12282 (2004).

[31] H. Z. An, M. E. Helgeson, and P. S. Doyle, Adv. Mater. **24**, 3838 (2012).

Appendix A

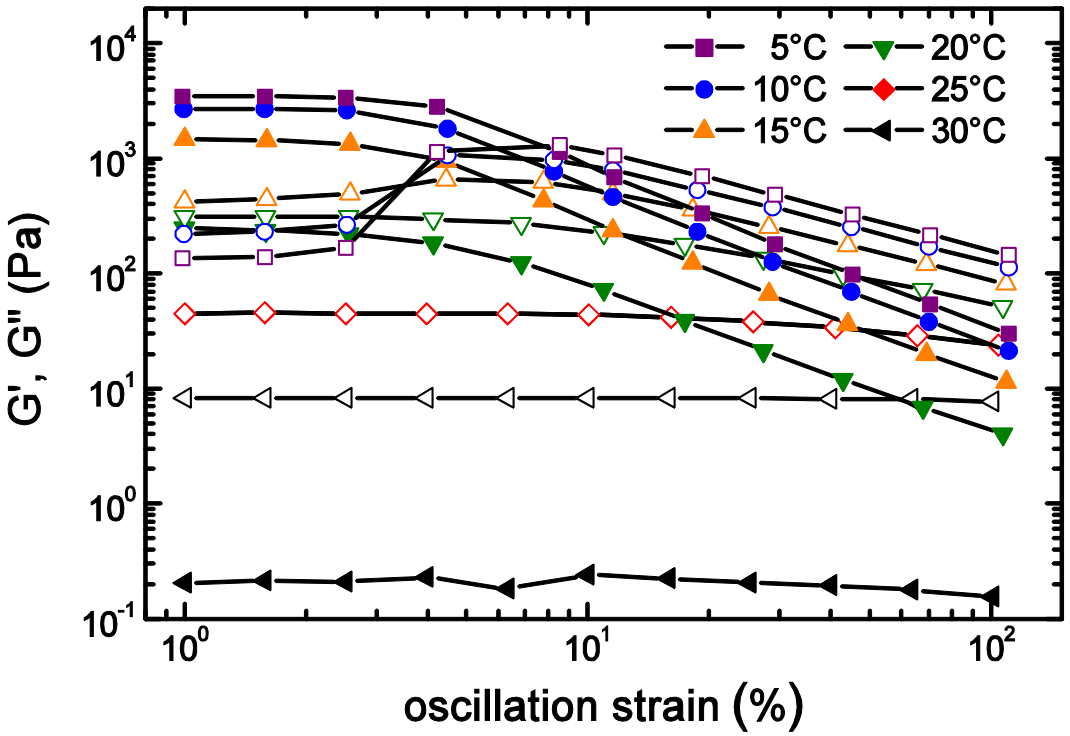

Figure A.1 Dynamic strain sweep measurement for nanoemulsions containing ϕ = 0.33 PDMS droplets in water with P=0.33 PEGDA and C_s=100 mM SDS at 20 rad s^{-1} frequency and the temperature indicated.

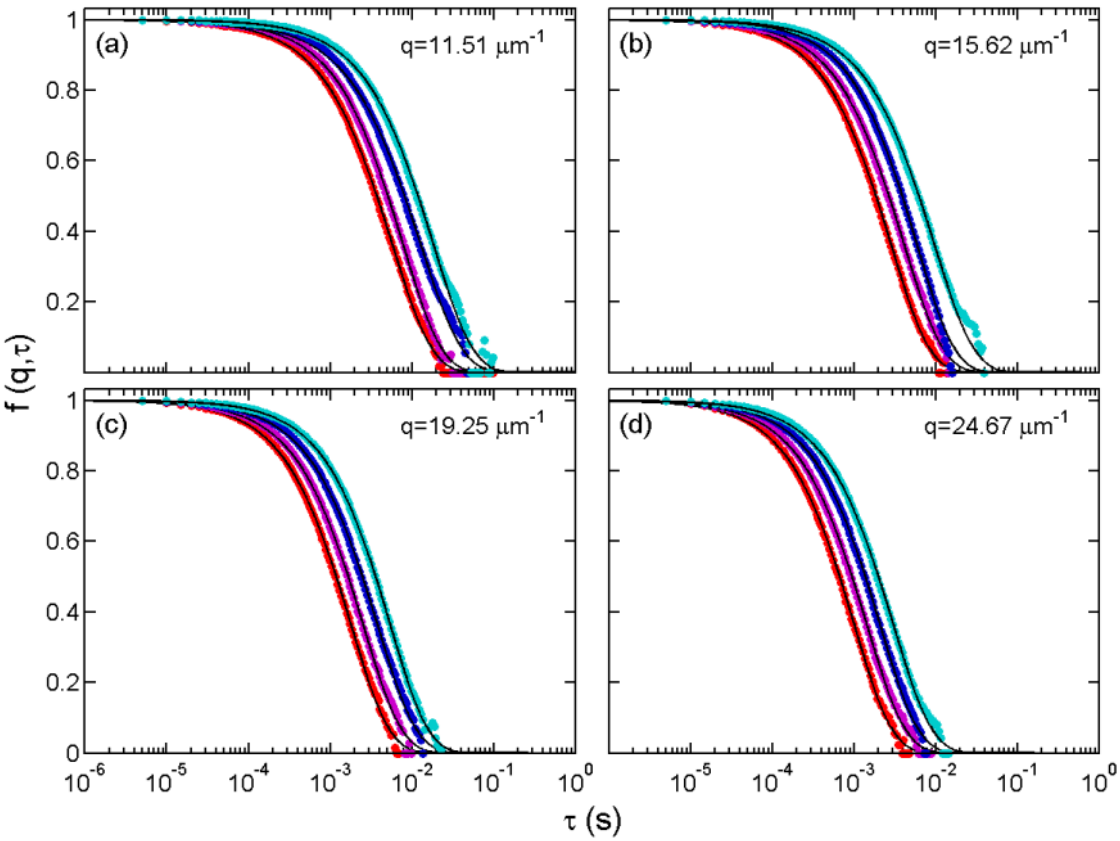

Figure A.2 Intermediate scattering functions for ϕ=0.01 measured at T= (a) 35 °C, (b) 25 °C, (c) 15 °C and (d) 5 °C. Solid lines are fits to stretched exponentials.

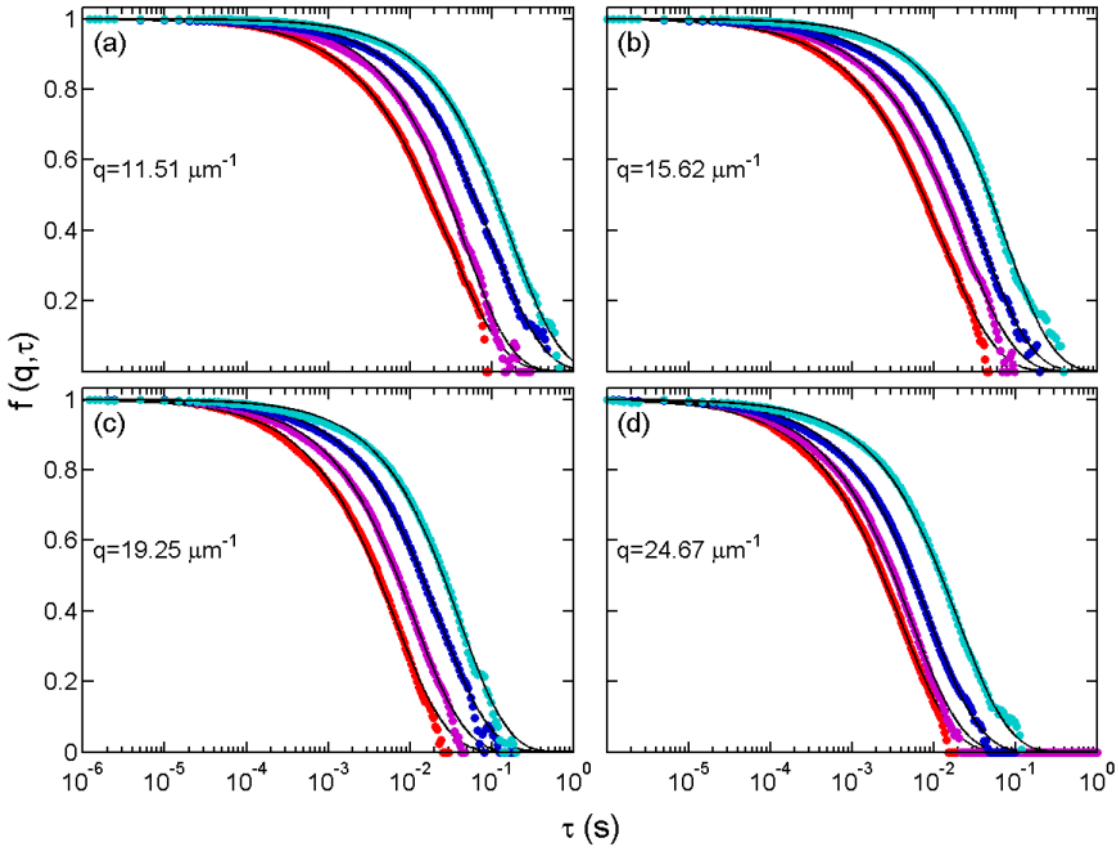

Figure A.3 Intermediate scattering functions for ϕ=0.20 measured at T= (a) 35 °C, (b) 25 °C, (c) 15 °C and (d) 5 °C. Solid lines are fits to stretched exponentials.

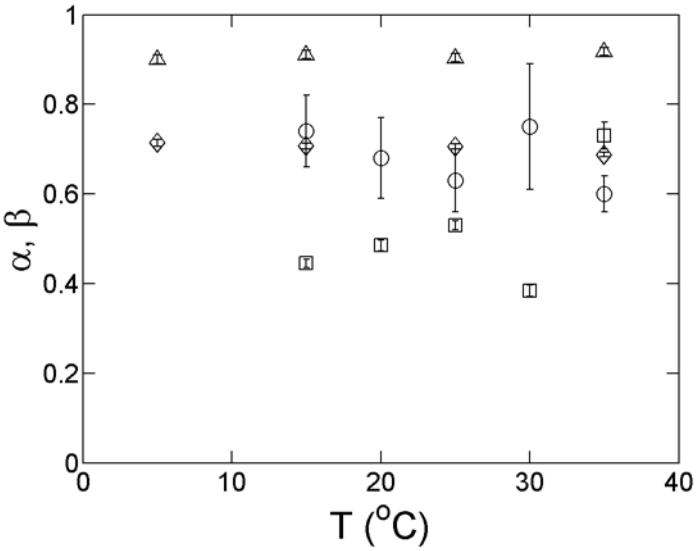

Figure A.4 Exponents of stretched exponentials for ϕ=0.01 (triangles), ϕ=0.20 (diamonds) and ϕ=0.33 (circles for the fast mode and squares for the slow mode)

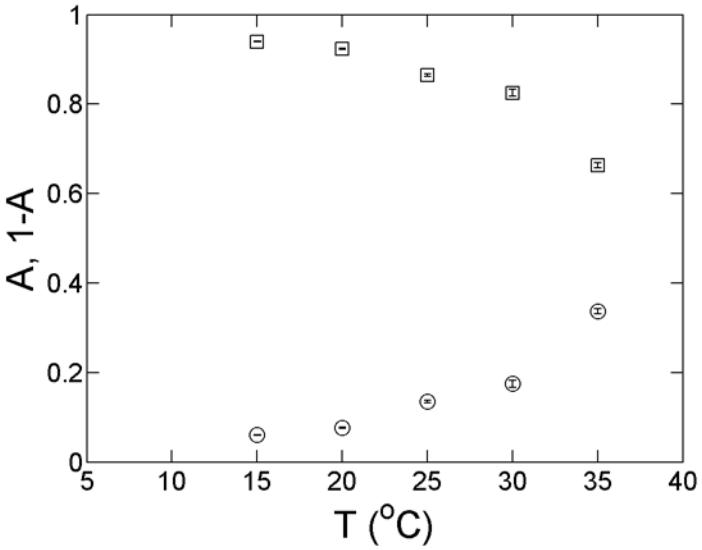

Figure A.5 Temperature dependence of the amplitudes of the fast mode (circles) and the slow one (squares). φ=0.33

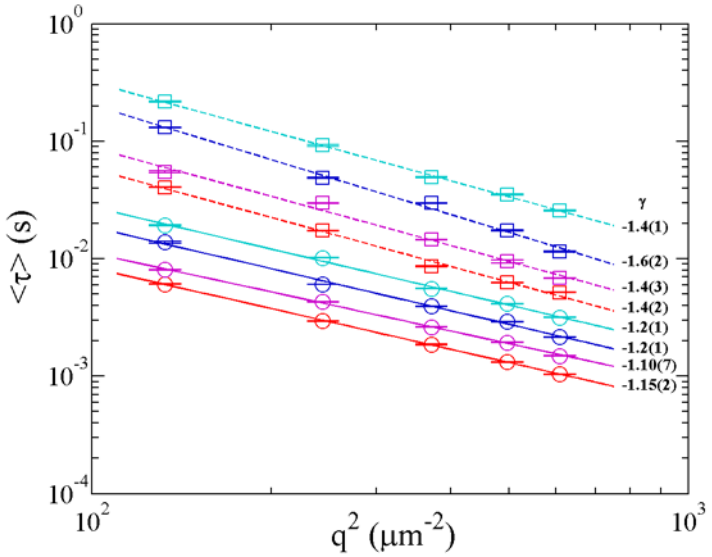

Figure A.5 q-dependence of average relaxation times for φ=0.01 (circles) and φ=0.20 (squares). The measurements were done at 35 °C (red), 25 °C (purple), 15 °C (blue) and 5 °C (cyan). Lines are power-law fits, $< \tau > \sim (q^2)^{\gamma}$, to the data.

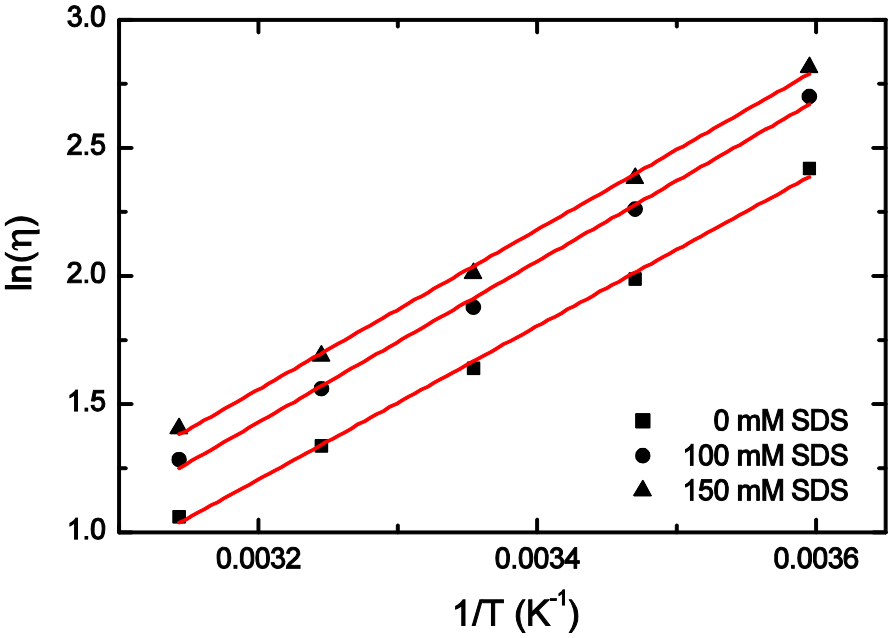

Figure A.7 Arrhenius plot of viscosity for the PEGDA/SDS mixtures. PEG/SDS mixture contains P=0.33 PEGDA and C_s=0 (squares), 100 (circles) and 150 (triangles) mM SDS in water. Lines are fits to the Arrhenius equation to extract activation energy, E_a, which are 10.0±0.29, 10.5±0.33 and 10.5±0.25 k_bT at 25°C, respectively.

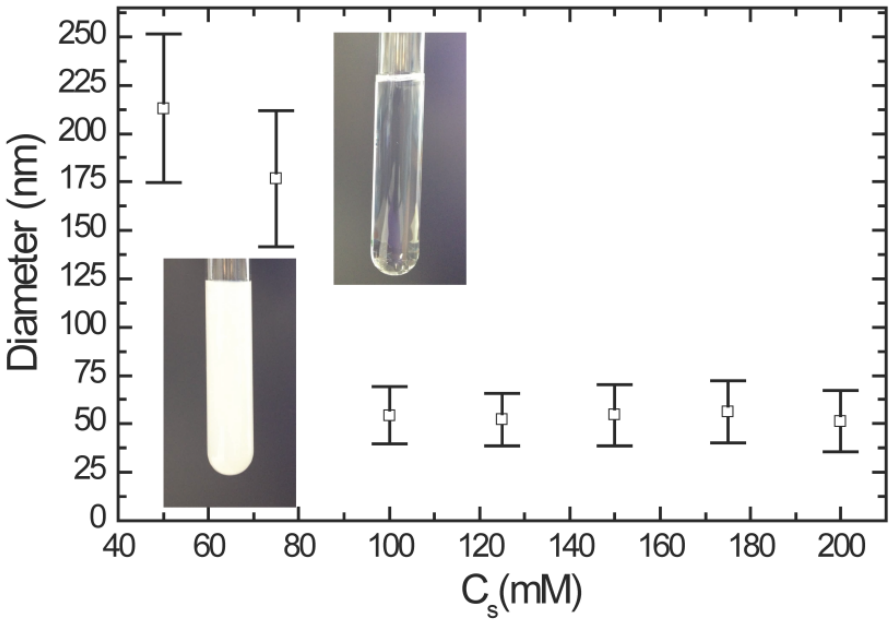

Figure A.8 Dependence of z-average diameter of droplet on SDS concentration. The nanoemulsions contain ϕ = 0.33 PDMS droplets in water with P=0.33 PEGDME and varying SDS. The samples were homogenized at 5 kspi for 20 passes. Inset photos: turbid nanoemulsions containing low SDS concentration C_s=75 mM (left) and transparent nanoemulsions containing SDS above C_s=80 mM (right).

Appendix B

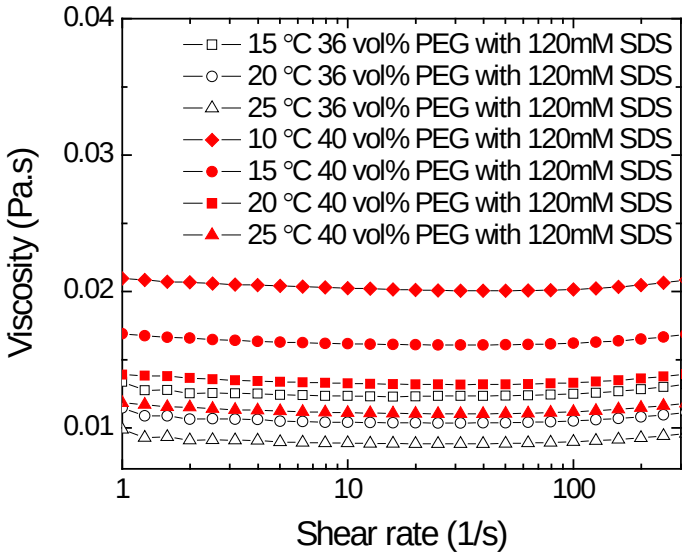

Figure B.1 Shear rate dependent viscosity of the continuous phase. Samples were measured at 10-25 °C. Samples contain PEG (ϕ_p = 0.36 and 0.40) and C_s = 120mM SDS.

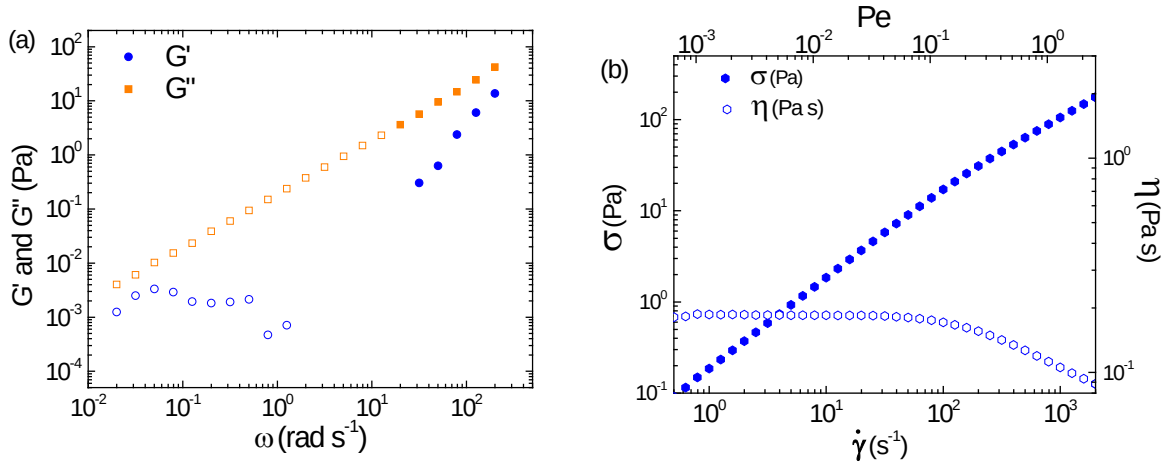

Figure B.1 (a) The dynamic shear moduli (*G'*, blue circle; *G"*, orange square) over a range of 0.02-200 rad s^{-1} at 1% strain amplitude. (b) Steady shear rheology. Sample was measured at 35 °C. Nanoemulsions contain ϕ_o = 0.33 PDMS droplets (<*a*> = 35.4 nm) with PEG (ϕ_p = 0.40) and C_s = 120mM SDS. Open symbols represent the out of the limits of the instrument. At 35 °C, the crossover of *G'* and *G"* is immeasurable.

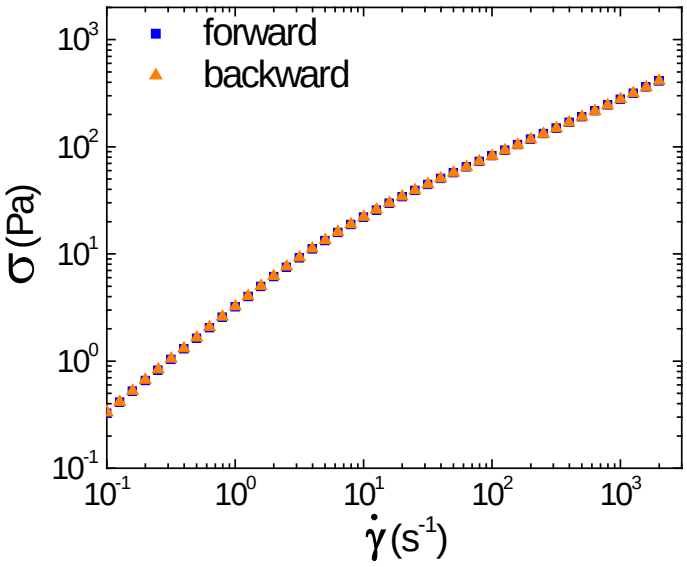

Figure B.2 Steady shear rheology for Nanoemulsions contain ϕ_o = 0.33 PDMS droplets (<*a*> = 35.4 nm) with PEG (ϕ_p = 0.40) and C_s = 120mM SDS at 10 °C. Blue squares and orange triangles represent forward and backward shear rate sweeps, respectively. The residence time at each point is 30 seconds.

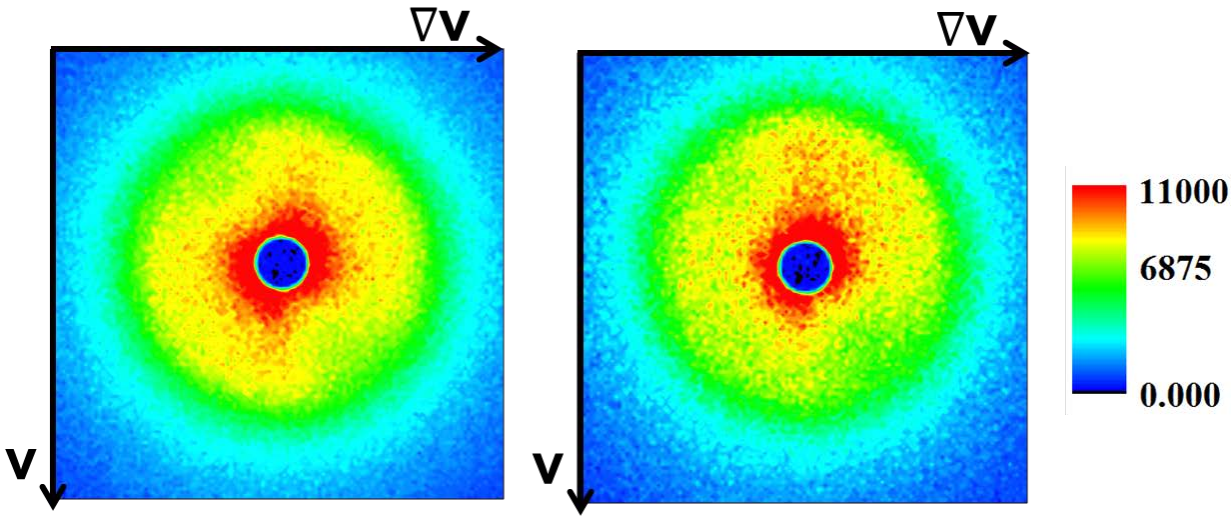

Figure B.3 2D Flow-SANS scattering spectra under backward (left: inner wall and right: outer wall) shear directions showing heat plots of absolute intensity in 1-2 (flow-gradient planes at Pe=2.17. Data is for the nanoemulsion containing ϕ_o = 0.33 PDMS droplets (<*a*>=34.6nm) with ϕ_p = 0.33 PEG and C_s = 120 mM SDS.

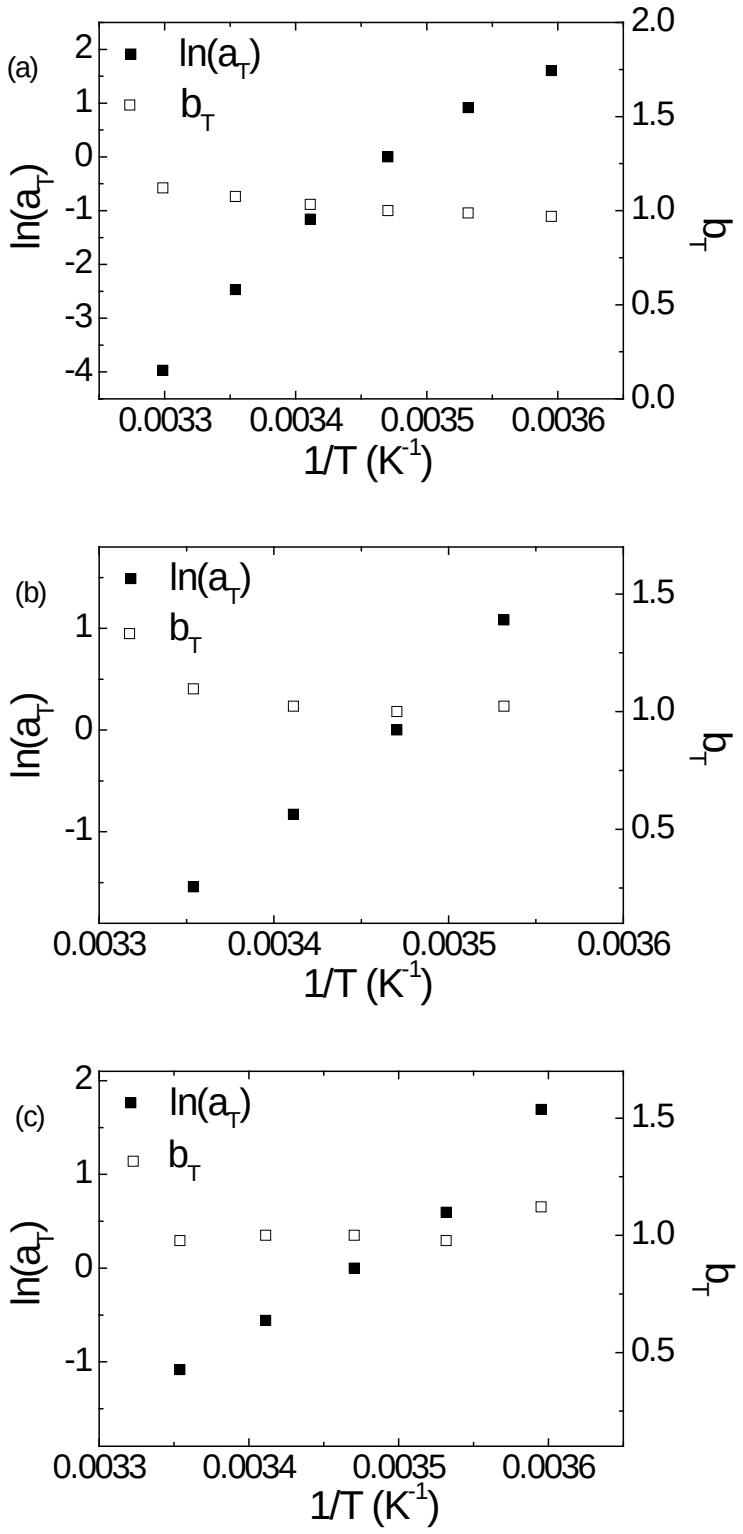

Figure B.4 The horizontal (a_T, closed symbols) and vertical (b_T, open symbols) shifting factors. Nanoemulsions contain ϕ_o = 0.33 PDMS droplets with PEG and C_s = 120mM SDS, with (a) $\langle a \rangle$ = 34.6nm and ϕ_p = 0.33, (b) $\langle a \rangle$ = 31.7 nm and ϕ_p = 0.36, (c) $\langle a \rangle$ = 35.4 nm and ϕ_p = 0.40. The reference temperature is 15 °C.

Table B.1 Carreau-Yasuda model fitting parameters.

	T (°C)	η_0 (Pa·s)	η_∞ (Pa·s)	λ (s)	b	n	τ_r (s)
Sample for $\phi_p = 0.33$	5	398599	0.001	9558	1.1	0.080	171.59
	10	203561	0.001	4929	0.73	0.081	85.11
	15	82586	0.001	2102	0.66	0.087	34.03
	20	15016	0.001	438.4	0.84	0.113	10.80
	25	3640	0.001	122.6	0.87	0.139	2.86
	30	713.8	0.001	29.07	0.98	0.183	0.64
Sample for $\phi_p = 0.36$	10	10.828	0.001	0.515	0.85	0.340	8.6×10^{-3}
	15	3.865	0.001	0.147	0.94	0.358	3.0×10^{-3}
	20	1.522	0.001	0.043	0.95	0.356	1.1×10^{-3}
	25	0.712	0.001	0.014	0.88	0.361	4.8×10^{-4}
Sample for $\phi_p = 0.40$	10	2.233	0.001	0.105	1.33	0.489	1.3×10^{-3}
	15	1.235	0.001	0.050	1.21	0.500	7.0×10^{-4}
	20	0.650	0.001	0.026	1.35	0.540	3.8×10^{-4}
	25	0.382	0.001	0.010	1.28	0.503	2.2×10^{-4}

Appendix C

Our interpretation of the rheo-USANS measurements assumes that the scattering is relatively isotropic due to the vertical slit-smearing of the USANS detector. Thus, it is critical to confirm isotropic scattering spectra during yielding. Figure C.1 shows the two-dimensional rheo-SANS spectra in the q-range, corresponding to the scale of single droplets and their mass fractal aggregates. There is no significant anisotropic scattering both at zero and high strain amplitude.

In order to confirm isotropic scattering at low q-values (i.e. those probed by USANS), we have performed rheo-small angle light scattering (rheo-SALS) measurements on the sample having similar rheology with the sample used in rheo-USANS/SANS measurement. Two averaged rheo-SALS images at the lowest and highest strain amplitude are shown in Figure C.2. The q-range of peak in these images correspond the q-range the

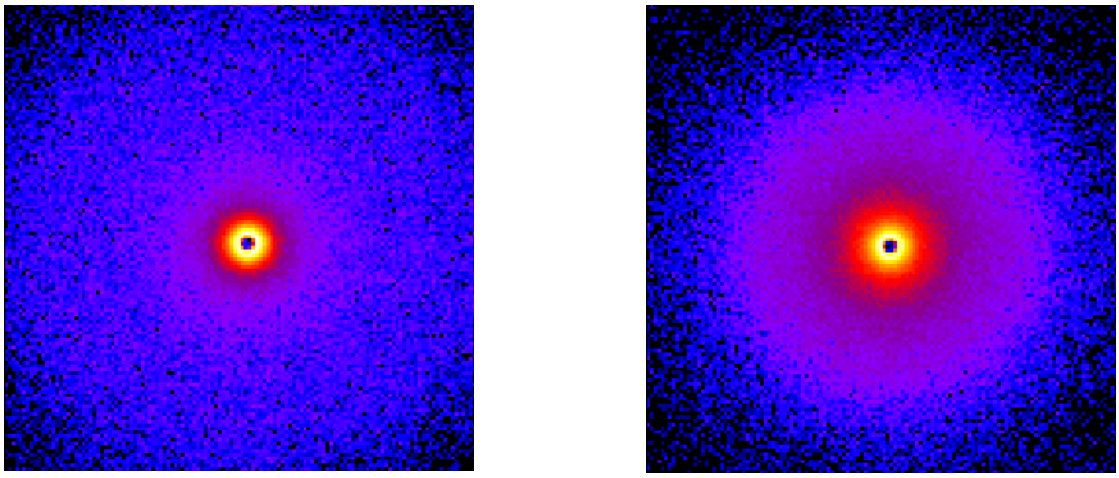

Figure C.1 Two-dimensional rheo-SANS spectra under LAOS at 10 rad/s and (left) γ_0 = 0%, (right) γ_0 = 100%.

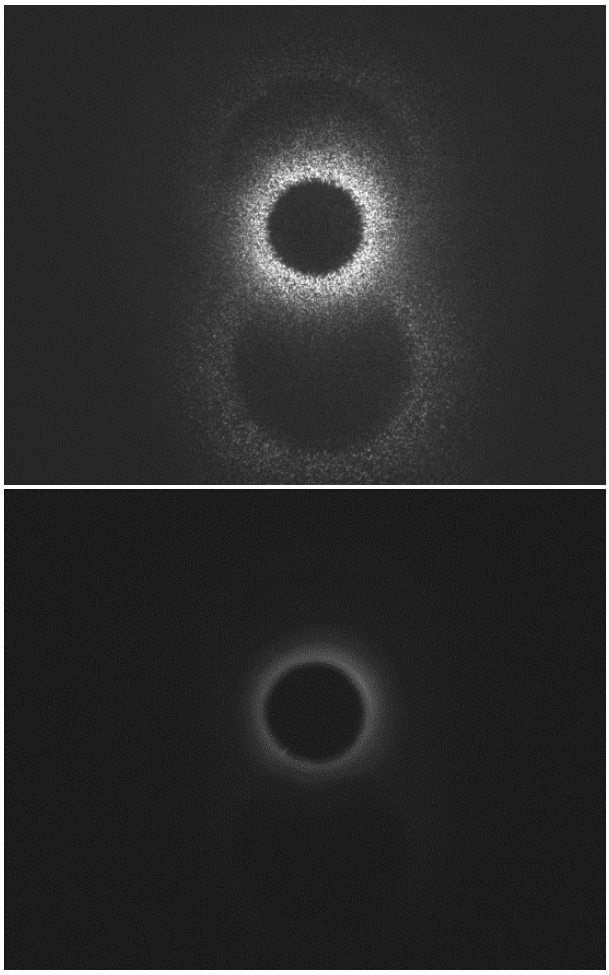

Fig. C.2. Two-dimensional rheo-SANS spectra under LAOS at 10 rad/s and (left) γ_0 = 0.1%, (right) γ_0 = 200%.

peak in USANS. Thus, the decrease in intensity as the strain amplitude increases in rheo-SALS correspond the decrease in peak intensity in rheo-USANS (note: the anomalous rings seen in the images are due to the slight underfocus of the optics required to penetrate the opaque sample). We found that there is no anisotropic scattering either at low or high strain amplitudes.

In Figure C.3 we show the complete range in strain amplitude and angular frequency covered by our LAOS experiments arranged in a Pipkin diagram. Note that intermediate angular frequencies and strain amplitudes have been omitted for the sake of clarity. At low

ω and γ_0 (upper left corner), elliptical waveforms in the linear regime are displayed. With increasing ω and γ_0 the waveforms become progressively nonlinear and exhibit complex shapes, with a stress overshoot and a subsequent local minimum. Upon even further increasing ω and γ_0, the overshoot becomes less pronounced and the waveform becomes more square-shaped, approaching the waveform of an ideal yield stress fluid.

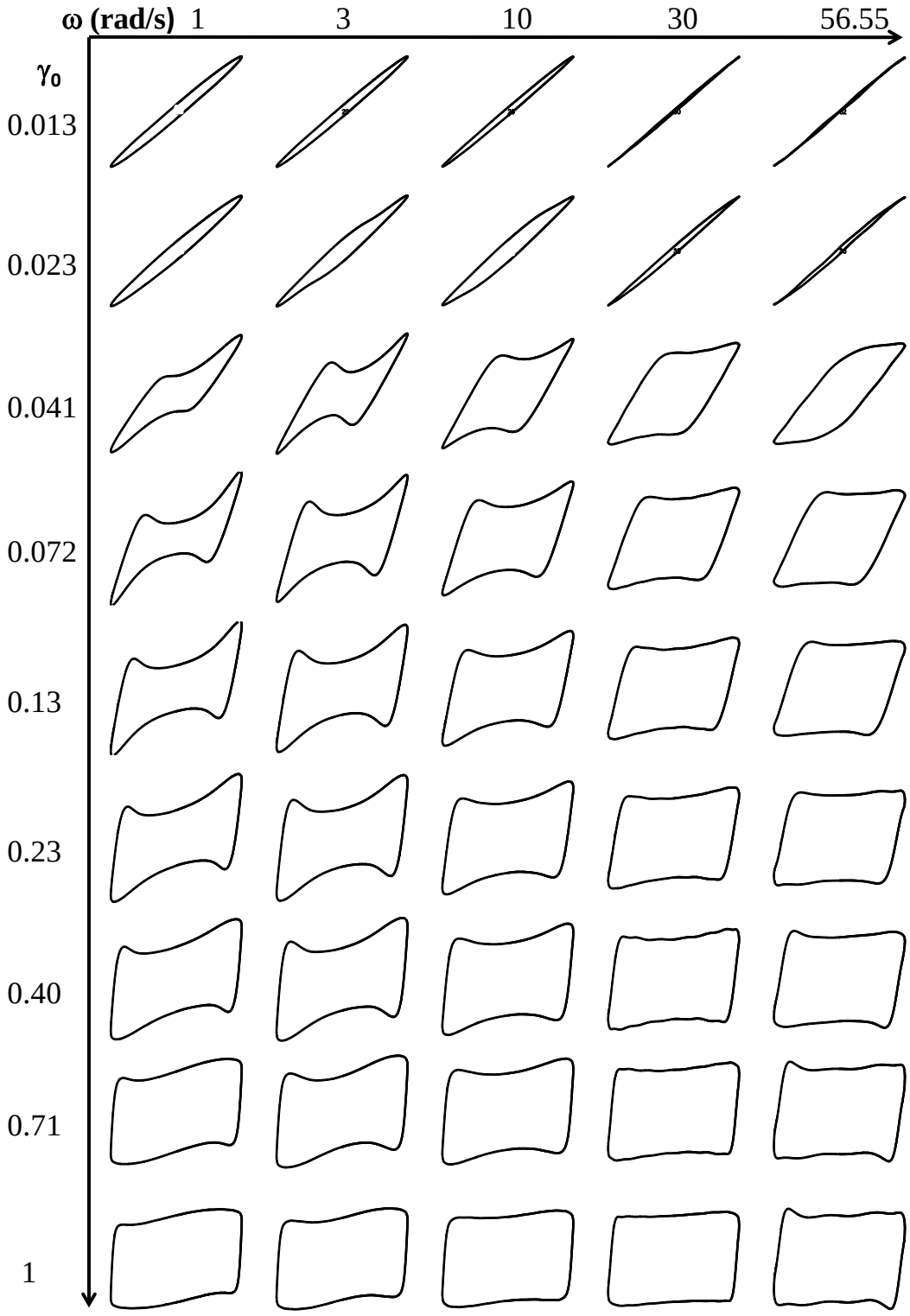

Figure C.3 Elastic Lissajous-Bowditch (strain vs stress) plots in the Pipkin space.

In Figure C.4, we show the effect of using roughened surfaces by attaching sandpaper to the cone and plate geometries in order to prevent slip artifacts. When smooth geometries are used, *G'* and *G"* appear to decrease in two steps. Furthermore, the reproducibility of the apparent two-step yielding with the smooth geometries was very poor, and in some measurements *G'* and *G"* even displayed a local minimum in the strain amplitude range $0.01 < \gamma_0 < 0.1$, as previously reported by Laurati *et al*. Roughened geometries eliminated slip artifacts and lead to reproducible results with a monotonic decrease for *G'* and *G"* (after its initial maximum). We therefore conclude that smooth geometries often lead to slip in these materials for strain amplitudes near the onset of yielding.

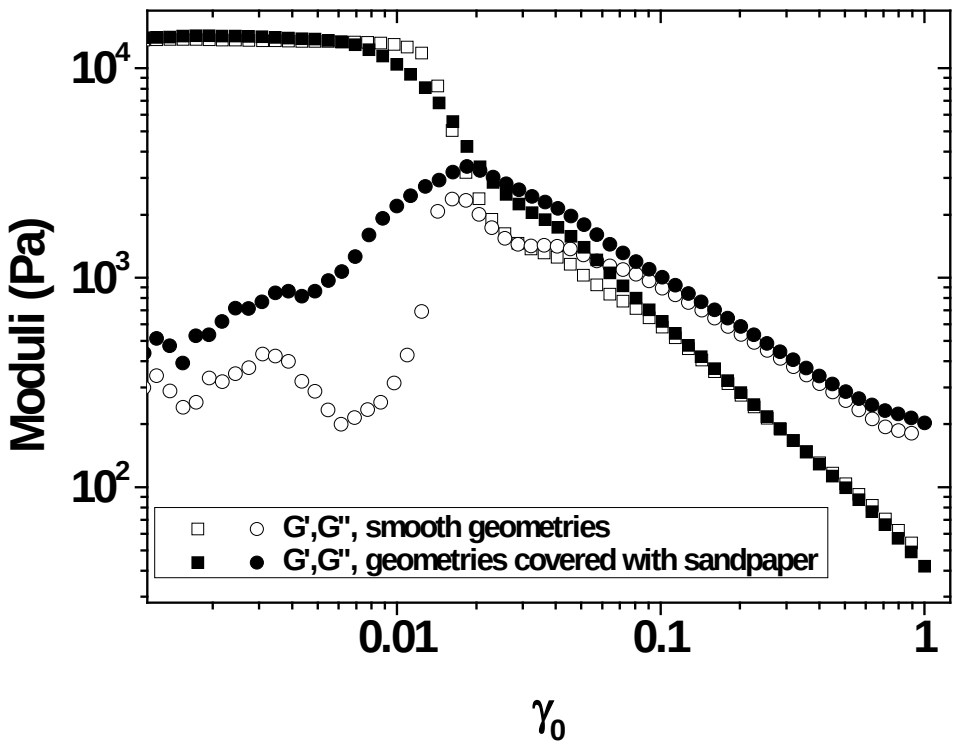

Figure C.4 Effect of slip artifacts on LAOS measurements of a nanoemulsion gel, if smooth geometries are used. Using geometries with a rough surface eliminates slip and gives reproducible results.

In order to determine the cause of the shift in position of the high-q shoulder for the rheo-SANS measurements, rheo-SANS was performed at zero strain amplitude after the highest strain amplitude. The sample for this measurement was the same sample used in rheo-SANS measurements in Figure 5.12. Figure C.5 shows the data in the SANS region for (i) the nearly zero strained material, (ii) the highest strain amplitude, and (iii) at rest after the final strain amplitude. First, at high strain amplitude, the high-q shoulder/peak shifts toward lower-q values and the intensity increases in the lower-q region after 10 hours. Second, the high-q shoulder/peak continues to shift to lower q-values even after the shear has ceased. This demonstrates that the shift in shoulder is in fact due to Ostwald ripening of droplets that proceeds regardless of whether or not the material is sheared, and not any reversible or irreversible changes in the nearest neighbor distribution of droplets due to yielding.

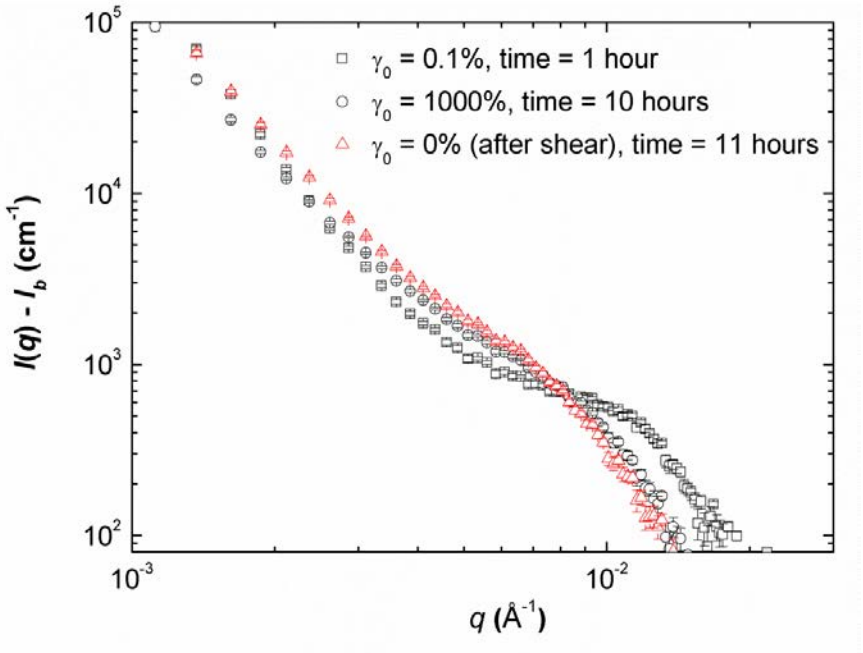

Figure C.5 Rheo-SANS spectra of nanoemulsion sample sample containing ϕ = 0.33 PDMS droplets with 33 vol. % PEGDA and C_s = 230 mM SDS in 50/50 (v/v) H_2O/D_2O at 0.1% (square), 1000% (circle), and 0% (triangle, after shear) strain amplitudes.